Controlling Waterglass Gelation for Binding Composite Bone Scaffolds

by

Marzieh Matinfar

A thesis submitted in partial fulfillment of the requirements for the degree of

Doctor of Philosophy

in

Materials Engineering

Department of Chemical and Materials Engineering

University of Alberta

Abstract

Bioactive glass bone scaffolds are promising for bone regeneration due to their ability to bond with bone, but current processing techniques face challenges, particularly regarding heat treatment and formability. To address these issues, our lab explored a new approach by creating formable composite scaffolds using 45S5 bioactive glass powder mixed with a sodium silicate binder (waterglass). However, achieving clinically practical setting times remained a challenge.

This dissertation addresses this issue by optimizing the sol-gel transition of sodium silicate solutions (waterglass) with acid initiators to create formable bioactive glass composites. Since the setting of the composite depends on waterglass gelation, the focus was on controlling this gelation process. Given the complex nature of waterglass and the existing knowledge gap compared to well-understood bioactive glass, the sol-gel transition of waterglass was the primary focus. The main goal was to reduce the gelation time of waterglass to a practical range, as well as to understand the relationship between processing conditions, molecular structure, and mechanical properties of the resulting gels. The experimental section was divided into three parts, each addressing a specific aspect related to the hypotheses: (1) gelation kinetics, (2) molecular structure, and (3) mechanical properties and microstructure.

In the first part of the research, by varying pH (from 2-11), waterglass concentration (from 15-50 wt.%), and acid initiator types (boric and phosphoric acids), the gelation time was successfully reduced from 10 days to ~10 minutes. The pH and waterglass concentration were found to significantly impact gelation kinetics and the final gel microstructure, while the type of acid was less significant. The gel point identified through a quantitative method (UV-VIS spectrophotometry) indicated the onset of gelation (~8 minutes), while the qualitative method (tube inversion) indicated the point where the gel network became rigid.

In the second part, molecular structure analysis using Raman spectroscopy revealed that basic gels contained higher-order silicate rings, with ~60-72% Q^3 units and ~10-17% Q^2 units, whereas acidic gels had ~70-80% lower-order silicate rings, predominantly Q^2 (~62-80%) and Q^0 (~20-38%). Moreover, real-time Raman spectroscopy revealed that gelation proceeds by agglomeration of silicate particle through physical interactions.

In the third part of the study, mechanical testing under compression showed that all hydrogels initially had similar strengths (7.3-9.9 MPa). Aging significantly increased their strength, with basic gels reaching 16.4-38.0 MPa and acidic gels reaching 21.2-53.7 MPa one hour after gelation. Engineering stress overestimated true stress by 21-66%. Real-time monitoring during compression, along with fractography, revealed radial, circumferential, and splitting cracks. Basic gels, with larger structural units, formed looser, mesh-like structures with large pores (3-5 µm), resulting in higher ductility and shrinking pores over time. In contrast, acidic gels, with smaller units, formed dense, brittle gels with small pores and strong internal connections.

This research provides a detailed understanding of the sol-gel transition in sodium silicate solutions, highlighting the influence of processing condition on gelation kinetics, molecular structure, and mechanical properties. These insights facilitate the design of optimized bioactive glass scaffolds, improving their clinical applicability for bone regeneration by enabling tailored scaffold properties.

Preface

This dissertation is an original work by Marzieh Matinfar. The review on sodium silicate solutions embodied in Chapter 2, section 2.2 of this dissertation has been published as a review paper: M. Matinfar and John A. Nychka, "A review of sodium silicate solutions: Structure, gelation, and syneresis." *Advances in Colloid and Interface Science* (2023). I was responsible for conceptualization, visualization, and writing the original draft with substantial feedback and ideas from J.A. Nychka. Chapter 3 of this dissertation is a manuscript in preparation with authors M. Matinfar and J. A. Nychka. I was responsible for the study design, data collection, analysis, and manuscript preparation with substantial feedback and ideas from J.A. Nychka. Chapter 4 of this dissertation is a manuscript in preparation with authors M. Matinfar and J. A. Nychka. I was responsible for the study design, data collection, analysis, and manuscript preparation with substantial feedback and ideas from J.A. Nychka. Appendix B of this dissertation is to be included with this latter publication as supplementary materials. Chapter 5 of this dissertation is a manuscript in preparation with authors M. Matinfar., A. Elias, and J. A. Nychka. I was responsible for the study design, data collection, analysis, and manuscript preparation with feedback and ideas from A. Elias along with use of her equipment. J.A. Nychka provided substantial feedback and ideas for the research and manuscript as well as experimental design and innovative apparatus fabrication.

To forever learners

Acknowledgement

I am extremely grateful to my supervisor, Dr. John Nychka. John has been much more than a supervisor; he has been a mentor, a guide, a supporter, and an inspiration. His wisdom, patience, and mindset have shaped my growth not only as a scientist, but also as a human being. His commitment to excellence and genuine care for my development have been invaluable throughout this journey. His unique way of seeing the world has opened my eyes to new possibilities and enriched my research in countless ways.

I would also like to extend my gratitude to my committee members, Dr. Anastasia Elias, and Dr. Hyo-Jick Choi, and in addition, Dr. Jonathan Veinot, for their valuable guidance and feedback throughout this journey. I deeply appreciate their time and expertise. Special thanks to Anastasia Elias for taking over my supervision during my supervisor's medical leave, allowing me to use her lab equipment, and being incredibly supportive.

Being far from home, I was blessed with great friends and colleagues in the *mati* research team, who felt like a research family. Many thanks to Terry Runyon, Kalan Kucera, Azin Vasegh, Laura Munevar, Caitlin Guzzo, Kendra Hartley, Jonathan Backs, and Omnath Ekambaram. Special thanks to Kalan for his valuable comments that greatly enhanced the clarity and quality of my review paper on sodium silicate solutions (section 2.2 of this dissertation), and more importantly, for being a great friend!

I would like to thank those who trained me on essential equipment. Thanks to the University of Alberta nanoFAB staff, including Nastaran Yousefi and XueHai Tan, for their help and guidance with SEM images, Raman spectroscopy, and UV-VIS spectrophotometry data. Thanks to Joshua Cunningham at the Elias lab for helping me with the uniaxial compression test. Also, thanks to Shiraz Merali for his help with preliminary experiments.

There were also people who didn't directly contribute to this dissertation but had a great impact on my PhD journey: Dr. Beth Lee.

I want to express my heartfelt gratitude to my family who made this journey possible. To my loving husband and best friend, Soroush, whose support has been the quiet force driving me forward. Thank you for keeping me sane with your constant love, encouragement, and care—

reminding me there is life beyond academia. I am truly grateful for you. To my parents, who have always made me feel special and warmed my heart along the way.

Valuable financial support was provided by The Natural Sciences and Engineering Research Council of Canada (NSERC) under grant RGPIN 2019-05379.

Contents

List of Tables

List of Figures

Chapter 1: Introduction

1.1. Problematization

Bone intrinsically demonstrates remarkable regenerative properties. The highly complex and dynamic process of regeneration occurs at different time and length scales and allows the bone to restore to its original form and function[1]. However, the healing capacity of bone is delayed or impaired by critically sized defects and open fractures caused by trauma, infection or diseases. Other factors like aging and comorbidities may also cause a reduction in the healing property of bone[2]. The treatment of these situations remains a clinical challenge. Delayed or non-union healing significantly affect the quality of life for the patient and increases the associate costs, especially in the elderly population[3]. Bone autografts (which are harvested from a donor site and implanted in the same patient) are considered the gold standard due to their osteogenic, osteoconductive (i.e., a stable bond to bone), and osteoinductive characteristics (i.e., induce osteogenic differentiation of the stem cells and osteoblasts to stimulate new bone formation). However, the need for multiple surgeries, potential morbidity, shape restrictions, insufficient quantity and complications associated with harvesting limit the clinical usage of autografts[4,5]. Allografts (harvested from human donors) and xenografts (harvested from other species) on the other hand, eliminate the need for a second surgery but may cause an immune response and there is risk of disease transmission[6]. These drawbacks motivated the development of effective and readily available bone graft substitutes. An engineered bone substitute that can mimic the structure and function of bone and ultimately be replaced by new bone would be ideal as an alternative solution. Bone substitute can be defined as "*a synthetic, inorganic or biologically organic combination-"biomaterial"- which can be inserted for the treatment of a bone defect instead of autogenous or allogenous bone*" (ref[7], p. 17). The number of procedures requiring bone implant materials is increasing, and probably will continue to rise as the aging population is increasing[8]. A $2.58 billion USD market was estimated for the global bone grafts and substitutes in 2018 and is expected to witness a CAGR[i] of 4.1% until 2026[9]. Nevertheless, so far, no product on the market fully satisfies the need for a material that performs as well as autografts without the associated risks.

---

[i] Compound Annual Growth Rate

Introduced by Langer and Vacanti[10], tissue engineering aims to provide a permanent solution for the repair and regeneration of tissues using cells, factors, and biomaterials alone or in combination. Bone tissue engineering (BTE) is a promising approach for bone regeneration as it has lower risk of disease transmission, infection and immune response, and vast availability. In BTE a 3D structure—a scaffold—is required to mimic the bone structure so that new bone tissue will grow in a 3D manner. Scaffolds made of engineered biomaterials are, in general, designed to act as temporary skeleton that provides an appropriate environment and mechanical stability supporting cell adhesion, migration, proliferation, and differentiation with the goal of new bone tissue formation.

The choice of suitable material is the first challenge in designing a biomaterial. A wide range of metallic, ceramic, natural and synthetic polymeric biomaterials, and their composites have been investigated for BTE. While many of these materials provide structural support and biocompatible surfaces for cell attachment and proliferation, they often lack stimuli that guide tissue-specific cellular responses and differentiation[11]. The problem that arises is the lack of interface between the implant and the tissue which triggers the immune system to isolate the implant from the host tissue through fibrous encapsulation. As opposed to these nearly "inert" materials, the concept of bioactive materials was introduced based on a hypothesis that a material that is able to form a hydroxyapatite (HA) layer *in vivo*, may not be rejected by the body because it mimics the mineral component of bone. This idea led to the revolutionary discovery of Bioglass® by Hench in 1969[12]. After exploring different glass formulation in the Na_2O–CaO– SiO_2–P_2O_5 oxide system, Hench selected the composition of 45% SiO_2-24.5% Na_2O-24.5% CaO-6% P_2O_5 which is close to a ternary eutectic. This glass composition termed as 45S5 Bioglass®, was the first synthetic bioactive material with the capability of bonding to living bone and tissues, without the formation of any fibrous layer. This discovery launched the field of bioactive ceramics, including bioactive glasses, glass-ceramics and ceramics such as synthetic HA and other calcium phosphates.

Bioactive glasses are not only osteoconductive[13], but also osteoinductive[14]; meaning that they support new bone growth along the bone–implant interface as well as within the implant. These glasses offer the advantage of stimulating bone regeneration at higher rates in contrast with other bioactive ceramics such as HA[15]. Surprisingly, after many years of research on bioactive glasses by numerous research groups, no other bioactive glass composition has been found to have better biological properties than the original Bioglass® 45S5 composition[16]. Being implanted in millions of patients, 45S5 glass has proved to be safe and effective in BTE applications. While all these features make Bioglass® an attractive biomaterial, it has some limitations as a scaffold material. One major issue is the difficulty of processing it into a porous 3D scaffold. All the well-known processing techniques (such as sponge replica method, foaming methods, sol-gel, freeze casting, freeze drying etc.) involve sintering the glass particles in order to bond them into the desired 3D structure. However, the 45S5 glass has poor workability due its narrow sintering window (the temperature difference between T_g[i] and $T_{c,onset}$[ii]) and usually devitrifies into a crystalline phase[16]. While this consolidation step improves the strength of the final scaffold, the full or partial transformation between the amorphous and crystalline phase adversely affects the bioactivity by altering the dissolution profile[17]. The current trend to suppress crystallization of phases in bioactive glasses is using additives (such as such as K_2O and MgO[18]) to widen the sintering window; again, at the expense of bioactivity. Therefore, it is quite a challenge to design a glass scaffold that can be sintered without crystallizing and also remain bioactive and mechanically stable. Moreover, surgeons prefer implants that can be easily cut/shaped in response to each patient's need; something that can not be achieved by already-shaped implants of fixed size. A ''one size fits all'' mentality would be unrealistic in the context of heterogeneous anatomy and physiology along with site specific considerations[19]. Traditional scaffolds need to be made *ex-situ* and are often formed in a mass. Therefore, they cannot fill the bone defect and there is no way to adhere pieces together (other than bone cement). Additive manufacturing (AM) or rapid prototyping methods can be very suitable for producing scaffolds with customized shapes and microarchitectures. However, bulk forming does not allow for the conformal application of a scaffold to undercuts. Another aspect that limits the use of AM techniques in clinical applications is that they are costly and time-consuming, as they require the use of a 3D model of the bone defect, usually acquired by micro-CT[iii,20]. Therefore, none of these *ex-situ* methods are in widespread clinical use.

In respond to this need, a number of Bioglass®-based products have been commercially developed that can be directly pressed into bone defects. The first one was PerioGlas® which was

---

[i] Glass Transition Temperature
[ii] Onset crystallization temperature
[iii] Computed Tomography

approved by FDA in 1993 and is used for repairing jawbone defects caused by periodontal diseases. Another example is NovaBone® that was cleared in 1999 for orthopedic bone grafting in non-load-bearing sites. These products are usually mixed with the patient's blood to obtain a putty-like consistency to completely fill the bone defect[16]. Products based on bioactive glasses still are limited to small bones or non-load bearing sites and would shatter or deform if utilized solely in large bone repairs. In some cases, metal screws and hooks are needed to secure them in place, and existing products cannot support such mechanical fasteners.

The full potential of bioactive glasses in bone regeneration is still yet to be fully exploited, and research for finding the "ideal" scaffold is still ongoing. While Bioglass® is a promising biomaterial, the question of "How to make the ideal scaffold from Bioglass®" remains unanswered. Despite the increasing quantity of research and discoveries, a gap usually exists between research and clinical application/commercialization. This gap can be termed as the "valley of death"; as a large number of attempts "die" in between[21]. Generally, the "valley of death" is particularly large for tissue engineering due to the high costs associated and/or the long path of gaining clinical approval by regulatory bodies. Designing and manufacturing processes are believed to be the gatekeepers to translate a research into clinical applications and the development of these entities will enable to bridge the gap between research and clinical practice[21,22]. It is critical to assess the challenges and clinical demands in choosing the manufacturing process to take a bone scaffold from bench to bedside.

Based on the reviewed challenges in processing bone scaffolds made of bioactive glasses (from both traditional ceramic processing and additive manufacturing methods), developing a new processing route for fabricating bioactive glass bone tissue scaffolds seems a serious need. A process method which involves neither heat for consolidating nor polymers to bind the ceramic; does not require additive manufacturing machines, CT scans, 3D models, and high-tech processes; and creates a porous and bioactive scaffold at room temperature. A sophisticated processing route will not necessarily have a high level of complexity. Suppose, as a design concept, we have a formable paste made by mixing powder and liquid that a surgeon can easily press into the shape of a bone defect in a patient, and let the implant set and harden in minutes.

I explored a design to develop a formable, in-situ setting bone tissue scaffold that is mechanically stable and degrades in a way that effectively stimulates bone regeneration. The proof-of-concept work, detailed in the next section, led to the development of a method for mixing sodium silicate solution (also known as waterglass) with 45S5 bioactive glass frit to create a formable paste capable of filling bone defects of various sizes and shapes. This paste sets through acidification of the sodium silicate solution, leading to the formation of a silica gel.

Blood putties, such as NovaBone®, while providing controlled degradation through their composition and some degree of mechanical integrity, do not "set" in place, which makes them less stable and less effective at locking into position in contrast to binders that form a gel in-situ. A binder such as waterglass offers customizable gelation kinetics—allowing surgeons to control setting times and match the specific needs of a procedure. In-situ gelation provides better mechanical stability and ensures the scaffold remains securely in place over time. This stability is specifically important for surgeries requiring sustained structural support and long-term tissue regeneration. Control over the gelation kinetics and mechanical properties of the waterglass binder is crucial, as it directly impacts the setting time and mechanical properties of the final composite scaffold. Achieving this control requires a fundamental understanding of the chemistry of waterglass, its gelation mechanism, the mechanical properties of silica gels, and the factors affecting gelation kinetics and mechanical properties.

Based on this background, the main research question proposed herein is: "***How can the processing conditions be optimized so that the waterglass binder transforms into silica gel with a gelation time and mechanical properties suitable for effective bone tissue scaffold applications?***"

1.2. Proof of concept work

The starting point for this research extends from the prior proof-of-concept work by Caitlin Guzzo[23,24] (a former MSc student). Guzzo's work aimed to explore the possibility of creating a porous and formable ceramic composite scaffold without using high temperatures for powder consolidation (i.e., processing at ambient temperature). The process involved mixing 45S5 bioactive glass frit and sodium silicate solution (waterglass) as a binder, creating an air-setting paste that sets in-situ to form a 3D porous bone scaffold capable of bearing loads. The results showed that the obtained paste was formable enough to fill and compact into a variety of geometries and that the final composite was porous, which is crucial for bone regeneration (Figure

1.1). Although the proof-of-concept demonstrated that forming a self-setting porous and formable ceramic composite scaffold was possible at ambient temperature, the setting time of approximately 10 days made it impractical for clinical application and surgery. Addressing this setting time issue is the main driving force for the present study, with the primary goal of accelerating the setting reaction and decreasing the setting time to a range practical for clinical applications.

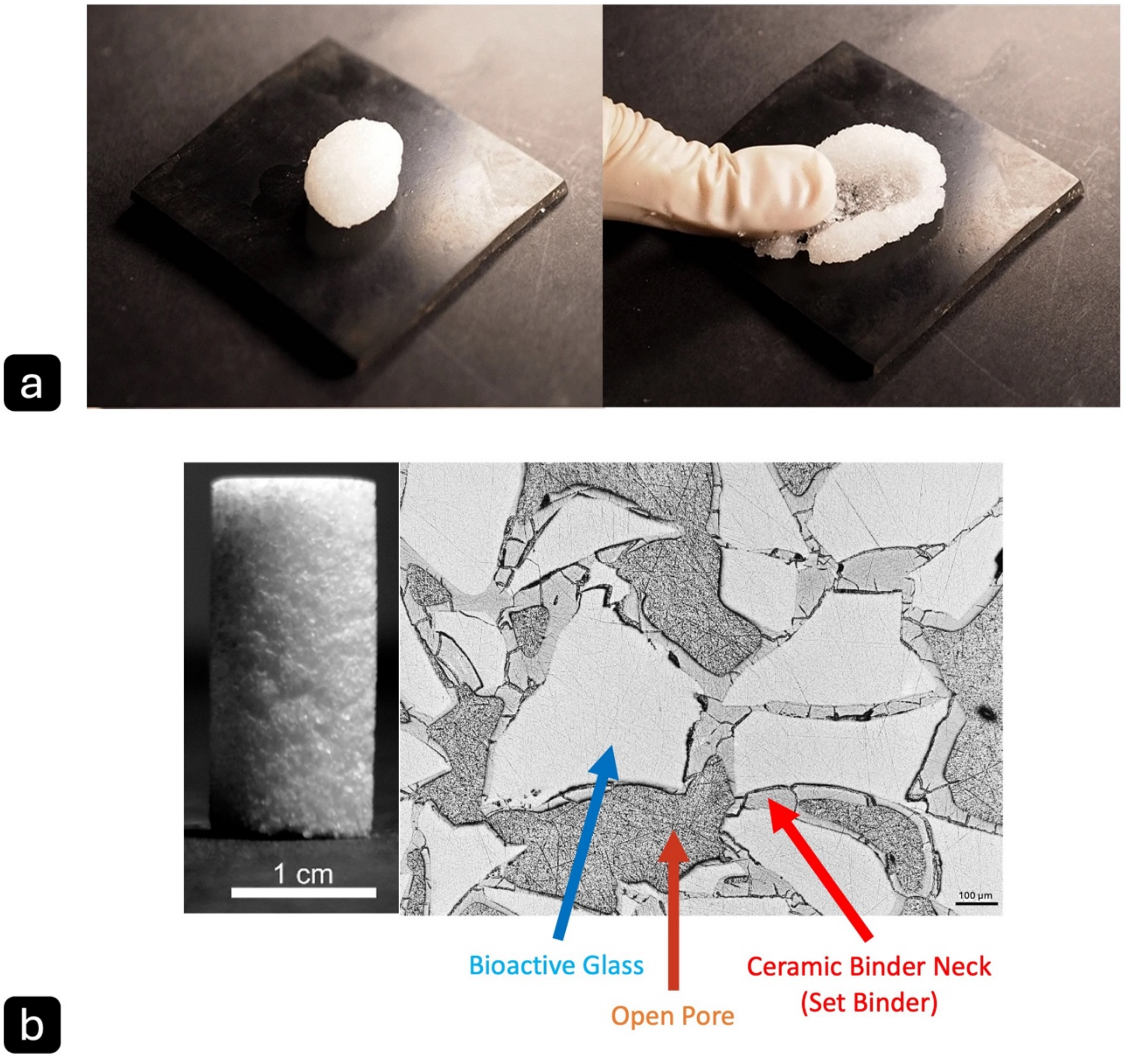

Figure 1.1 (a) a hand-formed mass of unset composite paste (left) and manual shearing of the paste (right), illustrating its formability and cohesion before setting, from ref[23]; (b) photo (left) and cross-sectional optical light microscopy micrograph (right) of porous bioactive glass-waterglass composite set in air, from ref[24].

Waterglass was chosen as a binder phase for its ability to set in air at room temperature. One important example is the carbon-dioxide process in foundry work, where sand is mixed with sodium silicate and carbon dioxide gas is passed through the compacted sand to harden the binder[25]. The approach herein is to create a formable tissue scaffold using two components: bioactive glass particles, and a liquid binder. When mixed, the bioactive glass particles are held in place by a silicate-based binder that wets the particles and then hardens upon exposure to carbon dioxide gas. Sodium silicate solution has been very successful in agglomeration processes that combine or consolidate fines or small particles into larger units[26,27]. Consolidation occurs as a result of the *in situ* formation of alkali silicate gels which act as bridges between the particles. The slow reaction rate between atmospheric CO_2 and the binder resulted in the long setting times in Guzzo's work. Therefore, it was hypothesized that the setting time could be accelerated by using concentrated carbon dioxide gas, which is often already present in an operating room. Moreover, in this application, washing the gels or performing ion exchange after setting is not feasible. Therefore, waterglass is a preferable choice over alkoxides such as TMOS or TEOS, which can be costly, and are also toxic unless the alcohol is fully removed.

To test this hypothesis, a set of preliminary experiments was performed, the details which can be found in Appendix A. The results demonstrated that the setting time of the composite could be reduced to less than ten minutes by applying concentrated CO_2 gas while maintaining shape retention and stability. However, there were major drawbacks to this method:

- Lack of repeatability
- Mass transport limitations at surface
- Being limited to a narrow basic pH range, despite the properties of silica gels being highly dependent on their pH

Due to these limitations, the research direction had to be changed. The first step was to understand the chemistry and gelation mechanism in waterglass, leading to extensive research and a comprehensive review paper on these solutions (section 2.2). After understanding the fundamentals, the project shifted to using acid solutions, instead of CO_2 gas, to induce volume mediated accelerated gelation (that is, silica gel formation from waterglass) and consequently, setting in composite scaffolds. As illustrated in Figure 1.2, the CO_2 method is surface-dependent, where a thin surface layer of silica gel forms and hinders further inward diffusion of CO_2, thereby limiting complete gelation of the entire volume. On the other hand, the acid initiation method is volume-independent, as hydrogen ions are uniformly dispersed and distributed, promoting homogenous gelation throughout the entire scaffold.

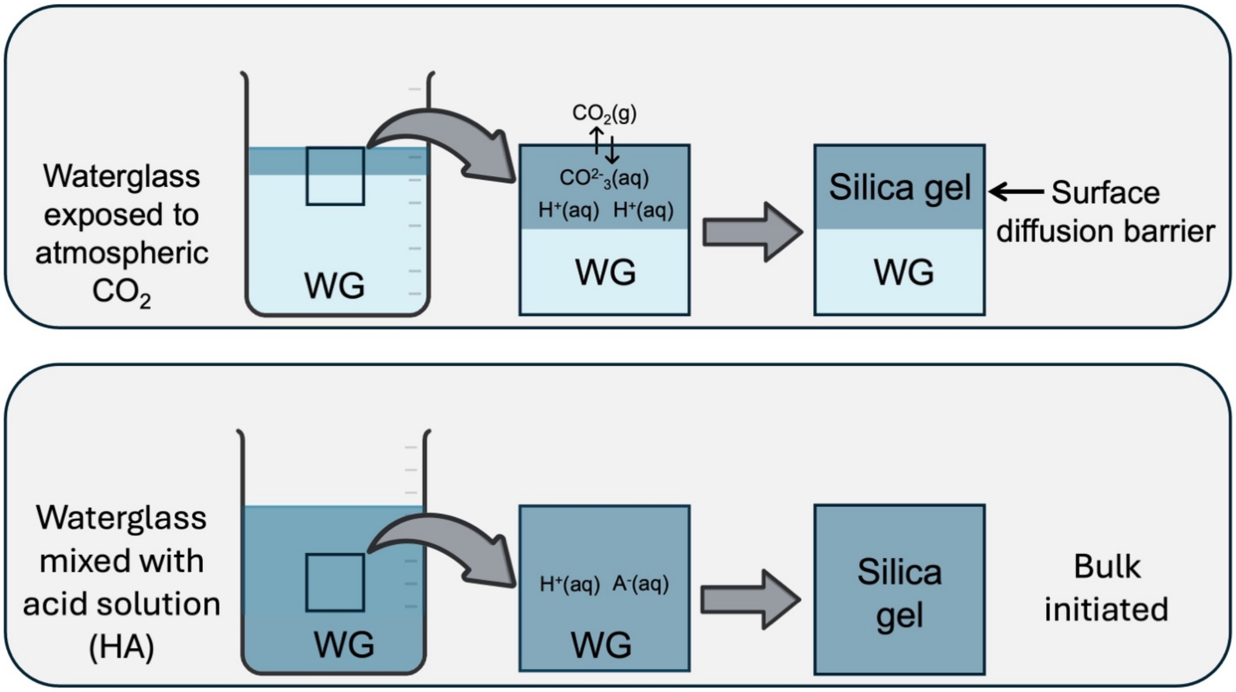

Figure 1.2 Schematic of the CO_2 and acid-initiated gelation mechanisms in waterglass. The CO_2 method is surface-dependent, where a thin silica gel layer forms on the surface, restricting further CO_2 diffusion and preventing complete gelation. In contrast, the acid initiation method is volume-independent, with hydrogen ions being evenly dispersed and distributed throughout the solution, enabling uniform gelation within the entire volume.

1.3. Objectives

The study was conducted to develop a workable, formable paste that can be inserted inside a bone defect of any size and shape and sets *in situ* into a rigid, porous 3D structure, promoting bone tissue regrowth in a safe and effective manner. The long-term objectives, as set by the grant application that funded this project[28], were to:

1) change how we design with glasses for use in bone tissue scaffolds;
2) create new ways of processing such materials for health benefits to Canadians;
3) surpass existing assumptions about how glasses should, and can be made to behave.

The goal of this work is to optimize the processing conditions of silica gels from waterglass and to control and predict their gelation kinetics, microstructure, and mechanical properties in the gel state over time. Since the structure and properties of silica gel directly influence the properties of waterglass-bioactive glass composite scaffolds, controlling these properties will enable us to create a formable composite material that can be formed and set *in situ* while maintaining open porosity and mechanical stability after implantation.

The short-term objectives of this work were to:

1. Develop a fundamental understanding of sodium silicate solution chemistry and its gelation mechanism to identify the parameters controlling gelation;
2. Determine the effect of the identified key processing variables on gelation kinetics by measuring gelation time, aiming to reduce the gelation to a clinically practical range of around 10 minutes;
3. Investigate the effect of the aforementioned processing variables on the optical properties of silica gels, including light scattering and transmittance, to gain insights into both gelation kinetics and the resulting gel structure;
4. Develop a quantitative understanding of the sol-gel transition and final gel structure of sodium silicate solutions at the macro and molecular level, and how processing variables impact this process, through real-time chemical analysis;
5. Assess the mechanical properties of silica gels under various conditions in their hydrogel state over time, including engineering and true compressive strengths, as well as deformation and failure analysis through real-time monitoring during compression tests;
6. Assess the microstructure, including morphology, pore size, and pore distribution of silica gels produced under different conditions over time;
7. Establish a connection between all obtained results to form a comprehensive processing-structure-property relationship for silica gels made from sodium silicate solutions.

1.4. Hypotheses

1.4.1. Hypothesis one

Acidifying waterglass binder with acid solutions will decrease its gelation time, and consequently the composite setting time, as a function of pH, waterglass concentration and type of acid used.

In a waterglass-bioactive glass mixture, waterglass binds grains of bioactive glass together to create a formable paste. Upon gelation of waterglass, the entire mixture hardens, making the composite's setting time dependent on the waterglass gelation time. Gelation or hardening upon acidification of waterglass occurs due to the hydrolysis and condensation reactions of the silicate species in the solution, ultimately forming a 3D gel network. In previous proof-of-concept work by Guzzo[23,24], acidification was achieved via atmospheric CO_2 being naturally dissolved in waterglass, which was a very slow process. My initial hypothesis was that using concentrated CO_2 gas would accelerate the reaction. However, preliminary experiments (Appendix A) revealed significant drawbacks with this method. Based on the preliminary results, I hypothesized that using an acid solution would offer major advantages over acidification by gassing, such as:

- Achieving a homogeneous mixture of acid and waterglass solution
- Eliminating the surface diffusion-limited barrier
- Attaining a wide range of pH levels for increased control of the gelation time

To meet research objective (1), extensive research was conducted on the available literature, resulting in a comprehensive review paper presented in Chapter 2 (section 2.2). Through this research I identified key parameters influencing the gelation of sodium silicate solutions, including pH, waterglass concentration, SiO_2/Na_2O ratio of waterglass, temperature, type of acid catalyst, and the presence of alkali ions. By using commercial waterglass, with no additives, and working at ambient temperatures, I narrowed down the independent variables to three: pH, waterglass concentration, and type of acid.

To test hypothesis (1) and achieve research objectives (2) and (3), I examined how independent processing variables—pH, waterglass concentration, and type of acid—affect gelation kinetics. I studied gelation kinetics using the tube inversion method and by analyzing optical properties. Additionally, I explored the relationship between optical properties and the final gel microstructure. All results are detailed in Chapter 3. The results confirmed hypothesis (1); the gelation time, and consequently the composite setting time, can be reduced from many days to few minutes. The type of acid used had a less significant effect than the impact of pH and waterglass concentration.

1.4.2. Hypothesis two

The pH, waterglass concentration, and the type of acid used significantly influence the molecular structure and the final microstructure of silica gels, enabling the formation of silica gels with tailored structures at a fixed gelation time.

A comprehensive review of waterglass solutions revealed a significant knowledge gap in the fundamental understanding of their sol-gel transitions at the molecular level. After evaluating the advantages and disadvantages of various chemical analysis techniques, I determined that real-time Raman spectroscopy was the most suitable method for studying sol-gel transitions in real-time in these solutions. To address the knowledge gap in the field, test hypothesis (2), and achieve objective (4), I performed real-time Raman spectroscopy on acid-initiated waterglass solutions under different processing conditions. The results were analyzed at various length scales, from molecular to particle and agglomerate levels, as well as microstructure. Additionally, connections were found between these results and those from testing hypothesis (1). All findings are detailed in Chapter 4. The results confirmed hypothesis (2): it was indeed possible to produce silica gels with the same gelation time but significantly different structures. pH emerged as the most significant variable affecting the molecular structure. Both pH and waterglass concentration played significant roles in shaping the microstructure. However, as the waterglass concentration decreased, the microstructure became increasingly similar, even across samples with different pH levels. The type of acid used had a less significant effect compared with pH and waterglass concentration.

1.4.3. Hypothesis three

The pH, waterglass concentration, type of acid used, and time significantly influence the mechanical properties, deformation behavior, and microstructure of silica gels, enabling the formation of silica gels with tailored mechanical properties at a fixed gelation time.

Based on hypothesis (2), it is possible to produce silica gels with the same gelation time—suitable for clinical applications—that exhibit different structures depending on the processing conditions. Consequently, I hypothesized that these gels would also have varying mechanical properties despite having the same gelation time.

After gelation, the gel undergoes an aging process where the network continues to develop, expels liquid, and shrinks. This gradual process increases the gel's strength over time. In other words, there is an initial rapid hardening at the gelation point, followed by a continued increase in strength. The rate of aging is influenced by the final gel structure, which in turn depends on the processing conditions. Thus, time was considered as a fourth independent variable for this particular hypothesis.

The ultimate goal was to create a silica gel that provides sufficient strength to the bioactive glass paste so it can retain its shape and stabilize within a bone defect. To address this goal, mechanical properties should be evaluated, not only in terms of strength, but also considering deformation mechanisms and ductility or brittleness.

To test hypothesis (3) and achieve research objectives (5) and (6), I assessed the mechanical properties of silica gels under uniaxial compression and monitored the instantaneous cross-sectional area in real-time. For objective (7), I integrated the results from all three hypotheses to complete the processing-structure-property relationship for silica gels derived from waterglass. All findings are detailed in Chapter 5. The results confirmed hypothesis (3): silica gels with different mechanical properties and same gelation time were fabricated. The effect of type of acid on mechanical properties and microstructure were found to be less significant than pH and waterglass concentration. Time had a significant positive impact on mechanical properties due to aging.

Chapter 2: Literature Review

2.1. Bioactive glasses

2.1.1. Why bioactive glass, and why 45S5?

Scaffolds play a key role in bone tissue engineering (BTE) as they mimic the mechanical and biological functions of the bone. Researchers *almost* agree on a set of criteria that needs to be met in order for scaffolds to serve their functions:

1) biocompatibility to support cellular activity without toxicity or inflammatory reaction; 2) biodegradability with a controllable degradation rate that let the scaffolds to be gradually replaced by the host tissue; 3) mechanical stability to maintain integrity and bear loads; 4) architecture with interconnected open pores to allow for cell migration, nutrient and metabolite transfer, vascularization and tissue ingrowth; 5) bioactivity so it can directly bond to the host tissue and create a stable interface; 6) osteoconductivity and osteoinductivity to enhance osteoblast attachment, migration, and proliferation and to induce differentiation; 7) be tailored into different shapes and sizes to allow in-situ treatment of individual patient bone defects; 8) be reproducible and sterilizable for commercial production and clinical use.

Materials currently used in bone repair and regeneration include metals, bioceramics, natural and synthetic polymers, hydrogels and related composites. Metals and metal alloys are generally not considered desirable for BTE due to the lack of biodegradability and biological recognition[1,2]. While magnesium, zinc, and iron alloys are considered biodegradable in this group[3], they may inhibit bone formation markers and release metal ions that can cause inflammatory responses in the host body[4]. Natural and synthetic polymers have been widely used as bone scaffolds due to their biocompatibility, degradability and ease of processing[5]. However, single polymeric scaffolds are usually poor in mechanical strength. Nowadays research is mainly focused on hybrid ceramic/polymer scaffolds[6,7].

Bioceramics including amorphous glasses, crystalline ceramics, glass-ceramics and their composites have been very promising in the field of BTE. Hydroxyapatite (HA) for example has been extensively used in bone scaffolds due to its excellent biocompatibility, chemical similarity to bone, osteoconductivity and osteoinductivity[8]. However, HA is more common as reinforcer (in form of fibers or nanoparticles) in polymer-based composites due to its slow degradation rate and brittleness[9]. Achieving a stable attachment to the host tissue is a key in determining the success of the biomaterial and the mechanism of this attachment is directly related to the type of tissue response at the tissue-implant interface[10]. The type of material response is mainly governed by its reactivity in physiological conditions[11]. Bioceramics are classified into four groups based on their tissue response: nearly inert (e.g., alumina and zirconia); bioactive (e.g., bioactive glass); resorbable (e.g., β-TCP[i]) and porous (e.g., HA coated metals)[12]. Nearly inert bioceramics are not good candidates for scaffolds as they trigger the immune system to form a fibrous layer on the implant surface which may result in complete encapsulation. This group of ceramics are generally used as femoral heads, acetabular cups for hip replacement or dental implants[13]. On the other hand, it was found that certain compositions of glasses, ceramics, glass-ceramics, and composites known as ‘‘bioactive" ceramics can form a mechanically strong bond to bone[14].

The concept of bioactivity was first introduced with the discovery of Bioglass® by Hench in 1969[15]. 45S5 Bioglass® was the first man-made bioactive material with capability of bonding to living bone and tissues, without encapsulation. The name of 45S5 was chosen to reflect the composition, which is 45% SiO_2–24.5% Na_2O–24.5% CaO–6% P_2O_5. A common characteristic in all bioactive materials is the time-dependent formation of a biologically active hydroxycarbonate apatite (HCA) layer on the surface, which provides the bonding of tissue at the interface[14]. Therefore, a bioactive material was defined as: "A material that elicits a specific biological response at the interface of the material which results in the formation of a bond between the tissues and the material" (ref[10], p.75). The HCA phase formed on these bioactive materials is chemically and structurally similar to the bone mineral phase and is responsible for the direct chemical bond to bone[16]. This mineral phase is formed via a series of dissolution, precipitation and ion exchange processes occurring at the bioactive ceramic interface, which eventually results in extracellular matrix formation[17].

Hench[18] classified bioactive materials into two types of class A and class B based on their level of reactivity with the surrounding tissue. Class A bioactive materials are both osteoconductive and

---

[i] TriCalcium Phosphate

osteoproductive[i], being able to bond to both bone and soft tissue. In contrast, class B bioactive materials are only osteoconductive. Relative bioactivity and time dependence of formation of interfacial bone bonding for various bioceramics are shown in Figure 2.1. Bioactive glasses belong to class A, and as can be seen in Figure 2.1, they exhibit higher rates of HCA and bone-bonding formation compared to other bioceramics (with Bioglass® being the top); making them promising materials in bone tissue engineering. This feature is attributed to the stimulatory effect of their ionic dissolution products (e.g., Si, Ca, P), which ultimately results in the formation of a hydrated silica and HCA bilayer on the glass surface.

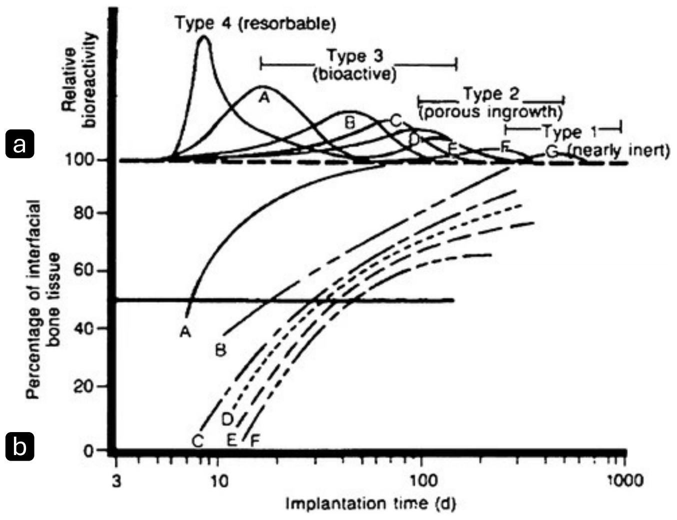

Figure 2.1 (a) Relative rate of bioreactivity and (b) Time dependency of bone formation.at implant interface for various biocerarnic implants ((A) 45S5 Bioglass® (6) KGS CeravitaP (C) 5584 3 Bioglass® (D) A/W glass-ceramic (E) HA (F) KGX Ceravitala', and (G) Al_2O_3-Si_3N_4 . Adapted from [20].

According to Hench[14], the formation of an HCA layer on bioactive glasses occurs in five stages (See Figure 2.2a). Briefly, the first reactions are the ion exchange between the alkali in the glass and water (stage I). This is followed by the rupture of the Si–O–Si bonds in the silica network (stage II), forming silanols that condensate and repolymerize to form a hydrated silica gel on the glass surface (stage III). This silica gel layer facilitates the formation an amorphous calcium phosphate layer through ion exchange between the glass and the media (stage IV), which then incorporates carbonate species that crystallize into HCA (stage V).

---

[i] “The process whereby a bioactive surface is colonized by osteogenic stem cells free in the defect environment as a result of surgical intervention.” ([19], p.495)

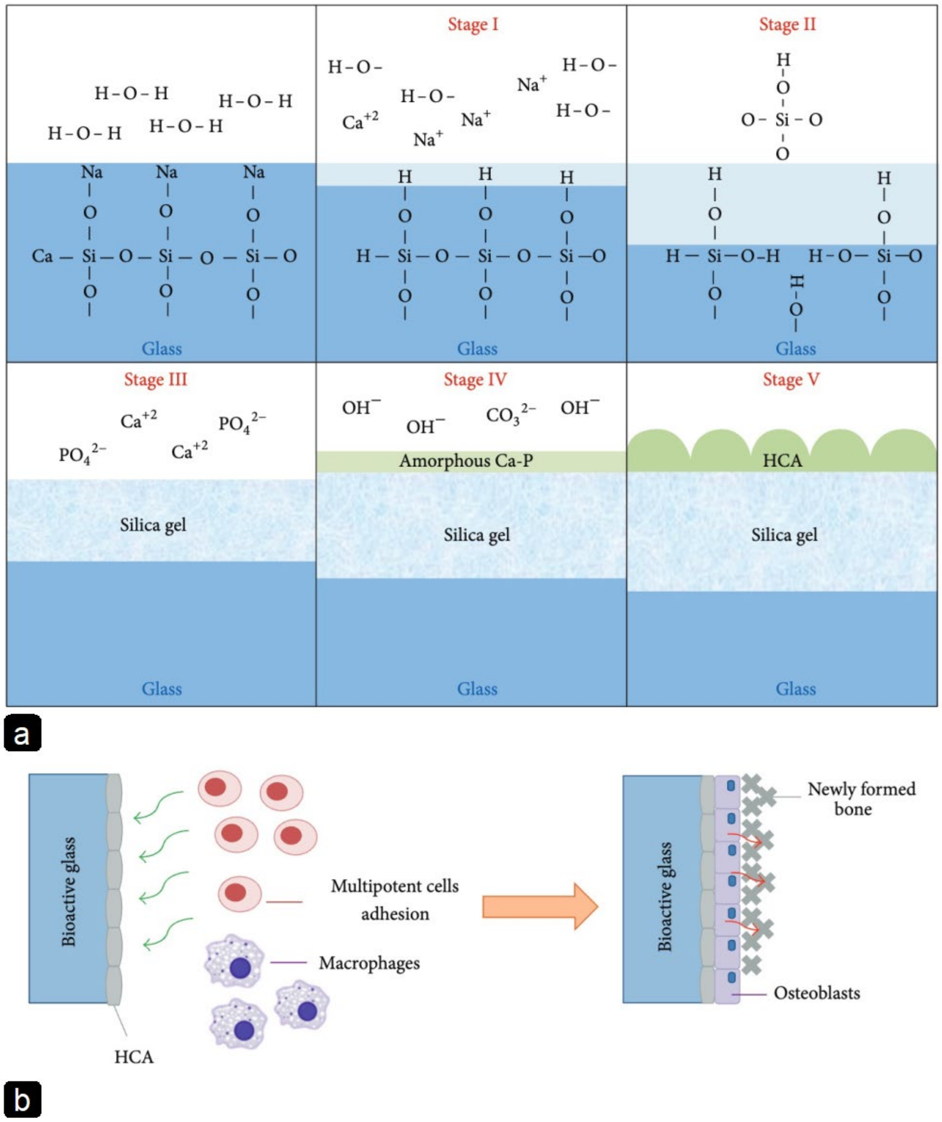

Figure 2.2 (a) Illustration of five stages of hydroxycarbonate apatite (HCA) formation on the surface of a bioactive glass in contact with body fluids (b) Schematic showing the adhesion of cells to the HCA layer formed on the glass surface, which leads to new bone formation. Adapted from [21].

To form a direct bond with bone, the timing of stages IV and V must align with the natural biomineralization process that occurs *in vivo*. Although the biological events preceding bone bonding are still being elucidated, it is known that extracellular proteins, primarily fibronectin, attract macrophages, mesenchymal stem cells, and osteoprogenitor cells[22]. Subsequently, osteoprogenitor cells proliferate and differentiate into osteoblasts, which initiate the synthesis and deposition of the organic matrix[23]. This organic matrix then undergoes a gradual mineralization process guided by osteoblastic cells, as illustrated in Figure 2.2b.

Generally, bioactive glasses can be synthesized using two methods: the melt-quenching route or the sol–gel route. The traditional melting method involves melting the precursors of the glass oxides inside a platinum/graphite crucible and then quenching either into graphite molds in order to obtain bulk pieces (rods or monoliths) or into water to obtain a frit[i,25]. The sol-gel is a wet chemistry process that involves creating a sol by mixing the metal-alkoxides in a solution that then undergoes hydrolysis, condensation and gelation. To obtain the glass material, the gel is aged, dried, stabilized and finally heat treated at low temperatures (600-700°C)[26,27]. Sol-gel glasses intrinsically have high level of porosity (in mesoporous range) and surface area, while melt-derived bioactive glasses are usually in the form of highly dense monoliths; resulting in higher solubility and bioactivity of sol-gel–derived glasses[28]. Moreover, sol-gel method offers advantages such as the possibility to simplify the glass formulation (Na_2O is no longer needed to lower the melting temperature), a broader range of bioactivity, and a better control of bioactivity by changing processing parameters. However, it is almost impossible to obtain crack-free glass monoliths (if diameter >1 cm) by sol–gel synthesis due to the large shrinkage that occurs during drying and evaporation of the liquid by-products of the condensation reaction[25,26].

The compositional range for bonding of bioactive glasses and glass-ceramics to bone in ternary diagram of Na_2O–CaO–SiO_2 (with constant 6 wt% P_2O_5) is illustrated in Figure 2.3. It can be seen that bioactivity is extremely sensitive to the glass composition. The most bioactive glasses belong to the middle (region S) of the Na_2O–CaO–SiO_2 diagram (with 45S5 being the optimum)[12]. The original melt-derived 45S5 glass has poor workability and usually devitrifies into a crystalline phase ($Na_2O.2CaO.3SiO_2$) prior to densification[25]. This instability is due to its limited viscous flow ability above T_g and narrow sintering window. As a result, a sintered Bioglass® scaffold is actually a glass-ceramic or ceramic scaffold which would adversely affect its bioactivity. In order to maintain the bioactivity of 45S5 glasses, sintering can be done at relatively low temperatures to supress or reduce crystallization. However, sufficient densification will not occur at low temperatures and the obtained scaffolds would be fragile and loosely packed[29]. Lots of research

---

[i] A frit is composed by small chunks of glass, that are cracked due to residual stresses that are generated by thermal shock, and it is very useful in the production of glass powders, since it can be easily milled [24]

and effort have been done to optimize and/or create glass compositions with higher levels of bone-bonding activity, controlled dissolution properties, improved mechanical properties and better workability. By modifying 45S5 composition within the ternary system of Na_2O-CaO- SiO_2, other glass compositions with different properties such as wider sintering window have been achieved. However, this is usually at the expense of bioactivity. 13–93 glass for example (with higher SiO_2 content and additional network modifiers, such as K_2O and MgO), has more facile viscous flow behavior and less tendency to crystallize[30,31]. While 13–93 bioactive glass has been shown to be as effective as 45S5 in supporting the proliferation and function of osteoblastic cells *in vitro*[32], it may degrade more slowly (and have lower bioactivity) than 45S5 glass. Hench also introduced sol-gel silicate-based bioactive glasses with exceptionally fast apatite-forming ability in spite of their high silica content (from 60 to 90 mol%), owing to their ultrahigh specific surface area (well above $10m^2/g$ vs. less than $0.5m^2/g$ for melt-derived glasses)[26]. However, sol–gel glasses may degrade too rapidly for certain applications where the bone will take a long time to regenerate.

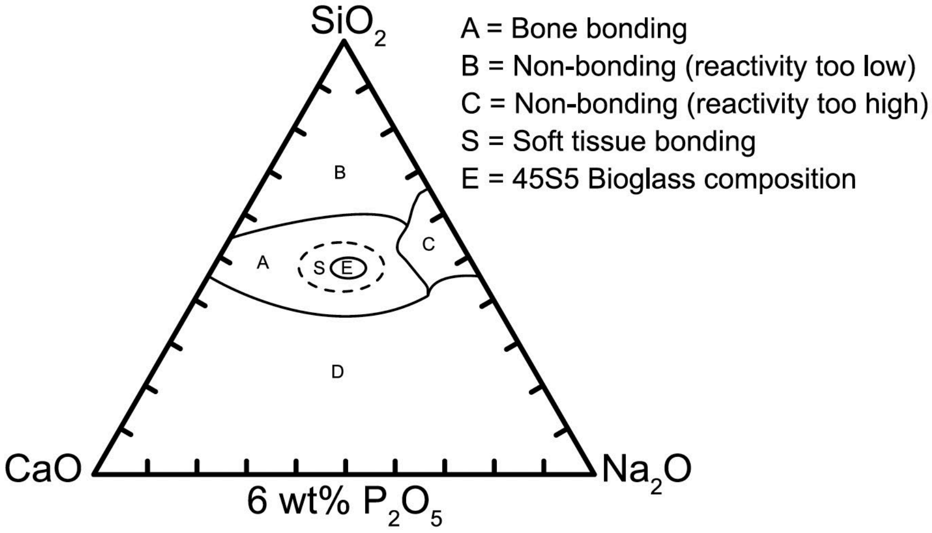

Figure 2.3 Compositional dependence (in wt.%) of bone bonding and soft tissue bonding of bioactive glasses (including 45S5 composition) and glass-ceramics. Adapted from[33].

Silicate glasses based on the SiO_2 network are not the only bioactive glasses; certain compositions in other systems such as borate[34–36] and phosphate[37,38] glasses have been also found to be bioactive. Phosphate glasses are based on the P_2O_5 glass-forming network with CaO and Na_2O as modifiers. The dissolution rate in these glasses can be varied from a few hours to months by incorporating metal oxides such as Fe_2O_3, Al_2O_3, ZnO, and TiO_2 into the structure[39]. Phosphate-based glasses can be prepared at relatively low temperatures and can be easily drawn into fibers[40]. Borate and borosilicate glasses can convert more quickly to HA compared with traditional silicate glasses due to their higher reactivity and lower chemical durability[41], and they can reach complete conversion into HA in less than 200h[42]. The complete degradation rate and bioactive properties of these glasses can be controlled within a wide range of time periods by replacing SiO_2 with B_2O_3. However, this change causes them to experience rapid decrease in strength with immersion in SBF[42].

In conclusion, bioactive glasses, particularly 45S5 Bioglass®, are excellent candidates for bone tissue engineering due to their unique combination of properties. Their ability to form a stable hydroxycarbonate apatite layer on the surface is crucial for direct bone bonding. They not only bond directly to bone, enhancing stability and integration, but also induce osteogenic differentiation and enhance osteoblast adhesion, growth, and proliferation, and bone formation. Moreover, bioactive glasses such as 45S5 are antibacterial due to the local increase in aqueous pH value during their dissolution[43]. Surgical-site infections (SSI) cause severe complications in orthopaedic and dental surgeries and increase health care costs through extending hospital stays and doubling rehospitalisation rates[44,45]. These features, along with the continuous advancements in optimizing bioactive glass compositions, make 45S5 an ideal material for developing effective and reliable bone scaffolds, offering promising solutions for bone repair and regeneration in clinical applications.

2.1.2. State-of-the-art

Despite the significant clinical potential of bioactive glasses, especially 45S5, their success is hindered by issues related to monolith bioactivity and osseoincorporation. To overcome these challenges, bone tissue scaffolds have been created using bioactive glasses. Generally, fabrication of bioactive glass-based scaffolds can be categorized into two main groups: conventional methods and additive manufacturing techniques (also referred to as RP[i] or SFF[ii])[25,46,47]. The first group of methods involves using a sacrificial template that act as a pore former to create a structure with desired shape and porosity. The second group involves layer-by-layer or piece-by-piece deposition starting from a computer-aided design (CAD) or a computed tomography (CT) model. It is

---

[i] Rapid Prototyping
[ii] Solid Free-form Fabrication

important to notice that almost all the typical methods used for glass-based scaffold fabrication involve a final consolidation step (high-temperature sintering). This high temperature step is a crucial issue since it has a negative impact on bioactivity. To date, no single fabrication method currently fulfills all the required design criteria for bone scaffolds. Here, we briefly go over some of the most common methods used to make bioactive glass scaffolds and their main benefits and drawbacks:

Conventional methods

1) Sol–Gel Processing

The sol–gel method involves creating a sol with a surfactant, leading to foaming, followed by condensation and gelation. The gel is aged to increase strength, dried to remove by-products, and sintered to form porous, three-dimensional scaffolds[48,49,49,50].

- **Pore Structure:** Results in hierarchical pore structures with interconnected macropores (10–500 µm) from the foaming process and mesopores (2–50 nm) inherent to the sol-gel process.
- **Advantages:**
    - High surface area (100–200 m²/g), facilitating faster degradation and conversion to hydroxyapatite (HA) compared to melt-derived glass scaffolds.
    - Mimics the hierarchical structure of natural tissues, which is beneficial for cell response and simulating a physiological environment.
- **Disadvantages:**
    - Low mechanical strength (0.3–2.3 MPa), limiting use to low-load applications .

2) Thermal Bonding of Particles or Fibers

Thermal bonding or consolidation involves thermally bonding a loose packing of bioactive glass particles or fibers in a mold. A porogen (such as NaCl, starch, or organic polymer particles) may be mixed to increase porosity and pore size, which is removed prior to sintering[51–54].

- **Pore Structure:** Pore size and structure depends on porogen loading
-

- **Advantages:**
    - Ease of fabrication without the need for complex machinery.
- **Disadvantages:**
    - Poor pore interconnectivity at low porogen loading, limiting its effectiveness

3) Polymer Foam Replication

In polymer foam replication a natural or synthetic foam template (e.g., coral, polyurethane) is coated with a bioactive glass suspension. The coated foam is dried, and the polymer template is burned out, followed by sintering of the glass[55–57].

- **Pore Structure:** Results in scaffolds with open and interconnected porosity similar to trabecular bone.
- **Advantages:**
    - Produces highly porous scaffolds with porosity ranging from 40% to 95%.
- **Disadvantages:**
    - Low mechanical strength, making it suitable only for low-load applications

4) Freeze Casting of Suspensions

In Freeze casting method, a suspension of bioactive glass particles is rapidly frozen in a mold. The frozen solvent is sublimated, and the scaffold is sintered to enhance mechanical strength[58–60].

- **Pore Structure:** Can produce oriented microstructures with directional porosity, offering higher strength in the orientation direction.
- **Advantages:**
    - High mechanical strength in the orientation direction, suitable for load-bearing applications.
    - Capable of supporting cell proliferation and differentiation.
- **Disadvantages:**
    - Requires precise control over freezing conditions.

    - Lamellar microstructures may have pore widths (10–40 μm) too small for effective tissue ingrowth

Rapid prototyping

Techniques such as 3D printing, ink-jet printing, fused deposition modeling, selective laser sintering and robocasting falls within this category[61–64]. Scaffolds are built layer by layer from a CAD file, without relying on traditional tools like dies or molds. This technique allows for the creation of scaffolds with structures that precisely follow a pre-designed architecture modeled on a computer.

- **Pore Structure**: Allows for precise control and optimization of internal architecture for specific mechanical and biological needs.
- **Advantages**:
    - High control over scaffold design.
    - Customizable for specific applications, including load-bearing sites.
- **Disadvantages**:
    - High equipment costs.
    - Requires imaging and computer design for each patient

It worths mentioning that a surgeon's list of criteria does not always match that of an engineer. Surgeons would prefer a porous material that can either be pressed or injected into a bone defect, such that it then expands to fill the defect. An ideal scaffold material would not be bound by the need for typical ceramic processing techniques, nor would it require additional imaging or manufacturing infrastructure (like SFF techniques). Bioactive glass fulfills many of the requirements of an ideal scaffolding material; exploring new processing routes for making scaffolds of bioactive glasses may present an avenue to overcome the aforementioned shortcomings, i.e., brittleness and the challenges associated with manufacturing a customizable 3D porous structure. Setting in-situ using a binder does not require any thermal treatment. While this process may result in a lower strength, it allows the scaffold to be fully customized to a unique bone defect. "The goal is not to replace bone, but instead to provide a structurally stable scaffold that does not migrate from the site, and one that induces and supports osteogenesis" (ref[65], p.13).

2.2. A Review of sodium silicate solutions: structure, gelation, and syneresis

2.2.1. Abstract

Sodium silicate solutions, also known as waterglass, have been found to have remarkable utility in a variety of applications. The cumulative weight of evidence from 70 years of varied analysis indicates that silicate solutions consist of a wide range of species, from monomers through oligomers, up to colloids. Moreover, the structure and distribution of these species are greatly dependent upon many parameters, such as solute concentrations, silica to alkali ratio, pH, and temperature. The most interesting and characteristic property of silicate solutions is their ability to form silica gels. Overall, despite extensive research using different spectroscopic and scattering techniques, many questions related to sodium silicate's dynamic structure, stability, polymerization, and gelation remain difficult to answer. The multitude of simultaneous reactions which restructure the silicate species at the atomic scale in response to variation in solution and environmental parameters, makes it difficult to investigate the individual events using only experimental data. Molecular modelling provides an alternative way to study the unknown areas in the aqueous silicate and silica gel systems, generating key insights into the chemical reactions at microscopic length scales. However, sufficient sampling remains a challenge for the practical use of molecular simulation for these systems. Based on both experimental and modelling studies, this review provides a detailed discussion over the structure and speciation of sodium silicate solutions, their gelation mechanism and kinetics, and the syneresis phenomenon. The goal is not only to review the current level of understanding of sodium silicate solutions, silica gels and characterization techniques suitable for studying them, but also to identify the gaps in the literature and open up opportunities for advancing knowledge about these complex systems. We believe that the future direction of research should be toward correlating atomistic, molecular, and meso-scale level details of interactions and reactions in silicate solution and establishing a fundamental understanding of its gelation mechanism and kinetics. We believe that this knowledge could eliminate the "trial and error" approach in manufacturing, and improve structural control in the synthesis of important materials derived from these solutions, such as silica gels and zeolites.

2.2.2. Introduction

Knowledge of sodium silicate solution, also known as waterglass, dates back to at least the period of the early Roman Empire. Pliny the Elder (Gaius Plinium Secundus, AD 23/24-79)[66] told the story of Phoenician mariners who accidentally melted sand and soda preparing a meal, resulting in a substance described as “a strange translucent liquid [that] flowed forth in streams” (Figure 2.4)[67]. Throughout the 17th and 18th centuries, many alchemists and scholars documented soluble silicates, including Goethe, the poet[68–70]. However, these solutions were not of industrial importance until the pioneering work of Johann Nepomuk von Fuchs [71], to whom we owe the name "waterglass"[72].

Figure 2.4 Pliny's story of Phoenician mariners, preparing their meal on the seashore using blocks of nitre (aka: sodium/potassium nitrate) to hold their cauldrons. After the fire burnt for the whole night, in combination with the sands of the beach, they observed transparent streams of a liquid hitherto unknown flowing from the hearth. The product, sodium silicate, readily becomes a liquid, i.e.,“ water glass”. From [73]

Since the work of von Fuchs, sodium silicate has become one of the most widely used industrial chemicals, with a global market size valued at US$ 7.5 billion in 2022[74]. Waterglass applications continue to grow in both traditional areas and ever-increasing numbers of novel areas, such as detergents, adhesives, sealants, water treatments, cements, deflocculants, protective coatings, catalysts, buffers, paper industries, zeolites, and geopolymers. Moreover, sodium silicate solutions are the main source for production of silica gels, which are commercially used as absorbents, thickeners, and carriers. The great success and multi-functionality of waterglass is due to many factors including its relative low cost, abundance, alkalinity, buffering ability, emulsification, nontoxicity, and viscosity regulating ability.

Although sodium silicate solutions are widely being used, scientists are still investigating questions regarding their chemistry. Sodium silicate solutions are complex mixtures of water, anionic silicate species, and sodium cations, in dynamic equilibrium. For many years, the precise nature of silicate species present in waterglass had been a matter of speculation rather than proof, with some saying that "it sounds foolish to study this element"[75]. Dent Glasser[76] once called these silicate anions "Cinderella anions" because their chemistry was so intractable that they had little appeal to classical inorganic chemists. Using such a metaphor is suitable, as the structure and attributes of these species were unknown, and they received very little attention.

Of course, the development of characterization techniques over time provided a clearer picture of the chemistry of these solutions. The first direct evidence of the structure of silicate anions in alkaline solution was provided by Lentz[77] in 1964, who pioneered the technique of Trimethylsilylation and challenged the prevailing view of the time that silicate species are entirely monomeric in such solutions. The first Raman spectroscopy analysis of aqueous silicates[78] proved another prior theory to be incorrect, indicating that silicon is actually coordinated with four oxygen atoms in silicate ions, not six[79,80]. Later, many distinct silicate species beyond the monomer and dimer were identified by ^{29}Si Nuclear Magnetic Resonance (NMR) spectroscopy [81–85]. To date more than fifty silicate structures have been identified in these solutions. The transition of sodium silicate solution to silica gel has also been of interest in the literature over the past decades[79,86,87], investigations which have mainly contributed to developing a physicochemical understanding.

Despite years of experimentation with different techniques, many studies still describe the chemistry, stability, and factors governing speciation of sodium silicates as "not fully understood"[88–92]. Moreover, insights into the underlying principles and molecular chemical aspects of silica gel formation are still limited; as Wijnen et al.[93] point out: "preparation of silica (gels) has more or less become an art rather than a science based on fundamental knowledge of the preparation conditions." A detailed understanding of waterglass speciation, properties, and gelation mechanism and kinetics are prerequisites for optimizing performance in current and future advanced applications. The first step to bridging the knowledge gap is identifying it. It is still unclear in which areas the information is insufficient or incomplete, and why. Moreover, it is important to understand the value and limitations of the methods that can be effectively employed to characterize these systems, in order to identify the methodological gaps and overcome them.

There are a number of books that comprehensively cover the subject of soluble silicates[79,94–96]. Knight and Kinrade[97] have also provided a thorough history of the evolved techniques for chemical analysis of waterglass. However, to the best of our knowledge, there is no updated review paper focused on sodium silicate solutions. This review aims to provide an up-to-date overview of on the chemistry, dynamic speciation, and gelation of sodium silicate solutions, and covers both modelling and experimental research. First, we start from aqueous sodium silicates production methods and compositions. Second, we outline an understanding of waterglass as a complex dynamic solution by discussing its speciation and factors governing it. Then, we address the waterglass gelation mechanism, kinetics, and syneresis process, followed by molecular modelling studies on sodium silicate solutions and gels. Finally, we summarize the findings so far, the knowledge gaps, and the future scope. We hope that this review will shed light on the knowns and unknowns regarding these complex and complicated solutions.

2.2.3. Composition

Sodium silicate solutions can be produced over a wide range of compositions, and are distinguished by the ratio of silica to alkali (with the general formula of $(Na_2O)_x.(SiO_2)_y.(H_2O)_z$ (x,y,z = molar ratio)). The SiO_2:Na_2O ratio can be given in the molar form, $R_M = n_{SiO_2}/n_{Na_2O}$, or the equivalent weight form, $R_W = m_{SiO_2}/m_{Na_2O}$, where n_i is amount of constituent i in moles, and m_i is the mass of constituent i in grams. The SiO_2 concentration and SiO_2:Na_2O ratio are the two main factors that govern the physical and chemical properties of these solutions and varying them results in solutions suitable for diverse applications.

Figure 2.5 shows the ternary Na_2O-SiO_2-H_2O phase diagram subdivided into eleven areas which roughly correspond to the types of products used in this system. The zone corresponding to waterglass in the Na_2O-SiO_2-H_2O three component phase diagram is the red area (area 9). The boundaries of the waterglass area are fixed by two curves representing the limits of viscosity (top and bottom lines), and another two curves representing the limits of stability (right line for colloid materials and left line for crystallized materials, respectively). Based on this diagram, when $R_M<1.6$, fully or partially crystalline alkaline silicates are formed, and when $R_M>3.75$, all the silicates transfer to colloid particles and form alkaline gels or unstable liquids. When the water content is too high, the obtained solutions are too dilute; and when the water content is too low, the solution is too viscous to be pumped, or solids are formed. Therefore, the molar SiO_2:Na_2O ratio of commercial sodium silicate solutions varies between 1.6 and 3.75, and their silica concentration is in the range of 25-35 wt.%. The gray areas represent other commercial products in this system, which are used in a wide range of applications including refractory cements, construction, coatings, personal care, and food and beverage processing. Compositions in the white areas are not commercially produced but might be of scientific interest.

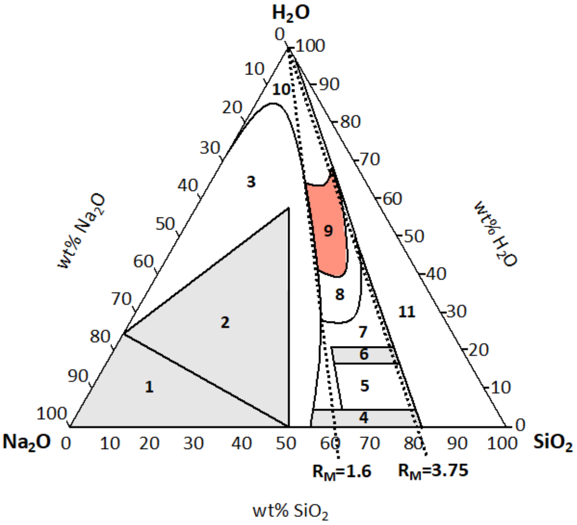

Figure 2.5 The isothermal ternary phase diagram of the SiO_2-Na_2O-H_2O system illustrating various regions with different properties, based on weight fractions of components. Some of these regions correspond to materials that are used in practical applications, while others are less commonly employed. Sodium silicate solutions are typically commercially produced in region 9 (red region). The two dashed lines represent the limits for the molar SiO_2:Na_2O ratio, which define the area where aqueous sodium silicate solutions can exist. Other regions are as follows: (1) anhydrous sodium orthosilicate and mixtures with NaOH; (2) crystalline alkaline silicates; (3) uneconomical partially crystallized mixtures; (4) glasses; (5) uneconomical hydrated glasses; (6) dehydrated liquids; (7) uneconomical semi-solids; (8) economical viscous liquids; (9) typical commercial liquids; (10) dilute liquids; (11) unstable liquids and gels. Re-drawn from[72]. (For interpretation of the references to colour in this figure legend, the reader is referred to the web version of this article.)

Waterglass can be produced via two main methods. In the conventional route, sodium silicate glasses are used as raw materials to produce waterglass (Figure 2.6a). For this purpose, glasses with >20 mol% sodium (which have poor resistance to water attack) and molar SiO_2:Na_2O ratios equivalent to the desired solution are dissolved at elevated temperatures in water. NaOH is sometimes added to the solution afterwards to adjust the SiO_2:Na_2O ratio to lower values.

However, for a given ratio and concentration, the adjusted silicate solution might have different species as compared with the one manufactured directly [24]. This method has the disadvantage of generating CO_2 from the decomposition of Na_2CO_3 as well as the fuel used to reach high temperatures.

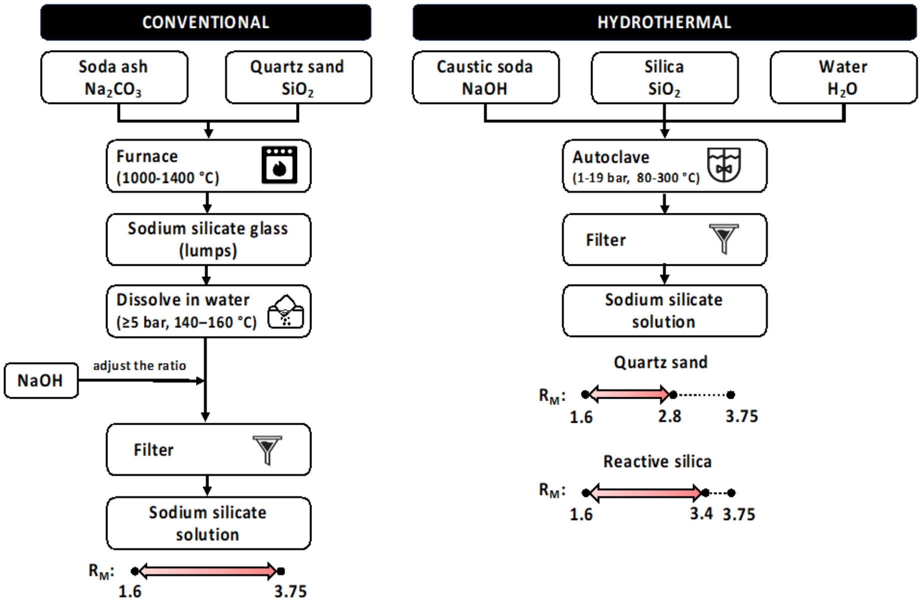

Figure 2.6 Process flow of sodium silicate solution production by (a) conventional method and (b) hydrothermal method. The range of SiO_2:Na_2O molar ratio obtained by each process is shown. In hydrothermal method, aqueous silicate solution of high SiO_2:Na_2O molar ratios (R_M values of >2.8) can only be achieved by using reactive silicon dioxide sources (such as amorphous silica, diatomite, or cristobalite).

The hydrothermal dissolution of the raw materials of silica is the second standard method for waterglass production (Figure 2.6b). The hydrothermal process involves dissolving a reactive silica source—mainly quartz sand—in sodium hydroxide solution. The molar SiO_2:Na_2O ratio that can be achieved with this method is restricted by thermodynamics, as the concentration of SiO_2 in the liquid phase approaches saturation. If quartz sand is used as silica source, the R_M is limited to 2.89[98]. Higher R_M and dissolution rates can be obtained if raw materials with higher reactivities, such as cristobalite or vitreous silica, are substituted for quartz. For example, Pfeiffer et al.[99] obtained RM values of 3.4 by using common opal as a silica source. Although this method requires less energy and creates less CO_2 output compared with the conventional method, the energy requirement is still high. Attempts to find alternative methods with reduced CO_2 footprint and better sustainability are mainly focused on producing silicate solutions from by-products such as rice husk ash[100,101], condensed silica fume[102,103], and waste glass cullet[104,105].

2.2.4. Chemical structure

Whether in the form of amorphous solids, crystalline solids, or aqueous solutions, silicates are complex systems. Silicates are based on tetrahedral unit groups of $(SiO4)^{4-}$, which tend to bond together at the corners through the sharing of one oxygen atom (bridging oxygen (BO)), forming networks such as chains, rings, sheets, and three-dimensional networks. In sodium silicate glass networks, sodium ions modify the network by breaking up the Si−O−Si bonds and producing a terminal non-bridging oxygen (NBO) (Figure 2.7a). But the main question here is, what does the structure of sodium silicate solution look like? Only by answering this question, it may be illustrated how the properties of these solutions change with modifications in composition and processing, and their behavior in different environments may be predicted.

2.2.4.1. Silicate species

During the past five decades, much experimental work has been performed to specify silicate species in aqueous solutions (Summarized in Table 2.1). Among various characterization techniques, ^{29}Si NMR spectroscopy has been the most useful method to identify different silicate species in waterglass, as it can obtain in situ information on the connectivity of silicon atoms in the solution. Engelhardt et al.[106,107] introduced "Q-units" for describing the silicate structural units, which then became a standard for describing ^{29}Si spectra. Five main classes of NMR signals have been identified and labeled Q^n, where Q represents a fourfold coordinated silicon atom and n indicates the number of neighboring silicon atoms linked through an oxygen atom (Figure 2.7b). Thus, Q^0 denotes a monomeric silicate tetrahedral while Q^4 is assigned to a silicon atom bound to four other silicon atoms

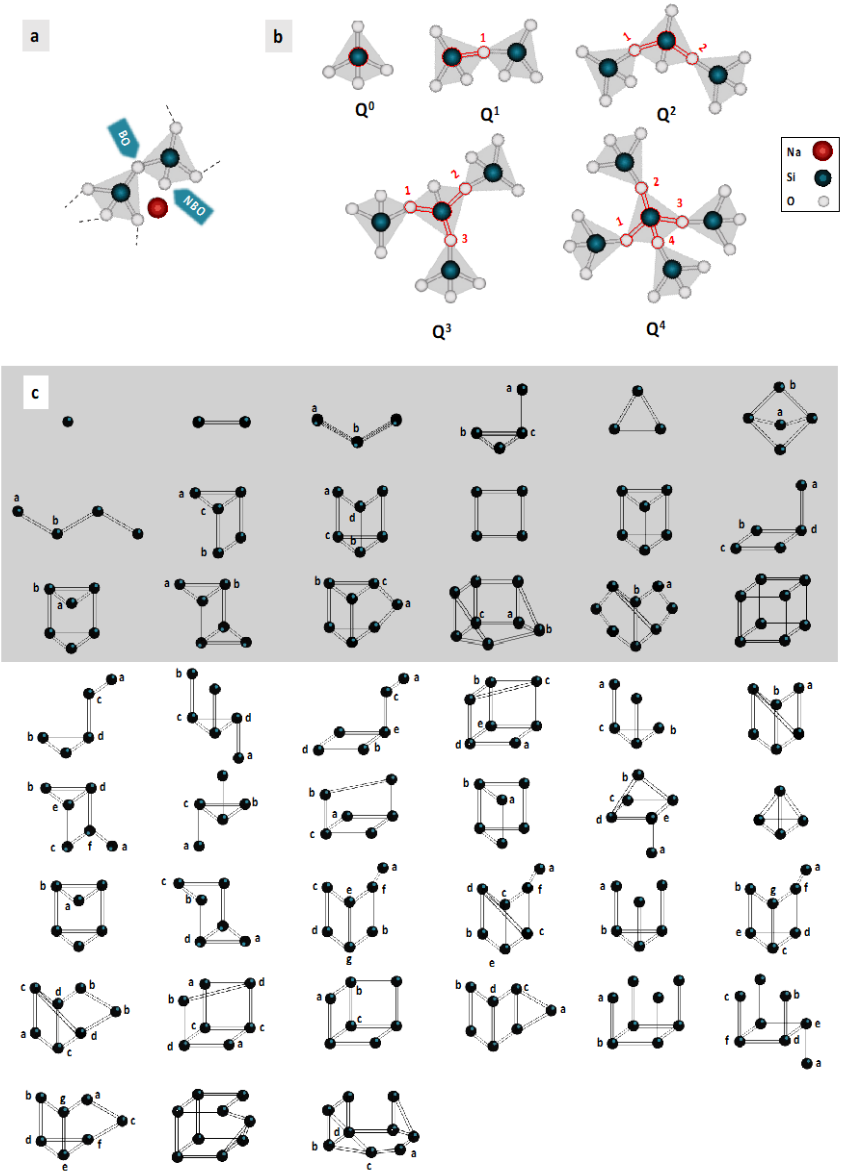

Figure 2.7 (a) Schematic representing two silicate tetrahedra connecting by sharing a bridging oxygen (BO) and a sodium ion compensating a charge near a non-bridging oxygen (NBO) (b) Schematic showing different silicate structural units labeled as Q^n, where Q represents a fourfold coordinated silicon atom and n indicates the number of neighboring silicon atoms linked through a bonding oxygen atom. (c) Silicate structures identified in aqueous silicate solutions by ^{29}Si NMR, proposed by Knight et al.[84], including those identified by Harris and Knight[83,85] (gray background). Balls and sticks represent silicon atoms and oxygen bridges between silicon atoms, respectively, with NBO omitted. Three proposed oligomers (6B, 6C, and 7A in[84]) have been excluded from this schematic due to the finding by Knight et al. that such structures' various isomeric forms were unable to be resolved as definitive, re-drawn from[84].

.

Table 2.2.1 A summary of studies investigating different silicate species in alkali silicate solutions.

Characterization techniques	**SiO_2:M_2O (R_m, molar)**	**Cation (M^+)**	**[SiO_2] (molar)**	**Year**	**Findings**	**Ref**
1D ^{29}Si NMR	unknown	Na^+	unknown	1973	^{29}Si NMR can differentiate between various types of silicate structural units.	108
1D ^{29}Si NMR	0.5-50	Na^+	3.6-6.6	1974	Increasing solution purity and external magnetic field strength results in better resolved NMR spectra.	81
1D ^{29}Si NMR	unknown	unknown	unknown	1974	Introduced Qi units for describing the silicate structural units.	107
1D ^{29}Si NMR	2	Na^+	0.01, 0.1, 0.5, 0.65	1980	Monomeric silicate ions present at low concentrations.	109
1D ^{29}Si NMR	0.5	K^+	0.65	1981	Evidence for the structures of eleven silicate species.	110
1D ^{29}Si NMR	0.5	K^+	0.65	1982	Definite evidence for the structures of twelve silicate species.	75
1D ^{29}Si NMR	1	K^+	3	1983	Definite evidence for the structures of six silicate species.	83
1D ^{29}Si NMR	1	K^+	3	1983	Evidence for the structures of twelve silicate species.	85
1D ^{29}Si NMR	1-3	Na^+	1-3	1986	Evidence for nineteen silicate structures containing up to twelve Si atoms.	111
1D ^{29}Si NMR	1-3.3	Na^+	2.1-9.3	1986	Speciation distribution diagrams in solutions with different R_M and [Si].	112
1D ^{29}Si NMR	0.5	Na^+, K^+, Rb^+	0.1-1.8	1988	• Silicate polymerization is favored by low temperature, low alkalinity, and high [Si]. • Larger M^+ atoms preferentially stabilize the highly polymerized silicate anions.	113
1D ^{29}Si NMR	>0.5	Na^+-Cs^+	0.9,3	1992	The level of condensation decreases systematically from M=Na to M=Cs.	114
1D ^{29}Si NMR	2-4	Na^+	>5	1993	Q4 species may indicate the formation of colloidal particles.	115
1D ^{29}Si NMR and FTIR	2,4	Na^+, K^+	4	1996	• ^{29}Si NMR is very sensitive to changes of the structural surroundings of silicon. • FTIR gives information on hydrogen bonding.	116
1D ^{29}Si NMR and FTIR	0.2-3.3	Na^+	0.4-6	1997	FTIR can show changes in anion distribution much faster than NMR.	117
1D ^{29}Si NMR and SAXS	2.3	Li^+, Na^+, K^+	1.5	1999	The type of cation affects the fraction of the species but does not appreciably change their structure.	118
2D ^{29}Si NMR	0.5	K^+	1.4	1984	More confident assignments consistent with earlier results.	119
2D COZY ^{29}Si NMR	0.5	K^+	1.5	1988	Evidence for the structures of twenty-two silicate species.	120

2D ^{29}Si NMR	unknown	Na^+	unknown	2006	Evidence for nine novel solution state silicate oligomers.	121
2D ^{29}Si NMR	3.4	Na^+	3.32	2006	Presented five novel silicate cage structures.	122
2D ^{29}Si NMR	0.5	K^+	1	2007	Identified forty-eight different silicate structures (45 definite).	84
1- and 2D 29Si NMR and SAXS	0.85	Na^+	1.76-7	2010	Concentrated solutions could include silicate cages containing Q^2, Q^3 and Q^4 groups.	123
Raman	unknown	Na^+	2.5	1956	Si is coordinated to four oxygen in the monomeric silicate species.	78
Raman	unknown	Na^+	0.003	1985	Silicate solutions at low concentrations contain polymeric species as well as monomers.	124
Raman	0.1-1	Na^+	1	1985	Gradual change in the polymerization degree of silicate species as a function of Si/Na.	125
Raman	3.22	Na^+	0.2-3	2007	• Raman is adequate to measure the concentration of dissolved silicates. • Dilution of silicate solution reduces the polymerization degree of silicate species.	126
Raman	1.25-2	K^+	0.05-5	2011	Increasing the [Si] will polymerize the system, but increasing P, T, or the K_2O/SiO_2 ratio will depolymerize the system.	127
Raman	1.1-3	Na^+	unknown	2014	The silicate speciation is much more strongly controlled by fluid composition than by temperature and pressure.	128
Raman	0.1-0.8	Na^+, K^+	unknown	2017	The nature of the alkali cation affects the silicate species.	129
IR	0.5-100	Na^+	2.5	1973	As the R_M increased, monomers and dimers change to high-Mw polymers.	130
FTIR and Raman	0.5-3.3	Na^+	6,1	1999	Trends in vibrational closely follow the trends observed by ^{29}Si NMR.	131
FTIR	4-100	$Na^{+,}$ K^+	3.3	2006	FTIR can be used to determine the alkali content and particle sizes of alkali silica solutions.	132
FTIR and Raman	2.5-5	Li^+, Na^+, K^+	0.2-3	2008	FTIR is not reliable for estimating the ratios of Q^i connectivities. Raman on the other hand, is a useful for studying the structure of silicates both in aqueous and solid phase.	133
FTIR	1-3.5	Na^+	1.6-8.8	2010	FTIR can be used to determine the ratio of silicate solutions with a relative error of better than 1%.	134
FTIR and Raman	1.6-3.22	Na^+	0.2-3	2010	The Raman spectra of dissolved silicates are better resolved than FTIR.	91
^{29}Si NMR, FTIR and Raman	0.7-3.4	Na+, K^+	0.6-6.4	2016	• NMR data revealed high depolymerization of the silicate entities for as Si/M decreased. • Presence of M O bonds and oligomers for Si/M <1 in Raman spectra FTIR could be used to measure [Si].	135

Early works depended primarily on 1D ^{29}Si NMR methods. However, because ^{29}Si is a "rare spin" (with natural abundance of 4.7%), no ^{29}Si–^{29}Si coupling was visible and only a single signal for each chemically distinct site was given. Moreover, 1D ^{29}Si NMR spectra consisted of a series of closely spaced and overlapping signals and only a few species were identified in solutions with natural isotope distributions[97]. A common way to improve the resolution of that method was to introduce dilute alkaline silicate solutions or solutions enriched with the isotope ^{29}Si to high magnetic fields. By such means, Harris and Knight[83,85] identified 16 distinct oligomers beyond the monomer and dimer with up to 8 Silicon atoms with a high degree of certainty (Figure 2.7c, gray area). Despite their success in discovering the dominant oligomers, there were still many features in the ^{29}Si NMR spectra of silicate solutions that could not be assigned to any of the known species.

In 2D NMR techniques, the problem of overlapping spectra lines is solved by putting chemical-shift and coupling information into two different frequency dimensions. The improved dispersion and additional insights provided by the 2D spectra enabled researchers to identify several new oligomers[119–121,136] and cage structures[122,123]. However, the silicate structures which were detected contained only a small number of chemically inequivalent silicon sites, and were proposed with varying degrees of confidence. Knight et al.[84] obtained ^{29}Si Correlation Spectroscopy (COSY) NMR spectra of an isotopically enriched potassium silicate solution at the highest possible external magnetic field (17.6 T). They identified 48 different structures (including those of Harris and Knight[84,85]), providing the most complete picture of silicate speciation to date (Figure 2.7c). Still, these structures accounted for only 85% of the silicon in the solution, leaving hundreds of weak signals indicating unassigned, minor structures. The authors concluded that, even at such high magnetic field, NMR spectral overlap and sensitivity still limits structural determination. Moreover, their proposed structures did not include some of the species tentatively claimed in earlier NMR studies, such as species 1-4 in reference [121] and species 15 and 16 in reference[120]. Although the ^{29}Si NMR signal assignments are still incomplete, frequently speculative, and contain some conflicting experimental results, these studies have formed most of our current view of possible silicate structures present in aqueous solutions. It should be noted that, in some of the studies, including the references[84] and[120], it is the chemical structure of potassium silicate solution being investigated. Although it has been proven that the type of alkaline ion affects the fraction of the species, it does not appreciably change their structure[118]. Therefore, one cation may favor an individual silicate anion structure over others (the larger cations preferentially stabilize the more highly polymerized silicate anions[114]), but there are no specific species that are unique to a given cation.

While high resolution ^{29}Si NMR spectroscopy has shown the most promise in investigating the chemical structure of silicate solutions, it is important to bear in mind that it requires sophisticated laboratory equipment and personnel, is expensive and slow, needs sample preparation (dilution and ^{29}Si enrichment), and that the spectrum assignments can be conflicting. Therefore, a relatively simple, inexpensive, and non-invasive analytical technique that allows quick structural comparisons in realistic conditions would be highly desirable. Infrared (IR) and Raman spectroscopy can fulfill these requirements and are also robust enough for in situ silicate analysis, both in aqueous and solid phases.

As mentioned earlier, the first Raman analysis of aqueous silicates[78] revealed that Silicon is coordinated to four Oxygen in the monomeric silicate species. These findings were later confirmed by Freund[137], who monitored the protonation of monomeric SiO_4^{4-} as a function of pH. Later Raman studies[124,138] showed that silicate solutions at low concentrations contain polymeric species and not just monomeric species. Dutta and Sheih[125] observed a gradual change in polymerization degree of silicate species to lower orders (depolymerization) with increase in alkali metal ions. Bass et al.[131] found that the trends observed in Raman spectra of silicate solutions with different concentrations and alkalinity closely follow the trends observed by ^{29}Si NMR. They also found the band locations to be consistent with results reported for crystalline silicates and silicate glasses. Halasz et al.[133] demonstrated that Raman spectroscopy can distinguish the structural differences (i.e., the Q^n connectivity ratios of $[SiO_4]$ tetrahedra and the dominating siloxane ring structures) between the silicate species of solutions with different alkaline ions, alkaline/silicon ratio, and concentration. In another study, Halasz et al[139] suggested that contrary to contemporary assessment, dissociation of Na^+ ions could affect the IR and Raman spectra of dissolved sodium metasilicate monomers. Vidal et al.[129] used Raman spectroscopy to evaluate the reactivity of silicate solutions by determining variations of ring and chain size, which was found to be highly dependent on the cation type, preparation method, and Silicon to alkali ratio. Raman spectroscopy also proved adequate to measure the concentration of dissolved silicates, as a good linear correlation between the absolute intensity of the Raman band and the silicate concentration was found[126,127]. The most recent Raman studies are mainly focused on in situ investigation of reactions involving sodium silicate solutions, such as geopolymers[140,141] and silica gel formation[142].

Like Raman, the first IR spectroscopy studies could only distinguish between monomer and a generic polymer species[116,130,138]. In the late 1990s, Bass and Turner[117] could assign a number of IR band components to different silicate structure types by correlating IR spectra with 29Si NMR data for a wide range of solution compositions. Later, methods were developed to quantitatively measure the concentration and molar ratio of sodium silicate solutions by FTIR[132,134,135]. For example, Osswald and Fehr[132] used FTIR to determine the alkali content and particle sizes of alkali silica solutions. They found that the size of primary silicate particles in solution is correlated with the IR peak intensity of the band between 1070 and 1020 cm^{-1}, assigned to vibration modes of SiO_2 on the particles' surface. They suggested that as the particle size is correlated with the alkali content of the solution, the peak intensity could also be used for determination of the alkali content. FTIR have also been used for following the evolution of different silicate species as a function of pH and silica concentration[143].

Both FTIR and Raman spectra can be used to determine both the solution concentration and R_M, and can reflect the changes in distribution of silicate species. However, the Si–O vibration related Raman spectra of silicates are reported to be better resolved than the corresponding IR spectra[91]. Raman can also characterize the O–Si–O bending vibrations of various siloxane ring systems at <400 cm^{-1}, which are not accessible for the commonly used mid-IR spectrometers[126]. Moreover, Raman spectroscopy requires little to no sample preparation and is ideal for in situ studies, while the FTIR method has constraints on sample thickness, uniformity, and dilution. Lastly, water is a weak Raman scatterer and, consequently, the technique is ideally suited to probing processes under aqueous conditions. O^n the other hand, fluorescence could be problematic with Raman as it can mask its signal, which would not be an issue with FTIR. It is noteworthy that neither of these techniques can directly quantify different silicate species as NMR does. For instance, Halasz et al.[133] concluded that FTIR is not reliable for estimating the ratios of Q^i connectivities in aqueous alkaline silicate solutions, with the exception of Q^0.

3.1.1 Silicate species distribution

The complex speciation of silicate solution is governed by two sets of equilibria[144], defining which silicate anions will be present in the solution:

1. The acid-base equilibria:

$$\equiv \mathrm{Si{-}OH} + \mathrm{H_2O} \leftrightarrow \equiv \mathrm{Si{-}O^-} + \mathrm{H_3O^+} \tag{2.1}$$

2. The polymerization-depolymerization equilibria:

$$\equiv \mathrm{Si{-}OH} + \mathrm{OH{-}Si} \leftrightarrow \equiv \mathrm{Si{-}O{-}Si} \equiv + \mathrm{H_2O} \tag{2.2}$$

or

$$\equiv \mathrm{Si{-}OH} + \equiv \mathrm{Si{-}O^-} \leftrightarrow \equiv \mathrm{Si{-}O{-}Si} \equiv + \mathrm{OH^-} \tag{2.3}$$

What makes these systems even more complicated is that their equilibrium distribution is dependent on many factors, such as the solution concentration, SiO_2:Na_2O ratio, pH, and temperature. A slight variation of each of these chemical parameters may induce drastic changes on the connectivity of silicon atoms and the resulting distribution of silicate species in the solution. Generally, it can be stated that the degree of polymerization increases as Si concentration and/or R_M is increased, as pH is decreased, or as temperature is decreased (Figure 2.8a). In the following sections, the effect of each parameter is described in detail.

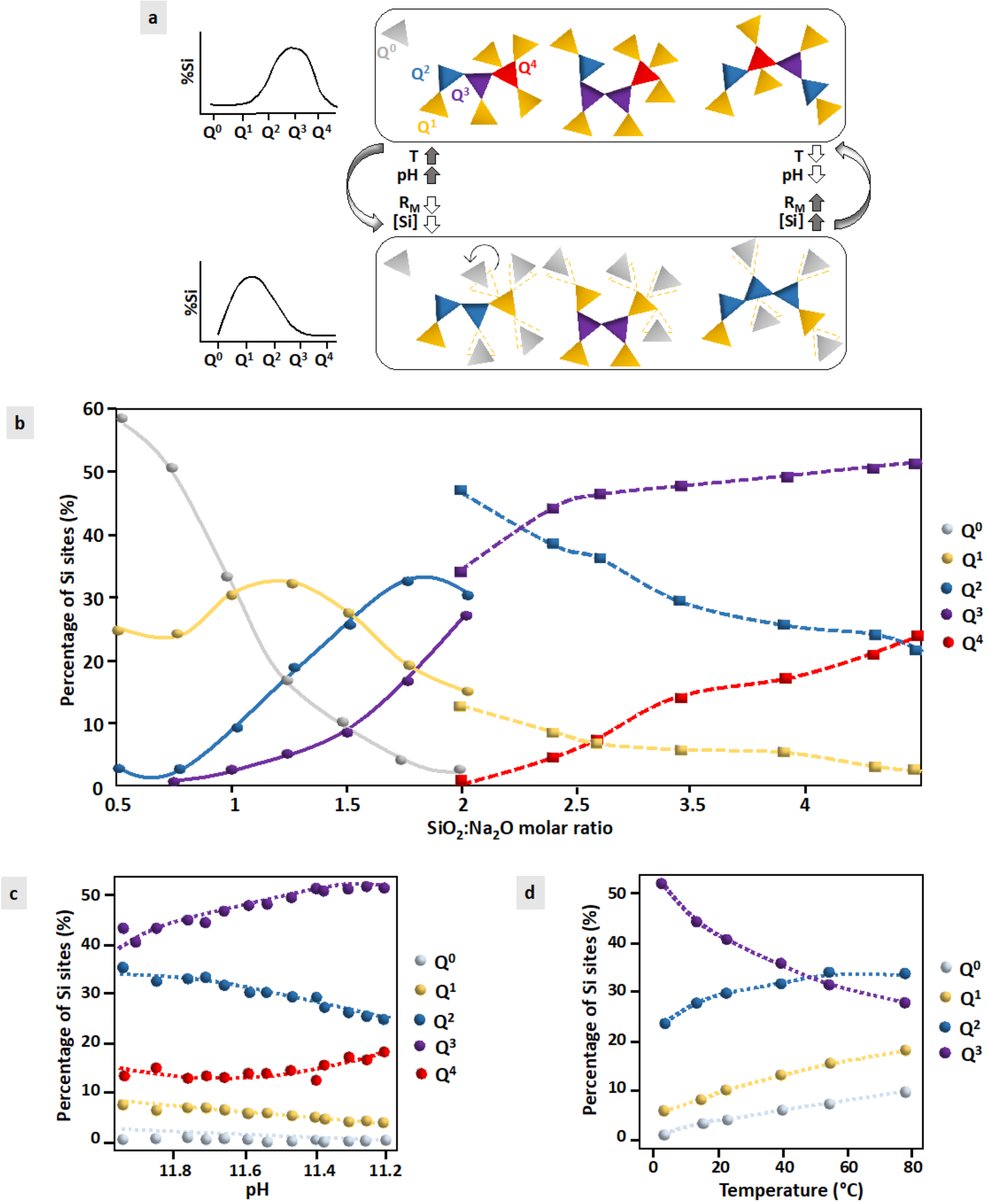

Figure 2.8 (a) Schematic showing the effect of different parameters on the degree of connectivity of silicate species and their distribution in solution (b) Distribution of different silicate species in sodium silicate solutions as a function of R_M, obtained by NMR spectroscopy. Solid lines are re-drawn from[145], p. 8905. Dashed lines are re-drawn from[115], p. 744 (Q0 is reported to be <2 %) (c) The integral values of the NMR spectral peaks corresponding to Q^0–Q^4 silica species as a function of pH value of sodium silicate solution, re-drawn from[146]. (d) Distribution of different silicate species in sodium silicate solutions as a function of temperature obtained by NMR spectroscopy, re-drawn from[113].

Effect of composition

Several studies have been done to quantify the changes in the silicate species distribution according to concentration and alkalinity in sodium silicate solutions[111,112,115,117]. Although these studies were involved different ranges of SiO_2 concentrations and ratios of SiO_2:Na_2O, a general trend in the distribution of structural units can be observed:

1. As the silica concentration or SiO_2:Na_2O in the solution increases, so too does the extent and range of polymerization at any given pH. As shown in Figure 2.8b, at very alkaline solutions, the species are mainly monomer, dimer, and trimer.
2. As solutions become more concentrated and siliceous, the complexity and quantity of silicate species increases, polymerizing to more complex structures (i.e., the fractions of Si atoms in Q^3 and Q^4 environments increase at the expense of Q^0, Q^1 and Q^2 units as R_M increases).
3. At R_M>1.5, polymerization leads to silicate species containing Q^3 branching groups and, at higher ratio silicates with R_M>3.5, cage-like species with three-dimensional cross-linked Q^4 Si environments and surface Q^3 units are observed.
4. According to Harris et al.[115], Q^4 units have only been certainly detected in highly concentrated (38 wt% SiO_2,) or aged silicate solutions and are considered an indication of the formation of colloidal silica particles (discussed in section 3.2).

Models have been proposed to predict the speciation in alkaline silicate solutions over a wide compositional range, which are in good agreement with the experimental results[112,145].

Effect of pH

The same pattern of change in the distribution of silicate ions can be seen as a function of pH in the basic range: a decrease in Q^0, Q^1 and Q^2 species and the opposite for Q^3 and Q^4 species with decrease in pH (Figure 2.8c). Generally, as the pH is reduced, silicate species condensate to higher-order oligomers and larger particles. With a further decrease in pH (~10), the gelation process is initiated in the solution. Conversely, increasing the pH causes Si-O-Si bonds to break, which leads to depolymerization of silicate species to form smaller, more reactive, and more ionic species. Tognonvi et al.[87] studied the effect of increasing the pH on sodium silicate solution speciation by IR spectroscopy. They observed a decrease in Q^3 and Q^4 contributions to the benefit of Q^2 with increase in pH value, meaning there was an increase in the Q^2/Q^3+Q^4 intensity ratio. Furthermore, an increase in the intensity of the Si-O-(Na^+) band was observed. These results suggest that the increase in the pH value of the sodium silicate solution favors the breaking of Si-O-Si bonds to form anionic Si-O^- which can be associated with Na+ cations to form ionic Si-O-Na bonds.

Effect of temperature

It has been established that temperature influences the silica solubility and polymerization reaction rate[147]. Steele-MacInnis and Schmidt[128] used Raman spectroscopy to study the dependence of silicate connectivity upon temperature and pressure—up to 600°C and 2GPa—in sodium silicate solutions. Their results showed that increasing temperature would depolymerize the system. The same effect was observed by Hunt et al.[127], who studied potassium silicate solutions at 25-200°C and pressures up to 2GPa (Figure 2.8d). The observed depolymerization trend with temperature increase aligns with NMR studies at comparable temperatures (-5 to +144 °C) by Kinrade and Swaddle[113], who also showed that silicate polymerization is favored by low temperature, meaning the condensation equilibria shift in favor of the monomer, and species of low molar mass as the temperature is increased. Since these studies were performed at near-isochoric conditions, a part of depolymerization could be explained by the thermal pressure applied, but it does not account for all of it. Such temperature-driven depolymerization implies the increase of the OH^-/H_2O ratio in the solution with increasing temperature, as previously described by Nowak and Behrens[148]. Hydroxide ions can break the Si–O–Si bonds by nucleophilic attack, leading to depolymerization of silicate species of high connectivity. It is worth mentioning that the silicate speciation is controlled much more strongly by solution composition than by temperature[128].

2.2.4.2. Colloid particles

Sodium silicate solutions consist of silicate species with different degrees of connectivity, as denoted by Q^0-Q^4. However, some NMR studies[113,119] reported that no peaks were detected in the Q4 region. In fact, the Q^4 units were only detectable at highly concentrated solutions with R_M above 2, where there seems to be a structural change in the sodium silicate solutions, indicated by the formation of "colloidal silica"[149]. Colloidal particles are in range of 1-1000 nm in size, which are sufficiently small not to be affected by gravitational forces but sufficiently large to show marked deviations from the properties of true solutions. These colloids have a fully polymerized (Q^4) dense core, and a surface covered by silanol groups (Q^3). As the silica concentration and/or R_M increases, the silicate particles aggregate, and large particles grow at the expense of monomers, dimers, and smaller particles. Above a R_M of 3.75-4 (silica solubility limit), the solutions produced are unstable. Nordström et al.[150] showed that in the instability region colloidal particles continue to grow until they are no longer stable and undergo aggregation/agglomeration into fractal structures—thus, the system gels.

The sizes of colloidal particles in sodium silicate solution have been investigated using various methods. Some older studies such as Iler[151], and Dietzel and Usdowski[152], found only evidence of small particles of 1-2 nm in diameter. However, their employed methods, which included strong dilution/filtration and chemical extraction, may have inadvertently eliminated the larger aggregates. The application of light scattering techniques allowed the investigation of solutions without affecting their structure. Early investigations, such as Nauman and Debye[153], applied static light scattering to determine the molecular weights of particles present in sodium silicate solutions by measuring the turbidity of filtered solutions. The obtained values for average molecular weight ranged from 60 to 400 g/mol, which increased as the R_M increased from 0.5-3.75. Due to the fact that they could not directly measure the particle size, though, their method was more suitable for molecules in diluted solutions than for colloids in concentrated sols.

Investigations by dynamic light scattering (DLS) and small-angle X-ray scattering (SAXS) confirmed the colloidal particles as the major component of concentrated alkaline silicate solutions. For example, Roggendorf et al.[116] observed a maximum particle diameter of 30 nm in solutions with an R_M value of 2, and a slightly larger maximum size of 35 nm in solutions with an R_M value of 3.3. Böschel et al.[154] found three size classes of colloidal particles in concentrated sodium silicate solutions (R_Ms of 2.2, 3.3, and 3.9) by DLS, with respective colloid diameters of 0.8–1.2 nm, 5-26 nm, and 150–170 nm, existing in parallel in the solutions. They described the bigger particles as random packing of primary colloids or secondary aggregates. Tognonvi et al.[123] applied SAXS to investigate the size distributions of the silicate species present in concentrated sodium silicate solutions ([Si]=7 mol/l, R_M=3.4). The analysis of SAXS results led them to conclude that these solutions contain colloids of about 0.6–0.8 nm diameter which can also be more or less gathered together through weak bonds to form aggregates slightly larger than 2 nm.

The discrepancies between investigations on the colloid size of sodium silicate solutions obtained by SAXS and DLS are difficult to elucidate, as neither method disturbs the solution. Nordström et al.[150] performed both SAXS and DLS measurements to study the size and structure of particles present in silicate solutions ([Si] ≈ 2.1 mol/l, R_M = 3.3,3.8). There was an overall agreement between the SAXS and DLS measurements that the solutions contain two fractions of objects, and the diameter obtained for smaller objects are similar (0.6-0.9 nm). The calculated average particle size of the larger particles, however, did not correspond well between the two methods, with the diameter calculated by DLS being almost five times larger than the diameter determined from SAXS (300 vs. 60 nm). This difference could be due to the fact that both DLS and SAXS measurements can be affected by aggregation/agglomeration, but the effects can differ due to the different physical principles behind the two techniques. DLS is prone to overestimating the particle size if particles aggregate. SAXS on the other hand, is prone to underestimating the particle size if aggregation occurs.

Although it is widely accepted that colloidal particles exist in sodium silicate solutions, uncertainties about their size range continue to exist, and the effect of various parameters, such as concentration, R_M, and temperature on colloid size is not yet known. Furthermore, the specific minimum of [Si] or R_M, above which the colloidal particles are formed is still unclear. Perhaps, a comprehensive study on the size of colloidal particles in sodium silicate solutions, over a full range of concentrations and R_M values, using both DLS and SAXS, and combined with a complementary direct visualization method (such as SEM/TEM) could shed more light on these areas.

2.2.4.3. Sodium ions

The preceding sections were concerned with different silicate species in sodium silicate solutions, and the evolution of the distributions of these species in response to various chemical parameters. The question arises: what is the role of sodium ions and where are they located in the structure with respect to silicates? In a silicate glass network, sodium ions act as glass modifiers by breaking part of the Si-O bonds, reducing the connectivity of silicates, and compensating a charge near a NBO. NBOs are also present in silicate species in the solution state. The monomeric silica can be considered as silicic acid (H_4SiO_4) and can release a few hydrogen ions in the solution. Silicic acid can also polymerize and form silicate oligomers. Sodium ions can ionize the weak hydrogen ions of silicate oligomers, leaving $-O^-$ groups behind, forming NBOs. The repulsion between the charged/deprotonated silicate particles is the key for maintaining the solution stability, as it prevents coagulation. Since both sodium cations and deprotonated silica oligomers are present in the solution, formation of sodium–silicate complexes, or ion pairs, are possible. Many studies have detected bands assigned to symmetric and asymmetric vibrational modes of (Na)O–Si–O(Na) and (H)O–Si–O(Na) in IR and Raman spectra of sodium silicate solutions[91,112,126,132,139]

As mentioned previously, the system responds to changes in alkali content, by increasing or decreasing the level of silica polymerization inversely with the alkali level (Figure 2.8a). When the alkali content decreases, the system responds by reducing the surface area of silica and the number of Si-OH (silanol) units on the surface. This reduction in surface area is achieved by forming silicate species with a higher degree of polymerization, allowing for the accommodation of the reduced sodium content and minimizing the formation of charged sites. In other words, polymerization of the silicate species producing larger particles, with a lower total surface area, affords the system a way to maintain a surface charge density sufficient to avoid coagulation/gelation. Conversely, a larger amount of sodium favors species of lower degree of polymerization. Pavlova et al.[155] found that the presence of sodium could contribute to an increase in reaction barriers for silica oligomerization. They assigned this finding to the rearrangement of the hydrogen bond network of water solution around the reactants.

Dupuis et al.[156] combined experimental and molecular modelling approaches to study the roles of sodium (Na^+), hydroxide (OH^-), and water on the stability of silicate chains. They showed that the silica clusters depolymerize in the presence of sodium hydroxide. However, they concluded that the role of Na^+ in the depolymerization is minimal and it is the effect of pH, or OH^-, which is important due to the ability of these groups to directly dissociate a Si–O–Si bond. Overall, studies indicate the existence of strong interactions between sodium ions and deprotonated silicate species as well as hydroxide ions, which produce the differences in measured interactions associated with pH. The hydroxide ions are also responsible for the differences in the distribution of species observed at a constant molar ratio and varying sodium ion content.

Sodium ions can also be present as solvate species (i.e., free Na^+) in solutions. Halasz et al. produced a series of studies[91,126,133] measuring the dissociation level of dissolved silicate species and sodium ions using electrical conductivity and ion selective electrode measurements. Their results suggested that the level of Na^+ ion dissociation in silicate solutions is a strong function of silica concentration, and a weak function of Na/Si ratio. For example, in commercial silicate solutions with an R_M value of 3.22 and a concentration of 3 mol SiO_2/L, approximately 30% of the total sodium ions were found to be free (unbound). Upon dilution to a concentration of 0.2 mol SiO_2/L, the percentage of free sodium ions increased to around 50%. These results are in agreement with findings in Dupuis et al.[156], according to which the protonation state of silicate particles is modified by dilution in pure water.

Now, we can complete our picture of the "structure of sodium silicate solutions". Figure 2.9 represents a schematic of this structure containing sodium ions, silicate species and colloidal silica. It should be noted that each specific sodium silicate solution has its own equilibrium distribution of silicate species at a given silica concentration, R_M, pH, and temperature. The structure, number, and charge of silicate species vary to accommodate the variations in different parameters.

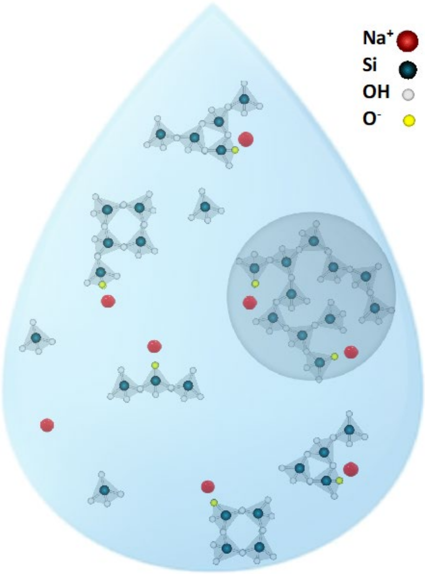

Figure 2.9 A schematic illustration showing a possible scenario for different silicate species and sodium ions present in a single drop of sodium silicate solution. The gray sphere represents a colloidal particle which may form in concentrated solutions.

2.2.5. Gelation

It is well known that waterglass can undergo a gelation reaction to form a semi-solid state, known as "silica gel". Silica gels are a class of amorphous silicas which are formed as a result of an ion exchange of Na^+ for H^+, followed by lowering the pH of the sodium silicate solution. The result is a three-dimensional network of silica polymers that encloses the liquid phase. Here we review a widely accepted theory of silica gelation, gelation kinetics and factors affecting it, as well as the syneresis phenomenon—the removal of water from the polymeric silica network.

2.2.5.1. Gelation mechanism and silica gel structure

Prior to 1979, most researchers improperly applied the organic polymers gelation theory to soluble silicates, and believed that silica gel formation involved cross-linking of pre-existing linear polymers. Carman[157] was the first to propose that silicic acid polymerizes to discrete particles which then aggregate into chains and networks. However, this idea was not generally accepted until the publication of the book, The Chemistry of Silica by Iler, in which he clearly stated "there is no relation or analogy between silicic acid polymerized in aqueous silicate solution and condensation type organic polymers"[79], p.172. Instead, aqueous silica gels consist of discrete colloidal particles which are linked together into branched chains to form extensive networks throughout the liquid medium.

Iler[79] provided a theory for silica polymerization based primarily on the electrostatic forces between the silicic acid monomers. According to this theory, polymerization occurs in essentially three stages:

1. the polymerization of $Si(OH)_4$ monomers to oligomers and then to particles;
2. the growth of particles; and
3. particle aggregation into branched chains and networks that eventually give rise to a gel structure extending throughout the liquid medium.

Stages 2 and 3 depend on the pH and salt concentration. In Iler's theory, the term "salt" refers to the presence of cations and anions in the aqueous system, including substances that introduce ions such as sodium (Na^+), potassium (K^+), or other similar species into the system. Two distinct situations—sol and gel—can arise depending on the interparticle interactions, governed by surface properties and the nature of the aqueous medium (Figure 2.10). The 3D particles formed at stage 1 can grow further by Ostwald ripening, where larger particles grow at the expense of smaller particles being dissolved. In the absence of salts, and at a pH of 7-10, the silicate particles are negatively charged and repel each other, meaning growth continues without aggregation (path A). As a result, a stable colloidal suspension of silicate particles (sol) of some size will form.

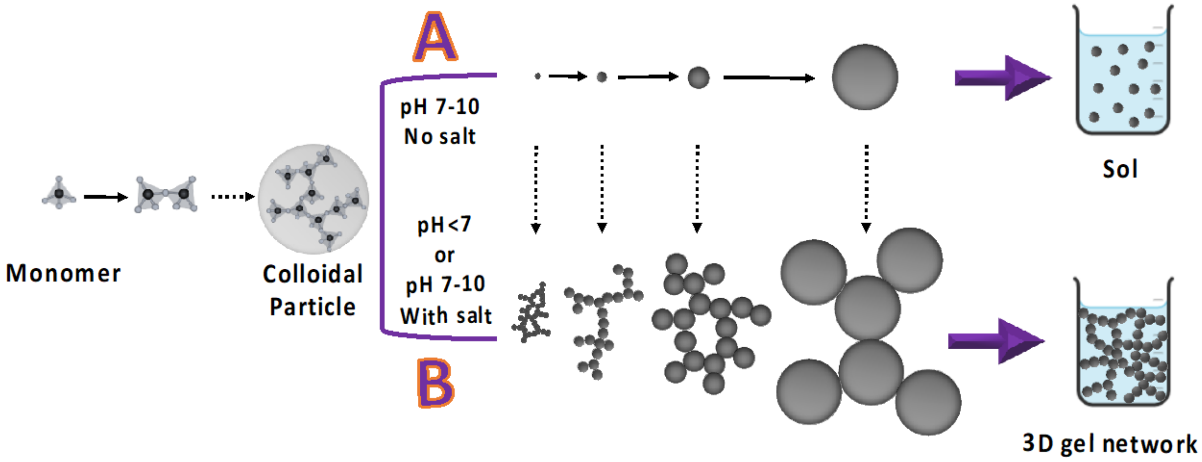

Figure 2.10 Schematic showing the generally accepted growth pathways of silica polymerization from silicic acid over time, according to Iler [79], p. 174. In basic solution particles grow in size and decrease in numbers and form sols (path A). In acidic solution or in the presence of flocculating salts, particles aggregate into three-dimensional gel network (path B). Re-drawn from [79].

If pH is lowered, or salt is present, the charge repulsion is reduced, and particles can come close enough to aggregate and form gel (path B). One should note that the Iler's theory is a general theory of nucleation and polymerization in water-silica systems of only monomeric species. While applying this theory to the gelation of sodium silicate solutions, the characteristics specific to this solution should be taken into account. Sodium silicate solutions consist of complex spatial configurations with different silicon environments on the surface (Q^0-Q^3), making for complex interactions between particles. This complexity is indicative of the reality that the gelation mechanism of sodium silicates is significantly more complicated than pure silicic acid sol.

The findings from ^{29}Si NMR studies of sodium and potassium silicate solutions largely support Iler's view: Silicate species condense internally to the most compact state with maximum number of Si-O-Si bonds and minimum number of terminal Si-OH groups remaining on the outside. Eventually, this condensation will lead to the formation of particles of nearly spherical shape, likely due to a tendency to decrease the surface area in order to minimize the interfacial energy. Contrary to the Iler's theory, however, the gelation process of sodium silicate solutions does not start with only monomeric species. A broad spectrum of structurally different silicate species, including oligomers and even colloidal particles exist in the solution in addition to the monomers. Still, stage

1 would happen in these solutions as the decreasing pH of a waterglass solution favors condensation over hydrolysis and, therefore, silicate species of lower degree of connectivity can further polymerize and form particles (Figure 2.11a).

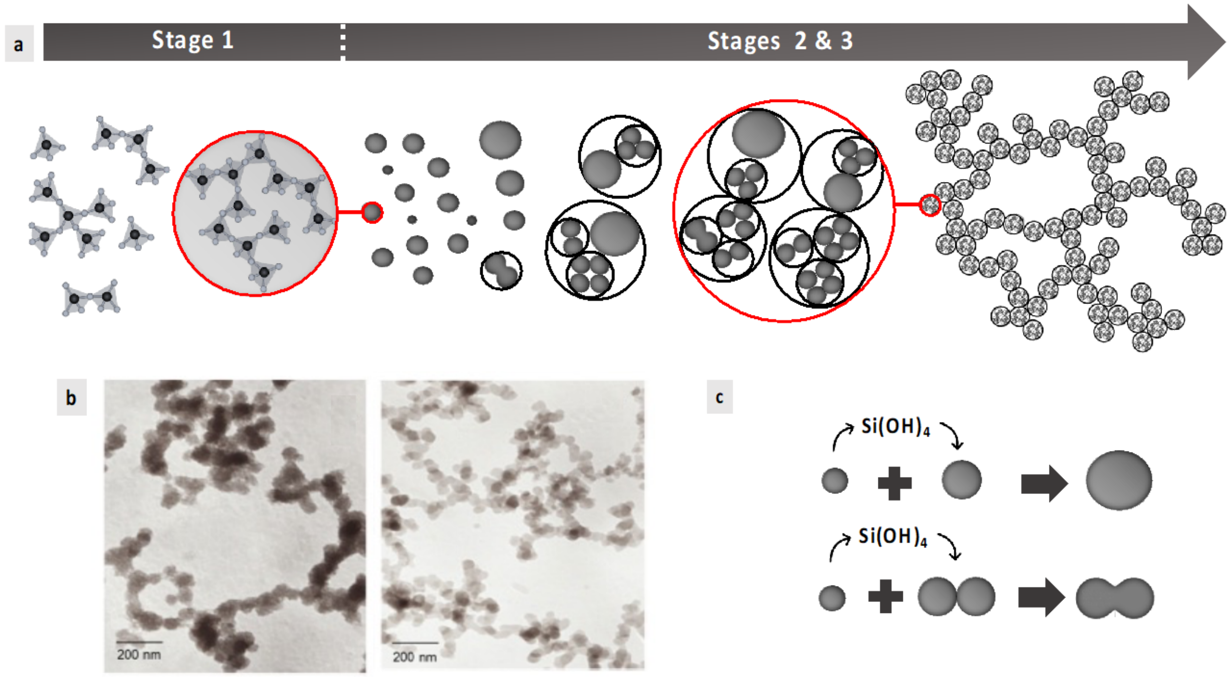

Figure 2.11 (a) The stages of gelation in sodium silicate solutions over time: formation of silicate particles (stage 1), and growth of particles through Ostwald ripening and formation of aggregates which happen simultaneously (stages 2&3). (b) TEM micrographs of silica gels prepared by acidifying sodium silicate solution with H_3PO_4 (left) and H2SO4 (right) – reprinted with permission from[158] (c) Representation of silica deposition on individual particle (upper) and the aggregate necking (lower) during Ostwald ripening, re-drawn from[159].

According to Iler, if salt is present, such as when sodium silicate is neutralized with acid, silicate particles tend to aggregate into 3D gel networks (path B). Decreasing the pH of waterglass increases the Si-OH/Si-O^- ratio and, therefore, the reactivity. The so-called primary silica particles, which are either initially present in waterglass or made during stage 1, may form inter-particle bonds via reactions between reactive SiOH surface groups (Equations (2.2) & (2.3)). These connected particles form aggregates that exhibit mobility and move collectively to form larger aggregates (Figure 2.11a). Interactions are not restricted to the formation of particle-particle or particle-aggregate bonds. Interactions between aggregates are also possible, which ultimately result in a 3D gel network that entraps solvent. The formation of these silicate aggregates and their continuous growth during sodium silicate gelation have been reported in SAXS studies[93,160–163].

Moreover, the finite size of fractal silica aggregates observed in silica gels indicate the presence of elongated, intermingled structures, suggesting that the growth process of silica aggregates must be anisotropic. This anisotropic growth is also evidenced by direct observation: Figure 2.11b shows a TEM micrograph of a silica gel obtained from sodium silicate solution. The silica gel structure can be described as a continuous, percolating network of elongated branches. The directions of bonds formed during aggregations seem highly variable, which is due to both the random distribution of reactive groups on the particles' surface and the large range of Si-O-Si bond angles that can vary between 90°-150°.

Although path A in Figure 2.10 is not the case for waterglass—due to the presence of sodium ions—the question becomes whether Ostwald ripening (stage 2) contributes to the growth of primary particles in silicate solutions before, or simultaneously, with aggregation. Generally, distinguishing between the two particle growth mechanisms (i.e., Ostwald ripening vs. aggregation) is challenging, and less attention has been given to this area. Gerber et al.[160] claimed to observe an Ostwald ripening of the primary particles during waterglass gelation but did not provide any evidence for it. BaŁdyga et al.[164] were able to distinguish the stages of waterglass gelation, including Ostwald ripening and aggregation, by investigating the rates of variation of particle number, particle volume, and dissolved silica concentration. They interpreted an exponential decrease of the number of particles as a characteristic of aggregation and decrease in concentration of dissolved silica as a characteristic of Ostwald ripening. Their results suggested that Ostwald ripening may happen simultaneously with aggregation, increasing the sphericity of aggregates. Therefore, one can assume that stages 2 and 3 happen simultaneously during waterglass gelation, as shown in Figure 2.11a. Since both individual and agglomerated particles are present in the solution, silica would deposit on larger individual particles, as well as the agglomerates necking, due to the negative radius of curvature[159] (Figure 2.11c). It is expected that Ostwald ripening would contribute little to the growth of primary particles when the aggregation rate is fast.

2.2.5.2. Gelation time

The methods used to measure silica gelation time can be divided into qualitative and quantitative categories. In qualitative methods, the amount of time it takes for the solution to stop flowing upon tilting[87,165,166] or inversion[167] is reported as the gelation time. Semi-quantitative methods, using predefined codes to describe the sodium silicate gelation process, have also been proposed[88]. Although these methods are fast, simple, and inexpensive, they depend on the observer's judgment, as well as the gel size and shape, and rely on an imprecise definition of gelation. Quantitative methods, on the other hand, are more sensitive and rely on rheological measurements. The classic quantitative method uses an infinite shear viscosity criterion, in which the gel point is defined as the inflection point where the static shear viscosity deviates from linearity and begins to rise sharply[168,169]. In this method, the transition state is defined by extrapolation, which may be a source of error. Moreover, continuous shearing may affect the gel formation. Another quantitative approach is to study the viscoelastic behavior by dynamic oscillatory shear measurements, also known as dynamic mechanical analysis (DMA). In DMA, the storage and loss modulus of the sample can be calculated from the shear stress that is necessary to obtain a given deformation. The storage or elastic modulus G' represents the elastic portion of the viscoelastic behavior, which describes the solid-state behavior of the sample. The loss or viscous modulus G", characterizes the viscous portion of the viscoelastic behavior, which can be regarded as the liquid-state behavior of the sample. The ratio of viscous-to-elastic (loss-to-storage) moduli reflects the viscous-to-elastic components, commonly named loss tangent (Equation (2.4)), where δ is the phase angle:

$$\tan\delta = {G''}/{G'} \tag{2.4}$$

As the gel network develops, the behavior of the sample becomes more and more elastic. The point at which the elastic modulus G' exceeds the viscous modulus G'' ($G''=G'$ or $\tan\delta=1$), meaning the elastic counteraction of the deformation starts to get stronger than the viscous contribution, can be regarded as the gel point. The G'- G'' cross-over-point method has been used to define silica gelation point[170–172]. Hatzignatiou et al.[171] compared the conventional tube inversion and G'- G" cross-over-point methods to measure the gel time in silica gels obtained from waterglass. The results from the two methods were generally in agreement, with the gelation time obtained from the dynamic oscillatory tests being shorter than the tube-testing results. This result is expected, due to the fact that a sol-gel transition time obtained from the G'- G'' crossover point represents the point at which the elastic contribution outweighs the viscous one, which always occurs prior to the formation of a completely rigid gel. One disadvantage to this approach is that the exact time of crossover depends on the oscillation frequency. To overcome the issue, the intersection of the *G'* and *G"* moduli as a function of time at different frequencies can be used to define the gel point. In other words, the gel point is defined as the point at which the value of *tan d* becomes frequency independent. According to Katoueizadeh et al.[92], who performed rheological measurements at different frequencies on gels formed by mixing waterglass and sulfuric acid, the frequency-independent method is the most accurate way to define the gel point. Despite its accuracy, however, this method is time intensive and requires many measurements at different frequencies.

The gelation time of sodium silicate solution can range from a few seconds to several hours. To control the gelation time, one should consider the factors controlling silicate polymerization and aggregation. These factors are pH, SiO_2/Na_2O molar ratio, solution concentration or dilution rate, presence of salts, and temperature. The following section addresses the influence of each factor on gelation time in sodium silicate solutions.

Effect of pH

The pH of a solution is a key parameter in gelation. Two different charge-catalysis reactions govern the silica gelation process below and above the isoelectric point of silica in water, where pH is approximately equal to 2. Below this point, the polymerization rate is proportional to $[H^+]$ and the system has a net positive charge. According to the mechanism proposed by Okkerse[173], an equilibrium condition between the excess H^+ ions and the silanol groups is established, which results in a temporarily positively charged species (Equation (2.5)). These species attract the remaining silanol groups and form siloxane bridges (Equation (2.6)). The additional proton is later removed by either a water molecule or another silanol group[174,175]. Above the isoelectric point, the polymerization rate is proportional to [OH-] and the system has a net negative charge. The OH^- ion deprotonates a neutral silicate species (Equation (2.7)) and the deprotonated silicate anion subsequently condenses by reacting with silanol groups according to Equation (2.8). The produced OH^- ions are abstracted by H^+ ions to maintain the required pH.

$$\equiv \mathrm{Si{-}OH} + \mathrm{H}^+ \rightarrow \equiv \mathrm{Si{-}OH}_2^+ \tag{2.5}$$

$$\equiv \mathrm{Si{-}OH}_2^+ + \mathrm{OH{-}Si} \equiv \leftrightarrow \equiv \mathrm{Si{-}OH^+{-}Si} + \mathrm{H_2O} \tag{2.6}$$

$$\equiv \mathrm{Si{-}OH} + \mathrm{OH}^- \rightarrow \equiv \mathrm{Si{-}O}^- + \mathrm{H_2O} \tag{2.7}$$

$$\equiv \mathrm{Si{-}O^-} + \mathrm{OH{-}Si} \equiv \leftrightarrow \equiv \mathrm{Si{-}O{-}Si} \equiv + \mathrm{OH^-} \qquad (2.8)$$

Figure 2.12 represents schematically the effect of pH on the stability/gelation time of silica-water systems. As can be seen, there are two pH regions of rapid gelation, one in the strongly acidic region below the isoelectric point and one in the neutral-to-slightly-alkaline region. The decrease of the gel formation time for pH<2, and from pH 2-7, can be explained through the two types of condensation reactions which are catalyzed by H^+ and OH^- groups, respectively. The increase in gel time above pH ≈ 7 is due to an increase in the silica solubility and because the silicate species are appreciably ionized so that particle growth can occur without aggregation. For example, in a solution with 0.1 M Si, the amount of charged silicate anions shifts from approximately 50% at a pH of 8 to almost 100% silicate anions at a pH of 10.8[147]. Above pH ≈ 11, no aggregation or gelation occur, because particles are mutually repulsive. Researchers have studied the effect of pH on gelation time of sodium silicate solutions for more than seven decades[87,92,161,166,168,174,176–178]. Overall, the results follow the trend proposed by Iler[79], which suggests a minimum gelation time around pH 7 and a maximum gelation time around PH 2. It should be noted that the exact pH at which gelation time is at a minimum varies depending on the silica concentration, R_M, and the type of acid used.

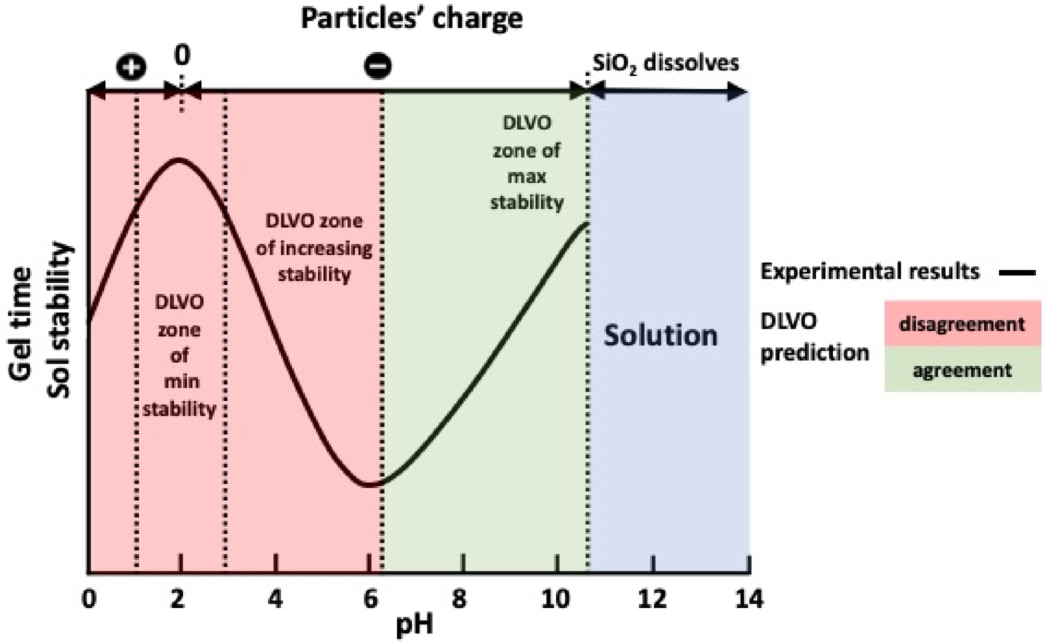

Figure 2.12 Schematic showing the effect of pH on the stability (gel time) of the colloidal silica–water system. Thick solid lines represent experimental results. Shaded areas are approximate zones corresponding to behavior predicted by the DLVO theory, some in contrast with experimental results: minimum stability predicted at pH around 2–3, increasing stability predicted at pH between 3 and 6–8, and maximum stability predicted at pH higher than 8. (Redrawn from [79], p. 367).

According to the DLVO theory, the total interaction between two colloidal particles approaching each other, due to Brownian motion, is the combination of van der Waals attraction and electrostatic repulsion forces that exist between them. Therefore, to maintain the stability of the colloidal system, the repulsive forces must be dominant. However, the maximum colloidal stability of silica solutions is, surprisingly, found at their isoelectric point (pH ≈ 2), where the net charge is zero. Therefore, although silicate solutions are composed of colloid particles, DLVO theory can not predict their stability[95,179,180]. Figure 2.12 illustrates the problem, comparing the stability–pH curve of silica sols from experimental results and zones predicted by DLVO theory. The minimum stability predicted by DLVO is at the isoelectric point, because the silicate species are uncharged. In addition, DLVO theory predicts a gradual rise to maximum stability from pH 2 to 6, which is completely in contrast with experimental results. Although DLVO is still generally acceptable, it fails to capture essential behaviors of the silicate solutions and remains largely unresolved for silica-water systems (for more details the reader is referred to Chapter 3 in[95]).

Therefore, the pH-dependence stability of silica sols does not follow the pattern followed by almost all other oxides and latex colloidal materials, giving another example of how the chemistry of silicate solutions can be extraordinarily complex and complicated.

Effect of temperature

Generally, since aggregation involves a kinetic phenomenon, the rate of gelling is expected to increase with temperature due to increase in Brownian motion, and higher mobility of the molecules which promotes the aggregation of polymeric clusters. Additionally, silicate species tend to depolymerize with increase in temperature (recall Figure 2.8), which has a dual effect: on one hand, the smaller particles exhibit greater mobility and can readily form new aggregates; while on the other hand, the formation of aggregates from smaller particles requires the establishment of more connections compared to larger particles. Although a strong acceleration of gelation with rising temperature has been observed for the acid-catalyzed gels[172], the situation for base-catalyzed gels is less clear. The effect of temperature on gelation time of sodium silicate solutions has been reported to be less pronounced in range of 20-40°C compared to higher temperatures reaching up to 90°C[88,168,172,179]. For most chemical reactions, the temperature dependency of reaction rates follows the Arrhenius equation. Although the relation of gelation time of waterglass with the inverse temperature shows a linear relationship above 40°C, and is in good agreement with Arrhenius equation, temperature dependency becomes more complicated below this temperature (Figure 2.13a).

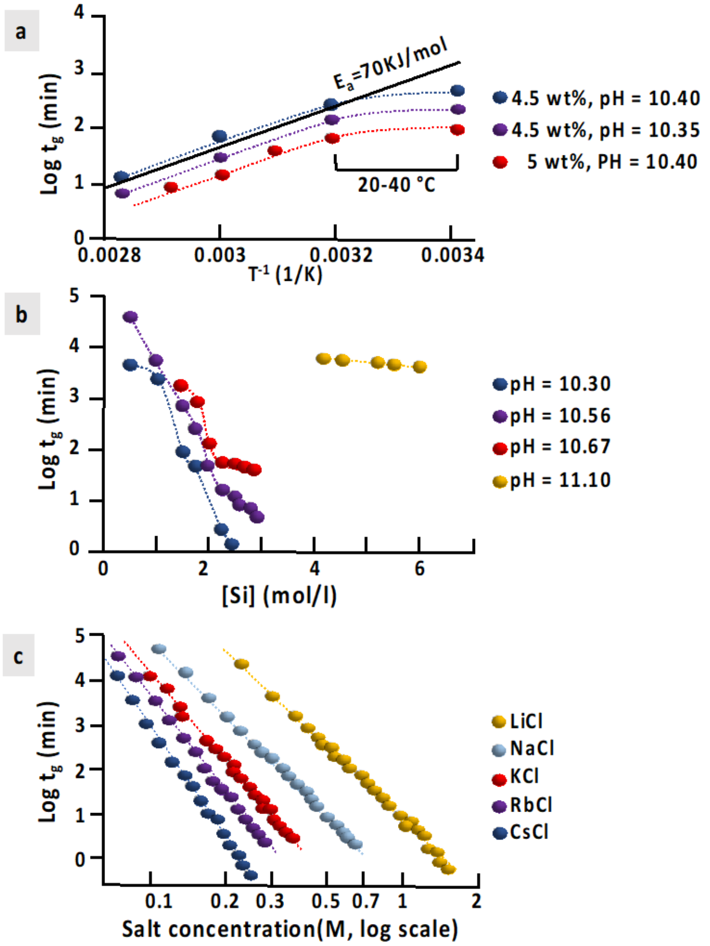

Figure 2.13 (a) Gelation time (tg) as a function of reciprocal absolute temperature for 4.5 wt% and 5 wt% Na-silicate solutions with different pH values. The solid line corresponds to the Arrhenius equation with Ea ≈ 70 kJ/mol. Re-drawn from[168]. (b) Gelation time (tg) of sodium silicate solutions as a function of silicon concentration at different pH values. Re-drawn from [87]. (c) Gelation time (tg) of silicate solutions as a function of different salts concentrations. Re-drawn from[181].

This peculiar behavior has been attributed to a reduction in the activation energy of polymerization. The average activation energy of silica polymerization reported in the literature ranges between 55-77 kJ/mol[88,168,170,182]. According to Bishop and Bear[182], the activation energy drops to a negative value of ~ -67 kJ/mol in the 25-35°C temperature range, meaning that the rate of reaction decreases with the increase of temperature in this region. They suggest that the drop in activation energy in this range implies a pre-equilibrium step in the polymerization that acts as an induction period. This step involves the formation of a hydrogen-bonded intermediate between two silicate particles, which would allow them to be held in proximity and eventually form a siloxane bridge. Above this temperature range, the reaction may occur without the hydrogen bonding mechanism and siloxane bridges are formed by simple collision. This theory, however, has been neither proven, nor further studied. Other factors that may play a role are the effect of temperature on the size of silicate colloids and their surface charge. Generally, the available data on the effect of temperature on gelation time is limited, and more studies are needed to comprehensively address the sodium silicate solution gelation behavior at different temperatures.

Although the temperature affects the gelation rate, it should be noted that variations in pH have a much stronger affect on gelation time. For example, Kristensen et al. [178] showed that the gelation time of a 6 wt% silicate solution will be reduced by a factor of 10 when changing the pH from 11.40 to 11.15, while an increase in temperature by ~10°C will only reduce the gelation time by a factor of 2.5.

Effects of silica and metal ion concentrations

For a specific pH and temperature, gelation is accelerated with the increase of sodium silicate content in water. This tendency is primarily due to the increase in the silica content of the solution. As can be seen in Figure 2.13b, the gel time greatly decreases with an increase in silica concentration at a given solution's molar ratio and pH. Increasing the silica concentration increases the concentration of reactive species in the solution, such as silanol groups, which can promote polymerization. Moreover, more silica particles are present at higher silica concentrations, which can act as nucleation sites for the polymerization reaction.

Additionally, the accompanying cation content reduces the gelation time by permitting closer proximity among the particles. This reduction in gelation time can be explained by the charge screening effect of the cations, and the electric double layer theory (see[86,183] for more details). In the solution, both surface charge determining ions and counter ions always exist. Although charge neutrality is maintained in a system, the concentration of counter ions is the highest near the solid surface and decreases as the distance from the surface increases, whereas the concentration of surface charge determining ions changes in the opposite manner. Such inhomogeneous distributions of ions lead to the formation of the so called "double layer." The properties of the double layer greatly influence the gel formation. When two charged silicate particles are present in the vicinity of one another, attractive (van der Waals) and repulsive (electrostatic) forces will act on them, the sum of which can be seen as a (total) potential energy. For two particles to come near to one another and condense, they need to overcome the potential barrier. A way to reduce this potential energy barrier is adding an electrolyte (e.g., Na^+) to the solution, which decreases the thickness of the electrical double layer and permits the particles to be physically closer to one another. The addition of salt increases the ionic strength of the solution, I, which is a measure of the concentration of ions in that solution:

$$I = \frac{1}{2}\sum_{i=1}^{n} c_i z_i \tag{2.9}$$

Where c_i is the molar concentration of ion *i,* and z_i is the charge number of that ion. The Debye length λ_D is a measure of the thickness of the electrical double layer, which is proportional to the reciprocal of the ionic strength:

$$\lambda_D = \sqrt{\frac{\varepsilon_r \times \varepsilon_0 \times k_\beta \times T}{2 \times e^2 \times N_A \times I}} \tag{2.10}$$

Here, ε_r and ε_0 represent the relative and vacuum permittivity, respectively, k_β is the Boltzmann constant, *T* is the absolute temperature, *e* is the elemental charge, N_A is the Avogadro constant, and *I* is the ionic strength. With the addition of salts to a solution, the ionic strength increases, and the Debye length decreases. Therefore, the electrical double layer surrounding each particle is compressed, resulting in a reduced range of electrostatic forces. As a direct consequence, the addition of salt could facilitate particle aggregation by reducing the repulsive interacting forces. This effect becomes more pronounced as either the concentration or the valance of the salt increases.

Raising the ionic strength by adding salts to silicate solutions has led to a decrease in gelation time[168,170,172]. Salts can also be used to induce gelation by destabilising the silicate particles, even without introducing acids[86,167,183]. Van Der Linden et al.[181] measured gel times for silica sols with five different monovalent salts and found the gel time to decrease over four orders of magnitude while changing the type of cation at constant salt concentrations (Figure 2.13c). The interaction of monovalent ions with silica particles followed the $Li^+ < Na^+ < K^+ < Rb^+ < Cs^+$ order, with Li^+ and Cs^+ ions resulting in the longest and shortest gelation times, respectively. By extrapolation, they expected the gel time to go up to two years in the absent of salts. However, this contradicts Iler's theory, according to which gel time increases to infinity as the salt concentration goes to zero (see Figure 2.10).

Divalent cations were shown to have a stronger effect on the gelation time compared to monovalent cations. Hatami et al.[184] showed that, individually, increased concentrations of Na^+, K^+, Ca^{2+}, and Mg^{2+} reduce gelation time in silicate solutions of fixed silica and HCl acid concentrations. Divalent ions resulted in faster gelation, and immediate gelation was induced when the concentration of Ca^{2+} ions reached above 0.011 M. Moreover, it was shown that the gelation process at the same concentration of Ca^{2+} is significantly faster when Na^+ is present. Hamouda and Amiri[168] investigated the effects of adding various concentrations of Ca^{2+} and Mg^{2+} on the gelation time of sodium silicate solutions, and found that the addition of these ions reduced the gelation time from 50 h to less than 10 min. According to Quarch and Kind[172], sodium silicate solutions are much more sensitive to the addition of salts in the alkaline region compared to the acidic region. The ionic strength of I = 12 mol/l was calculated for the acid-catalysed gel (pH ≈ 0-1), which is large compared to that of the base-catalysed gel (pH ≈ 12-13) which is I =0.8 mol/l. Therefore, the addition of even small amounts of salt to basic mixtures strongly influence the ionic strength and, consequently, the gelation time. Based on these results and the double layer theory, it is expected that at a fixed silica concentration, sodium silicate solutions of higher SiO_2:Na_2O ratios will gel more slowly compared to ones with lower SiO_2:Na_2O ratios, due to a lower concentration of sodium ions. To the best of our knowledge, there is no data available comparing gelation time of waterglass within different ranges of R_M.

2.2.6. Syneresis

After the gel is formed, polymerization continues. The continued condensation between and within the silicate particles results in the expulsion of liquid from the gel pores. As a consequence, the gel network consolidates and shrinks, and its volume, porosity, and internal surface area will change over time. This rather slow process is known as "syneresis". Figure 2.14a is a schematic representation of the process of silica gel syneresis. For the sake of simplicity, the pore liquid is represented by blue (H_2O), although it is a mixture of water, sodium ions, dissociated acid ions, and silicate oligomers. After gelation, as shown in Figure 2.14b, some silicate particles are still held together by hydrogen bonds through water molecules (Figure 2.14 (b.i)), or connected by direct hydrogen bonds (Figure 2.14 (b.ii)). During syneresis, the silanol groups at the surface of primary particles continue to react by forming siloxane bridges, which release water as a by-product (Figure 2.14 (b.iii), Equations (2.7) and (2.8)). The new siloxane bond pulls the particles closer together, contracting the gel network. This dimensional change, and the additional water formed, develop a pressure differential between the gel network and its environment, leading to the expulsion of the pore liquid. Over time, the gel becomes less flexible due to a higher number of stiffening siloxane bonds, followed by the depletion of the reactive groups, all leading the process to slow down (Figure 2.14 c). Ultimately, syneresis is ended due to the remaining repulsive forces and steric hindrance[185].

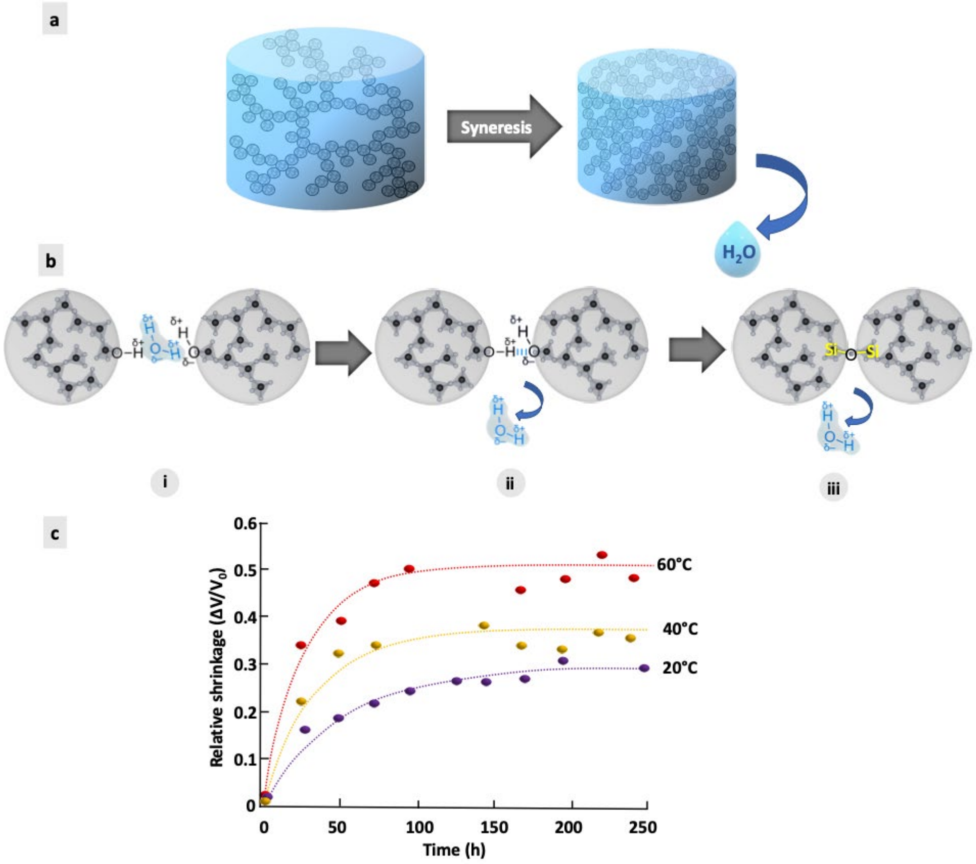

Figure 2.14 (a) Schematic showing the restructuring of the silica gel network during the syneresis process, which results in shrinkage and water expulsion. (b) Primary silicate particles held together by hydrogen bonds through water molecules (i) or by direct hydrogen bonds (ii). During syneresis, the silanol groups at the surface of primary particles form new siloxane bridges, which release water as a by-product (iii). (c) Silica gel shrinkage as a function of time at different temperatures. Re-drawn from[186]

The proposed mechanism for syneresis is supported by many studies. during gelation and syneresis by FTIR spectroscopy. They specifically followed the bands corresponding to bending of water molecules (δH_2O) and asymmetric stretching of the Si─O─Si bond (ν_{as}Si─O─Si) at 1640 cm^{-1} and 1250–970 cm^{-1}, respectively. They found that the ν_{as}Si─O─Si/δH_2O intensity ratio continues to increase after gelation and finally stabilizes, suggesting the development of Si-O-Si bonds during syneresis. Moreover, they noticed that new bands were formed at 550 and 772 cm^{-1} after gelation, which are attributed to O-Si-O bending and symmetric stretching vibrations. These observations suggest an increase of bonds between silicate species along with the release of a H_2O molecule. According to SAXS studies, the size of silicate aggregates continues to increase over time after the gelation point[95,187].

Since the syneresis process is driven by the same condensation reactions as gelation, it is controlled by the same factors upon which gelation depends. According to Scherer[188], the kinetics of syneresis depend on the condensation rate, the mobility of the gel network, and the rate of fluid flow through the contracting network. According to Vysotskii and Strazhesko[189], the slowest shrinkage happens at pH_{iso}, where the condensation rate is at a minimum, and increases as the pH is either raised (pH ≈ 5) or lowered (pH ≈ 0.3). Hamouda and Amiri[168], on the other hand, reported an increase in silica gel shrinkage rate when pH was lowered from 10.5 to 10.1. These results could suggest a pattern similar to Figure 2.12 for syneresis rate vs. pH, meaning there is a minimum shrinkage rate at pH_{iso} and a maximum shrinkage rate somewhere between pH 5 and 10. Nonetheless, to complete the picture and achieve greater understanding of the effect of pH on the syneresis rate, a comprehensive study over all pH ranges is required.

The low permeability of silica gels also causes the syneresis rate to depend on the size of the gel body. According to Wilhelm and Kind[186], smaller samples consolidate much faster compared to the larger ones, clearly showing the dependency between the syneresis rate and physical specimen size. This observation might be due to the difference in the pressure of the pores, or to the length through which the pore liquid must flow. Additionally, the syneresis rate is reported to increase with temperature[168,186]. This effect is shown in Figure 2.14c for silica gels made at pH ≈ 10, and is expected since the temperature increases the polymerization rate, facilitates the movement of the pore liquid, and results in a reversal in the osmotic pressure difference which promotes liquid expulsion from the pores. It has also been shown that the syneresis rate and total shrinkage increase with concentration of silica in the solution [168]. In conclusion, the rate at which syneresis occurs and the total shrinkage of the gel is greatly influenced by the choice of composition, pH, temperature, and specimen size for any solution.

2.2.7. Molecular modelling studies

Molecular modelling can help scientists to unravel the mechanisms of molecular-level events, and predict the behavior of complex systems at a level of detail that cannot be directly measured in experiments. Water-silica systems and the mechanism of silicate-based reactions have been subjects of intensive computational research during the last three decades[190–196] . Figure 2.15 shows various techniques used to simulate molecular interactions in silicate systems and the length- and timescales they can currently sample. The approaches used in molecular modelling cover a broad range of scales from subatomic quantum mechanical (QM) through atomic levels, to mesoscales, and further to continuum descriptions on a macroscopic scale. The detail each model can represent has an inverse relation with its length- and timescale. This trade-off between the resolution of a model and the spatiotemporal scales it can sample, dictates the suitability of the model for the system of interest.

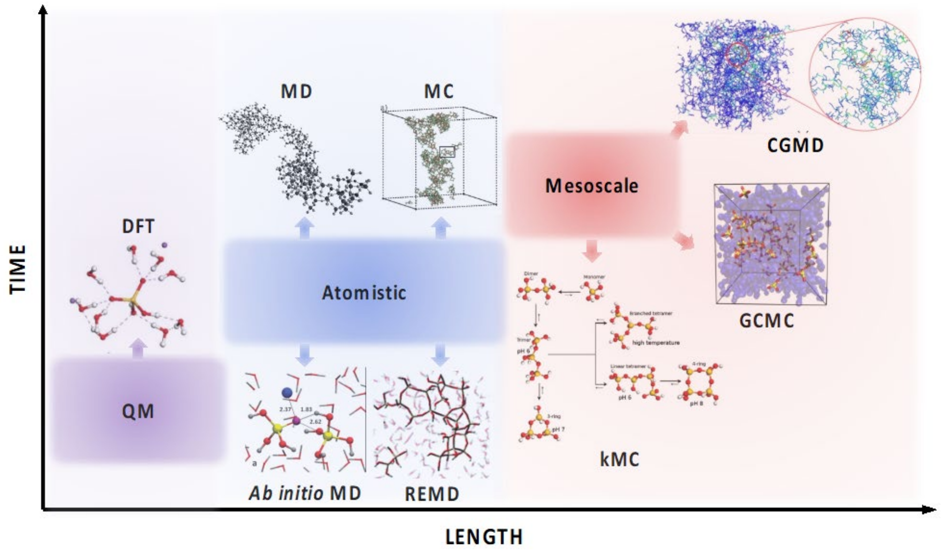

Figure 2.15 Molecular modelling methods at different scales used for simulating molecular interactions in aqueous silicate and silica gel systems. DFT reprinted with permission from[192]. MD reprinted with permission from [193]. MC reprinted with permission from [194]. Ab initio MD reprinted with permission from[155]. REMD reprinted with permission from[195]. kMC reprinted with permission from[196]. GCMC reprinted with permission from[197]. CGMD reprinted with permission from[198].

In the following section, we will explore molecular modelling studies conducted on silicates. Although there have been a number of modelling studies primarily focusing on sodium silicate solutions[199–201], the majority of these investigations have taken a broader perspective by examining silica-water systems. Nevertheless, these studies provide significant insights into the fundamental mechanisms driving silica polymerization and gelation, which can also be applied to understand sodium silicate solutions and gels.

Silicate Polymerization is the initial step in the sol-gel process, and understanding its mechanism is of great importance in order to get insight into the mechanisms underlying gelation. Silicate oligomerization reactions have been studied using quantum-mechanical (QM) calculations at various levels of theory (meaning different levels of approximation or complexity)[190,196,202–205]. These calculations support an ionic two-step mechanism involving penta-coordinated silicon intermediates leading to silica condensation. In the first step, a negatively charged silica oxygen attacks the silicon of another monomer, forming a penta-coordinated intermediate. In the second step, a water molecule is removed. Earlier studies mainly focused on the modelling of the silica oligomerization reaction between two monomeric silicic acids[202,205]. Trinh et al. [190] investigated the formation of oligomers, from dimer to tetramer, and showed that the ionization of silanol groups promotes the condensation reaction. White et al.[192] found that the Gibbs free energies of deprotonation and dimerization reactions of a silicate solution depend greatly on the pH value, indicating the need to accurately replicate the solution environment present, especially for high pH systems.

QM methods are limited to obtaining the energetics of systems containing a few silicate monomers and water molecules, and cannot be used to probe structures formed during gelation or gelation kinetics. An alternative approach is the use of atomistic simulations, such as molecular dynamics (MD)[155,193,195,199,206], which are capable of capturing the kinetics of polymerization. Using MD simulations, Trinh et al.[191] and Pavlova et al.[155] focused on the very first instants of silicate polymerization, studying the condensation reaction up to tetramers and trimers, respectively. Trinh et al.[191] found that the energy barriers obtained from modelling the condensation reaction in explicit water solutions significantly differ from those obtained from gas phase calculations, reflecting the importance of incorporating explicit water molecules when modelling silica condensation. Pavlova et al.[155] also studied the role of sodium ions, concluding on its repressing impact on silica dimerization and trimerization. They assigned this finding to the rearrangement of hydrogen bonds of water surrounding reacting species, forced by sodium.

MD simulations are also suitable to track the silicate particles/clusters in their evolution from an initial mixture of molecules. For example, Rao and Gelb[193] investigated the oligomerization of a set of 729 silicate monomers at 1500 K<T<2500 K, and water-to-silicon ratios of up to 26. After 12.5 ns of simulation, they detected a cluster 6.72 nm in length, which was very elongated and not dense enough to be called a particle, likely due to the relatively primitive reactive potential which was used. It is, however, the largest silicate cluster detected in MD simulations to date. Kamińska et al.[207] used MD simulations to investigate the reaction mechanism and species evolution in sodium silicate solutions with total N0 monomers. They observed a four-step process, starting with the formation of small species (Si_1-$Si_{N0/5}$), followed by the emergence of a large cluster ($Si_{N0/5}$-$Si_{N0/4}$) and a subsequent decrease in small species concentration. The large species stabilized while the intermediate species dissolved, resulting in an equilibrium state where a stable large cluster coexisted with smaller species (Si_1-Si_4). The researchers suggested that the stable large cluster might serve as a pre-nucleus or solid particle, but further analysis of the temporal evolution of the spatial structure is needed for confirmation. While the findings of this study align with the widely-accepted polymerization theory, they also uncover certain unknown aspects, particularly regarding the sequence of events in the evolving species.

Due to present limitations in computational resources, only a few nanoseconds can be simulated with MD methods during which only the oligomerization of silica could be observed. Such simulations often require elevated temperatures to accelerate the condensation kinetics in order to increase the extent of reactions that can be probed.

The use of elevated temperatures has caused concerns that such an approach in MD simulations might not represent experiments at ambient conditions[194,208]. However, Du et al.[206] showed that MD simulations performed at high temperatures can reliably investigate the mechanism and kinetics of silica gelation. They examined systems of Si(OH)4 monomers and water molecules with different water-to-silicon ratios (0–9) and at various temperatures (1500–3000 K). According to their results, although the polymerization rate increases with increasing temperature, the structure of the final gel remains unaffected by the choice of reaction temperature. Still, developing force fields that accurately describe the interactions present at silica-water interfaces is a challenging task[209].

Monte Carlo (MC) simulations are believed to be simpler than MD, as they do not require detailed reactive force-fields[210]. The simplicity of the model makes large system sizes accessible on a modest computational budget. Malani et al.[194] used MC methods to simulate silica polymerization of gel networks for large system sizes. Their results on the evolution of the Qn distribution were in good agreement with Q^n distributions obtained from NMR experiments. A technique for sampling larger systems is the replica-exchange parallel tempering technique. In this method, simulation systems running at different temperatures are swapped periodically to overcome the energy barriers, allowing access to a large phase space[156,195,200]. Jing et al.[195] used the replica exchange MD method to study the evolution of a system containing 300 H_2O, 60 $Si(OH)_4$, and 20 NaOH molecules at 600 K, which lead to the formation of a cluster of ~ 30 Si atoms after 480 ns. Their result showed that 4-ring oligomers evolve to a cage structure with edge-sharing 4- and 5-rings around one sodium ion, consistent with experimental studies where gelation started from 4-rings [140]. It should be emphasized that both MD and MC methods are limited to the length and time scales of atomistic simulations, and only capture the initial stages of the reactions and aggregation process.

Kinetic Monte Carlo (kMC) attempts to overcome the time-scale limitation by filtering out atomic vibrational movements, which allows it to run over much larger space and macroscopic time scales. This method has allowed researchers to explore the reactions in complex solution environments. For example, Zhang et al.[196] used a continuum kMC approach to figure out how pH affects oligomer structure formation in large-scale silicate-solution systems. According to their results, the oligomers favored linear growth at neutral pH conditions, while a higher pH facilitated ring closure by making the silicate species anionic. They also found the silicate oligomerization to be fastest at pH 8. Later, Zhang et al.[211] studied the mechanism of aggregation of silicate oligomers and their subsequent gelation. Their results revealed that 4-rings dominate the ring population during gelation, while 5- and 6-rings were rare and mainly formed during syneresis, leading to more condensed silicate clusters. They also observed fast monomer exchange between silicate oligomers, which is consistent with experimental findings.

Given the complex structures of silicate gels and the high number of molecular events during silica condensation and aggregation, simulating their molecular structure and formation demands high computational power. Coarse-grained (CG) models are aimed at lowering the computational cost by building simplified representations of complex systems while allowing them to maintain key chemical and physical characteristics. The desire for simplification has motivated the development of coarse-grained Monte Carlo (CGMC) models, which can simulate large systems over long time-scales with a reasonable computational cost, making them useful for studying silica polymerization [208]. Jin et al.[212] used CGMC by coarse-graining OH groups of $Si(OH)_4$ molecules into single particles. Their investigation revealed that a body-centered cubic (BCC) lattice system is the most realistic model for replicating the bonding environment present in silicate systems, allowing for variation in the Si–O–Si bond angle. They observed silica polymerization to proceed in the following order: (1) formation of dimers, small oligomers, non-cyclic chains, ring structures, and spherical particles; (2) Ostwald ripening of larger particles; and (3) particle aggregation. This model is in excellent agreement with the proposed mechanism for gelation mentioned in previous sections. However, their model only included pure silica systems. The simplicity that CG models offer comes at the price of the difficulty in obtaining quantitative insights into mechanisms and processes. To resolve this issue, these models have been used in combination with atomistic resolution models. White et al.[213] were the first to use QM calculations in a CGMC simulation to study the initial stages of gel/cluster formation in sodium silicate systems. Their results showed that at high-silica concentrations, above 4 M, the system tends to form a single large cluster in preference to the many small oligomeric clusters observed at lower silica concentrations. In good agreement with the Q^n connectivity distribution observed by ^{29}Si NMR.

Grand canonical Monte Carlo (GCMC) is another powerful technique that is suitable for studying dynamic systems like silicate solutions. Unlike methods such as MD, the number of atoms and molecules in a GCMC simulation is variable and no prior knowledge of the number and location of molecules is required. Dupuis et al.[197] developed a method that couples GCMC and parallel tempering. The GCMC simulation allowed them to add or remove water molecules, and the parallel tempering increased the gelation rate by at least two orders of magnitude compared to MD simulations. This approach allowed them to not only simulate the gelation, but also to reproduce the effect of diluting or drying the silica gels. Finding agreement with experiments, they observed that the siloxane bridges between silicate chains increase during syneresis and drying, the structure of gels becomes denser, and glasslike structures form. Given these findings, it appears that multiscale models such as this could bridge the gap between atomistic and mesoscale levels, and provide quantitatively accurate simulations of the behavior of silicate species in both solution and gel state. Still, direct development of sodium silicate solution, or silica gel models is relatively rare.

2.2.8. Conclusions and future scope

Aqueous silicate solutions contain a complex mixture of silicate species with varying degrees of polymerization, in a dynamic equilibrium. ^{29}Si NMR is currently the best method for identification and quantification of these species and, to date, the structures of all the major species representing up to 85% of the silicon in the solution, have been determined. To the best of our knowledge, no new structures has been presented during the last decade, and recent studies have applied ^{29}Si NMR only to investigate the reactions involving waterglass (e.g., zeolite formation). This lack of recent attention and progress might be due to a combination of a lack of need and lack of adequate instrumentation. It is clear, though, that advances in NMR spectroscopy will further extend the array of structures able to be determined in these solutions.

Raman and IR spectroscopy are considered useful and inexpensive techniques for rapid analysis of the structure of silicates, both in the aqueous and solid phases. Overall, Raman spectroscopy presents a better option when compared to IR spectroscopy because: (1) the spectra obtained from Raman spectroscopy are usually better resolved than the corresponding IR spectra; (2) no sample preparation is needed; (3) Raman does not detect water and is ideal for aqueous environments. Like NMR, however, some details of the spectra remain unclear, especially for weaker bands.

SAXS and DLS are powerful tools to investigate the size distributions of the silicate colloidal particles, and have provided structural information concerning the way in which primary particles grow and aggregate. However, two main areas remain unclear: (1) The density and internal structure of colloids; (2) The effect of solution concentration, R_M, and temperature on colloid size. Discrepancies between the results obtained from the two methods persist, the origin of which remains unclear.

The theory proposed by Iler for silica polymerization is widely accepted and is in good agreement with experimental results. However, this theory is proposed for silica-water systems of monomeric species. In this section, the silica polymerization theory has been modified specifically for sodium silicate solutions for the first time. The effect of various parameters on sodium silicate gelation kinetics has been extensively studied. However, the lack of a standard methodology for measuring the gelation time cast doubts on the repeatability of the experiment results and make comparisons between the results of different techniques almost impossible. Generally, insights into the underlying principles and molecular chemical aspects of silica gel formation and syneresis are still limited.

Overall, there are many questions which remain unanswered. For example, the interplay of water, silicate species and sodium ions at the atomic scale is unclear:

- What are the differences between acidic and basic gels' chemical structures?
- How does the gel structure evolve during syneresis?
- What is the effect of aging on waterglass, and how can it be controlled?

This lack of clarity is probably due to:

1. the complexity of the structure of silicate solutions;
2. the rapid exchange rate between the silicate species, which changes according to various parameters;
3. complications in analysis that occur because of experiments carried out under insufficiently controlled conditions; and
4. most of the applied analytical methods require diluted, or enriched, solutions for obtaining best results.

In our opinion, the answers to these questions are most likely to come from a thorough exploration at the atomic and molecular level.

One of the most promising ways to mediate the complexity associated with experimentally characterizing the structure of water-silica systems is molecular modelling. A variety of sub-atomic to meso-scale computational techniques have been applied to study these systems in both liquid and gel state. However, in most cases the studies are still limited to rather small numbers of molecules, and the very first moments of the process, which are not fully representative. Multiscale approaches have the potential to resolve the problem by combining the strengths of different computational techniques at different scales. Overall, investigations in this area have been complicated by many factors, including:

1. the high number molecules and individual processes occurring concurrently in alkaline silicate systems;
2. the dynamicity of speciation and its dependence on many factors; and
3. the current computational cost limitations in the implementation of full multiscale models.

Therefore, although molecular modelling can open paths for developing a complete understanding of the molecular structure of waterglass and silica gels, there is still a long way to go until modelling may be routinely applied to entire waterglass and silica gel systems. Hopefully, with rapid progress in both hardware and software capabilities, that point lies in the foreseeable future.

2.3 Sodium silicate solutions in biomedical applications

Sodium silicates show great promise in biomedical applications, in both solution and gel state. For instance, sodium silicate solutions are used in creating dense calcium phosphate-based bone cements, where they not only act as a hardening agent but also help control properties like setting time, pH, in-vitro degradation rate, and mechanical strength[214–216].

Silica aerogels, formed by removing the liquid from the gel network while preserving its structure, are noteworthy in nanotechnology due to their low density, large surface area, and adjustable nanometer-sized pores. These aerogels are employed in various biomedical fields, including antibacterial agents[217], tissue engineering[218,219], nerve regeneration[220,221], and drug delivery[222]. Their unique features—such as biocompatibility, high and customizable porosity, mechanical strength, and active surface functionalities—make them particularly suited for bone tissue engineering[223]. Even more promising, sodium silicate gel have been shown to biomineralize when immersed in simulated body fluid[224,225], suggesting their potential to be used as an "bioactive binder". For example, silica hydrogel has been used as a coating to bioinert polymeric materials as an alternative nucleating agent to bioactive glasses for inducing the formation of HCA layer and make them bioactive. Using silica gel instead of bioactive glass has the advantage of being able to coat efficiently both compact materials and porous 3D architectures aimed at being used on tissue replacement applications and as tissue engineering scaffolds[225,226]. Silanol groups on their surfaces enhance bioactivity, promoting cell attachment, proliferation, and differentiation while allowing controlled biodegradation as new tissue forms[218,219,227,228]. This is not surprising because as shown in Figure 2.2 in section 2.1., a layer of silica gel is formed on bioactive glass surface before HCA is being deposited.

Silica hydrogels are mostly preferred in pharmacy, medicine, and transdermal drug delivery because they have high water content, with soft and rubbery surface, mimicking human tissue, muscles, tendons and cartilage[229]. These hydrogels have rarely been used in their wet state for bone scaffold applications, except as coatings. However, they hold considerable promise for this study because a similar approach is applied—where waterglass coats bioactive glass particles and then transforms into a gel. Additionally, silica gels have demonstrated excellent cell viability under encapsulation conditions in their wet state[230].

Chapter 3: Mapping The Sol-Gel Transition in Acid-initiated Sodium Silicate Solutions

3.1. Abstract

Bioactive glass bone scaffolds, known for their unique ability to bond with bone, have proven effective for bone regeneration. Despite various techniques, large-scale porous bioactive glasses still face challenges. Our design builds on prior proof-of-concept work aimed at creating formable composite scaffolds by mixing 45S5 bioactive glass powder with a sodium silicate binder (waterglass). This study aims to reduce the setting time of the composites from ~10 days to a clinically practical range (~10 minutes) by combining waterglass with an acid initiator before mixing with bioactive glass. The effects of pH (2-11), waterglass concentration (15-50 wt.%), and acid initiator type (phosphoric acid and boric acid) were investigated to optimize waterglass gelation kinetics and final gel microstructure. Overall, gelation kinetics and microstructure were mostly affected by pH and waterglass concentration, with the type of acid initiator being less significant. A 10-minute gelation time was achieved with boric acid at pH 10.6 and with phosphoric acid at various pH levels (10.63, 10.35, 9.7, 5.3, 4.8, and 3.36) by adjusting waterglass concentration. Exponential and polynomial models were suggested to predict gelation time in basic and acidic regions, respectively. The optical properties of gels were studied qualitatively (transparency change and Tyndall effect) and quantitatively (UV/VIS Spectrophotometry), providing insights into gelation kinetics and microstructure. It was found that concentrated acidic gels consisted of smaller particles forming a tightly packed network (pores<~550 nm) with higher light transmittance at the gel point (%T), while basic gels had larger aggregates forming a less dense network with pores of ~5 μm, resulting in lower light transmittance (%T) at the gel point. The light transmittance and pore size of the gels in both groups converged with decreasing waterglass concentration. UV/VIS Spectrophotometry marked the gel point at 8 minutes, indicated by a rapid change in light transmittance, which was shorter than the tube inversion method, signifying the onset of gelation. This work contributes to controlling waterglass gelation by identifying key parameters and understanding their relationships with gelation kinetics. Additionally, it elucidates how these parameters influence the final gel structure, allowing the tailoring of processing conditions to create a formable, *in situ* setting bioactive glass composite bone scaffold.

3.2. Keywords

Sodium silicate solution, Sol-gel transition, Gelation kinetics, Optical properties, Silica gel, Bone tissue scaffold

3.3. Introduction

The very first material that was found to form a bond with bone was the original bioactive glass composition, 45S5 Bioglass (45 wt% SiO_2, 24.5 wt% CaO, 24.5 wt% Na_2O, and 6 wt% P_2O_5), which has been in clinical use since 1985[1]. Since then, particles and putties containing a variety of bioactive glass particulates are widely used in clinical settings. However, surgeons sometimes require large interconnected macroporous scaffolds for the regeneration of large bone defects. These 3D porous structures, known as scaffolds, act as temporary templates to support and stimulate bone regeneration while they gradually degrade and are eventually replaced by new bone tissue.

The first attempt to produce a bioactive glass-based scaffold was made in 2002 using a sol-gel process combined with in-situ foaming to obtain a macroporous structure[2]. Since then, many researchers have worked to identify the optimal manufacturing process for fabricating an "ideal" scaffold from bioactive glass. Multiple attempts have been made to define what constitutes an ideal scaffold[3–5], which can be summarized by the following points:

- Sufficient mechanical properties and controllable degradation rate, capable of providing short-term strength that transitions into load-bearing bone before being resorbed;
- Ability to bond to bone (bioactivity);
- Interconnected porosity and controllable pore size to allow for cell growth and vascularization;
- Reliable, repeatable, fast, and economically convenient for mass production;
- Free from any toxic substances and safe for people and the environment;
- Customizable to meet the needs of each patient.

The technologies developed so far for producing glass-based scaffolds can be categorized into two main groups: 1) conventional methods and 2) additive manufacturing techniques (AMT), also known as rapid prototyping (RP). The first group follows the top-down manufacturing approach, which involves removing selected pieces or parts from a bulk material to create the desired shape and porosity. The second group uses a bottom-up approach, building the scaffold layer-by-layer or piece-by-piece. Details about the methods in each group and their advantages and disadvantages can be found elsewhere[4,6]. Despite the variety of techniques available, there are still no large-scale porous bioactive glasses on the market. Applying problematization[7] on the field of processing methods for ceramic-based tissue scaffolds revealed three major challenges:

1. Conventional methods require heat treatment for consolidation, which adversely affects the glass bioactivity;
2. AMTs, such as 3D printing, require 3D models and imaging for each patient, which can be costly and time-consuming;
3. There is a lack of formability, despite bone defects coming in various sizes and shapes.

Suppose we could create a binary mixture of a powder and a liquid binder that a surgeon can form into a paste and then press directly into a bone defect in a patient, and let the implant set (i.e., harden to prevent migration from the wound site) in seconds to minutes. As a proof-of-concept, a design was explored in our lab in which 45S5 glass powder was combined with a sodium silicate solution binder to create a formable paste that sets upon exposure to CO_2 gas in air and hardens into a rigid, porous scaffold[8,9]. Sodium silicate solution, also known as waterglass, was chosen as a binder phase for its ability to set at room temperature,efficiently wet and coat the glass surface, and set glass frit into a porous 3D structure. Additionally, some reports indicate the promise of sodium silicates for biomedical applications. For example, soluble silicates have been used in the fabrication of dense calcium phosphate-based bone cements [10–12] and drug delivery agents[13]. In these examples, sodium silicate solution not only served as a hardening liquid but also controlled various properties of the composites, including setting time, pH, in-vitro degradation rate, and mechanical properties. Even more promising, sodium silicate gel coatings on polymeric substrates have been shown to biomineralize when immersed in simulated body fluid[14,15]. Therefore, waterglass has the potential to be used as a “bioactive binder.”

The proof-of-concept studies[8,9] showed that fabrication of porous bioactive glass composites at ambient temperature is possible: a formable paste was successfully made that set in air with geometric stability, and the resulting structure of the compacts was porous with sufficient compressive strength to permit handling. However, the setting time of these bioactive glass composite bone scaffolds were more than 10 days (~300 hrs), making them impractical for clinical use. Therefore, the main goal of this research is to decrease the setting time of bioactive glass-waterglass composite bone scaffolds to a range that is practical for clinical applications. Specifically, we aim to develop a workable, formable paste that can be inserted inside a bone defect of any size and shape and sets *in situ* into a rigid, porous 3D structure, promoting bone tissue regrowth in a safe and effective manner.

To decrease the binder setting time, we first need to understand the setting mechanism. Sodium silicate solutions, with the general formula of $(Na_2O)x.(SiO_2)_y.(H_2O)_z$ (x,y,z =molar ratio), are complex mixtures of water, anionic silicate species, and sodium cations, in dynamic equilibrium. The SiO_2 concentration and the SiO_2:Na_2O ratio are the two main factors that govern the physical and chemical properties of these solutions. Waterglass can readily transform into sodium silicate gel upon acidification. Silica gel formation is initiated by destabilizing waterglass with acids (HX), which triggers the partial neutralization of $Si\text{-}O^- Na^+$ ion pairs and leads to the formation of reactive silanol (Si–OH) groups and sodium salts[16] (Equation (3.1)). Silanol groups on the surface of silicate particles connect by forming Si-O-Si bridges or physical interactions, forming silicate aggregates that form a 3D network of silica gel. Both the formation of reactive Si–OH groups and overcoming of repulsive interactions between silicate species are prerequisites for the aggregation/agglomeration of colloidal silicate particles and gel formation, and are mainly governed by the pH.

$$\equiv Si - O^- \cdots Na^+_{(aq)} + HX_{(aq)} \longrightarrow \equiv Si - OH_{(aq)} + NaX_{(aq)} \qquad (3.1)$$

In the initial composite design, the waterglass binder was exposed to CO_2 in ambient air for an extended period, allowing CO_2 to partially dissolve into the waterglass to form carbonic acid (Equation (3.2)). Carbonic acid introduces hydrogen ions into the solution through dissociation (Equations (3.3) and (3.4), which then react with silicate species, resulting in the formation of a sodium silicate gel. Silica gel binds adjacent Bioactive glass particles together, leading to hardening and setting of the composite. Notably, over this lengthy period (>10 days), all the water in the waterglass evaporates, leaving any formed gel and any remaining binder fully dried. The reaction between waterglass and CO_2 is inherently slow because carbon dioxide is present in the atmosphere in very small amounts (~0.04%).

$$CO_{2\,(g)} + H_2O_{(l)} \leftrightarrow H_2CO_{3\,(aq)} \tag{3.2}$$

$$H_2CO_{3\,(aq)} \leftrightarrow HCO^{-}_{3\,(aq)} + H^{+} \tag{3.3}$$

$$HCO^{-}_{3\,(aq)} \leftrightarrow CO^{2-}_{3\,(aq)} + H^{+} \tag{3.4}$$

To accelerate composite setting process, acid solutions can be mixed with waterglass before combining with bioactive glass, acting as acid-initiators. Therefore, the setting time of bioactive glass-waterglass composite bone scaffolds is primarily controlled by the gelation time of the waterglass, which is the focus of this study (see Figure 3.1).

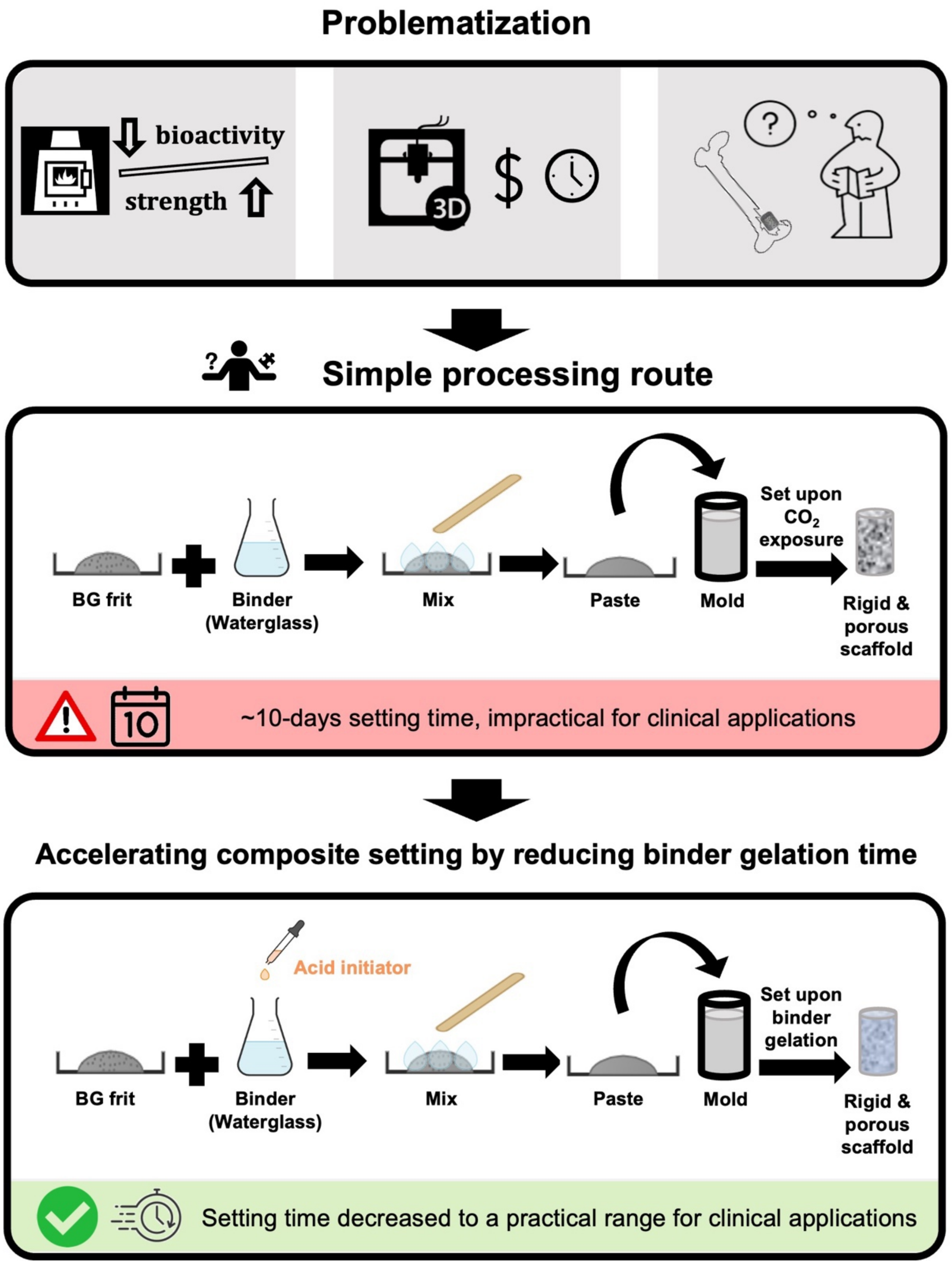

Figure 3.1 Progression from problematization to design approach in this study: three major challenges were spotted applying problematization in bioactive glass bone scaffold processing techniques, which led to the development of a new processing technique (the previous proof-of-concept work) which resulted in composites with long setting time impractical for clinal application. This study aims to develop of a new approach aimed at accelerating the setting time to a practical range for clinical applications.

The gelation time of sodium silicate solutions can be controlled and accelerated by controlling the parameters influencing silicate polymerization and aggregation/agglomeration, and consequently gelation kinetics in these solutions. These parameters include pH, waterglass concentration or dilution rate, the SiO_2/Na_2O molar ratio of waterglass, the presence of salts, type of acid initiator, and temperature, which is comprehensively discussed in our recent review paper[16]. Considering the degree of effectiveness and the conditions specific to our target application (bone tissue scaffolds), we narrowed down the parameters investigated here to these main three:

1. **pH:** pH is a key parameter controlling gelation in silica-water systems. Although many studies have examined the effect of pH on waterglass gelation time, they are typically limited to narrow pH ranges of 1-2 units[17–19]. A comprehensive study conducted by Iler[20] in the 1970s focused on silica-water systems in general, but not specifically on waterglass, leaving the general trend for gelation time across the entire pH range for waterglass uncertain. Detailed data on the relationship between gelation time and pH is essential for precisely modeling and controlling the gelation process, which is critical for tailoring the properties of the resulting gel. Although applying soluble silicates to biomaterials limits us to a pH range safe for human tissue, data on gelation time across the whole pH range is the missing puzzle piece for developing gels from waterglass. This information is crucial for optimizing the gelation process, regardless of the target application.
2. **Type of acid initiator**: various acids —both strong (such as hydrochloric acid [21], nitric acid [22], phosphoric acid [23], and formic acid [24]) and weak (such as boric acid [25], acetic acid [26] and carbonic acid [27]) —are used for silica gel formation from waterglass for different applications. However, the rationale behind the selection of a given acid as an initiator is rarely explained in the literature and appears to have been chosen arbitrarily. Studies using multiple acid initiators for silica gels[28,29] typically fail to maintain constant pH, making it unclear whether the type of acid initiator affects gelation time beyond its influence on pH. Here, we seek to elucidate the effects of acid initiators by controlling and fixing other independent variables.
3. **Waterglass concentration**: Gelation is known to accelerate with an increase in sodium silicate content in water[16]. While higher concentrations initially promise shorter gelation

times, adjusting waterglass concentrations offers flexibility to achieve *specific* gelation times across varying pH conditions. Therefore, we investigate the impact of initial waterglass concentration on gelation kinetics to optimize the gelation processes tailored to bone tissue composite scaffolds.

In the investigation, we focus on the following points:

- How should pH and waterglass concentration be adjusted to achieve a target gelation time that is practical for making composite bone scaffolds?
- Can gels with the same gelation time be produced under different processing conditions (i.e., pH, waterglass concentration, type of acid initiator)? How do these conditions affect the final properties of the gels?
- At a fixed gelation time, does the type of acid initiator influence the final properties of the gel?
- Can the appearance and optical properties of the gels provide insights into the sol-gel kinetics and structure of final gels?

3.4. Experimental design

3.4.1. Independent variables:

pH: Our specific requirement is to develop a paste consisting of bioactive glass and WG that can be applied to fill bone defects and set within a practical timeframe for surgical procedures. Considering the time necessary to manipulate and shape the paste at the defect site before it solidifies significantly, and to ensure adequate time for sample preparation and characterization, we set a target gelation time of 10 minutes. The variable in our study is the pH at which these gels achieve the desired gelation time of 10 minutes. This variability in pH allows us to explore different formulations to ensure the gel remains effective and safe for clinical use. We limited the pH range to above 2 because pH levels below this threshold are generally considered unsafe or impractical for most applications.

Type of acid initiator: We selected boric acid (BA) and phosphoric acid (PA) as acid initiators because both have been used in different biomaterials such as contact lenses[30], and dental and bone cements[31,32]. Moreover, this selection allows us to compare and contrast the effects of a weak acid (BA) and a strong acid (PA) on gelation kinetics and final gel properties.

BA (H_3BO_3) acts as a monobasic acid in aqueous solutions. BA either consumes a strong base like a hydroxide ion, or reacts with water to release a proton[33]:

$$B(OH)_3 + H_2O \leftrightarrow B(OH)^-_{4(aq)} + H_3O^+_{(aq)} \quad , \mathrm{p}k_\mathrm{a} = 9.24 \tag{3.5}$$

PA (H_3PO_4) is a polyprotic acid and its dissociation occurs in three steps depending on the pH[34]:

$$H_3PO_4 + H_2O \leftrightarrow H_2PO^-_{4\,(aq)} + H_3O^+_{(aq)} \quad , \mathrm{pk_a}=2.12 \tag{3.6}$$

$$H_2PO^-_{4\,(aq)} + H_2O \leftrightarrow HPO^{2-}_{4\,(aq)} + H_3O^+_{(aq)} \quad , \mathrm{pk_a}=7.21 \tag{3.7}$$

$$HPO^{2-}_{4\,(aq)} + H_2O \leftrightarrow PO^{3-}_{4\,(aq)} + H_3O^+_{(aq)} \quad , \mathrm{pk_a}=12.68 \tag{3.8}$$

Waterglass concentration: Waterglass concentration significantly affects its viscosity and tackiness, and consequently influences its properties as a binder. A key criterion to consider is that after mixing the binder with bioactive glass the paste should be formable and stable enough to fill a bone defect of any shape. Waterglass:water ratio of 1:1 was the minimum ratio at which the viscosity of the binder allowed homogenous mixing with acid solution. Conversely, a ratio of 1:5 was found to be the maximum at which the binder maintained enough adhesion to create a formable paste that retained its shape after demolding from a cylindrical mold.

3.4.2. Materials

The starting commercial sodium silicate solution (Sigma-Aldrich, CAS number: 6834-92-0), St. Louis, MO, U.S.A) had the following characteristics: [SiO_2] = 26.5 wt.%, [Si] = 6.13 mol/l; relative density = 1.39 g/l; pH = 11.9; SiO_2/Na_2O molar ratio = 2.57. The acid initiators used were: phosphoric acid, 85% solution (Fisher Scientific, CAS number:7664-38-2, Toronto, ON, Canada) and boric acid powder, ≥ 99.5% (Fisher Scientific, CAS number: 10043-35-3, Toronto, ON, Canada).

From previous experience in the lab, the waterglass must be used within its shelf life and must be sealed swiftly after dispensing liquid and sealed tightly to reduce the possibility of chemical changes over time via evaporation of water, which could induce a change in the overall distribution of species.

3.4.3. Preparation of dilute waterglass and acid solutions

The dilute waterglass solutions were prepared by adding DIUF water to the commercial solution at room temperature under magnetic stirring to achieve waterglass to water weight ratios of 1:1, 1:3, and 1:5. To minimize the water introduced with the acid solution, a 0.7 M BA solution was prepared by dissolving 4.3 g of BA powder into 100 ml of DIUF water, which was near the maximum solubility of BA at room temperature. Additionally, a 14.8 M PA solution was prepared by mixing 11 g of 85% PA solution with 1 ml of DIUF water, achieving the maximum PA concentration with a sufficiently low viscosity for micropipette use. The compositions and pH values of the starting diluted waterglass and acid solutions are reported in Table 3.1:

Table 3.1 Compositions and pH values of the prepared starting waterglass and acid solutions

	WG:Water (wt. ratio)	Water (g)	WG (g)	pH
WG Solutions	1:1	10.00	10.00	11.48
	1:3	15.00	5.00	11.22
	1:5	16.66	3.34	10.91

	Acid type	Acid: Water (wt. ratio)	Water (g)	Acid (g)	pH
Acid Solutions	PA	11:1	1.00	11.00	1.50
	BA	1:24	96.00	4.00	3.20

3.4.4. Gelation time

Gelation time, defined as the interval between acid introduction and the gel formation point, can be determined using qualitative, semi-quantitative, or quantitative methods. Qualitative approaches observe the point when the solution stops to flow upon tilting[18,25,35] or inversion[36,37], while semi-quantitative methods use predefined codes to describe the gelation process[38], subjective to observer judgment. Quantitative techniques on the other hand, employ rheological measurements in static[17,39] or dynamic[40–42] modes. Due to its simplicity, speed, good agreement with qualitative methods[43], and occurrence at the formation of a completely rigid gel, we utilized the tube inversion method to measure the gelation time.

Four series of pH-adjusted samples were prepared by adding increasing amounts of acid initiator to 20 g of initial diluted waterglass solutions of varying concentrations (1:1, 1:3, and 1:5) under continuous stirring. The volume of acid in each sample was adjusted based on the waterglass concentration solution and the type of acid initiator:

- **PA specimens:**

PA solution was added using a micropipette to achieve gelation times of less than 90 minutes, recorded as the minimum acid required in the basic region for each concentration. From the minimum acid amount, additional acid was added stepwise to subsequent samples of the same concentration. Specifically, 5 µl, 10 µl, and 20 µl of acid were added in each step for PA 1:1, PA 1:3, and PA 1:5, respectively. This process continued until the instant gelation zone in the basic region was reached. After this point, acid was added incrementally until the gelation time increased again, marking the minimum acid required in the acidic region. From this point, 100 µl of acid was added to the minimum amount in each step for all concentrations.

- **BA specimens:**

BA solution was added using a 10 ml syringe to achieve gelation times of less than 90 minutes in the basic region. Then, 1 ml of acid was added at each step until reaching the instant gelation zone. The initial waterglass concentration of the solution for all BA specimens was 1:1 (total one series of BA specimens) which was increased in each step (up to reaching rapid gelation) based on the amount of water introduced from the BA solution. No acidic gel was prepared using boric acid due to its weak acidic nature.

For both PA and BA specimens, the pH of each mixture was measured using a pH meter (Accumet Basic AB15 Plus, Fisher Scientific, Toronto, Canada) with the pH probe inside the solutions and the final pH was recorded two minutes after acid addition. The pH meter was calibrated using buffer solutions on a daily basis. Based on the pH range being measure, three buffer solutions among pHs of 2, 4, 7, 10, and 12 were used for calibration. The solutions were then transferred to 15 ml glass vials, filling up to ¾ of the total volume. The vials were gently inverted 180° (turned upside down) at regular time intervals, depending on the gelation rate, to observe the flow of the solution. The time at which the solution ceased to flow upon inversion was recorded as the gelation time.

3.4.5. Optical properties

3.4.5.1. Macrographs

Macrographs were used in this study for qualitative analysis of optical properties and to observe the Tyndall light scattering effect during, and after, the sol-gel transition. All macrographs were obtained using a digital single-lens reflex camera (D300s, Nikon, Nikon Corporation, Minato City, Tokyo, Japan) equipped with an AF Micro-Nikkor 60 mm f/2.8D lens (Nikon Corporation, Minato City, Tokyo, Japan). A setup consisting of a stand holding a black non-reflective velvet fabric as the background was used for capturing photos. The camera exposure settings were kept constant for all photos. Only specimens with target gelation time of 10 minutes were photographed.

3.4.5.2. Sol-gel transition

Fresh mixtures of waterglass solutions and acid solutions were prepared, poured into 10 ml glass vials, and were placed on the non-reflective stage. Photos were taken at 2-minute intervals during the sol-gel transition, at the gelation point, and at 5, 15, 30, 45, and 60 minutes after gelation. Before reaching the gelation point, the samples were leaned against a metal piece at a 45-degree angle to show that they still had flow. After the gelation point, the samples were photographed in an inverted position.

3.4.5.3. Tyndall effect

One of the characteristic properties of disperse, or colloidal, systems is the Tyndall effect (or Faraday-Tyndall effect), which is the ability of these systems to scatter light in all directions when illuminated from one side with visible light. A colloidal dispersion, or colloid, is a suspension of tiny particles in some liquid medium. These suspended particles are single large molecules, or aggregates of molecules, or ions ranging in size from 1 to 1000 nanometers. Although undetectable in normal lighting, the presence of suspended particles can be demonstrated by shining a beam of intense collimated light—typically a laser beam—through the suspension. The beam is visible from the side because the light is scattered by the suspended particles. In a true solution, on the other hand, the beam is invisible from the side because the individual ions and molecules dispersed in the solution are too small to scatter visible light.

To observe the Tyndall effect, a set of specimens with gelation time of 10 minutes was freshly prepared, poured into 10 ml glass vials, and were placed on the non-reflective stage. The vials were then illuminated using a green 550 nm laser pointer to observe the Tyndall effect and light scattering in the gels. The laser setup was prepared with the laser beam aligned both horizontally and vertically to pass through the central plane of the sample. Photos were taken in a dark room with the laser being turned on to illuminate the samples at 2-minute intervals during the sol-gel transition, at the gelation point, and at 5, 15, 30, 45, and 60 minutes after gelation.

3.4.5.4. UV/VIS Spectrophotometry

The UV/VIS spectrophotometer is a rapid and non-destructive tool that is based on the interaction of chemical species with light in the ultraviolet and visible range. From the obtained spectrum, it is possible to determine various chemical and physical properties of a sample, such as characterizing optical properties across different wavelengths, identifying molecules, and determining concentrations. Additionally, UV/VIS spectrophotometry can be used to study the kinetics of chemical reactions and biological processes by tracking changes in optical properties over time, making it invaluable for studying phenomena like sol-gel transitions. Researchers have utilized UV/VIS spectrophotometry to study silica gels made from waterglass[44–46]. However, studies that link optical properties to the microstructure of silica gel are rare.

A UV/VIS spectrophotometer (Hitachi U-3900H, Hitachi High-Tech Corporation, Tokyo, Japan) was used to measure light transmittance in the gels. First, an empty cuvette was placed in the spectrophotometer, which was run from 400-700 nm for baseline correction. Fresh mixtures of waterglass and acid solutions were then prepared, poured into the cuvette, and placed in the spectrophotometer. Transmittance (T; in %) was measured at 2-minute intervals during the sol-gel transition, at the gelation point, and at 5, 15, 30, 45, and 60 minutes after gelation.

The numerical values obtained in UV/VIS experiments can be presented as Transmittance or Absorbance plotted against wavelength. Transmittance (T), representing the light passing through a sample, is typically expressed as a fraction of the transmitted radiation (I) over the incident radiation (I_0) and is defined as follows:

$$T = \frac{I}{I_0} \tag{3.9}$$

Using Lambert-Beer's law, "absorbance" (A) is calculated as follows:

$$A = -\log T = \log\frac{I_0}{I} = \varepsilon c d \tag{3.10}$$

where ε is molar absorption coefficient; c is concentration; and d is the path length of the measuring beam in the sample.

While absorbance values are commonly used due to their linear relationship with concentration and path length, it is essential to note that light can interact with samples in various ways beyond absorption and transmission. Reflection, scattering by particles, transmission through, and absorption are all possible interactions. Unfortunately, the terms "absorption" and "extinction" are often used interchangeably, which can be particularly misleading when dealing with colloidal solutions and gels. "Absorption" specifically refers to the process where light intensity diminishes due to molecules transitioning from the ground state to an excited state. On the other hand, "extinction" encompasses the total loss of light energy passing through the sample. As Mantele and Deniz[47] point out, extinction includes absorption, but also light scattering and reflection (if applicable), processes that are not related to the absorption process. According to Lambert-Beer's law, an ideal sample is a homogeneous solution without light scattering. However, for sol-gel transitions in colloidal solutions, such as waterglass, a significant amount of light is expected to be scattered by particles and aggregates. Therefore, UV/VIS results are reported as T in % , with the remainder being extinction, primarily due to light scattering.

3.4.6. Scanning electron microscopy

Scanning electron microscopy (SEM) was employed to image and compare the packing, porosity, and morphology of gels with a target gelation time of 10 minutes. The goal was to find correlations between the optical properties and microstructure of the gels prepared with different processing conditions.

To prepare the samples, fresh mixtures of waterglass solutions of different concentrations and acids were made and poured into 1x1x1 cm^3 silicon molds, where they were allowed to gel. 60 minutes after the gelation point, the samples were immersed in liquid nitrogen to freeze. After freezing, the samples were dried using a Savant SuperModulyo Freeze Dryer (Mechatech System Ltd, Thornbury, Bristol, U.K.) at a temperature of −40°C and a pressure of ∼0.08 Torr for 12 hours. Prior to imaging, the specimens were sputtered with gold using Denton Desk II (Denton Vacuum) for 90 seconds, resulting in a 12 nm gold coating to reduce charging. Imaging was conducted in Secondary Electron (SE) mode with a Zeiss EVO MA10 SEM (Carl Zeiss AG, Oberkochen, Baden-Württemberg, Germany) equipped with a LaB_6 filament.

3.5. Results and Discussion

3.5.1. Gelation time

pH is the most critical parameter influencing sol-gel reactions in silicate solutions. Figure 3.2a schematically illustrates the general stability/gelation time trend proposed by Iler[20] for silica-water systems across the whole pH range. Notably, silica particles point of zero charge (that is, zero net surface charge) and isoelectric point (that is, zero velocity for particles subjected to an external electric field) both happen at pH ≈ 2, where silicate solutions demonstrate maximum gelation time. The decrease in gel formation time observed for pH < 2 and from pH 2-7 is attributed to two types of condensation reactions initiated by H^+ and OH^- groups, respectively[48]. At pH ≈ 7, the gelation time dramatically decreases as silica particles rapidly aggregate with the aid of silanol functionality. Above pH ≈ 7, the gel time increases again due to an increase in the silica solubility and because the silicate species are appreciably ionized so that particle growth can occur without aggregation. Above pH ≈ 11, no aggregation or gelation occurs because particles are mutually repulsive. This complex behaviour indicates that electrostatic interactions alone cannot primarily dictate stability and particle aggregation/bonding in silicate solutions; instead, the silanol functionality and condensation reaction rate (initiated by OH^- or H^+), play a more significant role in the gelation of silicate solutions.

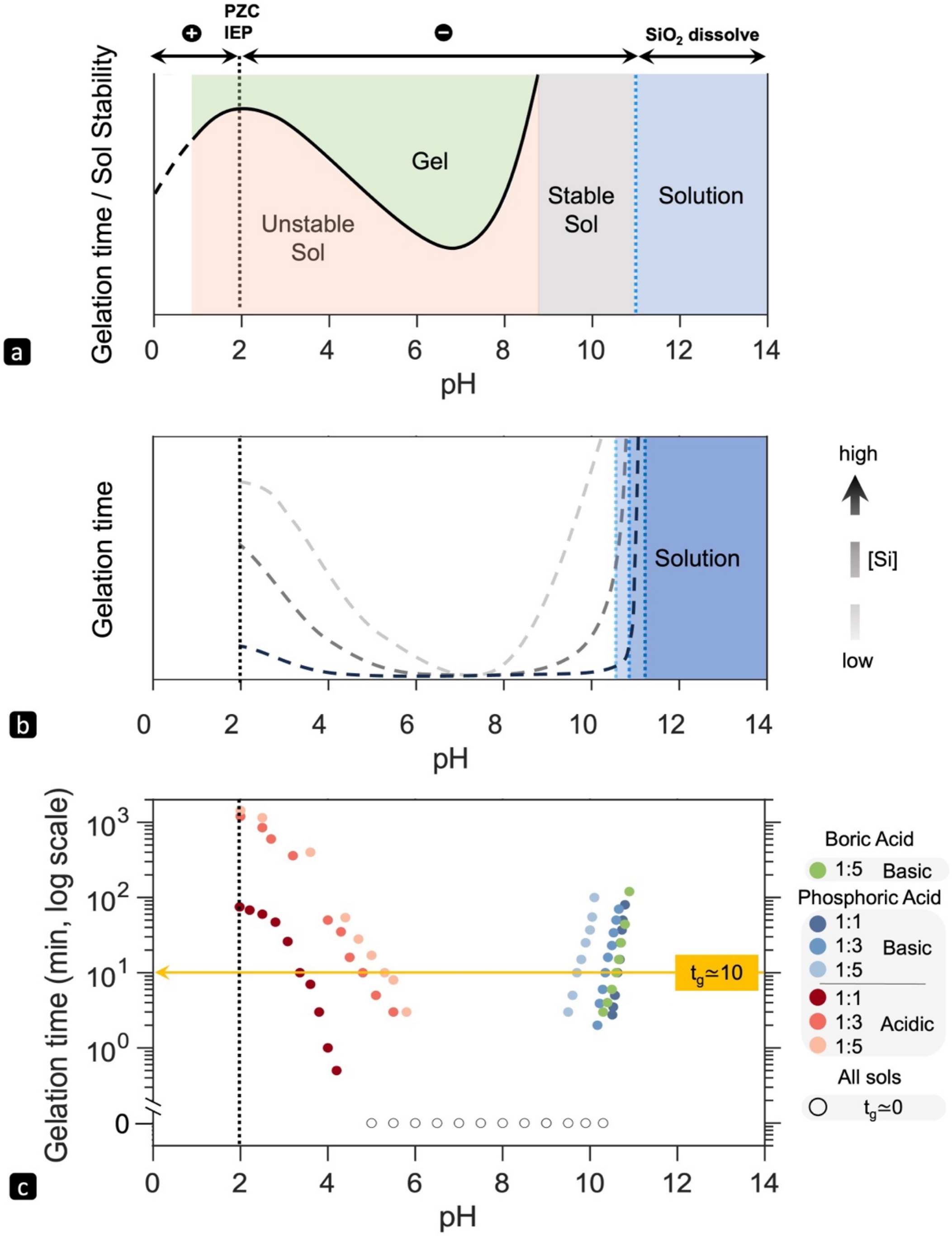

Figure 3.2 (a) the general trend for gelation time/sol stability versus pH for silica water systems, redrawn from[20] (b) the general trend for gelation time versus pH for waterglass solution of different concentrations observed in this study (c) semi-log graph of gelation time versus pH for specimens made of boric acid and phosphoric acid and different initial waterglass concentrations. The target gelation time of 10 min. is marked by the yellow arrow, which intersects the various solutions at different pH values, and hence permits multiple processing routes to fabricate a gel that forms in 10 min.

The pH-dependence of gelation time for sodium silicate solutions of different concentrations, acid-initiated with phosphoric acid and boric acid was measured using the tube inversion method. Our findings broadly agree with the trend observed in silica-water systems (Figure 3.2b). However, we did not observe the "stable sol" region. It is important to clarify that the terms "stable sol" (referring to colloidal dispersion) and "solution" (referring to molecular/ionic dispersion) are conventionally used for monomeric silicate species in silicate solutions. Waterglass, however, contains both ionic species and colloids depending on the SiO_2/Na_2O ratio, and is not a true solution despite common usage of the term. The disappearance of the stable sol region in waterglass implies that colloidal particles cannot grow below pH ≈ 11, unless they aggregate at some point. Additionally, waterglass exhibits a rapid or immediate gelation zone instead of a minimum gelation point.

In sodium silicate solutions, the presence of sodium cations facilitates closer proximity among silicate particles, likely due to the charge screening effect of the cations and implications from the electric double layer theory (see reference [49] for further details). The closer proximity of colloidal silicate particles in waterglass widens the minimum gelation zone. As shown in Figure 3.2b, both the width of the "rapid gelation" zone and the slope of the graph (indicating the dependency of gel time on pH) appear to be influenced by silica concentration. Specifically, as the dilution rate increases, transitioning from a WG:Water weight ratio of 1:1 to 1:5: (i) the slope in the basic region decreases, (ii) the "rapid gelation" zone narrows, and (iii) the maximum gelation time in the acidic region increases. Increasing silica concentrations (equivalent to decreasing WG:Water weight ratio) enhances gelation by fostering the formation of more silicate particles, and consequently increasing the likelihood of collisions. These collisions can result in the formation of siloxane bridges through chemical interactions or lead to physical interactions such as hydrogen bonding. Therefore, higher silica concentrations increase the probability of particles aggregating through chemical or physical mechanisms, which results in broadening the “rapid gelation” zone and decrease in max gelation time at pH ≈ 2. These findings are in agreement with previous studies investigating the effect of pH on the gelation time of sodium silicate solutions[17,19,41,50], although none such studies explored such a wide pH range.

The relationship between gel time and pH for all the gel specimens is shown on a semi-logarithmic scale in Figure 3.2c. Using phosphoric acid, a strong acid, gels can be prepared across the entire pH spectrum of 2-11. However, with boric acid, a weaker acid, the pH can only be lowered into the basic range. In the basic region, the gel time versus pH changes exponentially, moving towards near-infinite gelation time or stable solution with increasing pH. In contrast, in the acidic region, the curves fit to fourth-order polynomials, reaching a maximum as the pH approaches 2. The fitted equations in Table 3.2 reveal that the constant parameters in fitted equations vary with waterglass concentration, indicating that gelation kinetics change with concentration. By determining the relationship between the coefficients and waterglass concentration from experimental data, we can predict the gelation time for any given concentration and pH.

Table 3.2 The equations fitted to gelation time (t_g) versus pH curves obtained for basic gels made with boric acid, and basic and acidic gels made with phosphoric acid.

Acid catalyst		WG:Water (wt. ratio)		WG (wt%)	Fitted equation	Parameters			
						a	b	c	d
Boric Acid	●	1:5	Basic	15		1E-27	6.107		
Phosphoric Acid	●	1:1	Basic	50	$t_g=a.e^{b.pH}$	2E-60	13.135		
	●	1:3		25		5E-40	8.929		
	●	1:5		15		5E-26	6.221		
	●	1:1	Acidic	50	$t_g=a.pH^3+b.pH^2+c.pH+d$	-5E-5	0.002	-0.114	100.47
	●	1:3		25		-5E-5	0.004	-0.134	100.74
	●	1:5		15		-6E-5	0.011	-0.823	100.38

In the basic region, the parameters a and b in the general equation were found to be functions of waterglass concentration (C, wt%) (Figure 3.3). The general formula of gelation time (t_g) versus pH in the basic region, and the relationship between the equation parameters a and b with concentration can be expressed as follows:

$$t_g = a \cdot e^{b \cdot pH} \tag{3.11}$$

where:

$$loga = (4E - 80) \cdot C^{-65.9} \tag{3.12}$$

$$logb = (20.384) \cdot C^{0.6169} \tag{3.13}$$

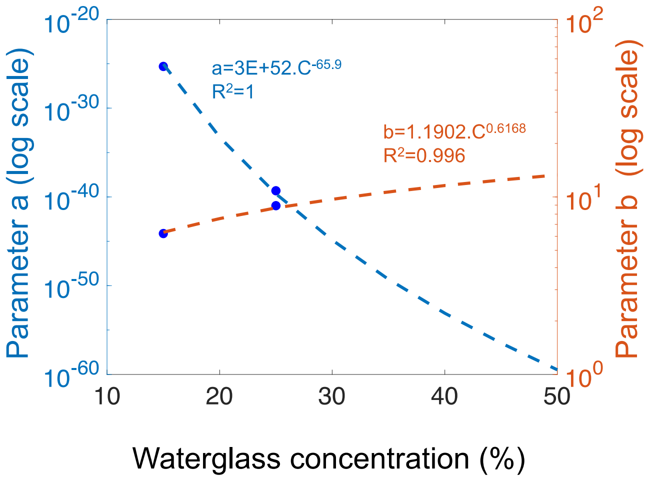

Figure 3.3 Dependency of Parameters a and b on Waterglass Concentration. These parameters are part of the fitted equation describing the relationship between gelation time and pH for basic gels (**Table 3.2**). The fitted equations and R-values are shown on the graph.

When comparing boric acid and phosphoric acid in the basic region, we observe that the a and b parameters for BA fitted equations are very close to that of PA 1:5. This similarity could be linked to the fact that, although the initial WG:Water ratio of the silicate solution was 1:1 for this sample, it increased to 1:5 by the large amount of water introduced through addition of BA. It appears that there is a general exponential equation for gelation time versus pH in the basic region, and its parameters depend solely on waterglass concentration (and not on the type of acid initiator used). It should be noted that the SiO_2/Na_2O ratio of waterglass is constant in these observations, so the general trend is limited to this condition. If the SiO_2/Na_2O ratio were to vary, the *a* and *b* parameters may also change. Overall, the impact of pH and WG concentration on gelation time is significantly more influential than the type of acid used.

Similarly, in the acidic region, the constant parameters of the general equation for gelation time versus pH vary with waterglass concentration. Due to the high number of parameters and the complexity of the equations, we could not fit the relation with high certainty. Fitting this relationship more accurately would require more data points and aid of computational methods, which could be the focus of another project. However, the maximum gelation time at pH = 2 was also a function of waterglass concentration (C, wt%) and followed a second-order polynomial relationship. This relation can be expressed for maximum gelation time (t_g^{max}) as follows:

$$t_g^{max} = -6000C^2 + (6E^{-11})C + 1575 \tag{3.14}$$

where the scalar quantity in the second term (i.e., $6E^{-11}$) can be neglected due to its extremely small magnitude.

The second-order polynomial relationships with concentration suggest that the influence of concentration on gelation kinetics is complex and potentially includes interactions between different contributing factors.

The amount of acid required to adjust the pH with BA and PA is illustrated in Figure 3.4. As expected, since BA is much weaker than PA, the required amount of BA is 28-38 times greater (depending on WG concentration) than the amount of PA needed to reach the same pH. Additionally, as the WG content in the initial solution decreases, the amount of acid needed to lower the pH also decreases. The pH is very sensitive to slight changes in the amount of acid in the PA 1:1 sample, and this sensitivity decreases as the WG concentration decreases or the pH moves into the acidic region. Consequently, controlling the pH and gelation time was most challenging with the PA 1:1 sample. Although the BA sample had the lowest pH sensitivity to changes in acid content, it cannot be considered the easiest to control. The BA pH-sensitivity is because the WG-to-water ratio changes abruptly with the addition of acid, leading to fluctuations and making predictions more difficult.

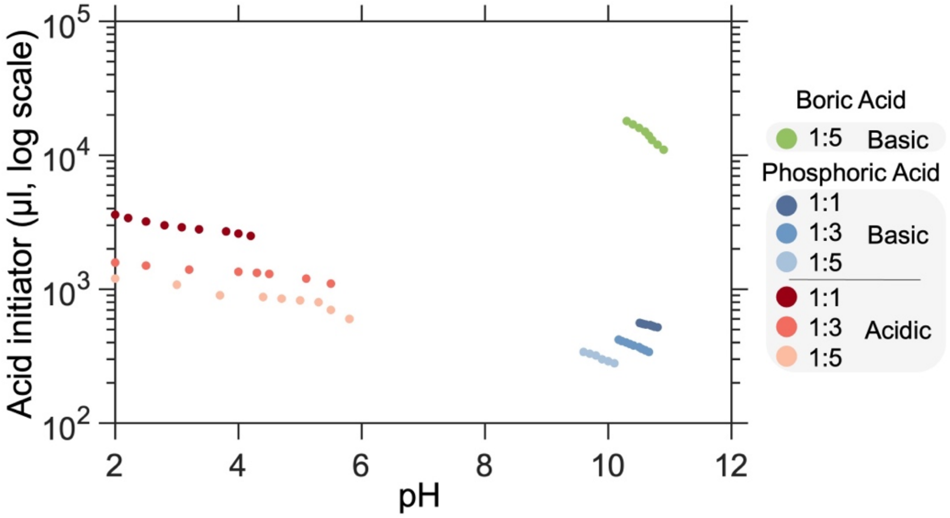

Figure 3.4 The amount of acid initiators (boric acid and phosphoric acid) needed to adjust the pH of silica gels made from waterglass at different concentrations. For clarity, the y-axis is presented in a logarithmic scale

Generally, the results indicate that achieving a desired gelation time is feasible across both acidic and basic pH ranges. Referring to Figure 3.2c, we observe that the target gelation time of 10 minutes is met by one point using BA in the basic region, and two points using PA at each of three different concentrations in both acidic and basic regions, totaling seven specimens, as detailed in Table 3.3. Moving forward, we will proceed with these seven samples, all of which exhibit a gelation time of 10 minutes, making them suitable for the desired clinical applications.

Table 3.3 The composition and final pH of silica gels made with boric acid and phosphoric acid at different waterglass concentrations. All gels have a gelation time of ten minutes, making them practical for clinical applications.

Acid catalyst	WG:Water (wt. ratio)		WG (g)	Acid content (µl)	pH	t_g (min)
Boric Acid	● 1:5	Basic	3.34	14000	10.60	10
Phosphoric Acid	● 1:1	Basic	10.00	545	10.63	10
	● 1:3		5.00	360	10.35	
	● 1:5		3.34	300	9.70	
	● 1:1	Acidic	10.00	2800	3.36	10
	● 1:3		5.00	1300	4.80	
	● 1:5		3.34	825	5.30	

Figures 3.2c and 3.4 present a comprehensive mapping of gelation times and acid initiator concentrations over a wide pH range for the formation of silica gels from waterglass and serves as a valuable guide for tailoring gelation kinetics, allowing precise control over the fabrication process. The next step involves understanding the properties of the resulting gels at each pH, which is crucial for applications requiring specific gelation times, such as the 10-minute setting time for bone scaffold applications. By consulting these processing maps, one can not only select the pH and acid concentration to achieve a desired gelation time, but also choose between different pH-concentration combinations based on the final properties of the gels. Since the most apparent differences between gels with identical gelation times—but varying pH and acid concentrations—lie in their appearance and interactions with light, I initiated a study of their optical properties. This exploration of optical behavior will expand into an analysis of molecular structure and optical characteristics in subsequent chapters

.3.5.2. Optical properties

During the sol-gel process, the colloidal particles present in the sol gradually form a network that evolves into a gel structure, which traps the surrounding solvent. These structural changes are also reflected in the optical properties of the resulting gels, leading to variations from transparent to translucent and even opaque appearances. Therefore, investigating the optical characteristics throughout the sol-gel transition can provide invaluable insights into the structural evolution during gelation. This investigation was performed through both visual observations and quantitative techniques such as UV/VIS spectrophotometry.

3.5.2.1. Visual Changes

Figure 3.5 demonstrates the sol-gel progression in acidic and basic gels prepared using PA and BA, spanning up to 60 minutes *after* gelation. Gelation of all samples occurred at the 10-minute mark, clearly indicated by the inversion method. Initially, the sols appeared clear and colorless after introducing the acid. However, during and after transforming to gel, the gels exhibited distinct optical behaviors influenced by pH and silica concentration. Basic gels transitioned from transparent to translucent, with a decrease in transparency persisting post-gelation. The PA 1:1 basic specimen, in particular, became opaque. A similar trend was observed in BA basic gel, highlighting that the effect of pH on the gelation process was more significant than the type of acid initiator used. Acidic gels were notably more translucent in contrast to basic gels. For instance, the PA 1:1 acidic sample remained completely transparent up to the gelation point, although it contained some entrained gas bubbles. The reaction between WG and the acid initiator is exothermic in the acidic region, generating heat that can be felt when handling the vial, and these bubbles are likely a result of this exothermic reaction inducing vaporization of the solvent.

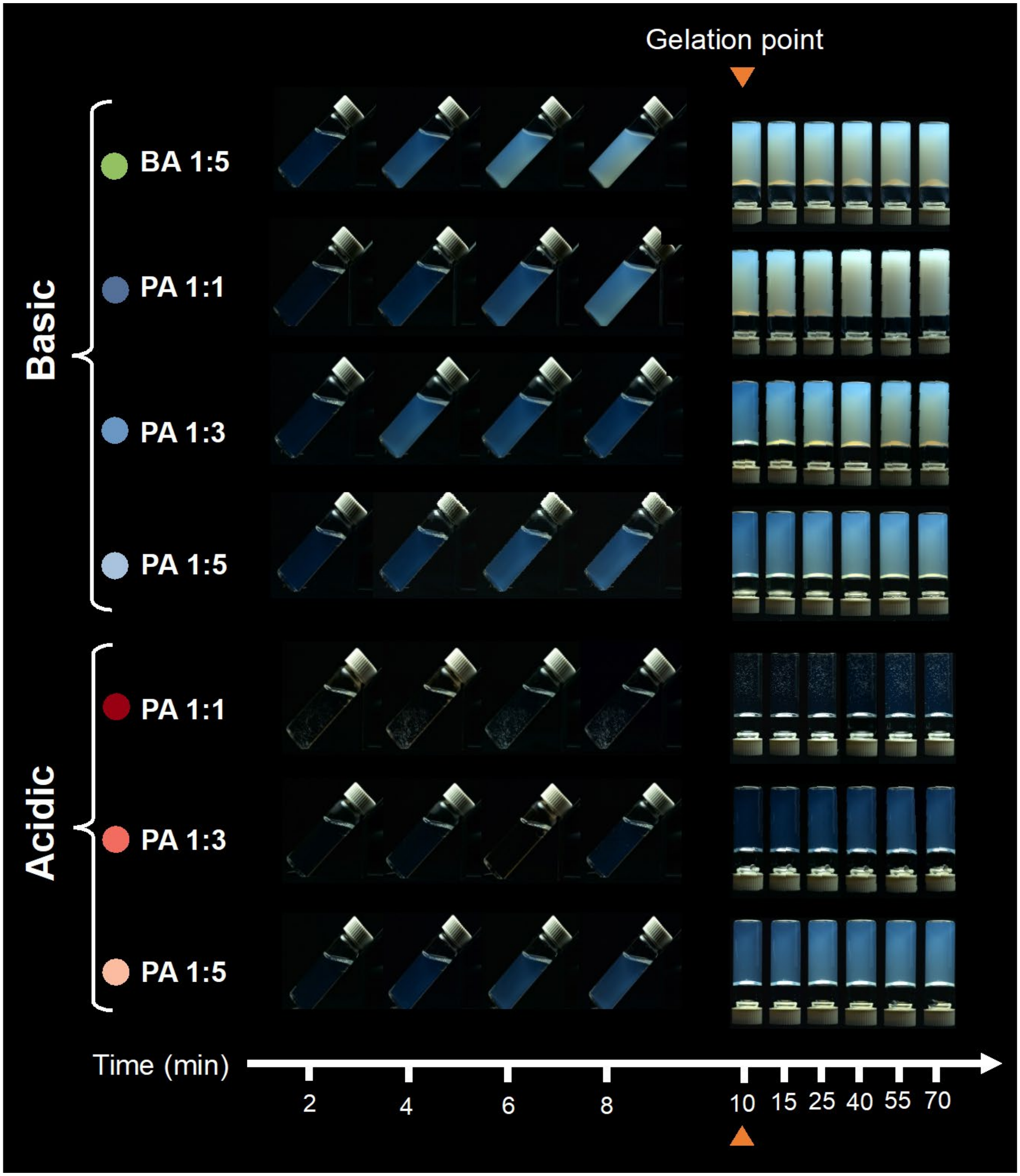

Figure 3.5 Macrograph of silica gels during sol-gel transiton and post gelation over time. All images were taken at constant white balance and exposure conditions and the blue cast to the images is true to what was usually observed.

Overall, a decrease in light transmission was observed across all samples, which continued after gelation, with all samples exhibiting a faint blue color along with reduced transparency. The differences in the appearance of basic gels in contrast to acidic gels suggest microstructural differences between these two groups of gels.

3.5.2.2. Tyndall effect

Waterglass consists of a wide range, and physical size, of species ranging from monomers to oligomers and all the way up to colloids. Investigations by dynamic light scattering and small-angle X-ray scattering have reported a wide range of colloidal particle sizes in waterglass–0.6 nm to 600 nm–and uncertainties about their size range continue to exist [51,52]. Upon acidifying waterglass, the silicate species, and colloidal particles, continue to grow until they are no longer stable and undergo aggregation or agglomeration through chemical or physical interactions into fractal structures[53,54]—thusly resulting in gelation of the system. The final size of the aggregates/agglomerates formed by these particles directly affects the microstructure and porosity of the final gel; the physical, chemical, and mechanical properties depend on the microstructure. The size of colloidal silicate particles and aggregates/agglomerates also affects how they interact with, and scatter, light. By observing the Tyndall effect, one can indirectly study the size of these particles and aggregates/agglomerates, thereby gaining insights into the differences in the final structure of gels formed under different processing conditions. It should be noted that aggregates are *irreversible* clusters of colloidal particles connecting through strong primary bonding (e.g., covalent bonds), while agglomerates are *reversible* clusters of colloidal particles connecting through weak secondary bonding (e.g., hydrogen bonding).

According to Rayleigh, the relative intensity of the light scattered at right angles to the axis of illumination by dilute sols of constant volume concentration, can be expressed as[55]:

$$I = \frac{kcv}{\rho\, \lambda^4} \tag{3.15}$$

where, k represents the Boltzmann constant, c is the concentration of the colloidal solution, v represents the volume of the scattering particles, ρ is the density of the particles, and λ denotes the wavelength of the incident light.

Equation (3.15) indicates that, at a fixed wavelength, the intensity of the scattered light is directly proportional to the average volume of the particles. However, this relationship assumes certain conditions, such as particles being optically isotropic and randomly distributed. In concentrated colloidal solutions like ours, not all these assumptions hold true, complicating the straightforward relationship between intensity and particle size, and a definitive solution to this issue remains unresolved . Overall, the nature of particles—specifically their size, shape, refractive index, and surface characteristics—all play significant roles in scattering behavior. Nonetheless, it is widely accepted that an increase in either the number, or size, of particles typically results in higher intensity of the scattered light. Therefore, we anticipate that the size and arrangement of silicate particles and aggregates/agglomerates in our system directly influences the amount of light scattered by them. Although, finding a mathematical model for quantitatively relating these two parameters would be a challenge and was not in the scope of this work.

A green 550 nm laser was used to qualitatively investigate light scattering and the Tyndall effect during the sol-gel transition and post-gelation across all seven specimen types (Figure 3.6). Our observations yielded the following insights:

- Initially, all samples exhibited the Tyndall effect to some degree, confirming the colloidal nature of the initial waterglass solution.
- The overall trend of the light scattering in our samples closely mirrors that seen in Figure 3.5, indicating that the reduction in light transmission results from increased scattering by colloidal particles or aggregates/agglomerates.
- Over time, after introducing the acid-initiator, the intensity of scattered light in each sample increases. This increased scattering is evident from both the increased brightness of the beam path and the glow that expands around it, often illuminating the entire vial. This glow is attributed to multiple scattering centers within the specimen, which redistributes light in various directions, making scattered light visible beyond the direct laser beam path. This scattering phenomenon suggests: the formation of new colloidal particles; increase in colloidal particle; or both.

- At a constant waterglass concentration, acidic gels scattered less light compared to basic gels at any given time. This result indicates that acidic gel networks are formed from smaller aggregates/agglomerates than those in basic gels.
- In acidic gels, the glow started only *after* the gelation point, whereas in basic gels, glowing began *before* gelation. This difference suggests that in acidic gels, the glow primarily arose from re-scattering within the gel pores, which formed only *after* gelation. In contrast, in basic gels, both pores and particles or aggregates/agglomerates contributed to the observed glow.
- Specifically, in the case of acidic PA 1:1 gel, the slight increase in the density of the beam path with no glow suggests that particles or aggregates/agglomerates were small and light was not re-scattered from the surrounding.

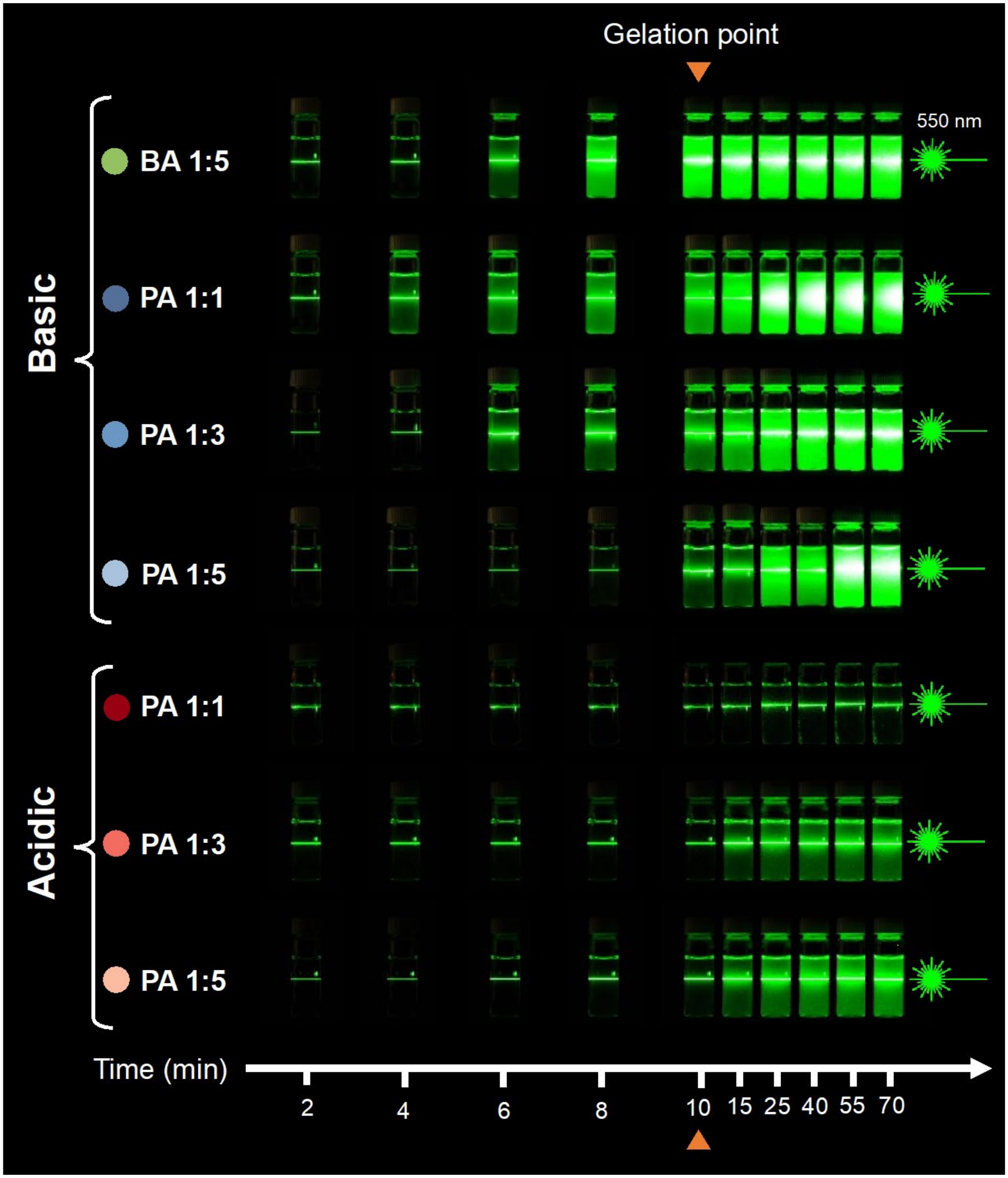

Figure 3.6 Macrographs showing the Tyndall effect of silica gels during sol-gel transiton and post gelation over time while shining a 550 nm green through the specimens. The laser is casuing a reflection above the laser line from the top surface of sol-gel meniscus, or oven the top cap on the vials in some cases. All images were taken at constant white balance and exposure conditions and the green reflection is true to what was usually observed.

3.5.2.3. UV/VIS pectrophotometry

The UV/VIS spectra of all gels during the sol-gel transition, at the gel point, and up to 60 minutes after gelation are illustrated in Figure 3.7 within the visible region. Several observations are evident at first glance:

(1) There is an increase in transmittance with increasing wavelength, contributing to the bluish tint observed.
(2) The overall transmittance decreases with time within each sample, resembling the photos in Figure 3.5.
(3) There is a distinct difference between acidic and basic gels in their ability to transmit light, with acidic gels have higher %T, regardless of type of acid initiator used. However, the difference in the light transmittance behavior diminishing as the dilution rate increases.
(4) Basic gels show an increase in transmittance with decreasing silica concentration, whereas acidic gels exhibit a decrease in transmittance with dilution.
(5) The BA basic gels' transmittance spectra over time are similar to those of the PA 1:3 gel.

Generally, more light is transmitted as the wavelength increases from 400 to 700 nm, with the difference being more pronounced in basic gels compared to acidic gels. According to.(3.15), the intensity of the scattered light is inversely proportional to the fourth power of the wavelength. If we consider the extinction to be solely due to light scattering, and accept that the intensity of the incident light equals the sum of the transmitted and scattered light, then %T should be directly proportional to the fourth power of the wavelength. From Figure 3.7, there is a general agreement with this direct proportion; however, the light transmittance dependency on wavelength is not constant and is influenced by concentration, pH, and time.

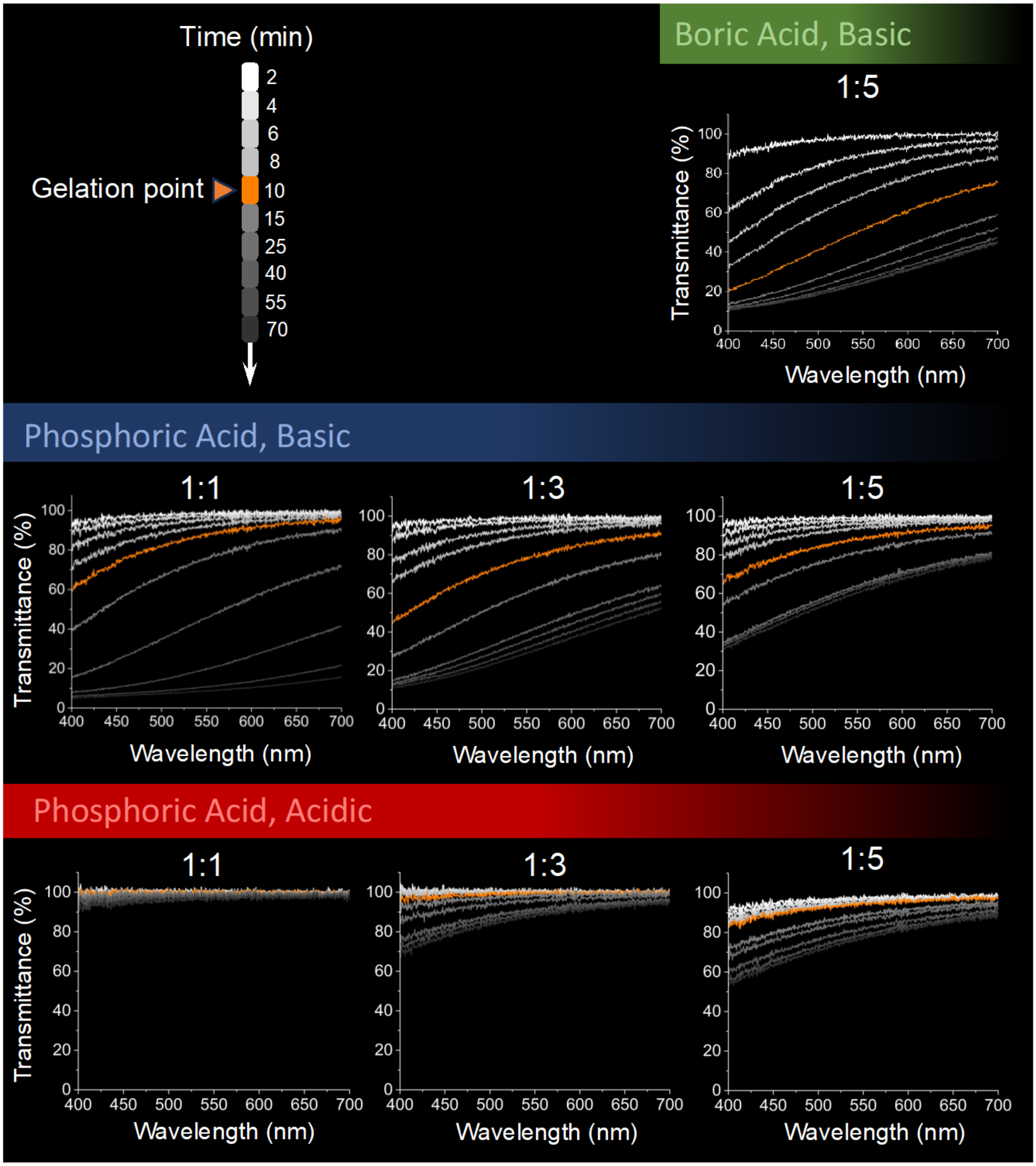

Figure 3.7 UV/VIS Spectra of Silica Gels During Sol-Gel Transition. The spectra show light transmittance in the visible light region (400-700 nm) at various time intervals after mixing waterglass solutions of different concentrations with boric acid and phosphoric acid. The measurements were taken at the gelation point and up to 60 minutes after gelation.

While concentration dependency is expected from Equation (3.15), pH and time also play significant roles as they affect the silicate particle size. Even at a fixed time, concentration, and pH, %T does not follow the inverse relation with fourth power of wavelength dependency in any sample. if such relation existed, the ratio of %T at 700 nm to 400 nm should be always proportional to:

$$\frac{\%T_{400}}{\%T_{700}} = \frac{700^4}{400^4} \approx 9.37 \tag{3.16}$$

However, for example at the gelation point, the ratio of %T at 700 nm to 400 nm varies between approximately 1.1 and 5, ranging from almost independent of frequency to dependency on the third power (~5.35) of the wavelength. Thus, as mentioned in previous section, the relationship between %T and wavelength is more complex than suggested by Equation (3.15), due to the complex nature of our system, which includes different ions, oligomeric and polymeric species, particles, aggregates/agglomerates, and pores. Nonetheless, light at 400 nm is more scattered than at 700 nm, explaining the bluish tint observed in the specimens (recall Figure 3.5).

Combining the results from Figures 3.5-3.7, the general decline in transmission over time is attributed to the increased light scattering intensity due to the formation and/or growth of colloidal silicate particles and aggregates/agglomerates, as well as light scattered from gel-pore interfaces. The continued change in %T post-gelation indicates that the system remains dynamic, with ongoing particle growth and changes in pore size, a process known as syneresis[264]. Moreover, the differences in optical properties between acidic and basic gels suggest pH-dependent cluster-cluster aggregation/agglomeration. For example, in the PA 1:1 acidic gel, the sample shows more than 90% transmittance over the 400-700 nm wavelength range at all times, with a glass-like transparent appearance. In contrast, the PA 1:1 basic gel shows a decrease in %T to less than 10% over the same wavelength range, with an opaque appearance 60 minutes after gelation. This difference in behaviour indicates varying fractal and network structures in these gels, likely due to differences in the size and connectivity of the silicate particles forming them.

Finally, the light transmittance in basic gels is primarily influenced by pH and WG concentration, rather than the type of acid initiator used. The transmission spectra of the BA basic gel over time resemble those of the PA 1:3 gel. Despite starting with a solution concentration of 1:1, which increased to 1:5 after adding the acid initiator solution, it exhibits transmission characteristics that align more closely with the average of these concentrations. The gelation time-pH dependency, however, resembles that of the PA 1:1 sample, indicating variability in predictability and control.

3.5.3. What do optical properties reveal about gelation kinetics?

Chemical kinetics concerned with reaction rates are typically defined as the change in concentration over reactant or product per unit time. Gelation, however, is not a simple chemical reaction in which two, or multiple reactants, are consumed to form product(s). During sol-gel transition, silicate particles form and/or grow through polymerization-depolymerization reactions and these suspended particles cluster and extend throughout the system, forming a gel network. Aggregation/agglomeration kinetics is controlled by the particle–particle attachment efficiency, which is the fraction of particle–particle collisions resulting in attachment (through either physical or chemical interactions) and is dependent on solution chemistry, and the particle–particle collision frequency[287]. If we reasonably assume and accept that the transmitted light decay/increased light scattering is caused by the change in size, shape, and arrangement of colloidal silicate particles, then we can conclude that monitoring the change in transmittance over time allows us to study the gelation kinetics.

The light transmittance at an average wavelength of 550 nm is plotted against time for all seven samples in 8a. The decrease in light transmission continues after the gelation point due to syneresis, or aging of the gels. When the light transmittance stops changing, it usually indicates that the reaction is complete. As shown in Figure 3.8a, the curves do not reach a plateau during the testing duration, indicating that the structural development responsible for the light scattering (syneresis process) is ongoing. However, their shape suggests that they tend to reach a plateau over longer periods.

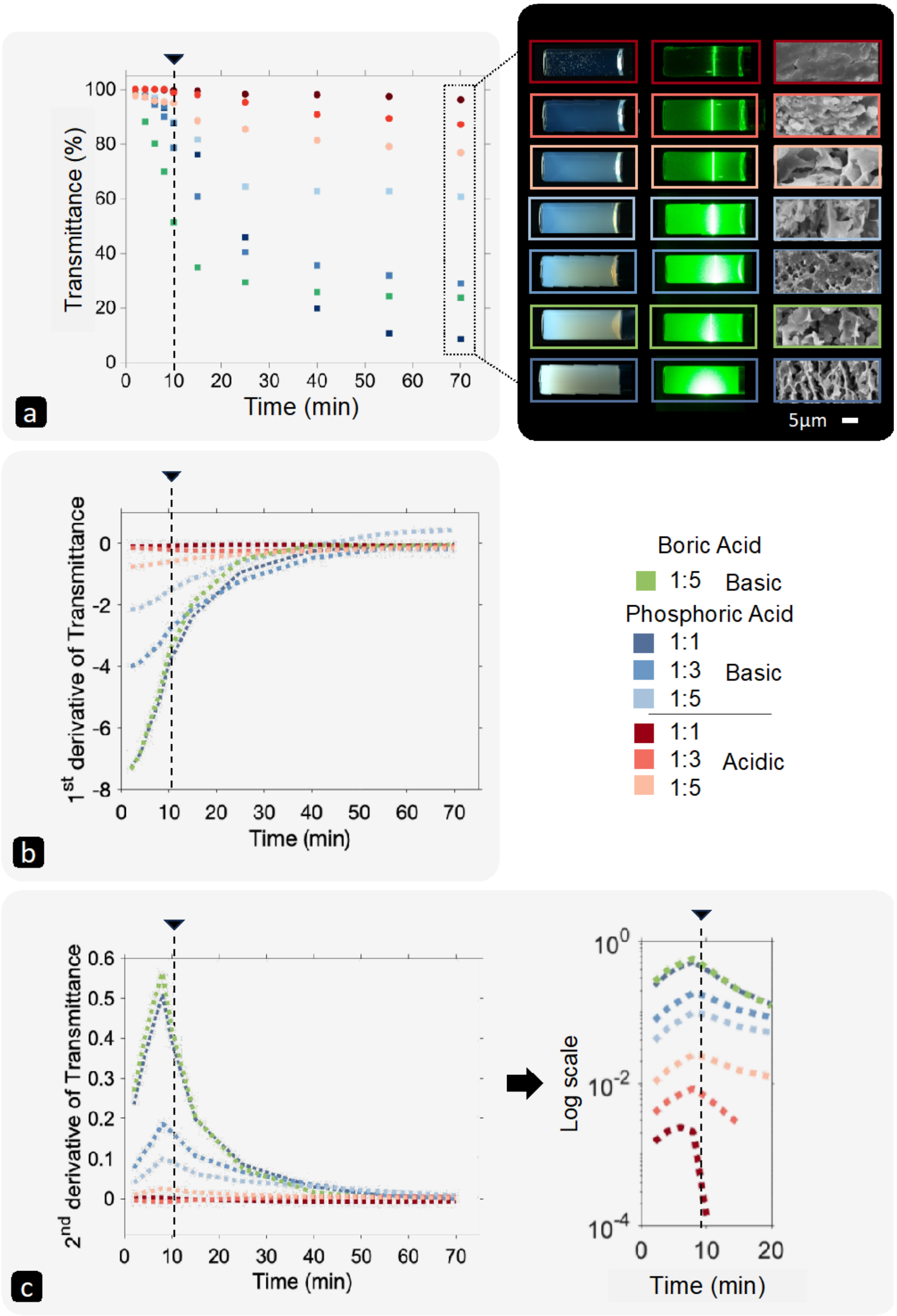

Figure 3.8 (a) Light transmittance at an average wavelength of 550 nm over time for silica gels made with phosphoric acid and boric acid at different waterglass concentrations. (b) he first derivative of light transmittance of silica gels versus time, showing a change in slope around the gelation point. (c) The second derivative of light transmittance of silica gels versus time, used to more clearly identify changes in the light transmittance rate. The maxima at ~8 minutes indicate the onset of gelation.

The %T curves were best fit to a third-order polynomial equation (Table 3.4). The non-linear model captured varying rates of change in light transmittance, indicating different stages of particle formation, growth, aggregation/agglomeration, and gel network development. Two stages were observed over time in Figure 3.8a: Firstly, rapid changes in light transmission up to the gelation point, followed by slower changes afterward. This change in slope near the gelation point is evident in in Figure 3.8b, where the first derivative of the fitted equations is plotted. During the sol-gel transition, the system undergoes massive changes. The colloidal particles move, form connections, create a 3D network and water-filled pores. Secondly, after gelation, the gel network continues to grow and densify, but the rate of change is much slower compared to before the gelation point. The mobility of particles within the gel decreases significantly, leading to a slower change in light transmission properties.

Table 3.4 The parameters of the third-order polynomials fitted to the light transmittance data of different silica gels.

Acid catalyst		WG:Water (wt. ratio)		WG (wt%)	Fitted equation	Parameters			
						a	b	c	d
Boric Acid	●	1:5	Basic	15		25E-6	0.321	-9.155	119.7
Phosphoric Acid	●	1:1	Basic	50	$\%T=at^3+bt^2+ct+d$	-23E-5	0.176	0.193	99.92
	●	1:3		25		-49E-5	0.081	-4.498	114.5
	●	1:5		15		-26E-6	0.041	-2.428	107.7
	●	1:1	Acidic	50	$\%T=at^3+bt^2+ct+d$	-19E-6	0.002	0.114	100.5
	●	1:3		25		51E-6	0.004	0.134	100.7
	●	1:5		15		56E-6	0.10	-0.823	100.4

The fact that the light transmission of gels over time can be fit by a polynomial equation raises the question of such an equation's suitability for gelation kinetics, and if it is chemically, or physically, meaningful for the multitude of processes occurring during the sol-gel transition. Several kinetic models have been proposed to describe the sol-gel process, such as Kinetic Monte Carlo Simulations[234], as well as diffusion limited cluster aggregation (DLCA) and reaction limited cluster aggregation (RLCA)[185,288]. Overall, considering the heterogeneous nature of gelation, the involvement of multiple stages and mechanisms, various influencing factors, the dynamic and non-equilibrium characteristics, as well as the distribution of particle sizes and shapes, it is not surprising that no exact analytical solution can be found for treating all kinetic gelation processes.

The reaction or gelation rate is usually described using power-law or exponential equations and polynomial equations for kinetics are less common. However, kinetic polynomials have been proposed as the most generalized form of kinetic equation *for complex reactions* and is proved to be consistent from a thermodynamic point of view[289,290]. Unfortunately, as Marin et al.[291] point out, the reasoning and details provided in the kinetic polynomial literature are mostly in favor of mathematical optimization and not very comprehensive of the chemical phenomena being described. Still, there are a few studies in which gelation time has been reported to be a polynomial function of the polymer and cross-linker/polymer ratio[292,293]. While a polynomial fit is not the most traditional model for gelation kinetics, its flexibility in fitting data with multiple inflection points seems appropriate for the complex systems and suggest additional factors at play. It is important to note that studying gelation kinetics is usually done by measuring various properties during sol-gel transition such as particle size[294,295] or viscosity[115] or like here, light transmission over time. However, these properties may exhibit different relationships with the gelation process itself. For instance, while viscosity in an acidic gel may sharply increase during gelation, light transmission might show minimal change. Therefore, expecting a single form of equation to universally describe *all* aspects of gelation would be impractical. While there exists a known link between fractal dimension and the type of cluster-cluster aggregation (DLCA vs RLCA) [296], no universal mathematical relationship exists for aggregation and light transmission.

Another reason to scrutinize a polynomial model of light transmittance over time is in the model's potential to predict the gelation point. There are a number of studies that have used difference in light transmission/scattering to define gelation point[189,297,298]. For instance, Boschel and Roggendorf[189] found that the first derivative of transmission obtained by UV-VIS spectroscopy may be used as a useful indicator of the gel point in borosilicate gels. Derivative spectrophotometry, involves differentiating a normal spectrum, and has been shown to be an effective method for enhancing the time resolution[299]. This technique highlights subtle spectral features by presenting them in a visually more accessible way and reducing the effect of spectral background interference. in Figure 3.8c reveals that interestingly, the second derivative of transmittance versus time of gels show a maximum at around 8 minutes, which closely aligns with the 10-minute gelation time obtained by tube inversion method. This maximum in the second derivate curve suggests a rapid change, or inflection, in the rate of gelation at the gelation point, which is also evident in the first derivate, though less obvious. The slight discrepancy in timing between the two methods of gel-point determination arises because the tube inversion method identifies the point at which the gel becomes *completely* rigid, while the point obtained through light transmission may signify the *onset* of gelation.

The PA 1:1 acidic gel stands out as the only sample that remains transparent even after gelation. However, even for this sample, there is a subtle change in the slope at the gelation point. This change can be intensified in a semi-log graph, as illustrated at right in in Figure 3.8c. Continuing the derivate to higher orders is another way to improve time resolution. It should be noted that if using the fourth derivative of transmittance as a function of time that the gelation point will occur when the fourth derivative equals zero—corresponding to the maximum or minimum of the third derivative. Overall, the results suggest that light transmission over time during the sol-gel transition can be used to detect gelation point, marked by a significant decrease in rate of change of light transmission. However, depending on the processing condition, this change may be easily observed in the raw data set, or that multiple derivates may be needed to improve the time resolution and therefore precise determination of the gelation point.

3.5.4. Relationships between gel structure and optical properties

How do the size of silicate particles, aggregates/agglomerates, pores, and the overall gel network arrangement affect optical properties? In this section, we aim to establish connections between qualitative and quantitative observations of optical properties and the microstructure of the gels.

3.5.4.1. Acidic versus basic gels

As mentioned earlier, acidic gels generally scatter less light compared to basic gels, which is consistent with prior studies[118]. At the highest silica concentration (1:1 ratio), basic and acidic gels represent two extremes: 60 minutes after gelation, the PA 1:1 basic gel becomes practically opaque (8.7% T at 550 nm), while the PA 1:1 acidic gel remains largely transparent (96.2% T at 550 nm). These gels also exhibit the lowest and highest pH among all samples (3.36 for acidic and 10.63 for basic). The difference in transparency at similar wavelengths is attributed to how the silicate aggregates/agglomerates form a 3D network. SEM micrographs clearly show the difference in these gels' microstructures (see in Figure 3.8a): the PA 1:1 acidic gel is dense and compact, while the PA 1:1 basic gel has a uniform porous structure with pore diameters ~ 2 μm. It is important to note that the PA 1:1 acidic specimen cannot be free of pores; both 1:1 hydrogels contain the same amount of water trapped inside the pores before freeze-drying. Therefore, the pores in the acidic gel are too small to be seen clearly. Moreover, the pores are not just filled with pure water; they may contain silicate monomers and/or oligomers, sodium ions, and ions from the acid, which remain inside the pores after water evaporation, filling some of the space. The compact structure of the PA 1:1 acidic gel gives it an almost glass-like appearance, suggesting that the refractive index of its aggregates/agglomerates closely matches that of the solvent in the pores. The compactness of a 3D structure made of almost spherical particles forming aggregates depends on many factors, including particle and aggregate/agglomerate size, particle and aggregate/agglomerate size distribution, the type and amount of bonding between the particles. Thus, the contribution of all of these parameters have made acidic gels glass-like features, likely composed of smaller particles that form smaller aggregates/agglomerates and smaller pores, resulting in less light scattering. In contrast, the PA 1:1 basic gel is made of larger particles and larger aggregates/agglomerates with larger pores in between that scatter light more effectively, resulting in reduced transmission and increased opacity. Larger aggregates/agglomerates also contribute to the formation of larger pores compared to acidic gels. The difference in the initial size of silicate particles in these gels is influenced by pH, which governs the polymerization-depolymerization reactions in waterglass, thus influencing the gel's microstructure and optical properties.

3.5.4.2. Effect of concentration and type of acid initiator

Two opposing trends are observed for acidic and basic gels: 1) as the water conent increases (waterglass:water ratio decreases), light transmission increases in basic gels but decreases in acidic gels. In other words, basic gels scatter less light while acidic gels scatter more light as silica concentration decreases. It appears that at some point above the waterglass:water ratio of 1:5, the light scattering of basic and acidic gels tends to converge. This opposing trend is evidenced in in Figure 3.8a, where the %T, appearance, Tyndall effect and SEM micrograph of gels can be compared 60 minutes after gelation. When examining the gels' microstructures, we see that gels in both acidic and basic groups become more porous and less uniform upon dilution. So why do these trends appear to be opposite?

Concentration is not the only factor changing herein; in each group, pH is also adjusted with concentration to achieve the same gelation time across all specimens (recall Figure 3.3). However, the trend of pH change in the two groups is opposite; in the basic group, pH decreases upon dilution, while in the acidic group, pH increases upon dilution. This difference in pH adjustment affects the particle size, contributing to the observed optical-related trends.

Particles and aggregates/agglomerates are not the only scatterers in these sol-gel systems. Once past the gelation point, pores form and also scatter light. The level of porosity (pore volume fraction) and the pore size, and size distribution, as well as the presence of other phases with different optical properties in the pores, all affect light scattering. Although both pore size and porosity increase from a waterglass ratio of 1:1 to 1:5 in both acidic and basic gels, the rate of increase is dissimilar due to different starting pore sizes. For instance, the pores in the acidic 1:3 gel are still much smaller than those in the basic 1:3 gel. However, both the 1:5 acidic and basic gels exhibit similar microstructures and pore sizes (>10 µm).

According to Hříbalová and Pabst [300], the van de Hulst approximation[301] is the only model that predicts both the decrease in light transmittance with increasing pore size in the small-size region (i.e., smaller than the wavelength) and the increase in transmittance with increasing pore size in the large-size region (i.e., larger than the wavelength). This model and experimental data show that light transmittance is minimal when the pore size is around the wavelength of the light used, with a steep increase towards maximum transmittance in the small-size region. For larger pore sizes, the increase in transmittance is more gradual and does not reach maximum levels.

In basic gels, the pores are at least 10 times larger than the wavelength, so according to the van de Hulst approximation, light scattering by pores decreases with increasing pore size from a waterglass ratio of 1:1 to 1:5. This trend in pore size explains the increase in total light transmission in basic samples with dilution, as both scattering by particles—due to the decrease in silica concentration and number of particles—and scattering by pores decrease, regardless of any changes in particle size caused by the pH decrease (~1). In acidic gels, the situation is different. The pores in acidic 1:1 and 1:3 gels fall into the small-size region where the pore size-scattering slope is negative, causing the 1:3 gel, with larger pores, to scatter more light compared to the 1:1 gel. In the 1:5 acidic gel, the pores are in the large-size region and scatter light similarly to the basic 1:5 gel, more than both the 1:1 and 1:3 gels. The acidic 1:5 gel scatters more light even before gelation, which could not be related to pores. This effect is likely due to the large difference in particle size in the 1:5 gel compared to the other two, because of the significant pH difference (~2).

3.6. Conclusion

In this study, we have shown that gelation kinetics of sodium silicate solutions could be controlled by adjusting the processing conditions. To optimize waterglass gelation kinetics and the final gel microstructure for enhanced performance as a binder phase in composite bone scaffolds, the effects of pH, waterglass concentration, and type of acid initiator were investigated. Key findings include:

- Gelation time changed exponentially with pH in the basic region and fit third-order polynomials in the acidic region, peaking near pH 2. The fitted equation parameters varied with waterglass concentration, allowing prediction of gelation time for any given concentration and pH.
- A wide range of target gelation time could be achieved in both acidic and basic regions. The specific pH for the target gelation time could be adjusted toward neutral pH by decreasing the initial waterglass concentration.
- Studying the optical properties of gels, while not directly critical in bone tissue engineering, provided insights into gelation kinetics and microstructure, which influence essential properties such as setting time, porosity, and presumably mechanical strength.
- With BA, being weaker than PA, 28-38 times more volume of acid was needed to adjust the pH and only basic gels could be made. Overall, the gelation kinetics, optical properties and microstructure of BA basic gel was similar to what was observed for PA basic gels, highlighting that the effect of pH and waterglass concentration on the gelation process is more significant than the type of acid initiator used.
- Based on light transmittance data and SEM micrographs, acidic gels likely are composed of smaller particles, forming smaller aggregates/agglomerates and pores with less light scattering, while basic gels have larger particles forming larger aggregates/agglomerates and pores leading to more light scattering and opacity.

- UV-VIS spectroscopy was useful for indicating the gel point, marked by a rapid change in light transmittance over time. Differentiating light transmittance spectra using various orders of derivatives enhanced time resolution for precisely and accurately determining the gelation point.

Chapter 4: Molecular Structure Determination of Acid-initiated Sodium Silicate Sol-Gels via Real-time Raman Spectroscopy

4.1. Abstract

Silica gels derived from sodium silicate solutions (waterglass) can be fashioned into in-situ setting composite bone scaffolds with adjustable properties. However, the relationship between their molecular constitution and final properties under varying processing conditions remains poorly understood. This study investigates acidic and basic silica gels formed by reacting waterglass of different concentrations (15-50 wt.%) with boric acid and phosphoric acid, aiming to correlate molecular structure with the resulting microstructure. Raman spectroscopy was used to monitor chemical and structural changes during sol-gel transition in real-time, complemented by quantitative analysis of silicate species using 29Si NMR-identified spectral interpretations. It was found that basic gels primarily consist of higher-order silicate rings (~60-72%) dominated by Q^3 (~53-80%), Q^2 (~10-17%), and Q^0 (~5-34%) units. Conversely, acidic gels exhibit lower-order silicate rings (~70-80%) with predominant Q^2 (~62-80%) and Q^0 (~20-38%) units. Particle agglomeration was found to occur through physical interactions, leading to different structures depending on the pH: basic gels form large, loosely agglomerated secondary particles contributing to large-pore gel networks, while acidic gels yield compact, smaller-pore networks. The presence of water facilitates hydrolysis in acidic conditions and polymerization in basic conditions. This study enhances the understanding of waterglass gelation by monitoring the changes and interactions in molecular structural units during sol-gel transition. We demonstrate the significant impact of pH and processing conditions on the final gel structure, which can be tailored to meet specific requirements for bone scaffolding applications.

4.2. Keywords

Sodium silicate solution, Sol-gel, silica gel, molecular structure, Raman spectroscopy

4.3. Introduction

Silica gels are amorphous forms of silica, and can be described as a coherent, rigid three-dimensional network of contiguous particles of colloidal silica, which are formed by the polymerization of silicic acid, or by aggregation/agglomeration of particles of colloidal silica [102]. Silica gels can be prepared by the sol–gel method using a variety of starting materials as the silicon source. Silicon alkoxides such as tetraethoxysilane (TEOS) and tetramethoxysilane (TMOS) are common precursors for silica gels, but their high cost and hazardous nature pose challenges[302,303]. In contrast, sodium silicate solution, also known as waterglass, stands out as an economical and non-toxic source for obtaining silica gels—it is a commodity product and is often used in food products and biomedical application [246,264,304,305]

Silica gels are suitable materials for bone tissue engineering due to inherent characteristics such as biocompatibility, high and tailorable porosity, active surface functionalities, mechanical strength, and bone bonding abilities[246,304]. The binder characteristics of waterglass before transitioning into a gel, and its tunability in physicochemical properties after transitioning into silica gel, can aid in developing a formable composite bone scaffold that can be tailored to fit any bone defect and sets *in situ* into a porous 3D structure, promoting bone tissue regeneration. Based on this concept, a design was explored in our lab where 45S5 glass powder was combined with a sodium silicate solution binder to create a formable paste which sets upon exposure to CO_2 gas in the ambient air to harden into a rigid bone scaffold[261,262]. To optimize clinical applicability, we accelerated gelation from 10 days to 10 minutes by combining waterglass with boric acid (BA) or phosphoric acid (PA) as acid-initiators before mixing with bioactive glass. The effects of pH, waterglass concentration, and type of acid-initiator on gelation kinetics, gels' optical properties, and microstructure were investigated in chapter 3. It was found that the target gelation time of 10 minutes could be achieved in both acidic and basic regions, with the specific pH for the target gelation time adjustable toward neutral by decreasing the initial waterglass concentration. Moreover, the effect of acid initiator was found to be insignificant. Studying the optical properties of gels, while not directly critical in bone tissue engineering, provided insights into gel formation and porosity: acidic gels consist of smaller particles forming tightly packed aggregates/agglomerates with less light scattering, while basic gels have larger particles forming less dense and larger aggregates/agglomerates, leading to more light scattering and opacity. Despite these findings, the molecular constitution of silica gels remains poorly understood.

Little is known about the molecular constitution of amorphous silicates. Iler's theory[102] is a widely accepted classic theory for silica gelation, which outlines three stages of polymerization for sol-gel transition in silica-water systems: 1) polymerization of $Si(OH)_4$ monomers to oligomers and particles, 2) particle growth, and 3) particle aggregation leading to formation of 3D gel structures. However, when applying Iler’s theory to gelation in sodium silicate solutions, notable differences emerge. The gelation process in sodium silicate solutions does not solely begin with monomeric $Si(OH)_4$ species; there is already a diverse range of silicate species, including monomers, low-order oligomers (such as dimers and trimers), and more complex polymerized networks, all based on $Si(OH)_4$ tetrahedra. These silicate species exist in a dynamic equilibrium, with variations in bridging oxygens (BO) and non-bridging oxygens (NBO)[264] (see Figure 4.1a), exhibiting varying degrees of connectivity (see Figure 4.1b). So far, forty-eight possible structures have been identified using ^{29}Si Nuclear magnetic resonance spectroscopy (NMR) spectroscopy in silicate solutions[107,108,306], with the most definitive forty-five shown in Figure 4.1c. Gelation in sodium silicate solutions is significantly influenced by the presence of sodium ions and the diversity of silicate species, resulting in a complex gelation process.

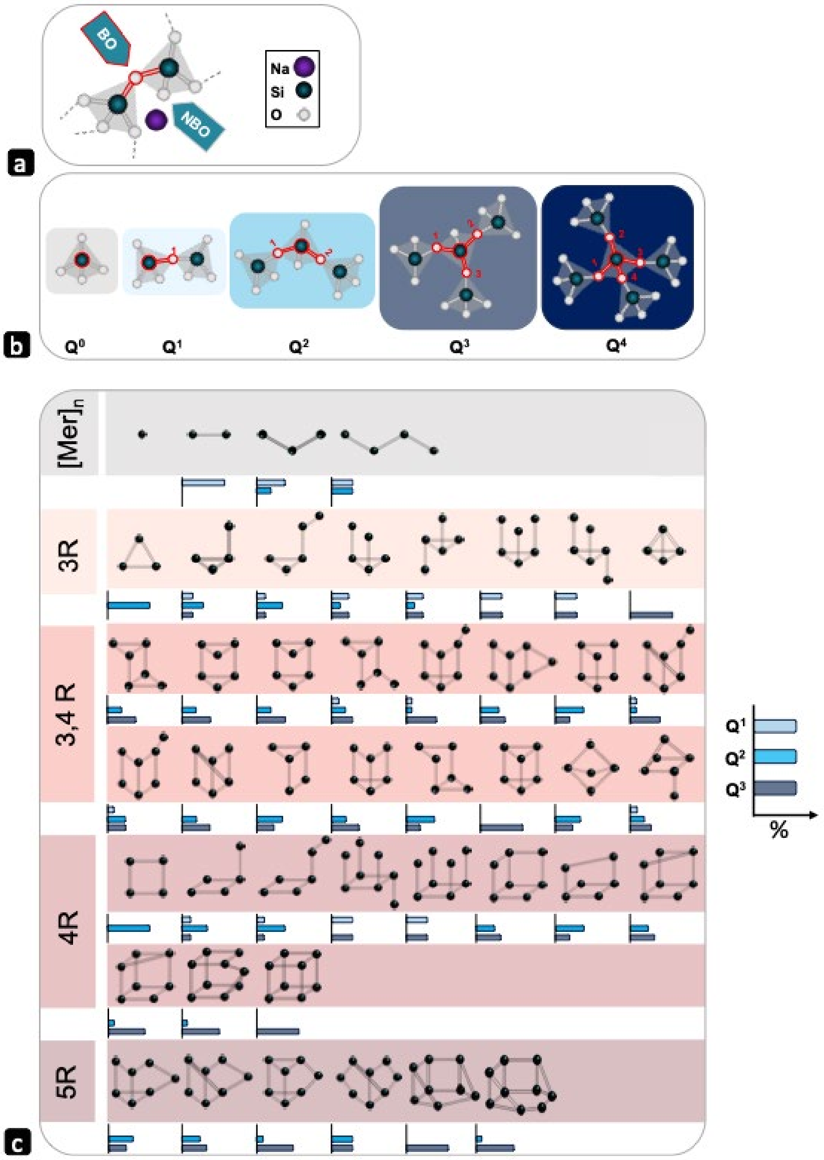

Figure 4.1 (a) Schematic representing two silicate tetrahedra connected by sharing a bridging oxygen (BO) and a sodium ion compensating a charge near a non-bridging oxygen (NBO). (b) Schematic showing different silicate structural units labeled as Q^n, where Q represents a fourfold coordinated silicon atom and n indicates the number of neighboring silicon atoms linked through a bonding oxygen atom. (c) Silicate structures identified in aqueous silicate solutions by ^{29}Si NMR, proposed by Knight et al.[107] Balls and sticks represent silicon atoms and oxygen bridges between silicon atoms, respectively, with NBO omitted, re-drawn from[107]. The fraction of Q connectivity in silicate tetrahedra in each structure was calculated and is presented as a bar graph beneath each structure. The silicate species have been divided into 3-membered ring structures, 3,4-membered ring structures, 4-membered ring structures, and 5-membered ring structures, based on the number of rings present in their structure. More details can be found in Section 3.1.2.

Silica gel formation in waterglass is believed to initiate by destabilizing the solution with acids, (HX) which triggers the partial neutralization of Si-O$^-$ Na$^+$ ion pairs, leading to the formation of reactive silanol groups and salts (Equation (4.1)). However, such an oversimplified equation doesn't capture all the simultaneous processes occurring in these solutions. Both the formation of reactive Si–OH groups and overcoming of repulsive interactions between silicate species are prerequisites for aggregation/agglomeration of colloidal silicate particles and gel formation, and are mainly governed by the pH. The formation of silicate aggregates/agglomerates and their continuous growth during sodium silicate gelation have been reported in SAXS and TEM studies[116,181,184,185]. Despite clear evidence of silicate particle aggregation/agglomeration leading to a 3D network that entraps solvent, the nature of molecular chemical interactions among particles, between particles and aggregates/agglomerates, and among aggregates/agglomerates during silica gel formation in waterglass is less understood. The fact that silica solutions do not conform to the DLVO[i] theory, which explains the aggregation and kinetic stability of aqueous dispersions as the sum of a weak attractive (van der Waals) and a repulsive (double layer) potential, complicate matters further[118,295]. For a detailed discussion on the current understanding of the structure and speciation of sodium silicate solutions and silica gels, and the existing gaps in the literature, the reader is referred to our recent review paper[264].

$$\equiv SiO^-Na^+ + HX \longrightarrow \equiv SiOH + NaX \tag{4.1}$$

Moreover, the classification of silica gels as either physical or chemical gel remains unclear. Generally, hydrogels are classified based on the nature and durability of their bonds. Physical gels are reversible due to the conformational changes and are achieved by agglomeration of particles

, whereas chemical gels are irreversible and are a result of aggregation of particles[307]. It should be noted that in this study, an agglomerate corresponds to the case when the dispersed particles are held together by weak secondary bonding and physical interactions such as hydrogen bonding and van der Waals force. An aggregate on the other hand, is comprised of strongly bonded colloidal particles by strong primary bonds such as covalent bonds. In silica gels, both formation of Si—O—Si covalent bonds *and* physical processes such as hydrogen bonds or Van der Waals forces may occur between particles and aggregates, making their classification ambiguous. Researchers

---

[i] Named after Derjaguin, Landau, Verwey, Overbeek

have reported the formation of both “reversible” and “irreversible” silica gels from sodium silicate solution in different pH and silica concentrations[265,308,309]. However, the exact boundary between these two types of gels and the definition of the so-called reversibility in these studies is ambiguous and is not directly linked to the nature of interactions among silicate particles/aggregates.

A useful chemical analysis technique that provides detailed information about chemical structure and interactions is Raman spectroscopy, which has been successfully applied for characterisation of silicate species in solution[114,149,152], gel[165,310,311], and glass[312–314] states. However, a drawback of using Raman spectroscopy for aqueous silicate solutions and gels is that interpretations of such spectral features are still limited due to the lack of well-established physical principles accurately describing vibrational modes in non-crystalline networks. Serious concerns and questions remain on the adequacy of widely cited and used peak assignments and interpretation schemes based on the analogy with molecular or cluster models[315,316]. Although some advances have been made through theoretical calculations of vibrational spectral features of amorphous networks and comparisons of computational results with experimental data[317,318], it remains challenging to calculate the Raman susceptibility of silicates within a molecular modeling framework. This challenge is due to the complexity of the dynamic structure of silicates and the high sensitivity of the calculation results to force and bond parameters. Despite these challenges, Raman spectroscopy offers advantages such as high speed and non-destructiveness, making it suitable for studying sol-gel transitions. Real-time investigations during gelation could provide additional insights into the waterglass sol-gel transition and the impact of processing parameters on molecular structure. Surprisingly, to the best of our knowledge, real-time Raman spectroscopy studies on silicate species are limited to silicate glasses[319], silicon alkoxides[320,321], silicate solutions[322], geopolymers[163], and silicate melts at high temperatures and pressures[322–324], and have not been employed to study sodium silicate solution sol-gel transition. Here, we use real-time Raman spectroscopy to investigate the effects of pH (acidic vs. basic), initial WG concentration, and type of acid initiator on the sol-gel transition and structure of the final gels—all within the same gelation time.

As the materials science paradigm highlights the correlations and relationships between processing, structure, properties, and performance it is crucial not only to investigate the molecular structure—examining the evolution of silicate species, the interactions within clusters, and the final network structure they form—but also to correlate these structural changes with both processing conditions and final properties. However, a significant portion of current research tends to focus either on the direct connection between processing methods and material properties, or solely on structural analysis without integrating processing and properties. The process of preparing silica gels seems to rely more on experience rather than on a solid scientific understanding of the preparation conditions and controlling properties. For instance, researchers have studied the effect of different processing parameters such as sodium silicate solution concentration and SiO_2/Na_2O ratio [195], pH [115,209,325], temperature [191,193], type of acid initiator[272], and presence of metal ions [191,207] on a variety of properties such as gelation time, viscosity, and the final gel morphology and porosity. However, the influence of these parameters on the molecular structure of resulting gels remains insufficiently explored. Specifically, suspicions about potential differences in the molecular structures of acidic and basic gels have been around for decades due to the noticeable variations in their properties. Yet, most of the studies have focused on silica gels derived from alkoxides[198,326–328] rather than sodium silicate solutions. It is important to note that polymerization and gelation processes differ between alkoxides and waterglass due to the diversity of silicate species involved. Even among different alkoxides such as TMOS and TEOS, the oligomerization pathways have been found to be significantly different[224,329].

Our goal is to improve the quantitative understanding of silica gel molecular structure and aggregation/agglomeration of particles into a gel to better control waterglass gelation and predict its properties in the gel state under different preparation conditions, such as pH, sodium silicate concentration, and type of acid initiator. Achieving consistent gelation times in both acidic and basic pH environments underscores the importance of investigating how pH affects the chemical structure and, consequently, the final gel properties, including microstructure and mechanical characteristics. These properties of the silica gel, to be used as a binder, directly influence the properties of bioactive glass composite scaffolds, such as setting time, porosity, and mechanical strength, which are crucial for bone scaffolds.

In the discussion, we aim to answer the following questions:

1. How can insights about identifying silicate structural units from 29Si NMR help resolve the uncertainties regarding peak assignments in Raman spectra of silicate solutions and gels?

2. What insights can real-time Raman spectroscopy provide into the sol-gel transition and structural evolution of silicate species in sodium silicate solutions prior to, during, and after gelation?
3. What role do attractive interactions, including Si-O-Si covalent bonds and physical processes like hydrogen bonding, play in the aggregation/agglomeration of colloidal silicate particles and the formation of silica gels? How do these interactions influence the classification of silica gels as physical or chemical?
4. Do acidic and basic gels, with the same gelation time, differ in microstructure, and if so, how are such differences correlated with the effects of pH, waterglass concentration, and type of acid initiator on their molecular structure?

4.4. Materials and methods

4.4.1. Preparing samples for Raman spectroscopy

The starting commercial sodium silicate solution (Sigma-Aldrich, CAS number: 6834-92-0), St. Louis, MO, U.S.A) had the following characteristics: [SiO_2] = 26.5 wt.%, [Si] = 6.13 mol/l; relative density = 1.39 g/l; pH = 11.9; SiO_2/Na_2O molar ratio = 2.57. The acid initiators used were: phosphoric acid, 85% solution (Fisher Scientific, CAS number:7664-38-2, Toronto, ON, Canada) and boric acid powder, ≥ 99.5% (Fisher Scientific, CAS number: 10043-35-3, Toronto, ON, Canada).

With the goal of creating a formable, *in situ* setting bioactive glass-waterglass composite bone scaffold, the effects of pH (2-11), waterglass concentration (15-50 wt.%), and acid initiator type (phosphoric acid and boric acid) were investigated as independent variables to optimize the setting time to a clinically practical range of approximately 10 minutes in chapter 3. It was found that the target gelation time of 10 minutes can be achieved at a single basic pH using boric acid and at various pH levels in both acidic and basic regions using phosphoric acid by adjusting the waterglass concentration, resulting in seven different specimen compositions, detailed in Table 4.1.

Table 4.1 Composition and pH of gels made with boric acid and phosphoric acid, with a gelation time of ten minutes, containing water, waterglass, and an acid solution.

Acid catalyst	WG:Water (wt. ratio)		WG (g)	Acid content (µl)	pH	t_g (min)
Boric Acid	● 1:5	Basic	3.34	14000	10.60	10
Phosphoric Acid	● 1:1	Basic	10.00	545	10.63	10
	● 1:3		5.00	360	10.35	
	● 1:5		3.34	300	9.70	
	● 1:1	Acidic	10.00	2800	3.36	10
	● 1:3		5.00	1300	4.80	
	● 1:5		3.34	825	5.30	

To prepare the specimens, we first created the dilute waterglass solutions by adding DIUF water to the commercial solution at room temperature under magnetic stirring to achieve waterglass-to-water weight ratios of 1:1, 1:3, and 1:5. Next, we prepared the acid solutions: a 0.7 M boric acid (BA) solution by dissolving 4.3 g of BA powder into 100 ml of DIUF water, and a 14.8 M phosphoric acid (PA) solution by mixing 11 g of 85% PA solution with 1 ml of DIUF water. Then, the acid solutions were added to initial diluted waterglass solutions at room temperature under magnetic stirring. Depending on the volume needed, a 20 ml syringe, 3 ml syringe, and 1000 µl micropipette were used to add the acid solutions. The mixtures were stirred for one minute and then transferred to 3.5 ml wells of a 48-well polystyrene plate to obtain Raman spectra instantly. The rest of each mixture was transferred to 30 ml glass beakers to double-check the gelation time by the tube inversion method (as described in section 3.4.4.).

4.4.2. Raman spectroscopy

4.4.2.1. Experimental

The Raman spectra were recorded using a Renishaw inVia Qontor confocal Raman microscope (Renishaw Engineering Company, Wotton-under-Edge, U.K.). Preliminary experiments were performed to optimize the experiment parameters, including the laser wavelength, laser power, exposure time, and number of accumulations (see Supplementary data).

Details of eliminating peaks coming from the well plate is provided in Supplementary data. Prior to each scan, spectral calibration was verified using an internal silicon standard with a Raman shift at 520.2 ± 0.5 cm^{-1}. Based on the results of preliminary experiments, the 532 nm (50mW) laser was operated at 50% power and focused on the solutions' surface through a 5× objective lens. The spectral range was 157.99 to 1364.02 cm^{-1} centered at 800 cm^{-1}, using gratings of 2400 grooves/mm. This setup ensured that the most intense peaks of the silicates were captured with a spatial resolution better than 300 nm and an axial resolution better than 2 μm . We set the exposure time for each scan at 1 second and accumulated 60 scans, with a 60-second interval between each scan. A total of 9 series of spectra were acquired from each specimen, with the first spectrum obtained at two minutes after mixing the waterglass with the acid solutions, and the last one 8 minutes after gelation. For each of the seven specimens, three replicates were measured, and their Raman spectra were averaged to ensure consistent results. All data acquisition was performed using Renishaw WiRE^{TM} v.5.2 software (Renishaw Engineering Company, Wotton-under-Edge, U.K.)

4.4.2.2. Pre-processing

The Raman results were subjected to the following data processing steps to make the spectra ready for further data analysis and interpretation:

(i) Baseline correction: The spectral background, which contained a background profile attributed to fluorescence emission, were removed using a polynomial fit. The advantages of polynomial fitting are its simplicity, effectiveness, and its ability to retain the spectral contours and intensities of the input Raman spectra. The spectra were first corrected by eliminating the wavenumbers lower than 350 cm^{-1}, and then subtracting the baseline, which was modelled by fitting a 5th order polynomial to the spectral region between 350-1350 cm^{-1}. The region below 350 cm^{-1} was omitted from the Raman spectrum due to a significant baseline elevation, likely attributable to Rayleigh scattering; excluding this region mitigates the impact of Rayleigh scattering, thereby enhancing the clarity and precision of the spectral information in the more relevant wavenumber range.

(ii) Normalizing: the spectra were normalized using an integrated signal, in which intensity values are modified so that the sum of all values in the given dataset is 1. while normalizing by intensity range (0 to 1) is a more common method, it may not account for differences in total signal strength, as it scales each spectrum to the same range regardless of the overall signal intensity. Using integrated signal normalization on the other hand, ensures the entire signal is considered, providing more accurate and meaningful comparisons between different specimens.

(iii) Smoothing:. Smoothing was performed using the Savitzky–Golay method, a local second-order polynomial regression with an eight-point window.

All pre-processing steps were performed using Renishaw WRE v.5.2 software.

4.4.2.3. Analyzing

Interpreting Raman spectra of silicates in amorphous or solution forms poses a challenge due to the presence of broad, overlapping bands and potential frequency shifts resulting from changes in the environment surrounding the Si-O bonds. To address this, Mysen et al. [330] suggested a statistical approach, assuming that all Raman bands are symmetric and Gaussian, and that a single (statistically the best) combination of Gaussian lines exists, which has since been widely adopted in the field[323,331,332]. Few studies have suggested that a Lorentzian fit is a more realistic approach[333,334]. In our study, we experimented with both Gaussian and Lorentzian fitting techniques. Ultimately, Raman peaks were fitted with Gaussian curves as it provided a better fit, indicated by R^2 value closer to 1.

However, a Gaussian fit might lead to very different peak linewidths. In response, some researchers have modified this approach by constraining the full width at half maximum (FWHM) of peaks to the range of 35–55 cm^{-1} for silicate glasses[335]. In this study, the FWHM was constrained between 15–75 cm^{-1}. This range was chosen because it reflects a range of linewidths larger than that used for silicate glasses, taking into consideration the broadening in linewidth in aqueous medium compared to the solid state. The number of Gaussian curves was not limited in this study because the vibrational modes in silicate solutions can be more complex and diverse due to their dynamic nature and possible interactions between different silicate species and/or with water or ions. Overall, we believe that a more flexible approach to peak fitting allows for a more accurate depiction of the complex vibrational spectrum and the interactions within the solution, so long as all the underlying mechanisms and physical meanings are considered. The Gaussian curves were fit to each spectrum using the nonlinear fitting tool in Origin (Pro), 2021 (OriginLab Corporation, Northampton, MA, USA). Fitting parameters were iterated until the fit converged, with R^2 values ranging between 0.9 and 1. Peak centers, FWHM, area under the peaks, and area percentage were obtained for each deconvoluted peak from the modeled spectra for all waterglass solutions and gel specimens. All Raman data were plotted using Origin (Pro), 2021. Error bars for the Raman spectroscopy bar graphs were calculated using the standard deviation of the mean for a sample size of N=3.

4.4.3. Scanning Electron Microscope

Scanning electron microscopy (SEM) was employed to image and compare the packing, porosity, and morphology of gels with a target gelation time of 10 minutes. The goal was to find correlations between the molecular structure and microstructure of the gels prepared with different processing conditions.

To prepare the samples, fresh mixtures of waterglass solutions of different concentrations and acids were made and poured into 1x1x1 cm^3 silicone molds, where they were allowed to gel. 60 minutes after the gelation point, the samples were immersed in liquid nitrogen to freeze. After freezing, the samples were dried using a Savant SuperModulyo Freeze Dryer (Mechatech System Ltd, Thornbury, Bristol, U.K.) at a temperature of −40°C and a pressure of ~0.08 Torr for 12 hours. Prior to imaging, the specimens were sputtered with gold using Denton Desk II (Denton Vacuum, Moorestown, NJ, U.S.A) for 90 seconds, resulting in a 12 nm gold coating to reduce charging. Imaging was conducted in Secondary Electron (SE) mode with a Zeiss EVO MA10 SEM (Carl Zeiss AG, Oberkochen, Baden-Württemberg, Germany) equipped with a LaB_6 filament.

4.5. Results and discussion

4.5.1. Peak assignments

The Raman spectrum of the commercial sodium silicate solution (WG, as is) is shown in Figure 4.2a. To enhance peak identification and quantitative structural analysis, Gaussian curve fitting was applied to deconvolute the Raman spectra into their constituent components. Assigning peaks in this complex and dynamic system presented significant challenges. The first step was identifying potential silicate species in sodium silicate solutions, which aided in understanding the possible chemical and physical interactions and interpreting structural changes during gelation. Such knowledge was crucial for navigating the complexities of broad Raman peaks, where multiple assignments were possible, ensuring the selection of the most plausible and probable option. The most reliable reference for species identification is the comprehensive set of structures derived from ^{29}Si NMR data, particularly relevant due to its proximity in concentration to our study (recall Figure 4.1c). Although it is not possible to quantitatively distinguish the contributions of each of these oligomers in the Raman spectrum, the NMR data can guide the assignment of Raman bands. While Raman spectroscopy does not offer the same molecular specificity as NMR spectroscopy, it can quantitatively interpret the degree of connectivity and bonding arrangements of silicate species. In both techniques structural units are described by "Q-units," labeled as Q^n, where Q represents a $Si(OH)_4$ tetrahedron, and n indicates the number of neighboring silicon atoms linked through an oxygen atom[129,130]. In other words, each Q^n structure consist of (n) BOs and ($4-n$) NBOs (see Figure 4.1b).

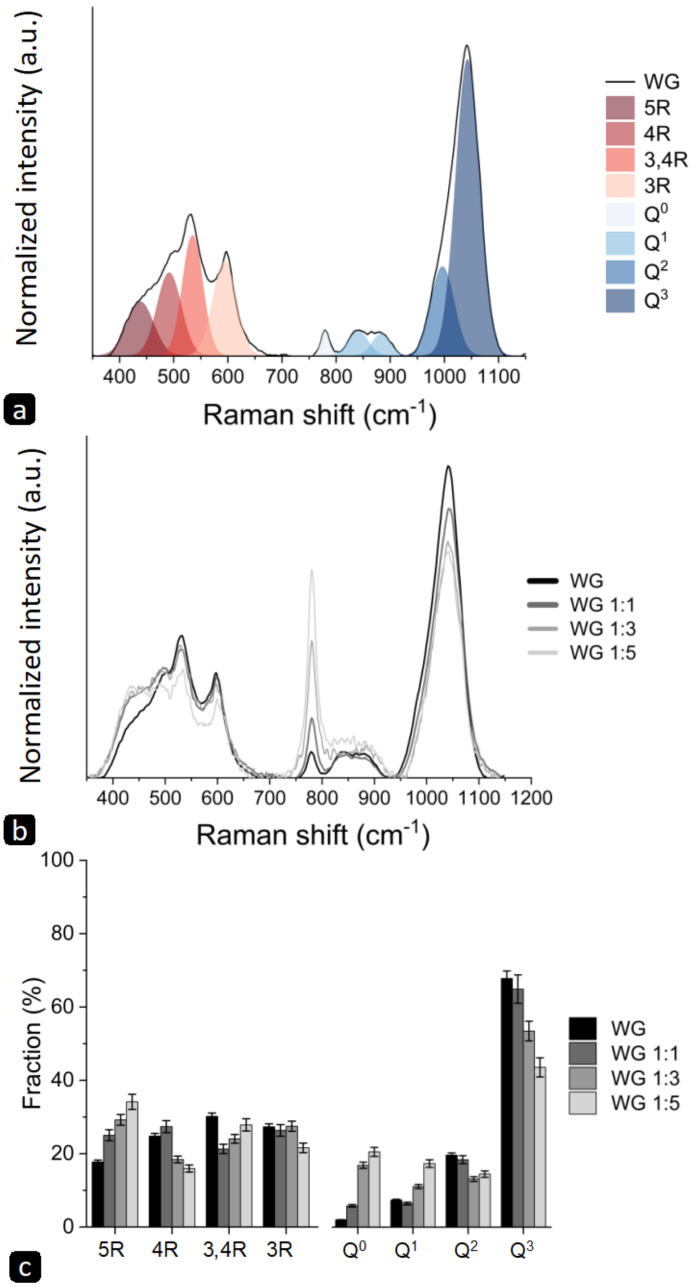

Figure 4.2 (a) The Raman spectrum of the commercial sodium silicate solution (WG, as is) and the bands obtained from deconvolution of spectrum by Gaussian curve fitting, and the Q^n species and ring structures assigned to each. (b) the Raman spectra of WG in its original state and when diluted to different waterglass:water weight ratios. (c) Changes in the fraction of Q^n species and ring structures present in waterglass upon dilution, calculated from the area under the peaks in the deconvoluted spectrum. The results show that waterglass is mostly composed of Q^3 connections and with no specific dominant ring structure. Silicate species depolymerize upon dilution. The error bars represent one standard deviation from the mean (N=3).

Generally, Raman spectra of silicates can be broken down into high-frequency and low-frequency regions. The high-frequency region (equivalent to 700-1200 cm^{-1}) is associated with symmetric and asymmetric Si-O stretching vibrations, corresponding to the Q^n connectivity of the tetrahedral [SiO_4] building blocks. The low-frequency region (equivalent to 400-700 cm^{-1}) is associated with Si-O-Si bending and the inter-tetrahedral Si-O-Si linkages. Although there are several publications that have used Raman spectroscopy to study silicate solutions and gels [149,158,162,322,324,336–339], some aspects of the interpretation of Raman spectra remain uncertain. Unfortunately, certain Raman band assignments were mainly developed for solids (i.e., silicate crystals and glasses). Even in the case of Raman analysis of silicate glasses, where there appears to be a general consensus, some researchers have raised concerns about the adequacy of widely cited peak assignment and interpretation schemes[315,340]. Band assignment ambiguities arise from several factors: (1) the abundance of potential species with diverse vibrational modes, local fluctuations in bond angles and lengths of structural units, as well as the randomness in their connectivity that results in broad overlapping bands; (2) the oversight of dissociation and neighboring (second shell) connectivity; and (3) absence of a standardized method for curve fitting and failure to constrain peak numbers or linewidths which contribute to a wide array of possible fits.

Figure 4.3 displays the peaks obtained from the deconvoluted spectrum of waterglass, compared with the peak ranges assigned to different structural units in both high- and low-frequency regions of the Raman spectra of silicate glasses, silicate solutions, gels, and other silicate materials (such as zeolites and alkoxides) according to the literature. As can be seen, although these assignments are generally consistent, they can be broad and often overlap, making it difficult to assign peaks with complete certainty. To achieve the most accurate peak assignments possible, we go beyond simply replicating widely cited peaks. Instead, we verify our findings by comparing and validating them with the silicate species present in WG, as indicated by NMR results from previous studies. We also question the origins of widely cited peaks to determine if they are appropriate references for our system. Additionally, we correlate the spectral features from low- and high-frequency regions to ensure that both kinds of identified species (including ring structures at low-frequency, and Q connectivity at high-frequency) are consistent with the overall structural framework. Moreover, we correlate our results with data obtained from physical and microstructural properties to complete the picture. The peak centers (X_c), peak width (FWMH), and species assigned to each deconvoluted peak is presented in Table 4.2 for all waterglass solutions and gel specimens. In the following sections, these peak assignments in high- and low-frequency regions are discussed in detail.

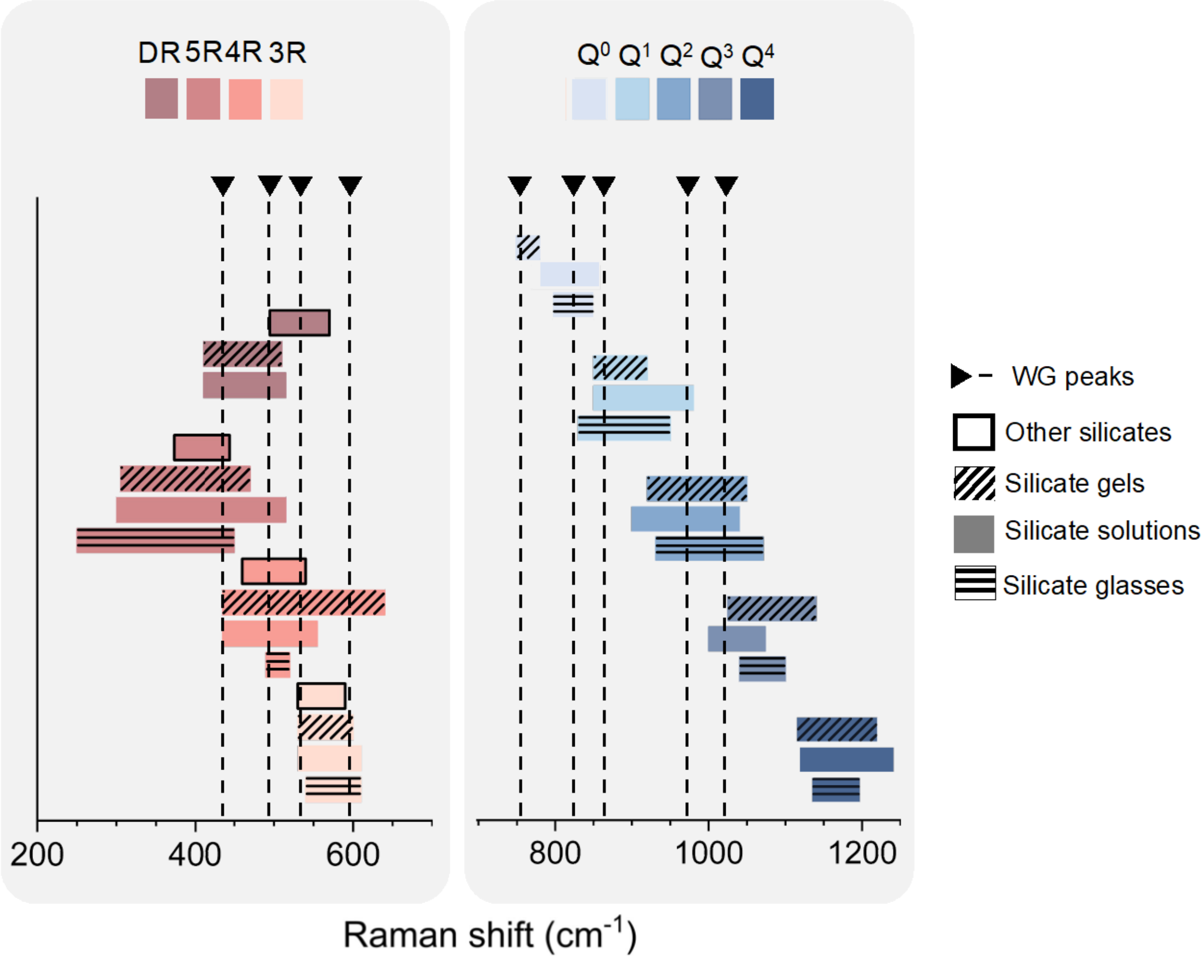

Figure 4.3 Comparison of the peaks obtained from the deconvoluted spectrum of waterglass (indicated by dashed lines) with the peak ranges assigned to different structural units in both high- and low-frequency regions in silicate glasses[313,333,341–345], silicate solutions[148,158,310,338–340,346,347], silica gels[310,337,338,348,349], and other silicate materials[224,327,350–355] according to the literature. In the high-frequency region, peaks are assigned to Q^0-Q^4 units, while in the low-frequency region, they are assigned to 3-, 4-, and 5-membered rings and double rings.

Table 4.2 the peak centers (X_c, cm^{-1}), peak widths (FWHM, cm^{-1}), different species assigned to each peak obtained from the deconvoluted spectra of waterglass solutions (WG as is, and diluted to different waterglass:water weight ratios), gel specimens (basic and acidic gels made with phosphoric acid (PA) ,and boric acid (BA) using initial waterglass solutions with different waterglass:water weight ratios).

		Waterglass				Basic gels				Acidic gels		
	(cm^{-1})	● WG	● WG 1:1	● WG 1:3	● WG 1:5	● BA 1:5	● PA 1:1	● PA 1:3	● PA 1:5	● PA 1:1	● PA 1:3	● PA 1:5
Q^3	Xc	1042.9	1043	1043	1043.8	1032.9	1036.9	1031.6	1032	-	-	-
	FWHM	52.1	50	50	50	49.3	51.6	50	55	-	-	-
Q^2	Xc	996.4	998	1001.5	1001.4	980	980	980.2	-	984	984	984
	FWHM	50.8	50	42	52	52.8	50	50		33.6	40	40
Q^1	Xc	883.4,840.5	858.9	865.1	853.6	858.1	-	880.2	-	-	-	-
	FWHM	39,43.2	64.2	70	75	46	-	65.9	-	-	-	-
Q^0	Xc	779.5	780.1	780	779	780.8	780.8	786.1	784.9	784.9	787.4	787
	FWHM	18.2	22.1	26	25	30	23.6	18.7	48.8	59.9	40	44.2
3R	Xc	594	593.9	592.5	597.6	-	-	-	585.7	570	570	570
	FWHM	50.6	55.4	64.4	48.8	-	-	-	73.7	55	49.4	50
3,4 R	Xc	534.8	534.3	531.1	530.6	508	512	498.2	508	492.4	491	491
	FWHM	44	40.9	41.8	48.8	51.7	50	42	40	30.6	41.9	50
4R	Xc	491.5	491.8	489.2	485.8	450	455.8	450	450	450	450	451.8
	FWHM	52.4	55.8	43.7	41.6	51.7	55	42	55	50	40	50
5R	Xc	438	434.3	437.7	435	415	415	415	-	-	-	-
	FWHM	57.6	62.7	67	65.1	51.7	60	42	-	-	-	-

4.5.1.1. High-frequency region

Within the high-frequency region, Raman bands are often deconvoluted into four components: Q^4 species at 1200 cm^{-1}, Q^3 species at 1050~1100 cm^{-1}, Q^2 species at 950~1000 cm^{-1}, Q^1 species at 850~900 cm^{-1}, and Q^0 species at 750~850 cm^{-1}. These components correspond to symmetric Si-O stretching motions of SiO_4 tetrahedral units containing four, three, two, one, and zero BOs, respectively[356–358] (see Figure 4.1b). These assignments are supported by a variety of research methods, including comparisons between Raman spectra of silicate glasses and crystalline silicate polymorphs[359], qualitative assessment of spectral variations with changing composition[360,361], computational studies[315,362,363], and comparisons with NMR studies[312,364].

Among the Raman bands of silicate materials in the high-frequency region, the most confidently assigned peak is around 770-850 cm^{-1}, attributed to the tetrahedral symmetric Si–O stretching of monomeric silica species (Q^0)[324,362,365]. The separation of the Q^0 region from other Q structure regions is also evident in Figure 4.3, as the Q^0 region is distinctly separate from other Q structure regions, which tend to overlap in some areas. Some studies propose an alternative interpretation of this band, suggesting it could be associated with transversal optical (TO) and longitudinal optical (LO) vibrational pairs[158,366]. In an ionic crystal lattice, the oscillatory displacement of atoms at optical frequencies can be described in two modes: TO mode, where atom displacement is perpendicular to the wave vector, and LO mode, where displacement occurs along the wave vector[367]. Such TO-LO splitting is well known in crystalline materials like quartz[368]. However, the occurrence of this phenomenon in amorphous and solution-phases of SiO_2 has been widely debated. Researchers[316,338,369] argue that given the non-equilibrium nature of the glass and solution, where there is no long-range order, and it is questionable whether the peaks in the Raman spectra can be explained in a similar manner to the TO-LO splitting seen in ionic or highly polar crystalline materials. Moreover, studies assigning peaks in the 650-850 cm^{-1} region to TO-LO in silicate solutions often reference a study by Galeener and Lucovsky[370], who proposed that Raman spectra of silica glass contain three TO-LO pairs at approximately 455 and 495 cm^{-1}, 800 and 820 cm^{-1}, and 1065 and 1200 cm^{-1}. We believe that study, which is based on an analogy with GeO_2 data and crystalline alpha-quartz, may be outdated. Additionally, the origin of the 650-850 cm^{-1} range for TO-LO splitting is unclear and does not even align with Galeener and Lucovsky's proposed range. Finally, neither our study nor the referenced studies show evidence of a doublet-like peak in this range. Therefore, we assign the peak at 779 cm^{-1} in Raman spectrum of WG to Q^0 species, which is in good agreement with a study performed on sodium metasilicate (Na_2SiO_3) solutions[162], containing only monomeric (Q^0) species.

Four peaks at 840, 883, 996, and 1043 cm^{-1} remain unassigned. One approach would be to attribute these peaks to Q^1, Q^2, Q^3, and Q^4 respectively. However, the peak at 1043 cm^{-1} does not fall within the region typically assigned to Q^4 according to the literature. Instead, as shown in Figure 4.3, the peak falls in an area where the Q^2 and Q^3 ranges overlap. Q^4 species has been reported to exist only in highly concentrated and high ratio sodium silicate solutions (>35 wt.% SiO_2, $SiO_2/Na_2O>\sim3$) [138,146]. However, even in those solutions, Q^4 has never been the dominant type of connection. Therefore, it is not surprising that no Q^4 species exist in our waterglass stock solution ($[SiO_2] = 26.5$ wt.%).

Referring to primary structural units suggested by NMR studies in Figure 4.1c, the silicate species are mostly compact, containing fewer than ten Si atoms, with 39 out of the 45 species containing at least one three-membered ring (exceptions being the monomer, dimer, linear trimer, linear tetramer, three-membered, and four-membered rings). These silicate species mostly consist of double or branched rings, indicating a predominance of Q^3 connections. Halasz et al.[114] assigned a peak at 1040 cm^{-1} in the Raman spectrum of silicate solutions to Q^2 and questioned the existence of double rings/cage structures. However, we challenge their assignment to Q^2 instead of Q^3, as the absence of Q^3 connectivity contradicts many potential structures identified by ^{29}Si NMR, as well as their assignments to double ring structure in the low-frequency region. Therefore, we assign the 1043 cm^{-1} peak, which is the most intense in the waterglass spectrum (see Figure 4.2a), to Q^3, and we rule out Q^2 as a possibility for 1043 cm^{-1} peak.

Ruling out Q^4, more Gaussian peaks remain than there are Q species. Recent studies have identified multiple energetically distinct types of NBO in silicate glasses that arise from interactions between alkali atoms and the "second coordination sphere" of NBO[371,372]. This finding was initially observed in sodium metasilicate crystals, where two types of NBO were found: those coordinated to a sodium atom and those that were not[373]. NBOs increase electron densities due to ionic interactions with alkali atoms (M), which in turn weakens the Coulombic force between Si and all four O atoms (both BO and NBO). The increased electron densities weakens the Si-O bond strength, force constants, and Si-O vibrational frequencies. Therefore, tetrahedra with an alkali atom attached to a BO are impacted by M-BO interactions, shifting the BO vibrational frequency to lower wavenumbers compared to silicate tetrahedra without these interactions[374]. Q^n species with varying degrees of M-BO interactions has been proposed to account for the "extra peaks" in the high-frequency region of the Raman spectra of alkali silicate glasses[333–335,374]. Koroleva et al.[323] developed the concept of the "second coordination sphere" in silicate glasses and melts based on the degree of polymerization of the neighboring tetrahedra. They introduced the parameter Q^{ab}, where 'a' indicates a central tetrahedron type and 'b' indicates the type of nearest tetrahedra connected by bridging bonds. For instance, Q^{21} and Q^{22} are Q^2 species connected to Q^1 (may be a part of trimer) and linked to the same Q^2 (in chains), respectively. Among the three peaks at 840, 883, and 996 cm^{-1}, the first two are closer in range, suggesting they could belong to the same Q species. While both the number of sodium ions around NBOs and the degree of connectivity of neighboring tetrahedra influence vibrational frequencies, the degree of connectivity (such as Q^1 at the end of a trimer versus Q^1 attached to a ring) likely has a greater impact on the frequency. The dynamic nature of the solution allows for more freedom in bond angles and structures, which reinforces our argument that the neighboring Q unit plays a more significant role in affecting bond lengths, angles, and consequently, peak wavenumber locations. While we accept the general concept used by Koroleva et al.[323], we don't agree with all of their assignments. Their assumption that silicate species form either chains (dimer, trimer, tetramer) or sheets overlook the possibility of various structures observed in NMR data, such as the formation of Q^{13} connections. We assign the peak at 996 cm^{-1} to Q^2 and both the 840 and 883 cm^{-1} peaks to Q^1, but we cannot make precise distinctions regarding the exact modes for Q^1 (such as neighboring Q structure or the number of sodium ions around it) with the data available to us. Looking at Table 4.2, none of the diluted waterglass solutions or gels contains two peaks for Q^1, still, their peak width is wide compared to other types of Q species.

4.5.1.2. Low frequency region

The low-frequency bands in the 400~700 cm^{-1} region are typically attributed to the inter-tetrahedral Si-O-Si bending vibrations of silicate rings of varying sizes. Similar to high frequency region, the peak assignments for low-frequency region in Raman spectra of silicate solutions often rely on assignments made for silicate glasses. Before applying these bands to our solution/gels, however, we must first understand the origins of the assignments made for glasses and their relevance to our study.

Supported by computational modeling[341], the two sharp peaks at approximately 495 and 606 cm^{-1} in the Raman spectrum of sodium silicate glasses, known as "defect" lines D1 and D2, have been attributed to breathing motions of oxygen atoms in of 4- and 3-membered ring structures (4R and 3R), respectively. Researchers often attribute bands in the ~400 to 650 cm^{-1} range to 3-, 4-, or ≥ 5-membered rings in silicate glasses[345,375]. Sodium cations act as network modifier and break Si-O-Si bonds, reducing the size of ring structures formed from interconnected SiO_4 tetrahedra. This reduction in ring size correlates with a decrease in the Si-O-Si angle, following a consistent trend where smaller rings are linked to peaks at higher frequencies. Peaks below ~350 cm^{-1} have been attributed to cation motions[345], and are not included in this study.

Most researchers have relied solely on silicate glass assignments to interpret Raman peaks in silicate solutions, linking peaks at 587–606 cm^{-1}, 453–550 cm^{-1}, and 400–490 cm^{-1} to 3-, 4-, and 5-membered ring structures (3R, 4R, and 5R), respectively [158,339,346]. They have attributed the remaining peak at 515–535 cm^{-1} to O-Si-O stretching vibrations in linear chains with more than five Si atoms, referring to a study on TMOS[363]. However, the presence of such long chains is inconsistent with NMR results and therefore, may not be accurate. We believe that just as crystals cannot fully represent the vibrational modes of glass, neither can glass or alkoxides fully represent the vibrational modes of silicate species in the dynamic liquid medium of waterglass. On the bright side, while glass forms a fully connected network, making it challenging to distinguish individual structural units, NMR studies have enabled us to identify major silicate structures in solutions. As shown in Figure 4.24c, these structures are not limited to just 3-, 4-, or 5-membered rings. Many of the possible silicate structures are cage-like or involve double-ring structures rather than simple "rings". For example, of the 45 structures in Figure 4.1c, there are: 7 structures containing 3-membered rings; 10 with 4-membered rings; 16 containing both 3- and 4-membered rings; 5 with 5-membered rings, and only one with a 6-membered ring.

Zeolites, which are porous hydrated aluminosilicate minerals containing alkali and alkaline-earth metals, also consist of SiO_4 tetrahedron units. The low-frequency region in zeolite literature is known to contain characteristic siloxane ring-related Raman vibrations[352,353,376]. Zeolites are helpful in this context because, they contain both silicate rings and double ring structures, and their well-characterized structures offer more clarity than the less defined forms found in silicate glasses. However, this aspect has been less explored in silicate solutions and gels. Similar to glasses, smaller rings have been corresponded to higher frequencies in Raman spectra of zeolites: peaks in 470-530 cm^{-1}, 370-430 cm^{-1}, 290-410 cm^{-1}, and 225-280 cm^{-1} have been assigned to T-O-T (T occupied with Si/Al) bending motions in 4R, 5R, 6R, and 8R respectively[354,377]. This assignment is based on an inverse correlation between the Raman shift and the T-O-T angles (or ring size) observed in synthetic zeolites[378]. If we extend this correlation, the 3-membered ring bending mode should occur in the frequency range of around 550-600 cm^{-1}, aligning with Raman experiments on 3-membered aluminosilicate rings[355,379] and silicate glasses[158,339,346]. According to NMR data, 3- and 4-membered rings are expected to be dominant species in silicate solution, with a low probability of 5- and 6-membered rings, and no larger rings. Therefore, our focus is primarily on 3- and 4-membered rings in the form of single, double, and cage structures.

The cage-shaped hydrogen silsesquioxanes, of general formula $(HSiO_{3/2})_{2n}$, n = 2,3,4, etc., which here are referred to as double ring structures, are appealing molecules for studying vibrational properties of silica cage structures and serve as molecular models for the building units found in zeolites. Bornhauser and Calzaferri[351] studied the vibrational spectra of the molecular models of $(HSiO_{3/2})_{2n}$, n = 2,3,4,… and introduced the so-called *ring opening* vibrations as simultaneous, in-phase displacement of all Si-O stretching and/or O-Si-O bending, with respect to the ring main axis. This type of vibration is characterized by a change in the size or shape of the ring, leading to an opening or widening of the ring structure. They reported that the Raman-active mode of double 4-membered ring (D4R) pore opening appears in the range of 420–455 cm^{-1}, consistent with computational modelling studies[380]. The differentiation between double ring (DR) and single ring (SR) structures using Raman spectroscopy presents a challenge. In a study by Inagaki et al.[353] on a BAE-type of zeolite, peaks at 462 cm^{-1} were assigned to single 4-membered rings (S4Rs) and peaks at 495 cm^{-1} were assigned to D4R. These assignments were based on comparisons with Raman spectra of SOD- and LTA- type zeolites, which contain mainly S4R and D4R as their structural building units, respectively. Moreover, they inferred that the broad peak around 530 cm^{-1} indicated the presence of sterically distorted 3- or 4-membered rings. These distorted structures could resemble many species in WG. Data on the Raman spectroscopy of double three-membered rings (D3R) is rare due to the scarcity of such structures in synthesized zeolites[381].

Halasz et al. conducted a series of studies on the molecular structure of sodium silicate solutions and gels using Raman spectroscopy, considering double ring structures [165,338,340]. They assigned the band at 485/495 cm^{-1} to D4R, D5R, and D6R siloxane rings; the band at 534/605 cm^{-1} to 3-membered rings; 375 cm^{-1} to 5-membered rings; 480/630 cm^{-1} to 4-membered rings; and 330/428 cm^{-1} to 6-membered rings. However, their overall assignment for single rings does not follow the expected inverse correlation between wavenumber and ring size. Moreover, they assigned all double ring structures to a peak around 490 cm^{-1}, based on the average of the ring-related molecular vibration data from the literature on zeolites. However, relying solely on average assignments can be misleading due to scattered data from different studies. The peak position of a given siloxane ring or double ring can vary based on the vibrational modes (breathing, ring opening, pore opening) and the Si/Al ratio of the aluminosilicate/zeolite. When assigning peaks, considering the correlation between bond angles, ring/double ring structures, and vibrational modes with peak positions (wavenumbers) is essential. The question remains: Does the inverse correlation between ring size and wavenumber apply to double ring structures in the same manner as it does for simple rings? Exploring experimental and computational[382,383] studies, we could not establish a consistent correlation between double ring size and wavenumber across all of them. This lack of clarity doesn't necessarily indicate the absence of a relationship; it may stem from limitations in the accuracy of calculations or ambiguities in experimental peak assignments.

In spring and ball models, when the balls are heavy or the spring is soft the system vibrates in the lower frequency and when the balls are light or the spring is hard, the system vibrates in a higher frequency. The same phenomena happen with molecule vibration; wider bond angles or longer bond lengths generally result in weaker bonds or softer vibrational modes, which correspond to lower vibrational frequencies/wavenumbers. Conversely, lower order structures with their potentially lower Si-O-Si bond angles, would result in stronger bonds or stiffer vibrational modes, leading to higher vibrational frequencies/wavenumbers. If we apply this general rule to the species found in silicate solutions, as observed in NMR studies, most of them are cage-like species consisting of combinations of 3-, 4-, and 5-membered rings rather than pure simple or double ring structures. These species can be divided to 3-membered ring structures, 3,4-membered ring structures, 4-membered ring structures, and 5-membered ring structures, based on the dominant type of ring present in the structure. Therefore, for example, a 3R in this study does not refer strictly to simple 3-membered rings but rather to species that primarily contain 3R in their structure, including a simple 3-membered ring (refer to Figure 4.1c for further clarification). These assignments include pure double ring structures as well, as they also involve combinations of different rings; for instance, D3R contains both 3R and 4R and therefore belong to 3,4-R group, and D4R consists solely of 4R, and therefore belong to 4R group. This insight suggests a fresh approach to interpreting Raman spectra for silicate solutions, rather than simply relying on the commonly cited peaks assigned to glasses or crystalline materials. In the low-frequency region, as we move from high to low frequency, we assign peaks at 594 cm^{-1} to 3R, 534 cm^{-1} to 3,4R, 471 cm^{-1} to 4R, and 438 cm^{-1} to 5R. Moreover, these assignments align well with the general trend seen in both glasses and zeolites. While we may not be able to distinguish between specific species (whether simple, double, or intermediate structures), we can confidently say that as we move towards lower frequencies, the complexity and size of polymerized species increase. Although this interpretation is not quantitative, we believe that comparing the spectra of solutions with gels made under different conditions can provide invaluable insights into the differences in their structures, especially when coupled with other observations made via different experimental characterizations of the gels.

Therefore, based on the Raman spectrum of WG in Figure 4.2a, we can conclude that there is no single dominant structure present in our solution. Instead, the initial solution is a mixture of different cage-like structures with mainly Q^3 connections.

It should be noted that the Raman signatures of the monomer, dimer, and linear trimer and tetramer have also been identified through experimental and theoretical studies[324,327]. The dimer is observed at ~600 cm^{-1}, the trimer at ~580 cm^{-1}, and the linear tetramer at ~540 cm^{-1}. These peaks overlap with those assigned to different ring structures, and Raman spectroscopy is insufficient to distinguish between peaks from different groups. However, since we primarily have Q^3 groups and a low probability of linear species, we have not included them in our peak assignment.

4.5.2. Effect of waterglass dilution

The Raman spectra of WG in its original state and when diluted to different waterglass:water weight ratios are displayed in Fig. 2b. The most significant change with increasing water content is the increase in the intensity of the peak at 779 cm^{-1}, along with decreases in the intensities of the peak at 1043 cm^{-1}. Moreover, the Q^1 displays a broader, noisy peak upon dilution. This change may be due to Q^1 connections that mainly exist as branches/ending groups to cage-like structures, which provides them with more steric freedom. This freedom allows for varied bond angles and, subsequently, different types of vibrations, creating a broader and noisy peak.

Quantitively, as shown in Figure 4.2c, upon diluting WG up to a 1:5 waterglass:water weight ratio (equivalent to decrease in silica concentration from 50 to 15%), the concentration of Q^0 increases from 2% to 21%, Q^1 increases from 7% to 18%, Q^2 decreases from 20% to 15%, and Q^3 decreases from 70% to 45%. These changes indicate depolymerization of silicate species with waterglass dilution, consistent with trends observed in these solutions in other studies[149,220,264]. Specifically, the decrease in both Q^3 and Q^2, along with an increase in Q^0 and Q^1, indicates depolymerization of structures containing both Q^3 and Q^2. Based on these observations, we propose the reactions depicted in Figure 4.4 to occur upon diluting waterglass.

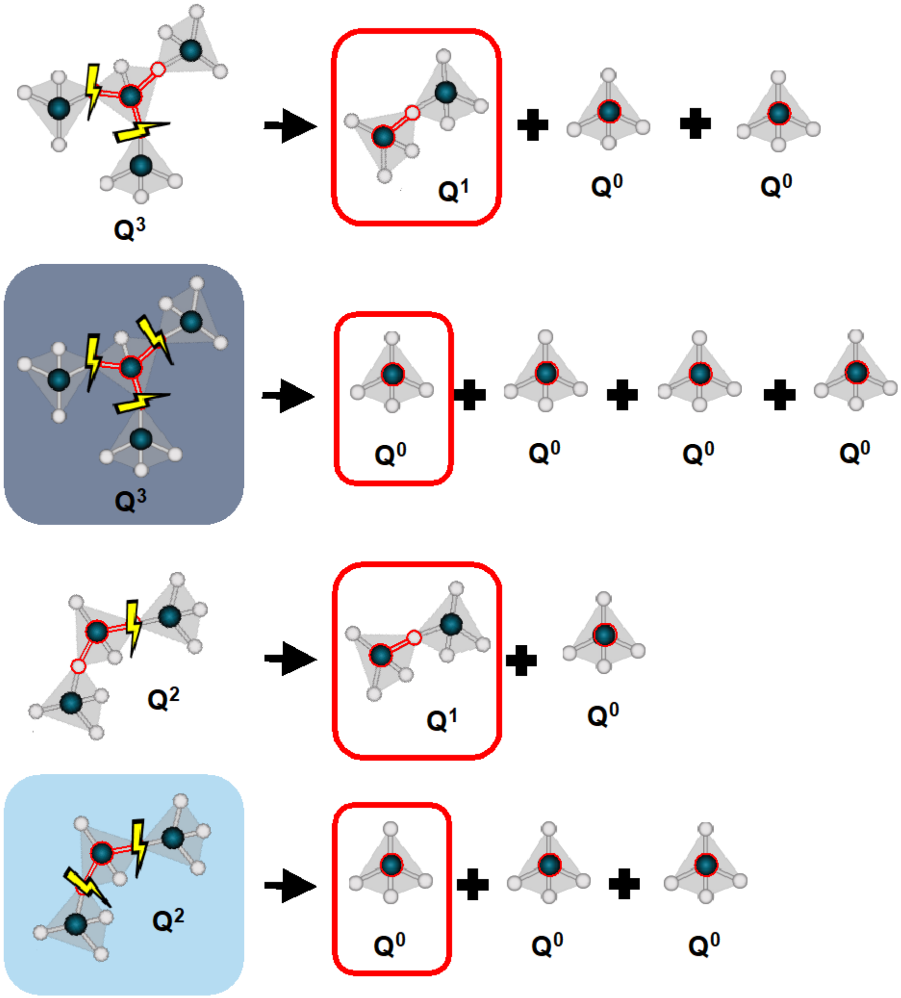

Figure 4.4 A schematic of the proposed depolymerization reactions occurring upon diluting waterglass, showing the conversion of Q^2 and Q^3 to Q^1 and Q^0. The yellow zig-zags represent hydrolysis of Si-O-Si bonds during depolymerization. Note: the depicted species might be a part of a larger structure. After depolymerization, only the Q-connectivity type of the central tetrahedron is definite (framed in red), while the Q-connectivity of the neighboring tetrahedra depends on the structure to which they belong.

Diluting sodium silicate solution leads to depolymerization through increased dissociation of Na^+ ions and hydrolysis of Si-O-Si bonds. The dissociation of sodium ions weakens the electrostatic interactions that help stabilize the silicate network. As sodium ions dissociate, they leave the silicate species more vulnerable to attack by water molecules. The hydrolysis process breaks the Si-O-Si bonds, facilitating the depolymerization of silicate chains into smaller units or monomers. Additionally, the added water molecules drive away the silicate species, decreasing the probability of forming crosslinks (either physical or chemical) between chains, and thus enhancing the effect of dissociation.

Examining the changes in structures obtained from the low-frequency region, the most significant observation is the increase in 5-membered rings (5R) and the decrease in 4-membered rings (4R) upon dilution. Since no polymerization is occurring (as indicated by changes in Q-connectivity), we can conclude that partial depolymerization of cage-like structures is happening. This depolymerization leads to the opening of the cage structure, leading to increase in Si-O-Si bond angles and causing the vibrations to shift to lower wavenumbers. This shift highlights the importance of interpreting the Raman spectra by connecting results from both the low- and high-frequency regions.

It should be noted that in Figure 4.4, we are only focusing on one type of connectivity of SiO_4 tetrahedron (highlighted in red) as part of a larger structure. While we can be confident about the type of connectivity that specific tetrahedron converts to after depolymerization (framed in red), the Q-connectivity of the neighboring tetrahedra will depend on the structure to which they belong.

4.5.3. Real-time sol-gel transition

Raman spectra recorded during the sol-gel transition at 2-minute intervals, starting from 2 minutes after mixing 1:1 waterglass solutions with phosphoric acid and boric acid, up to 8 minutes after gelation, are shown in Figure 4.5a. At first glance, we can make three general observations: (1) significant difference in the overall spectrum of sol/gels made at different conditions; (2) significant difference between the overall spectrum of sol/gels compared with the initial WG solution before adding acid initiator; (3) no significant change in the overall spectrum of sol/gels over time (before, at, or after the gelation point). The same trend was observed for sol-gel transition at other waterglass:water weight ratios (see Supplementary data).

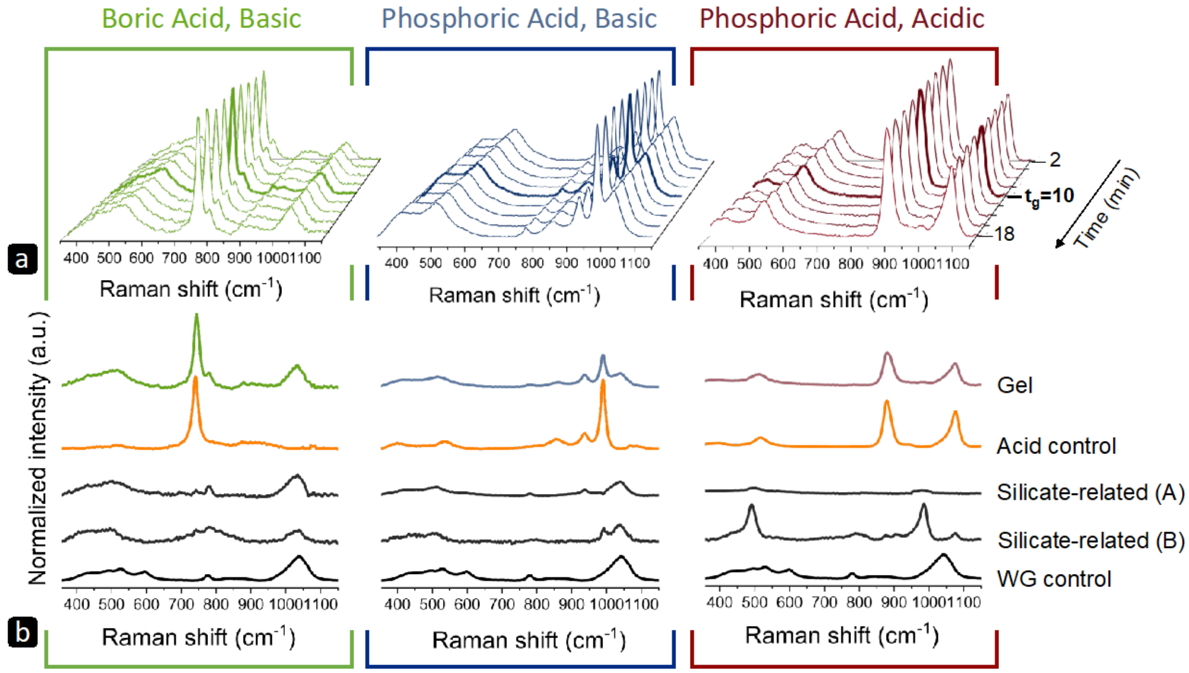

Figure 4.5 (a) Real-time Raman spectra of 1:1 waterglass solutions mixed with boric acid (pH~10.6) and phosphoric acid (pH~10.6, pH~3.3), recorded from 2 minutes after mixing up to 8 minutes after gelation. The gelation point (~10 minutes) is shown in bold. (b) Raman spectra of basic gels made with boric acid and phosphoric acid, and acidic gels made with phosphoric acid, with their respective acid control solutions, silicate-related peaks obtained from methods (A) and (B) (see Section 3.4), and the 1:1 waterglass control solution.

These observations indicate that any chemical changes at the molecular level occur *immediately* (< 2 minutes) after mixing the initial waterglass solution with the acid-initiator, with no further chemical changes as time progresses up to or after the gelation point. Because we started acquiring the *in situ* Raman spectra 2 minutes after mixing, we could not follow the transition of initial solution at the exact time of introducing the acid-initiator. Regardless, the lack of any changes at/close to the gelation point suggests two possibilities: (1) either the gel forms by agglomeration of existing silicate particles through physical interactions such as van der Waals forces, hydrogen bonding, or Coulombic interactions; or (2) the creation of new chemical bonds and aggregates during gelation is too minimal to be detected by Raman. In either case, the results indicate that the formed gels are primarily "physical" rather than "chemical".

To compare the silicate species and structural differences in gels formed under different conditions using the deconvoluted spectra, we must account for the fact that peaks in these spectra are not solely from silicate species. The addition of acid-initiators, such as PA (containing phosphate groups) or BA (containing borate groups), also generates peaks. Therefore, to accurately compare the structure of gels formed under different conditions, we must first differentiate and eliminate peaks arising from the acid-initiator and isolate the silicate-related signals.

4.5.4. Isolating silicate-related peaks

To identify the peaks coming from the acid initiator and isolate the silicate-related peaks in the Raman spectra of the gels, we used two different methods (Figure 4.6):

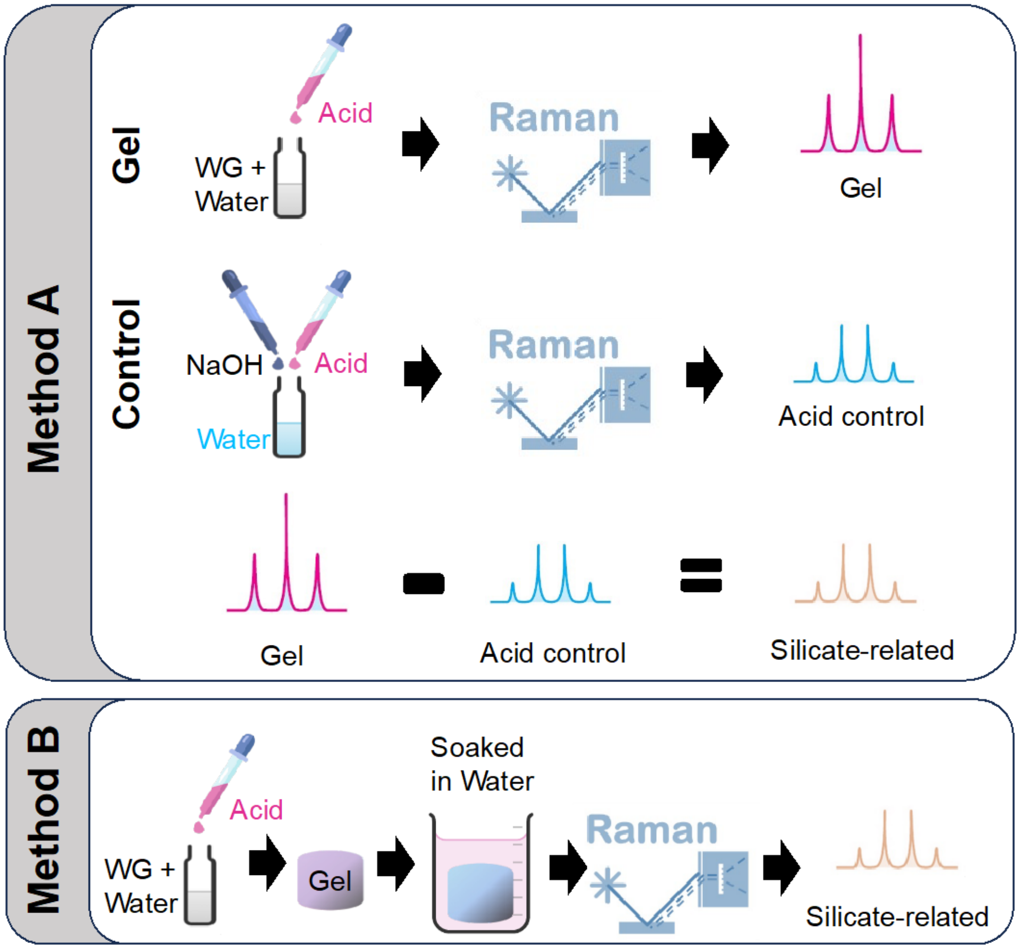

Figure 4.6 A schematic of the steps involved in Methods (A) and (B) to identify and eliminate the peaks coming from the acid-initiators and isolate the silicate-related peaks in the Raman spectra of the gels. Method A involves independent Raman spectra collection of controls, and subsequent subtraction of control spectra from gels,

whereas Method B involves soaking the gel in water to create an osmotic gradient to remove excess unreacted acid from the gel.

Method A: We collected the Raman spectrum of the gels and acid control solutions containing water, the acid solution, and sodium hydroxide (pH adjusted to match each gel). Then, we subtracted the spectrum of acid control solution from that of the final gel to get the silicate-related peaks.

Method B: We collected the Raman spectrum of gels after soaking in DI water and rinsing with DI water to remove any remaining acid-initiator in the gel pores via osmosis, and then collected the Raman spectrum to obtain the silicate-related peaks only.

In Figure 4.5b, the Raman spectra of acidic and basic silica gels made with PA, as well as basic silica gel made with BA, are compared with the initial WG solution, acid control peaks, and silicate-related peaks obtained from methods A and B. By comparing the spectra of gels with acid control peaks, we see that the most intense peaks in the gels actually originate from the acid-initiator rather than the silicates. These peaks include the 950 cm^{-1} peak for the basic PA gel, the 900 and 1080 cm^{-1} peaks for the acidic PA gel, and the 750 cm^{-1} peak for the basic BA gel. One might expect to see the same acid-related peaks in acidic and basic PA gels since both contain PA as gelation-initiator. However, PA (H_3PO_4) is a triprotic acid, and variations in pH alter the relative concentrations of its four protonated forms: H_3PO_4, $H_2PO_4^-$, HPO_4^{2-}, and PO_4^{3-} [384]. The Raman peaks associated with each of these species, the pH ranges in which they are present, and their intensities at each pH are shown in Figure 4.7a. Based on this graph, we can attribute the peak at 950 cm^{-1} in basic PA gel to PO_4^{3-}, and the peak at 900 and 1080 cm^{-1} in acidic PA to H_3PO_4 and $H_2PO_4^-$, respectively. Similarly, boric acid species are pH-dependent (Figure 4.7b). The borate monovalent anion $B(OH)_4^-$ dominates at higher pH, while nonionized boric acid $B(OH)_3$ is prevalent at lower pH. Between pH 6 and 11 and at high concentrations, highly water-soluble polyborate ions such as $B_3O_3(OH)_4^-$, is also formed[385]. According to a Raman study on boric acid and sodium hydroxide solution[386], the peak at 750 cm^{-1} in the spectrum of basic BA gel is attributed to $B(OH)_4^-$.

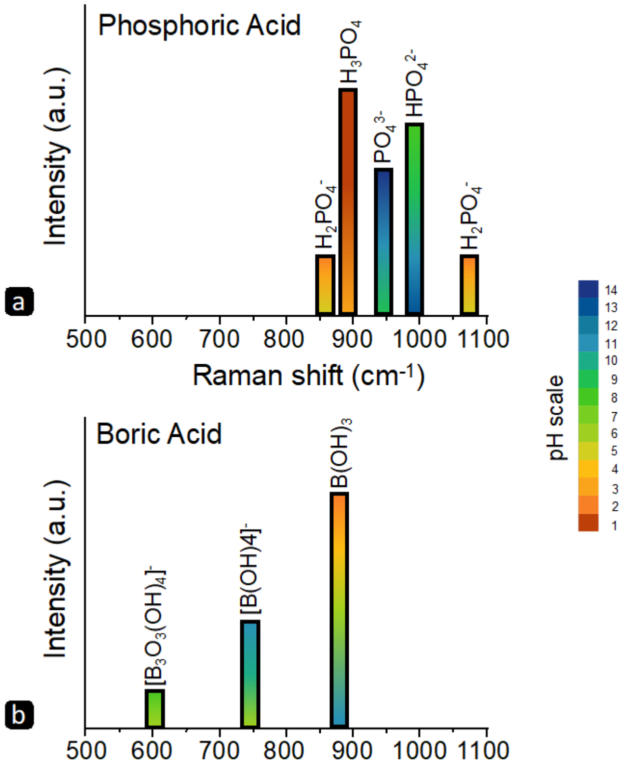

Figure 4.7 (a) Raman peaks in 1.0 M phosphoric acid solutions at different pH levels, attributed to its various protonated forms, based on data from ref [277]. (b) Raman peaks in 40 g/L boric acid solutions at different pH levels, attributed to its various protonated forms, based on data from ref[387]. Based on this graph, we can attribute the peak at 950 cm^{-1} in basic PA gel to PO_4^{3-}, and the peak at 900 and 1080 cm^{-1} in acidic PA to H_3PO_4 and $H_2PO_4^-$, respectively.

Comparing the silicate-related peaks of the final gels obtained from methods A and B in Figure 4.5b, for basic gels the spectra obtained from methods A and B are similar; however, in the case of the washed gels (method B), some acid-related peaks remain, particularly in the PA acid gel where a significant amount of acid was used. These acid-related peaks might be further reduced by continued washing of the gels, though this method involves trial-and-error to determine the optimal soaking duration. Additionally, prolonged soaking may cause the gels to dissolve back into water.

Method A eliminates the uncertainty of determining the point where the gel has been adequately washed in method B. However, we might not capture all the peaks in the subtracted spectrum with method A because acid-related peaks are generally much more intense, and silicate-related peaks might be too weak or masked to be detected. An example of this issue is exemplified for the peak at 500 cm^{-1} in the PA acidic gel, which is much more intense in the washed gel spectrum (method B) compared to the subtracted spectrum from method A. Therefore, we suggest using both methods complementarily (that is, using method B for deconvolution and method to identify and substract possible remaining acid peaks).

4.5.5. Structure of gels

4.5.5.1. Molecular structure

Effect of pH

Figure 4.8a displays the normalized intensity of each Q-species, calculated from the area under the peaks in the high-frequency region of the deconvoluted silicate-related spectrum of gels. Regardless of the type of acid used and the initial WG concentration, basic gels are primarily composed of Q^3 (~53-80%), Q^2 (~10-17%), and Q^0 (~5-34%) units. In contrast, acidic gels are composed mainly of Q^2 (~62-80%) and Q^0 (~20-38%) units. Q^1 units were only detected in PA 1:5 and BA 1:5 basic gels, which initially had the highest Q^1 concentration. To track changes in Q-species during the sol-gel transition, the change in intensity of Q peaks relative to initial WG solution was calculated, as shown in Figure 4.8b. Overall, the changes in acidic gels are more significant, with basic gels showing a distribution of Q-species closer to their initial solutions. In acidic gels, all Q^3 and Q^1 species were consumed (equivalent to -100% in Figure 4.8b) and depolymerized, generating Q^2 and Q^0 species. In basic gels, most Q^1 was consumed, except for PA 1:5 and BA 1:5, and some Q^3 was generated, with changes in Q^2 and Q^0 being insignificant.

Figure 4.8c displays the normalized intensity of ring structures, calculated from the area under the peaks in the low-frequency region of the deconvoluted silicate-related spectrum of gels. If we categorize the ring structures into lower-order (3R and 3,4R) and higher-order (4R and 5R) structures, basic gels mainly contain higher-order rings (~60-72%) and no 3R, whereas acidic gels primarily consist of lower-order rings (~70-80%) and no 5R. Comparing the ring structures after gelation with the initial solution, the most significant change in acidic gels is the depolymerization of all 5R and some of 3R structures and the formation of new 3,4-membered rings (Figure 4.8d). In basic gels, all 3R structures are transformed into new 3,4- and 4-membered rings.

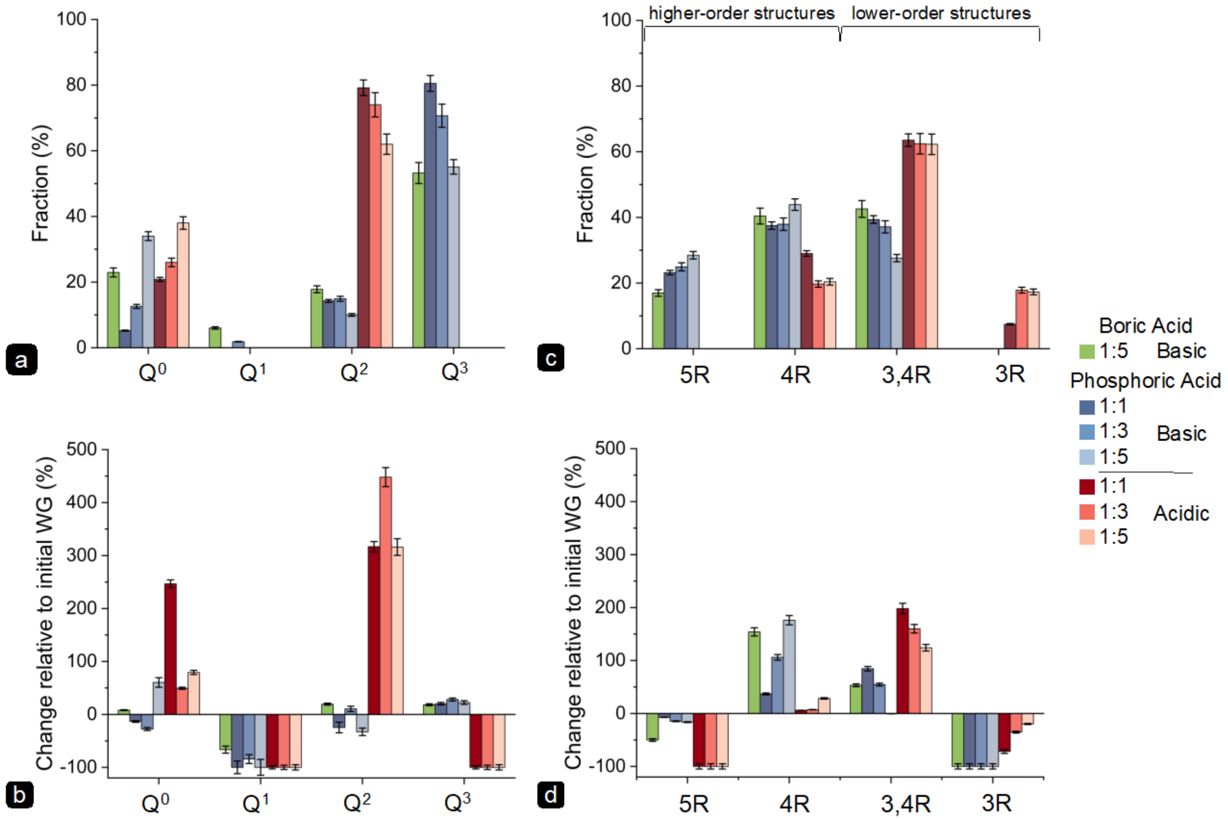

Figure 4.8 (a) Fraction of different Q species present in basic and acidic gels made with phosphoric acid, and basic gels made with boric acid and phosphoric acid, with varying initial waterglass concentrations. (b) Change in the fraction of different Q species in gels relative to their amounts in the initial waterglass solution. (c) Fraction of different ring structures present in basic and acidic gels made with phosphoric acid, and basic gels made with boric acid and phosphoric acid, with varying initial waterglass concentrations. The ring structures are divided into lower-order and higher-order structures based on their degree of connectivity and polymerization. (d) Change in the fraction of different ring structures in gels relative to their amounts in the initial waterglass solution. The results show the dominance of Q^3 connections and higher-order structures in basic gels and dominance of Q^2 and lower-order structures in acidic gels. The error bars represent one standard deviation from the mean (N=3).

In a highly basic environment of waterglass, the high concentration of hydroxide ions (OH$^-$) deprotonates the non-bridging oxygens (NBOs) on silicate species, making charged species that are stable in solution (Figure 4.9a). Now, putting all the pieces of information obtained from Raman and considering the possible silicate structures from Figure 4.1c, we can propose chemical reactions happening upon acidification in basic and acidic gels.

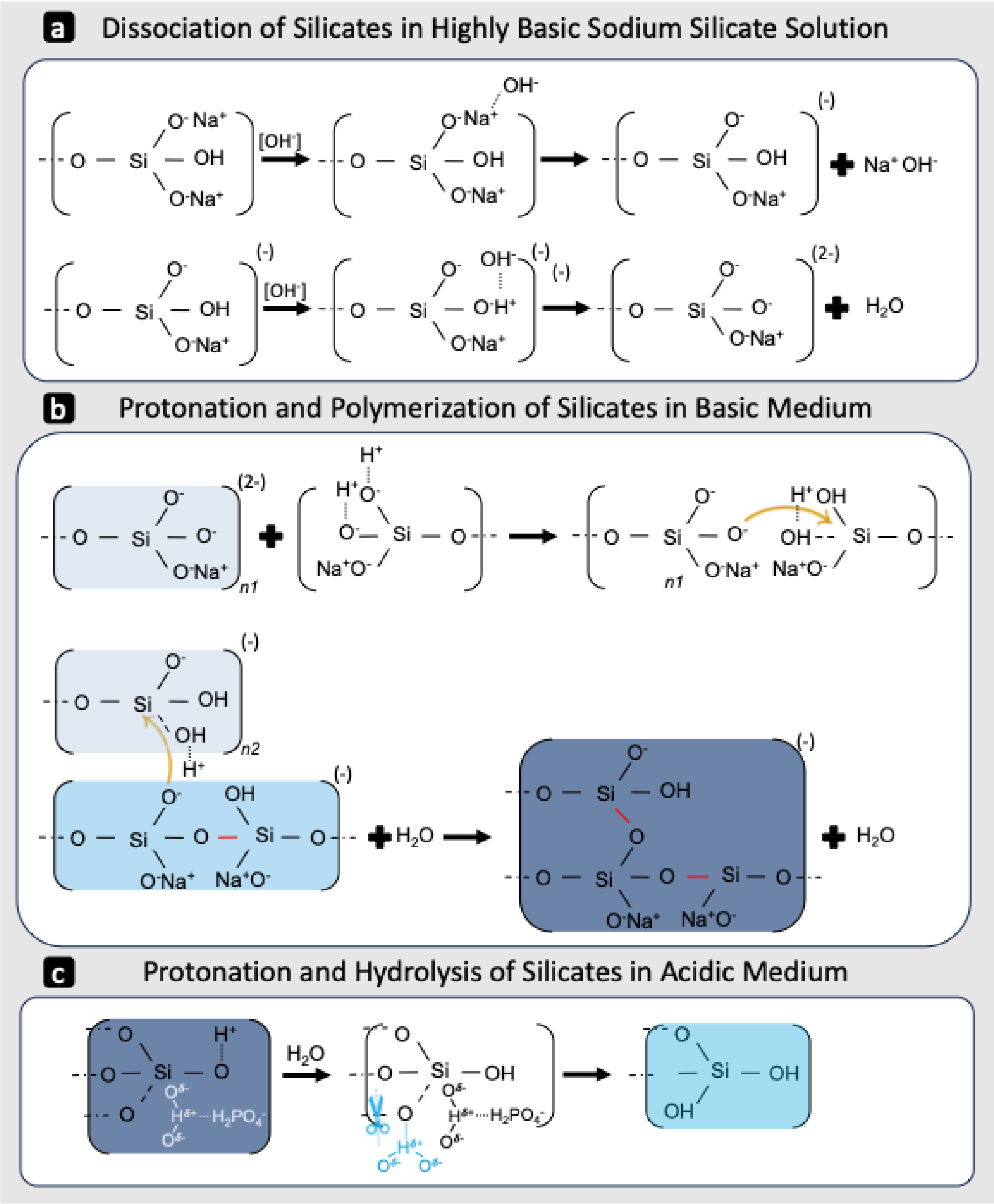

Figure 4.9 (a) Dissociation of Silicate Species at high alkaline pH. Elevated hydroxide ion (OH$^-$) concentrations displace sodium ions from the non-bridging oxygens (NBOs) in silicate species, leading to the formation of stable charged species in solution. (b) Polymerization of Q^1 species to Q^3 upon acidification in a basic medium: acidification converts some silanolate ions (Si-O$^-$) to silanol groups, which then form SiOSi bonds and Q^2 connecitities. These Q^2 species then quickly connect with other reactive parts or Q^1 units to form Q^3. (c) Depolymerization of Q^3 species to Q^2 upon acidification in acidic medium. increased proton concentration (H$^+$) protonates the oxygen atoms in Si-O-Si bonds, enhancing silicon's electrophilicity and making it more susceptible to nucleophilic attacks by water. Phosphoric acid may further facilitate Si-O-Si cleavage by forming hydrogen-bonded water complexes.

For basic gels: from Figure 4.8c, we observed that almost all Q^1 species are converted to Q^3, as a result of conversion of all initial 3-membered rings or dimers to 3,4- and 4-membered ring structures. If we examine the 3R group in Figure 4.1c, 7 out of 9 of these species have dangling Q^1 groups. Q^1 units, present as dimers or the ending units of 3R structures, act as reactive sites, connecting to other silicates and creating higher-order structures. Q^1 units are initially connected via one siloxane bond to the rest of the structure and have three NBOs. The transformation of a Q^1 unit to Q^3 upon acidification requires the creation of two new Si-O-Si bonds. Although forming two bonds at once is usually considered unlikely, the scenario where all Q^1 units are consumed and only Q^3 units are formed without the formation of Q^2 can be explained by considering the specific structural rearrangements and reaction conditions that favor direct transitions. After introducing acid while still in the basic region, a small portion of deprotonated species becomes protonated again, reducing the electrostatic repulsion and increasing their reactivity. The silanolate ion ($Si-O^-$) is highly nucleophilic and can react with a silanol group, forming a transition state where the oxygen of $Si-O^-$ is bonded to silicon, and the OH group is partially detached. To stabilize the transition state, a proton (H^+) is transferred to the leaving hydroxyl group, facilitating the formation of the siloxane bond (Si-O-Si). Once a Q^1 unit forms a single bond, it immediately forms another bond before stabilizing as a Q^2 unit (Figure 4.9b). This process can be seen as a nearly simultaneous two-step reaction facilitated by the high reactivity and close proximity provided by the cage-like structure. Thus, Q^1 units rapidly form Q^3 units by connecting to other reactive parts of the structure or other Q^1 units. As a result, bulkier structures that vibrate at the same wavelength as 3,4- and 4-membered rings are formed. These structures could be literal 3,4- or 4-membered rings (as defined in Figure 4.1c), or they might be bulky structures with bond angles wider and closer to 4R due to steric hindrance. It should be noted that the condensation reactions also depend on the size of the alkoxy group; the reactivity of silicates decreases as the size of the silicate group increases due to steric hindrance. This size dependency explains why polymerization predominantly occurs for 3R structures. Moreover, our result is in agreement with the general Ostwald ripening theory in which larger particles grow at the expense of smaller particles, especially in strongly alkaline solutions where the latter dissolve more readily. This change in particle size distribution results from the tendency of the smaller particles to condense, or redeposit, on the surfaces of the larger particles[388].

For acidic gels: significant depolymerization occurs upon the addition of acid, converting all Q^3 species to Q^2 and all Q^1 to Q^0, increasing the intensity of Q^2 and Q^0 up to 5 times more than initial waterglass. This change is correlated with conversion of all 5R and some of 3R to 3,4- and 4-membered ring structures. Structures in 5R groups are prone to depolymerization due to wide angles which make them less thermodynamically stable in contrast to 4R rings. 3R rings are also less stable than 4R because the SiOSi angles are strained, and their optimum configurations are necessarily restricted to be nearly planar[389]. The absence of Q^3 connections means the structure lacks double-ring or closed-cage formations, resulting in either plain rings or distorted/broken lower-order cage structures. The acidic environment introduces a high concentration of protons (H^+), that protonate the oxygen atoms in the Si-O-Si bonds, initiating hydrolysis. Hydrolysis occurs when water's oxygen nucleophilically attacks the silicon atom. Protonation significantly lowers the energy barriers for siloxane bond cleavage by enhancing silicon's electrophilicity, thereby increasing its susceptibility to nucleophilic attack by water[390]. The hydrolysis of Si-O-Si bond is generally understood to proceed via nucleophilic displacement reactions involving penta-coordinate intermediates or transition states[170,391]. For example, the conjugate base of HF acid, F^-, which are about the same size as OH^- can increase silicon's coordination to five. However, in the case of H_2PO^{4-}, the negative charge is delocalized over the entire phosphate group, making it less nucleophilic and less likely to form penta-coordinated silicon. Additionally, steric hindrance further impedes this process. Hydrogen-bonded water complexes, which may contain water, silanol, and acid, could also play a crucial role in facilitating proton transfer from nucleophiles to leaving groups[390]. These water cluster-siloxane hydrogen bond complexes reduce the energy barrier for siloxane bond cleavage, particularly as the number of water molecules in the hydrogen-bonded cluster increases. Therefore, phosphoric acid may facilitate Si-O-Si cleavage by forming some type of hydrogen-bonded water complex. Thus, we conclude that the siloxane bond breaks when its bridging oxygen is attacked by a proton, weakening the strength of the Si−O bonds. The proton donator could be water or phosphoric acid-water complex as illustrated in Figure 4.9c, which is in agreement with molecular dynamic study by Yue et al[392]. Therefore, lower pH values promote the growth of smaller particles.

Effect of silica concentration and type of acid

As the concentration of waterglass decreases, Figure 4.8a shows a decline in Q^3 and an increase in Q^0 for basic gels, while acidic gels exhibit a decrease in Q^2 and an increase in Q^0. Initially, more concentrated waterglass solutions contained higher Q^3 and lower Q^0 levels compared to less concentrated solutions. Thus, in basic gels, the proportion between Q^3 and Q^0 remains constant, whereas in acidic gels, the proportion exists between Q^2 and Q^0, as the initial Q^3 units are converted to Q^2 units. In Figure 4.8c, we observe a decrease in 3,4 R and an increase in 5R in basic gels (indicating more polymerization), and a decrease in 4R and an increase in 3R in acidic gels upon diluting the initial waterglass (indicating more depolymerization). This difference indicates that the presence of more water in the system (i.e., when the WG solution is diluted) promotes reactions occurring in the system, whether it is hydrolysis/depolymerization in acidic media or polymerization in basic media.

Comparing the fraction of species in basic gels made with boric acid to those made with phosphoric acid from Figure 4.8a and Figure 4.8c, we observe that while the distribution is generally similar to other basic gels, it does not specifically resemble any particular one. Therefore, we can conclude that the type of acid used does not significantly alter the gel's behavior. However, when a large amount of water is introduced into the system, predicting the structure becomes more challenging. This finding is consistent with our previous observations regarding the optical properties and the gelation time dependency on pH in these gels[118].

4.5.5.2. From particles to agglomerates to gel network

The hydrolysis and polymerization reactions are competing processes in all sol-gel systems, and their rates depend on pH. Depending on which process predominates, different structural silicate units with varying degrees of connectivity and polymerization will form. The type of structural units directly affects the size of the particles forming, and the arrangement of these particles during agglomeration, and eventually the network structure, which then directly affects the final gel properties. The presence of colloidal-size particles in waterglass was demonstrated in our previous study by exhibiting the Tyndall effect. Moreover, from our previous results on light transmittance and scattering during the sol-gel transition of waterglass, although we could not quantitatively measure the particle size, it was shown that basic gels contain larger particles compared to acidic ones, leading to more light scattering. From Raman results, we observed that at the molecular level basic gels are composed of silicate units with a higher degree of connectivity, which vibrate at lower wavelengths compared to acidic gels. Accepting the inverse relationship between vibration wavelength and Si-O-Si bond angle, although we cannot determine the exact type of structural units formed, we can generally say that basic gels contain larger quasi-cage structures in contrast to acidic gels.

However, the question remains: how do these structural units agglomerate into a gel? In solutions starting from monomeric species, such as silicon alkoxides, the answer is clear[326,328]: linear or weakly branched silica species are preferentially formed in acidic conditions, whereas highly branched and clustered silica species are obtained in basic conditions. In alkali silicate solutions, the answer is less certain and not as well explored.

In solutions starting from monomers, gelation happens through the following steps: monomers form oligomers, which then form particles, aggregates/agglomerates, and finally a network. In waterglass, however, there is already a wide range of species, from monomers to oligomers and up to colloidal particles. Researchers have reported a wide range in size of these colloidal particles in waterglass—0.6 nm to 600 nm[146,173]. Looking at the structural units identified by NMR in Figure 4.1c, most of these structures are already at the size of a colloid. For a simple 3-membered ring, for example, we can estimate the length by summing the total length occupied by silicon atoms (diameter = 0.264 nm) and oxygen atoms (diameter = 0.146 nm) and the Si-O bond lengths (~0.163 nm), which gives a total of ~1.6 nm (See Figure 4.10a). Therefore, many of the structural units are bigger than 1 nm, and in the size range of colloidal particles. As a result, there is no need for the formation of new Si-O-Si bonds or Q^4 type connections to consider these structural units as "particles".

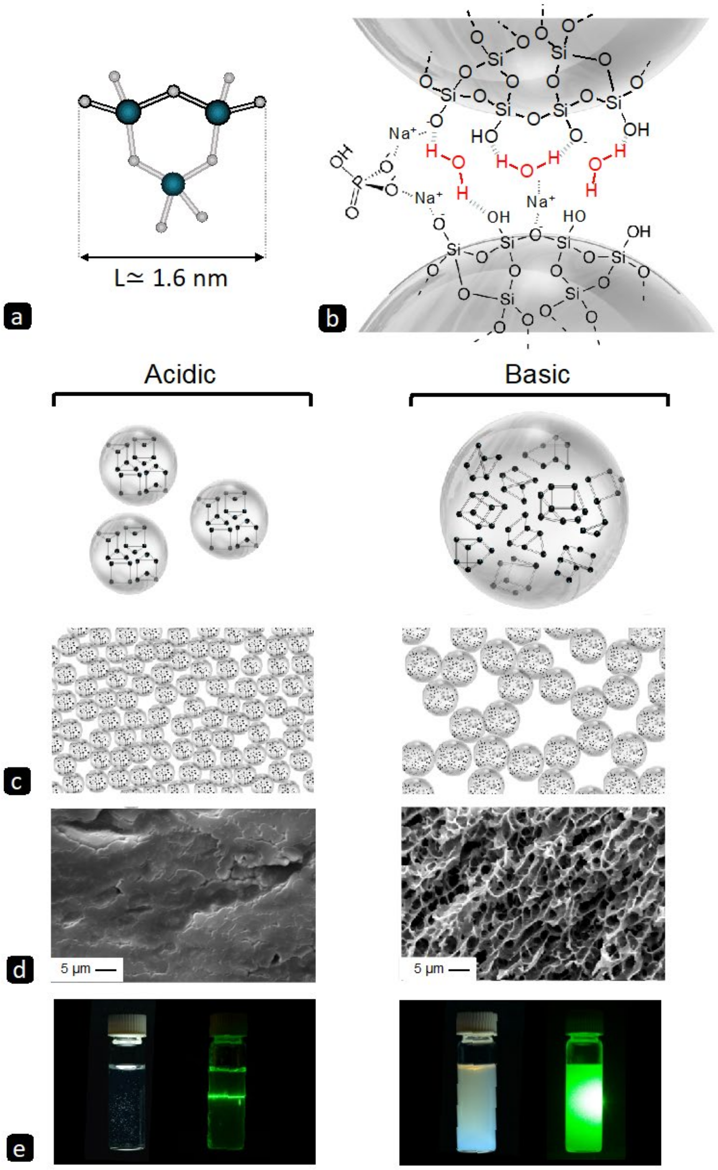

Figure 4.10 (a) Estimating the width of a 3-membered silicate ring structure by summing the diameters of two silicon atoms, three oxygen atoms, and four Si-O bond lengths, yielding an approximate total width of ~1.6 nm. (b) Agglomeration of primary or secondary silicate particles through physical interactions, including hydrogen bonding and electrostatic interactions. (c) A schematic representing that lower-order silicate structural units in acidic gels would result in a compact network of agglomerates with small pores, while higher-order silicate structural units in basic gels would result in a compact network of agglomerates with small pores (d) SEM micrograph of showing compact glass-like structure in concentrated acidic gels (left) and mesh-like network in basic gels (right) (e) Macrograph showing light transmission and light scattering (550 nm laser) of acidic (left) and basic gels (right). The smaller particles and pores in acidic gels lead to significantly less light transmittance and scattering compared to basic ones.

Now, we can imagine that at the same silica concentration, most of the bulky higher-order structural units in basic gels and lower-order structural units in acidic gels are actually colloidal particles. These primary particles may agglomerate, forming larger secondary particles. This concept might explain the wide range of colloidal particle sizes observed in waterglass, because analysis of the light scattering cannot distinguish whether it is the structural unit itself or the agglomeration of primary particles (secondary particles) that is scattering light. When the solution is acidified, more reactive sites are created and electrostatic repulsion decreases, which promotes the agglomeration of secondary particles into a gel. The absence of changes in the Raman spectra during the sol-gel transition (near the gelation point) across different gels suggests that the agglomeration is primarily driven by physical interactions, such as hydrogen bonding or Coulombic interactions, as illustrated in Figure 4.10b. The silica surface silanol groups are the main centers of adsorption of water molecules, which result in formation of hydrogen bonding. Sodium cations and anions from acid can also be picked up during the silica gel formation may be trapped inside the secondary particles or agglomerates. Since silanol groups become more protonated in acidic conditions and more acid is introduced in acidic gels, more physical bonding is expected compared to their basic counterparts.

The nature of physical or chemical nature of silica gels is somewhat ambiguous in the literature. Some researchers argue that silica gels are physical in nature[393–395]. For instance, Wang et al.[393] noted that the rheological properties of basic silica gel made from waterglass show several similarities to physical gels and weak colloidal gels, such as the logarithmic time-dependent growth of storage modulus, which is usually attributed to bond reversibility. Tognonvi et al. [265] have reported the formation of both reversible and irreversible silica gels in a basic medium and defined regions based on [Si] and pH. Our gels would fall into their irreversible gels category. However, their classification is primarily based on the behavior during syneresis, which may or may not relate to the physical or chemical nature of the gels. Reversibility versus irreversibility could be due to the number of hydrogen bonds formed and the pore size, affecting the rate of syneresis. Moreover, chemical bonds may start to form after syneresis when particles get closer to one another.

The formation of physical gels, mainly by hydrogen bonding, without the formation of new Si-O-Si bonds (as seen in acidic gels), might seem to contradict Iler's prerequisite for gelation: "The basic step in gel formation is the collision of two silica particles with sufficiently low charge on the surface that they come into contact, forming siloxane bonds that hold the particles irreversibly together" (ref[102], p.366). However, this classical gelation theory is based on starting from monomers, and again, it is not a good analog to be used for alkaline silicate solutions. Hydrogen-bonded structures likely serve as the basis for silica hydrogel formation because the activation energy is low, and entropy considerations are lessened due to fewer geometric restrictions[396].

Overall, we can conclude the following about particle formation, agglomeration, and network formation in acidic versus basic gels at constant silica concentration:

The lower pH in acidic gels means more silicates at the surface of structural units are protonated, and therefore, more reactive sites are available compared to basic gels. Moreover, the smaller size of primary particles in acidic gels provide higher surface area for physical interactions that lead to agglomeration. Both the smaller size of primary particles and more reactive sites in acidic gels facilitate the approach of particles due to less steric hindrance and electrostatic repulsion. As a result, small primary particles in acidic gels make compact small secondary particles, forming compact networks whereas basic gels which are made of large primary particles, form loose large secondary particles, leading to loose networks (see Figure 4.10c).

The micrographs of 1:1 basic and acid gels are displayed in Figure 4.10d. As can be seen, while both gels contain the same amount of water, and therefore, expected to have same volume of pores, they exhibit very different microstructures. PA 1:1 acidic gel is dense and compact with small pores that according to its light scattering data should be <550 nm, while the PA 1:1 basic gel has a porous structure with pores around 5 µm. The compact structure of the PA 1:1 acidic gel gives it an almost glass-like appearance that transmits light (Figure 4.10d). The microstructure observed in acidic gels is in complete agreement with the molecular structure obtained from Raman results (composed of small lower-order primary particles) as well as our theory that small secondary particles and tightly packed agglomerates are formed. In contrast, the loose network of PA 1:1 basic gel, with its larger pores, makes it scatter light more effectively, resulting in reduced transmission (Figure 4.10d). The microstructure observed in basic gels is also in complete agreement with the molecular structure obtained from Raman results (composed of large higher-order primary particles) as well as our theory that large secondary particles and loosely packed agglomerates are formed.

There have been previous attempts to experimentally demonstrate distinct differences in the molecular structures of silica gels made under acidic or basic conditions. For example, Kaide and Saeki[397] explained the differences in dynamic rheological properties between acidic and basic alkaline silicate gels by the difference in the size of silica particles. Similar to our findings, they proposed that small primary particles bond with each other to form a minutely homogeneous structure in acidic gels. In contrast, clusters in basic gels are formed by larger particles, resulting in a rougher network. However, they did not explore the underlying chemistry. Using Raman spectroscopy, Halasz et al. [337] reported that the average "n" connectivity of silicate species is higher in the base-set gels than in the acid-set gels. However, they did not investigate the possible reasons or mechanisms behind these structural differences, nor did they explore the relationship between Q-connectivity and ring structures. In another study by Kierys[310] et al. Raman spectroscopy was used to investigate silica gels made under different conditions. By observing substantial differences in the molecular structure of silica gels made at pH 4 and 7.4, they reported that acid-set gels have a loose, flexible composition of siloxane rings and chains with many Q^3 connected [SiO_4] tetrahedra, while the rigid base-set gels have a more compact, dense structure mostly with Q^4 connected tetrahedra. Their results contrast with ours and, according to them, with most previous studies. However, they did not provide any reasons for this contradiction. Overall, we believe that both our study and previous works convincingly demonstrate that the macroscopic physical properties of gels depend on their molecular constitution, which is strongly influenced by the pH at which they are made. Our study stands out as we have provided evidence for the differences between basic and acidic gels at all levels, from the molecular level to the microscopic and macroscopic levels, and have validated the processing-structure-properties relationship in silica gels.

4.6. Conclusion

Real-time Raman spectroscopy was proven useful for quantitatively studying the sol-gel transition in acid-initiated sodium silicate solutions under different processing conditions, such as pH, waterglass concentration, and type of acid initiator. Our research provides new insights into the molecular structure of silicate units, particle formation, and their agglomeration into a network. Additionally, we established connections between processing conditions, structural distinctions, and the optical properties and microstructure of silica gels. Key findings include:

- Re-examination of the commonly cited Raman peaks for silicate solutions and gels revealed that the assignment of Si-O-Si bending modes to plain n-membered ring structures is inconsistent with silicate structures identified by ^{29}Si NMR in these solutions.
- A fresh approach for interpreting the 400-700 cm^{-1} region of Raman spectra was provided based on silicate species identified by ^{29}Si NMR. Silicate structural units were divided into 3-membered, 3,4-membered, 4-membered, and 5-membered rings, encompassing various structures such as cage-like, quasi-cage, simple, and double-ring units, with the complexity and size of polymerized species increasing moving toward lower wavenumbers.
- Most silicate structural units present in sodium silicate solutions are within the colloidal particle size range (>1 nm) and act as primary particles during gelation, indicating that the formation of new Si-O-Si bonds is not necessary for gel formation.
- In acidic conditions, hydrolysis proceeds more rapidly than condensation, leading to depolymerization and the formation of smaller, lower-order silicate units. Conversely, in basic conditions, polymerization dominates, resulting in larger, higher-order units.
- Basic gels are made of large, loose secondary particles that agglomerate into a gel network with large pores, while acidic gels are made of small, compact secondary particles that agglomerate into a dense gel network with small pores.
- Consistent Raman spectra during the sol-gel transition suggest that particle agglomeration is primarily driven by fast-acting physical interactions, such as hydrogen bonding and electrostatic interactions.
- When diluted, the presence of more water in the system promotes hydrolysis/depolymerization in acidic conditions and polymerization in basic conditions. While the type of acid does not significantly alter gel behavior, predicting the structure with boric acid is more challenging.

These insights into the chemical structure of silica gels can inform the design of chemically controlled routes for modifying the macroscopic properties of final gels for specific applications, including the development of formable, in situ setting bioactive glass-waterglass composite bone scaffolds.

Chapter 5: Microstructure and Mechanical Properties of Hydrogels from Sodium Silicate Solutions

5.1. Abstract

Silica hydrogels from sodium silicate solutions (waterglass) are promising for formable composite bone scaffolds, but their mechanical properties and the impact of processing conditions are not well understood. This study investigates how pH, waterglass concentration, and acid initiators affect the mechanical properties, deformation, and microstructure of acid-initiated silica hydrogels. Real-time compression monitoring revealed three stress-strain patterns: (i) brittle fracture, (ii) plastic plateau, and (iii) continuous strain hardening. pH-basic hydrogels showed a transition from continuous strain hardening to a plastic plateau with increased water content, while pH-acidic hydrogels displayed brittle fracture, but shifted towards a plastic plateau with more water content. Mechanical strength was determined to depend on composition and aging time. Basic 1:3 hydrogels (25 wt.% waterglass) and acidic 1:1 hydrogels (50 wt.% waterglass) exhibited the highest strengths in their groups, reaching up to 38± 11 MPa and 53 ± 11 MPa, respectively. All hydrogels initially had similar strengths (7.3-9.9 MPa), but aging increased strength significantly, with basic gels reaching 16-38 MPa and acidic gels reaching 21-53 MPa an hour after gelation. Lower waterglass concentrations decreased strength in both groups, with no significant difference between them. Engineering stress underestimated true stress by 21-55% for basic gels and 21-66% for acidic gels. Gradient stress-strain curve features correlated with real-time observations of crack initiation and propagation, and revealed the presence of radial cracks, circumferential cracks, splitting cracks, fragmentation, and microcrack networks. Basic gels, with larger structural units, formed looser, mesh-like structures with large pores (3-5 μm), resulting in ductility and shrinking pores over the aging time. In contrast, acidic gels, with smaller units, formed dense, brittle materials with small pores and strong internal connections. Both hydrogel types exhibited increased ductility and larger pore sizes (15-20 μm) upon dilution. These findings provide insights into the mechanical behavior of silica hydrogels, which can guide the design of chemically controlled methods to tailor their properties for specific applications, including bioactive glass-waterglass composite bone scaffolds.

5.2. Keywords

Silica hydrogel, Mechanical properties, Microstructure, Deformation mechanism, Fractography, Aging, Syneresis, Waterglass

5.3. Introduction

Silica gels are versatile inorganic amorphous materials known for their unique physicochemical and biological properties. Such gels possess high and customizable porosity, active surface functionalities, thermal and mechanical stability, biocompatibility, and resistance to bacterial attacks[246,304,398]. These characteristics have made silica gels highly desirable materials in various biomedical applications such as tissue engineering[399,400], wound healing[401], drug delivery[402,403], and cosmetics[404]. Silica gels derived from sodium silicate solutions (waterglass), show particular promise in bone tissue engineering for several reasons:

- They can be spontaneously formed through simple acid addition, eliminating the need for additional cross-linking steps (common in organic gels) or the removal of toxic components (as required with silica alkoxides);
- Their solid-like mechanical properties, due to their three-dimensional framework, allow for deformation, shape retention, and resistance to fluidity making them easily mouldable to fit body cavities without collapsing or shifting;
- They demonstrate excellent potential for bone regeneration due to their ability to bond with bone tissue[405,406] and compatibility with bone cells[407];
- Their properties, including porosity and mechanical strength, can be finely tuned by adjusting processing conditions.

As a result, silica gels are ideal for developing formable composite bone scaffolds that can adapt to various bone defects, setting *in situ* into a porous 3D structure that promotes effective bone tissue regeneration. Based on this concept, a design was explored in our lab where 45S5 Bioglass® frit was combined with a waterglass binder to create a formable paste that sets upon addition of phosphoric acid (PA) and boric acid (BA) as acid-initiators. The effects of pH, waterglass concentration, and type of acid-initiator on gelation kinetics, gels' optical properties, and molecular structure were investigated in previous chapters. It was found that the gelation time of 10 minutes, suitable for clinical applications, could be achieved in both acidic and basic conditions, with the specific pH for the target gelation time adjustable toward neutral by decreasing the initial waterglass concentration. Major structural differences were found at both the molecular and macroscopic levels in gels produced under different pH and processing conditions. These findings demonstrate the significant impact of pH and processing conditions on the final gel properties, including mechanical properties, which can be tailored to meet specific requirements for bone scaffolding applications.

The mechanical behavior of bone scaffolds is fundamentally important for successful bone regeneration. This behaviour includes not only mechanical strength and elasticity but also, equally important, mechanical stability and integrity[408]. In our composite scaffold design, waterglass acts as an adhesive, binding bioactive glass particles together and physically setting the entire composite upon gelation. Therefore, the role of waterglass is to create a paste of bioactive glass capable of being formed to fit custom wound geometries. After gelation, the role of silica gel in the composite is to provide temporary cohesion to the implanted bioactive glass scaffold (that is, setting it in place) so that it persists long enough to stimulate bone growth and eventually be resorbed.

To investigate the mechanical properties of our waterglass-bioactive glass composite, we need to know how each component behaves independently. The original 45S5 Bioglass® is widely used in orthopedics. It was estimated that over course of 30 years (since its FDA approval in 1985 up to 2016), it had been implanted in 1.5 million patients to repair bone and dental defects[409]. Naturally, its mechanical properties have also been extensively investigated in the form of bone scaffolds obtained through various methods[410–412]. Silica gels on the other hand, have been mostly investigated in form of aerogels[413–416], and much less is known about mechanical properties of silica hydrogels (that is, silica gels in a wet state), especially in terms of their static mechanical properties in tensile or compression modes. Therefore, the focus of this study is on the mechanical properties and microstructure of silica hydrogels as an individual component material for bone tissue scaffolds.

As multi-phase materials comprising a porous solid matrix and a liquid phase, hydrogels exhibit low elastic modulus (in the kPa range) and intermediate behavior between solids and liquids, which presents challenges in mechanical measurement and interpretation. Their compliant and hydrated nature complicates tensile testing, making compression testing the preferred method for evaluating mechanical properties of hydrogels[417]. Given their softness relative to conventional materials and rubbers, and their non-linear behavior under strain[418], precise and sensitive measurement techniques are essential. While dynamic mechanical analysis (DMA) provides high strain sensitivity and detects minor variations in stiffness[115,419], compression tests offer a simpler and more cost-effective approach to assessing the mechanical strength and durability of silica gels.

In the literature, stress-strain data for silica hydrogels are typically reported using engineering stress-strain values, which are calculated by dividing the applied loads by the original cross-sectional areas and displacements by the original heights of the specimens[403,420–422]. However, due to the significant deformation and changes in cross-sectional area during compression, engineering stress does not accurately reflect the mechanical properties of hydrogels. To address this inaccuracy, several approaches have been used to define true stress-strain curves for hydrogels. For instance, Zhang et al. [423] used digital image processing to measure volume changes under uniaxial compression and calculate true stress-strain curves for polyvinyl alcohol hydrogels. Dastgerdi et al. [424] used 3D digital image correlation (3D-DIC) to measure cross-sectional area changes and compute true stress in different hydrogels. Kontou and Farasoglou[425] utilized a laser and photocell to measure reflections from a rotating mirror, allowing them to determine strain and strain rate, and consequently true stress-strain curves. In all these examples, the experimental setups measure strain (change in sample's height) and calculate changes in cross-sectional area based on the assumption that the total volume remains constant during the test. For this assumption to be valid, the rate and extent of displacement must be controlled to prevent significant water leakage from the hydrogel or any visible permanent deformation, which is challenging and limits the test range. Directly monitoring changes in cross-sectional area in real-time would allow for accurate true stress-strain curves without these limitations. In this study, we utilize an innovative experimental setup to directly monitor changes in cross-sectional area of silica hydrogels under compression in real-time. This approach not only yields precise true stress-strain data without the limitations of previous methods, but also provides a detailed investigation and evolution of failure mechanisms and crack initiation and propagation during the test.

The features in the nonlinear stress-strain curves of hydrogels are not as well defined as those in conventional materials like metals. The lack of clear definitions for the onset and strain ranges of different regions in the stress-strain curve can lead to inconsistencies in determining mechanical properties, making it difficult to compare results across different studies. Moreover, as the gel ages, condensation reactions and aggregation of particles continues, resulting in the expulsion of liquid from the gel pores[264]. As a consequence, the gel network consolidates and shrinks, and its volume, porosity, and internal surface area will change over time. This process, also known as "syneresis", would greatly affect the mechanical properties of the gels over time, however, it has been neglected in previous studies.

To achieve better control over the mechanical properties of silica hydrogels, it is essential to investigate their mechanical behavior and establish a correlation between mechanical properties with their structure and fabrication conditions. This correlation is the final piece needed to fully understand the processing-structure-property relationship in silica gels made from sodium silicate solutions. Our goal is to optimize the processing conditions of silica gels from waterglass—such as pH, waterglass concentration, and type of acid catalyst—and predict their microstructure and mechanical properties in the gel state over time. Since the microstructure and mechanical properties of silica gel directly influence the properties of waterglass-bioactive glass composite scaffolds, controlling these properties will enable us to create a composite material that can be formed and set *in situ* while maintaining open porosity and mechanical stability after implantation.

In the discussion, we aim to answer the following questions:

- How do silica hydrogels made under different processing conditions differ in their mechanical properties and microstructure, and how are these differences related to variations in their molecular structure?
- How do the mechanical properties of silica hydrogels change over time? How do aging and syneresis phenomena and changes in microstructure of gels over time correlate with mechanical properties?
- What are the distinct regions and characteristics in a stress-strain curve of silica hydrogels? How can the onset and strain ranges of these regions be defined in these materials? How are these regions related to observed mechanical behaviors and failure mechanism such as the onset of crack formation, crack propagation, and crack/fracture modes?
- How significant are the differences between the engineering and true stress-strain curves of silica hydrogels under compression? Is it worth using true stress-strain curves for a more accurate analysis?

5.4. Materials and methods

5.4.1. Materials

The starting commercial sodium silicate solution (Sigma-Aldrich, CAS number: 6834-92-0, Saint Louis, MO, U.S.A) had the following characteristics: [SiO_2] = 26.5 wt.%, [Si] = 6.13 mol/l; relative density = 1.39 g/l; pH = 11.9; SiO_2/Na_2O molar ratio = 2.57. Phosphoric acid, 85% solution (Fisher Scientific, CAS number:7664-38-2) and boric acid powder, ≥ 99.5% (Fisher Scientific, CAS number: 10043-35-3, Toronto, ON, Canada) were used as acid-initiators. Silicone oil (Sigma-Aldrich, CAS number:63148-58-3, Saint Louis, MO, U.S.A) was used as lubricant and isopropyl alcohol 70% v/v (Fisher Scientific, Toronto, ON, Canada) was used to dilute the dye for fractography.

5.4.2. Hydrogels' compositions

With the goal of creating a formable, *in situ* setting bioactive glass-waterglass composite bone scaffold, the effects of pH (ranging from 2-11), waterglass concentration (15-50 wt.%), and acid initiator type (phosphoric acid and boric acid) were investigated as independent variables to optimize the setting time to a clinically practical range of approximately 10 minutes in chapter 3. It was found that the target gelation time of 10 minutes can be achieved at a single basic pH using boric acid and at various pH levels in both acidic and basic regions using phosphoric acid by adjusting the waterglass concentration, resulting in seven different specimen compositions, detailed in Table 1.

Table 5.1 Composition and pH of gels made with boric acid and phosphoric acid, with a gelation time of ten minutes, containing water, waterglass, and an acid solution.

Acid catalyst	WG:Water (wt. ratio)		WG (g)	Acid content (µl)	pH	t_g (min)
Boric Acid	● 1:5	Basic	3.34	14000	10.60	10
Phosphoric Acid	● 1:1	Basic	10.00	545	10.63	10
	● 1:3		5.00	360	10.35	
	● 1:5		3.34	300	9.70	
	● 1:1	Acidic	10.00	2800	3.36	10
	● 1:3		5.00	1300	4.80	
	● 1:5		3.34	825	5.30	

5.4.3. Mechanical Characterization

5.4.3.1. Preparing specimens

Cylindrical syringes with a diameter of 2 cm, whose tips were cut off, were used as molds. Solutions were prepared according to Table 5.1 under mechanical stirring and then transferred to the cylindrical molds using plastic pipettes while the molds were placed on vial racks. The flat rubber stoppers of the syringes were lubricated with a single drop of silicone oil for easier demolding (Figure 5.1a). All syringes were filled to the same height, using the marks on the syringes, equivalent to a height of 4 mm (Figure 5.1b). After the gelation point (~10 minutes), and after waiting for the experimental time after gelation to elapse (i.e., 5, 15, 30, 45, 60 minutes post-gelation) the hydrogel discs were demolded by pushing the syringes out onto the lower platen of the mechanical testing machine, which was covered with a piece of aluminum foil and lubricated with silicone oil (Figure 5.1c).

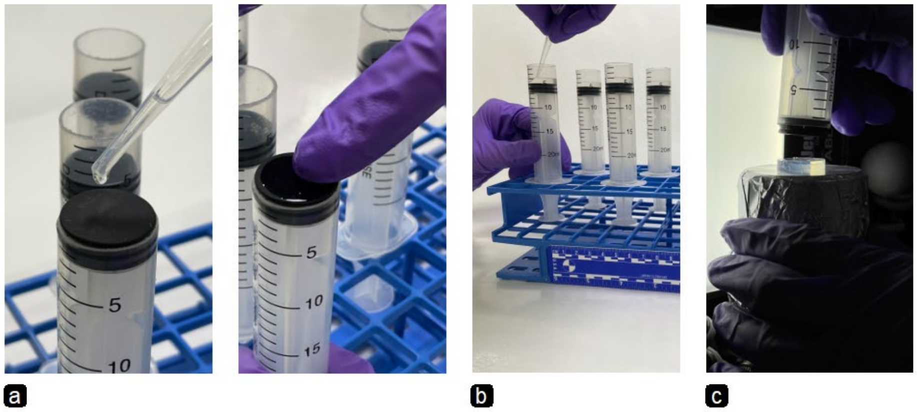

Figure 5.1 (a) Lubricating the syringe flat stopper for easier demolding. (b) Filling syringes with a mixture of water, waterglass, and acid solution to create hydrogel disks. (c) Demolding the hydrogel disk onto the compression test instrument platen, covered with aluminum foil and lubricated with silicone oil.

5.4.3.2. Compression test and engineering stress-strain curve

The mechanical properties of silica hydrogels in uniaxial compression were determined using an Instron 5943 (Instron, Norwood, MA, U.S.A) with a 1 kN load cell. The compressive tests were performed at room temperature with a strain rate of 1.0 mm/min. Each test was ended when the hydrogels reached 50% strain. All hydrogels were tested at intervals of 5, 10, 15, 30, 45, and 60 minutes *after* gelation (equivalent to t = 15, 25, 40, 55, and 70 minutes). Five replicates (N = 5) were tested for each type of hydrogel and each time point, resulting in a total of twenty-five replicates with the same compositions.

The obtained force (F)-displacement (l) curves were converted to engineering compressive stress (s)-strain (e) according to Equations (5.1) and (5.2), where A_0 and l_0 are initial disc samples' cross-sectional area and height, respectively. The engineering stress-strain curves, representing the average of five replicates and the range of standard deviations, were plotted using MATLAB_R2022b software (The MathWorks Inc., Natick, MA, U.S.A).

$$s = \frac{F}{A_0} \tag{5.1}$$

$$e = \frac{l}{l_0} \tag{5.2}$$

To assess the impact of various processing conditions and aging times on the mechanical properties of hydrogels, we performed a series of statistical tests. Normal distribution of the data was tested using the Shapiro-Wilk test before performing any statistical comparisons. Sphericity was tested with Mauchly's test. If sphericity was not met, the Greenhouse-Geisser correction was applied. One-way Analysis of Variance (ANOVA) was conducted to compare the different mechanical properties of hydrogels at various time points after gelation and between different types of hydrogels produced under various processing conditions. Additionally, comparisons were made between acidic and basic hydrogels of the same concentration. The Bonferroni Post Hoc test was used for multiple comparisons among all samples. A p-value of less than 0.05 ($p<0.05$) was set as the minimum alpha threshold to identify statistically significant differences.

5.4.3.3. Compression test and true stress-strain curve

To find the best way to monitor the hydrogels during compression, some preliminary investigations were performed. Specimens were video recorded from a side view in real-time using a smartphone equipped with a detachable macro lens (10x Macro M-Series Lens, Moment, Inc. Seattle, WA, USA) . Changes in height and barreling due to friction between the platens and the specimen, were observed. Moreover, some cracks on the edge could be seen, but the shape and length of the cracks and their propagation were not clearly visible (see Figure 5.2a). This challenge motivated us to design and fabricate an innovative device to record the cross-sectional area in contact with the lower platen in real-time during the compression test (Figure 5.2b).

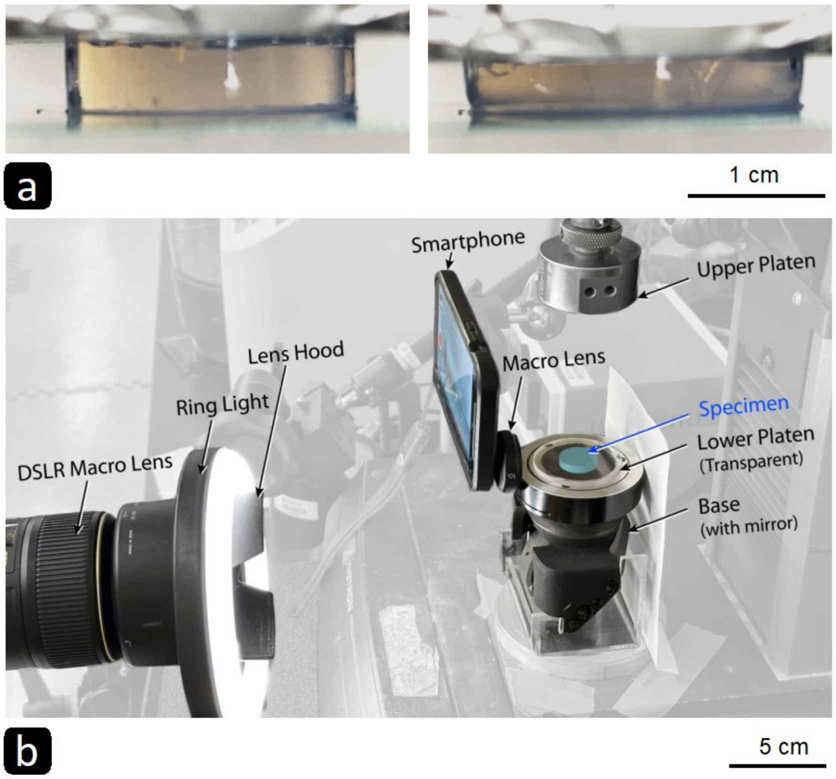

Figure 5.2 (a) Side view of hydrogels before (left) and during compression (right). Changes in height, barreling, and some cracks can be observed, though details of cracks and the deformation mechanism could not be studied in detail. (b) A view of the innovative setup with a transparent platen designed and fabricated to record the plan view of the cross-sectional area of hydrogels during compression.

Videos were recorded throughout the compression test using a digital single-lens reflex camera (D300s, Nikon Inc.) equipped with an AF Micro-Nikkor 105 mm f/2.8D lens. The camera settings were kept constant for all recordings. One replicate (N=1) was tested for each type of hydrogel and each time point, resulting in a total of five replicates with the same compositions. Screenshots of each video at time interval of 12 seconds (equivalent to 0.05 strain) were taken, and then the cross-sectional area at each screenshot was measured using the oval, or freehand, tool (depending on the final shape) in ImageJ software (U. S. National Institutes of Health, Bethesda, MD, USA).

The obtained force (F)-displacement (l) points were converted to true compressive stress (σ)-strain (ε) points using the real-time cross-sectional area (A_i) calculated from the image analysis of the screenshots, according to Equations (5.3) and (5.4):

$$\sigma = \frac{F}{A_i} \tag{5.3}$$

$$\varepsilon = \ln(\frac{A_0}{A_i}) \tag{5.4}$$

True compressive stress (σ)-strain (ε) curves were plotted using cubic spline data interpolation of the obtained points. All graphs were plotted using MATLAB_R2022b software. Due to the small sample size (N=1) statistical analysis was not performed to compare true versus engineering maximum strengths.

5.4.3.4. Real-time behaviour under compression

To analyze the deformation and failure behavior of hydrogels under compression, including the transition points between different deformation regions, we employed a combination of real-time video recording and detailed stress-strain curve analysis. Sharp changes in the slope of the stress-strain curves, as indicated by the 1st and 2nd derivatives, were used to identify critical transition points in the material's deformation to identify damage mechanisms. The critical points observed in the gradient stress-strain curves were correlated with visual observations from the real-time plan view video recordings. Screenshots were taken at the identified critical points during the video analysis to provide visual documentation of the deformation stages and failure mechanisms.

5.4.3.5 Fractography

To better analyze the fracture details, including the shape, size, distribution, and density of cracks and microcracks, we conducted a detailed post-test examination. At the end of the compression test (2 mm displacement for ductile gels and maximum force for brittle gels), the compressed hydrogels were transferred onto glass microscope slides and placed on a light transmission source. The surfaces in contact with the upper platen were dyed by depositing a drop of solution of blue Sharpie ink (Newell Brands, Atlanta, GA, USA) and isopropyl alcohol via a plastic pipette. Photographs of the specimens were taken from a top-down view using a high-resolution smartphone camera. Images of all seven types of specimens were captured at five different time intervals to document the changes over time.

5.4.4. Scanning electron microscope

Scanning electron microscopy (SEM) was employed to image and compare the structure, porosity, and morphology of different hydrogels. The goal was to find correlations between the mechanical properties and microstructure of the in hydrogels prepared with different processing conditions over time.

To prepare the samples, fresh mixtures of waterglass solutions of different concentrations and acids were made and poured into 1x1x1 cm^3 silicon molds, where they were allowed to gel. 5 and 60 minutes after the gelation point, the samples were immersed in liquid nitrogen to induce freezing. After freezing, the samples were dried using a Savant SuperModulyo freeze dryer (Thermo Electron, Waltham, MA, U.S.A) at a temperature of −40°C and a pressure of ~0.08 Torr for 12 hours. Prior to imaging, the specimens were sputtered with gold using Denton Desk II (Denton Vacuum Inc, Mooreston, NJ, U.S.A) for 90 seconds, resulting in a 12 nm gold coating to reduce charging. Imaging was conducted in secondary electron (SE) mode with a Zeiss EVO MA10 SEM (Carl Zeiss AG, Baden-Württemberg, Germany) equipped with a LaB_6 filament.

5.5. Results and discussion

5.5.1. Mechanical properties in compression

5.5.1.1. Engineering stress-strain

Figure 5.3 illustrates the engineering compressive stress-strain (S-e) curves for basic silica hydrogels made with boric acid, and both basic and acidic silica gels made with phosphoric acid at varying waterglass:water weight ratios

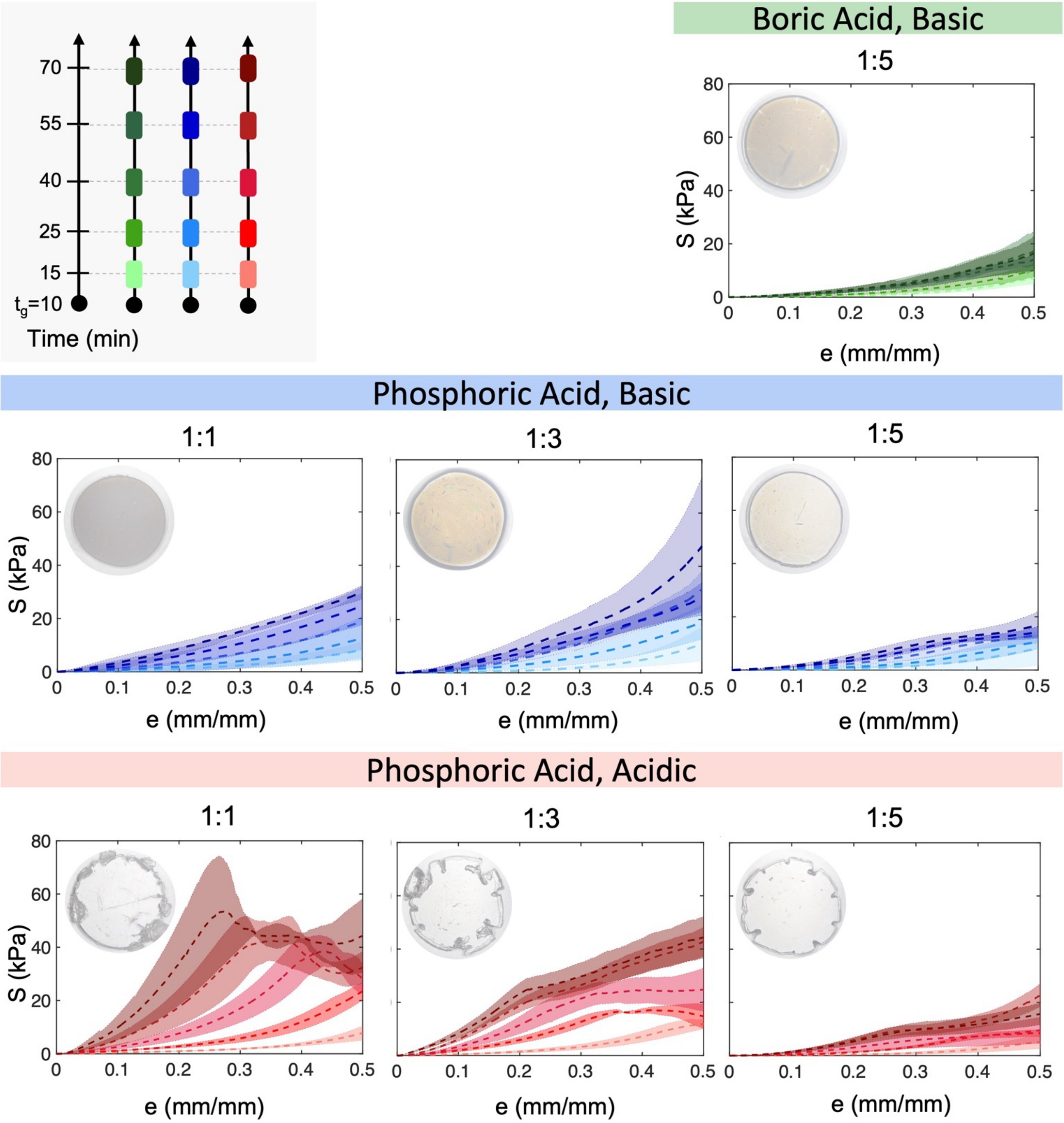

Figure 5.3 Engineering compressive stress-strain curves (the average and standard deviation for N =5) for basic silica hydrogels made with boric acid at a waterglass:water weight ratio of 1:5, and for basic and acidic silica hydrogels made with phosphoric acid at ratios of 1:1, 1:3, and 1:5. The stress-strain curves are shown at 5, 15, 30, 45, and 60 minutes post-gelation, represented by progressively darker shades in different color palettes.

The following observations can be made:

- All gels strengthen over time;
- All gels behave similarly shortly after gelation (t = 15 minutes);
- There is a distinct difference in the stress-strain curves between concentrated acidic and basic gels (1:1) made with phosphoric acid. However, this difference tends to diminish as the initial waterglass concentration decreases (1:5);
- Basic gels made with boric acid behave similarly to gels made with phosphoric acid at the same initial waterglass concentration (1:5).

When a hydrogel forms, it initially contains a high amount of water dispersed throughout its network. A metastable gel, like a silica hydrogel, spontaneously undergoes changes as time goes by.

The strengthening of silica hydrogels over time can be attributed to the aging process. It should be noted that while *syneresis* and *gel aging* are usually used interchangeably in the literature, they could convey different mechanisms. According to IUPAC Compendium of Chemical Terminology *gel aging* is defined as "*time-dependent changes in the chemical or the physical structure and the properties of a gel.*" (ref [426], p. 1823) which could involve *syneresis*, polymerization, aggregation, as well as chemical changes to constitutional units of the gel network. *Syneresis* is defined as "*spontaneous shrinking of a gel with exudation of liquid.*" (ref [426], p. 1826). Bond formation or attraction between silica particles or aggregates/agglomerates induces contraction and thereby the exudation of liquid from the network. Therefore, aging contributes to the overall increase in gel strength in two ways. Firstly, as the aggregates/agglomerates come closer together, they form new bonds (chemical bonds such as Si-O-Si, or weaker secondary bonds such as hydrogen bonds), which enhance the intermolecular forces between the silicate particles, leading to rearrangement of silica particles to form thicker strands, increasing the gel strength. Secondly, syneresis and the expulsion of water leads to a denser and more tightly packed network of silicate aggregates/agglomerates within the gel, further increasing the mechanical strength of the gels.

Generally, the kinetics of aging (including syneresis) depend on the driving force, the mobility of the gel network, and the rate of fluid flow through the contracting gel[427]. The driving force for aging is usually attributed to the same chemical and physical reactions that initiate gelation, such as hydrolysis and condensation reactions as well as the aggregation of silica particles through physical and chemical interactions. Since the rates of these reactions are sensitive to pH, the rate of syneresis should also depend on pH. Moreover, our results in chapter 3 and 4 have shown that gels made at different pH values and waterglass concentrations have widely varying chemical structures and microstructures, affecting the mobility of the network and the permeability of the pores. Therefore, it is expected that gels made under different conditions will have different rates of aging and consequently, exhibit varying effects of time on their mechanical strength and stiffness.

The maximum stress in the corresponding stress–strain curves of different hydrogels is shown in Figure 5.4a and Figure 5.4b for basic and acidic gels in different aging times. Hydrogels have been compared from two aspects: 1) effect of hydrogel composition in constant aging time (Figure 5.4a) 2) effect of aging time at constant composition (Figure 5.4b), which will be discussed in the following in detail.

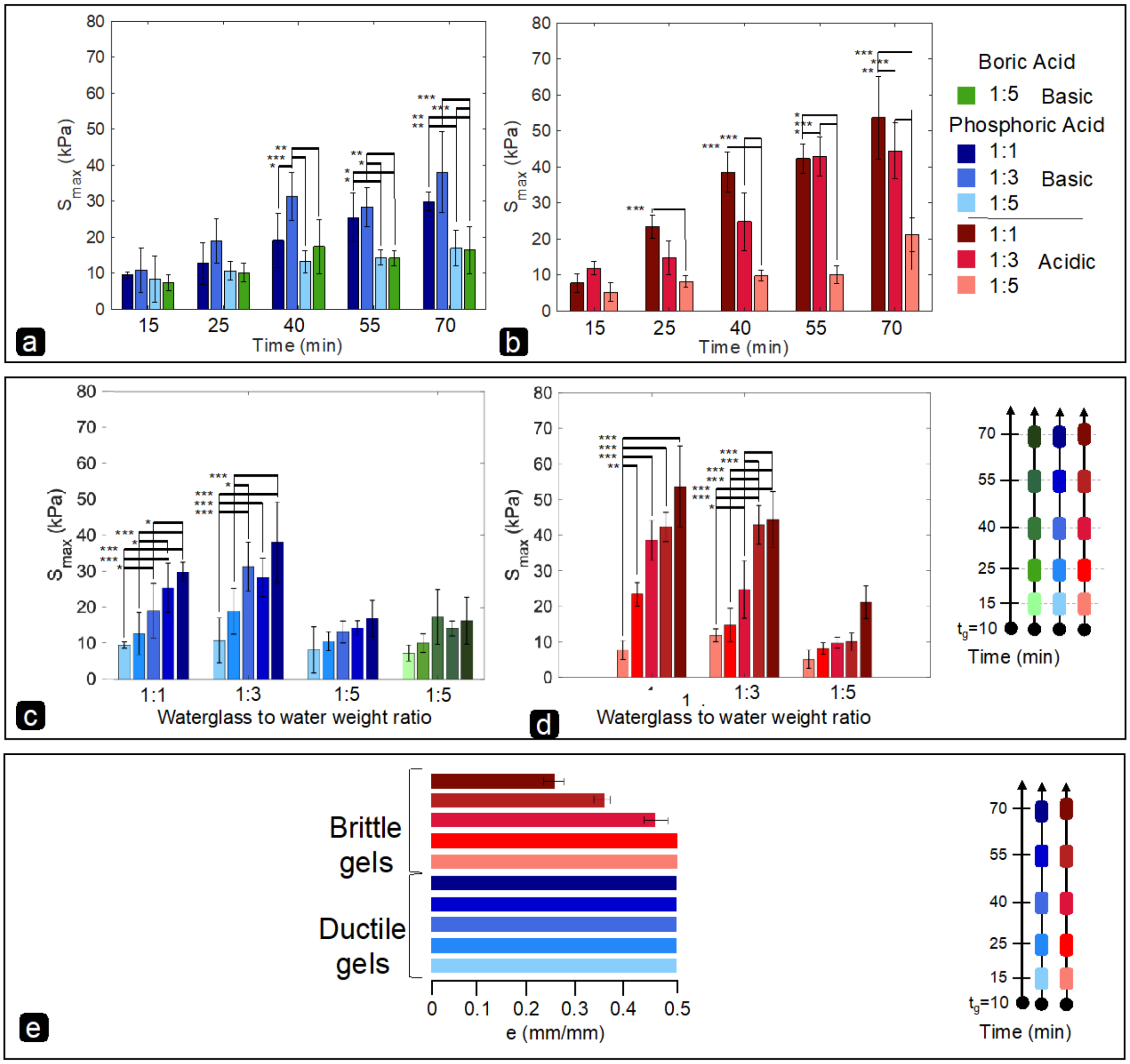

Figure 5.4 (a) Effect of hydrogels' composition on maximum compressive strength of basic hydrogels. (b) Effect of hydrogels' composition on maximum compressive strength of acid hydrogels. (c) Effect of aging time on maximum compressive strength of basic hydrogels. (d) Effect of aging time on maximum compressive strength of acidic hydrogels. Statistically significant differences for figures a-d are indicated as follows: $*P < 0.05$, $**P < 0.01$, $***P < 0.001$, where P represents the p-value. (e) Ductility in brittle (acidic 1:1) and ductile gels(basic 1:1, 1:3, 1:5 and acid 1:3 and 1:5) by determining the strain at their maximum strength according to Figure 5.3.

Effect of composition in constant aging time

As seen in Figure 5.4a and Figure 5.4b, there is no significant difference between different hydrogels shortly after gelation. The first differences arise 30 minutes after the gelation point (t = 40) in the basic gels group and 15 minutes after gelation (t = 25) in the acidic gels group. This delay is because, at the early stage after gelation, hydrogels are still not fully developed and remain soft and weak, regardless of their composition. As more time passes and the gels' network becomes more developed, the differences between hydrogels of different compositions become more pronounced, and differences in maximum strength can be found between any two kinds of compositions. The only exception is the basic 1:5 hydrogels made with boric acid and phosphoric acid, which do not show any difference at any time. This finding highlights the importance of pH and waterglass concentration over the type of acid used and is consistent with our previous observations regarding the gelation kinetics, optical properties, and molecular structure dependency on pH in these gels.

One would expect that the maximum mechanical strength of basic gels would decrease in the order of 1:1, 1:3, and 1:5 due to the decreasing silica concentration and increasing water content. However, the basic 1:3 gels showed the highest strength. As we dilute the solutions in basic gels, the pH lowers, leading to reduced repulsion and an increased rate of condensation. Both factors favor agglomeration and the formation of more bonds between the particles. On the other hand, decreasing the silica content reduces the number of particles, which works against the formation of new bonds. Therefore, basic 1:3 gels provide an optimal balance between these opposing factors, allowing for a more effective cross-linking network within the gel and resulting in higher compressive strength compared to the 1:1 and 1:5 ratios. Moreover, our statistical analysis results showed no significant difference in the maximum strength between acidic and basic gels of the same waterglass concentration (e.g., between acidic 1:1 and basic 1:1), even an hour after gelation. While this outcome was expected for the 1:5 gels due to their similar behavior in optical properties and pore size according to previous studies, it is surprising for the concentrated gels due to their very different molecular structure and optical properties. However, it is important to note that the maximum strength reported for acidic 1:1 gels occurs at their fracture point (see Figure 5.3), with strains ranging from 0.26 to 0.36, while for ductile basic 1:1 gels, it is reported at 0.50 strain.

Therefore, despite having similar maximum strength values, 1:1 acidic and basic gels exhibit distinctly different behaviors.

Effect of aging time at constant composition

The impact of aging time is significant for concentrated gels. In basic 1:1 gels, the maximum stress sixty minutes after gelation (29.9 ± 2.63, t = 70 minutes) is approximately three times higher than five minutes after gelation (9.5 ± 0.9, t = 5 minutes). In acidic 1:1 gels, the maximum stress sixty minutes after gelation (53.65 ± 11.43, t = 70 minutes) is about seven times higher compared to five minutes after gelation (7.77 ± 2.65, t = 5 minutes). This effect diminishes as the initial waterglass solution becomes more diluted. In acidic and basic 1:5 gels, the maximum stress sixty minutes after gelation (t = 70 minutes) shows no significant difference compared to five minutes after gelation (t = 15 minutes). This contrast suggests that the rate of gel aging, or the impact of gel aging, decreases with decreasing waterglass concentration.

A possible reason for the reduced impact of aging on the maximum stress at lower waterglass concentrations is that there are fewer silicate structural units available to form new chemical or physical bonds. This reduction in reactive sites limits the extent of additional bonding and network densification that can occur over time, thereby lessening the impact of aging on the mechanical strength of the gels. Moreover, at lower concentrations, the gels inherently have a more dilute and less interconnected structure. This less dense network does not have as many internal stresses driving syneresis, and as a result, the structural changes and strengthening due to aging are less significant.

Our previous studies have shown that (1) concentrated basic gels have larger pores compared to acidic gels, and (2) the silicate structural units and primary and secondary particles are larger in basic gels compared to acidic gels. Consequently, we conclude that the contribution of continued formation of bonds between particles is more significant than syneresis in increasing the strength of concentrated acidic gels. This claim is consistent with the fact that acidic gels have smaller pores (lower permeability), higher mobility of units, and more reactive (SiOH) sites, leading to a greater increase in strength over time compared to concentrated basic gels. On the other hand, in basic gels, the contribution of syneresis and shrinking is likely higher in their strengthening over time.

5.5.1.2. Identifying regions in stress-strain curves

Characteristic regions in the stress-strain curve of silica hydrogels provide insights into the underlying deformation mechanism and how the hydrogel structure rearranges under stress, its capacity for plastic deformation, and potential failure modes. Three different patterns can be observed in the stress-strain curves of gels in Figure 5.3, which are shown in Figure 5.5a:

(i) An increase in stress, a plateau, followed by a further increase in stress;
(ii) An overall increase in stress;
(iii) An increase in stress, reaching a peak, and then a decrease in stress.

All types of behavior, including an elastoplastic plateau followed by densification (type i) [428,429], continuous nonlinear strain hardening behavior (type ii)[430,431], and brittle fracture (type iii) [421,432,433], have been reported for silica and other types of hydrogels under compression. However, the corresponding regions in stress-strain curves and the underlying mechanisms causing these different behaviors remain unclear for silica hydrogels, or even hydrogels in general. The stages of deformation in hydrogels under compression can be compared to those of cellular solids or foams. Silica hydrogels are similar to foams because they can be modeled as a two-phase medium, consisting of a solid phase (a 3D network of silicate particles and aggregates/agglomerates) and a fluid phase (water molecules), with the solid phase essentially behaving like a foam.

Figure 5.5b shows schematic compressive stress-strain curves for an elastomeric, elastic-plastic, and brittle foam, as proposed by Gibson and Ashby[434]. All types of foams exhibit linear elasticity at low stresses, followed by a long collapse plateau, and finally a regime of densification where the stress rises sharply. The deformation mechanisms associated with each regime are as follows for foams: (i) cell-wall bending during loading in the linear-elastic regime, (ii) cell-wall buckling during loading in the non-linear elastic regime, (iii) cell-wall yielding during loading in the plastic regime, and (iv) cell yielding and fracture.

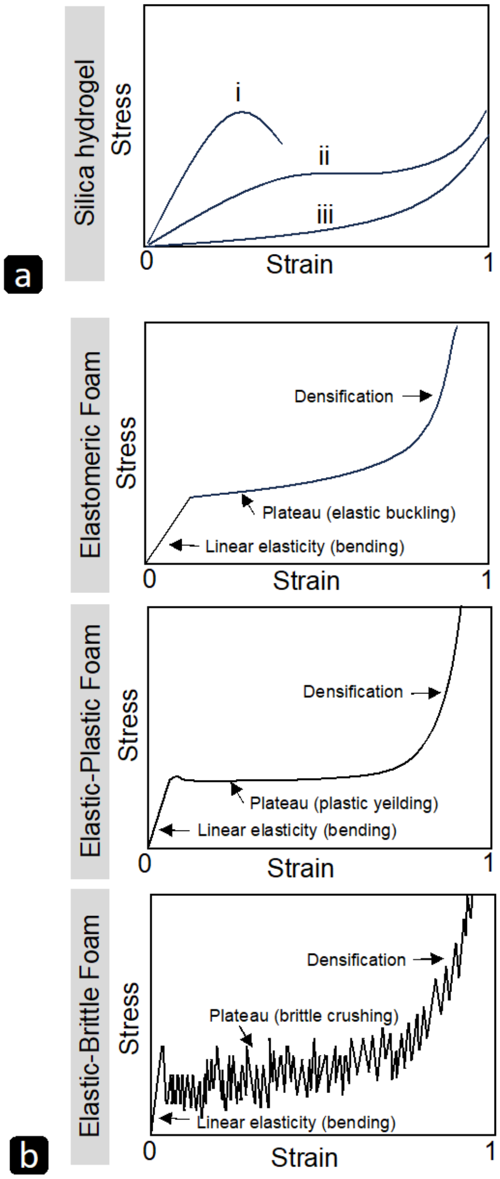

Figure 5.5 (a) schematic of typical compressive stress–strain curves observed in silica hydrogels in this study (i) brittle hydrogels that show brittle fracture followed by a sudden drop in stress (ii) ductile hydrogels with a plastic yielding plateau (iii) ductile hydrogels with continues strain hardening. (b) schematic of typical compressive stress-strain curves for foams showing the regimes of linear elasticity, collapse and densification in elastomeric, elastic-plastic and elastic-brittle foams, adapted from ref [434], p. 177.

Equivalent to cell wall bending in foams, the initial elastic region in silica hydrogels is controlled by the bending of silicate network *walls*, which are aggregates/agglomerates of silicate particles held together by strong primary or weak secondary bonds, respectively. Unlike rigid materials like metals and ceramics, where elasticity is limited to atomic bond stretching, the silicate particles in hydrogels can rearrange without breaking bonds. For highly elastic materials like rubber, elasticity is achieved through polymer chain folding and unfolding. The elastic region in silica hydrogels is defined by the movement of silicate structural units within the network. This movement is facilitated by the water medium, which allows for flexibility and prevents permanent deformation. Steric hindrance, repulsion between silicate species and other ions, along with the covalent Si-O bonds within particles, restrict this movement, so the material behaves elastically up to a certain point.

As compression continues beyond the elastic limit, the silica hydrogel enters the plastic region, where significant structural rearrangements go beyond mere bending of the silicate network walls. All gels exhibited plastic deformation and cracks (along with breaking for acidic 1:1 gel) at the end of the test, as can be seen from the macrographs in Figure 5.3. Comparing the typical stress-strain curves types in silica hydrogels (Figure 5.5a) with typical stress-strain curves in foams (Figure 5.5b), we see that only type ii silica hydrogels clearly exhibit stress-strain curves with characteristics similar to those observed in foams. This similarity is indicated by the presence of a plateau region (observed in acidic 1:3, acidic 1:5, and basic 1:5 gels 30-60 minutes after gelation), followed by densification. Their plateau resembles the plateau in elastic-plastic foams, which results from collapsing the cells by the formation of plastic hinges. In the case of silica hydrogels, when the rearrangement of silicate tetrahedra and particles within agglomerates become more constrained, silicate network walls collapse whilst the liquid is exuded because, unlike gases, the liquid is incompressible and therefore flows out of the silica hydrogel under large enough values of compression. This process absorbs energy and allows for significant deformation at nearly constant stress, leading to a plateau in the stress-strain curve.

However, this plateau is not observed for gels at the early stages after the gelation point, or at any time in the case of concentrated basic 1:1 hydrogels. Instead, a non-linear strain hardening is observed (type iii). In foams, the cell collapse stress and the post-collapse behavior depend on whether they have open or closed cells[434]. Open cell foams collapse at almost constant load, giving a long flat plateau, while in enclosed cell foams, the compression of the gas within the cells together with the membrane stresses, which appear in the cell faces, give a stress-strain curve which rises with strain. Therefore, type iii gels have behavior similar to closed cell foams. Plastic collapse in an open cell foam occurs when the moment exerted on the cell walls exceeds the fully plastic moment, creating plastic hinges. Closed cell foams are more complicated; in them, the plastic collapse load may be affected by the stretching as well as the bending of the cell walls and by the presence of a fluid within the cells. For plastic deformation in silica hydrogels, there is a combined effect of the plastic bending of cell edges and plastic stretching of their faces. To this must be added the contribution of the fluid contained in the cells, which in the case of water, the pressure is significant. Other factors, such as the formation of new bonds between silicate particles and their size, mobility, and flexibility (which is dependent on pH) also play a role here, making the behavior more complex and potentially leading to the absence of a plateau in some cases.

Concentrated acidic 1:1 hydrogels exhibit brittle behavior (type i)—characterized by abrupt failure and less plastic deformation compared to other gels—aligning more with the mechanical response of brittle polymers rather than elastic-brittle foams in Figure 5.5b. This behaviour is mostly because the water inside the gel network is incompressible, and does not allow a brittle crushing plateau. Acidic 1:1 hydrogels are composed of smaller particles with more contact points and reactive sites on surface, leading to stronger inter-particle interactions. These stronger interactions result in a more rigid network that resists deformation, causing them to exhibit brittleness and a glass-like behavior. The pores in these gels are very small, and the water trapped inside the pores has such strong interactions (hydrogen bonding) with the reactive sites on silicate walls that the entire gel behaves more like a bulk brittle solid than a viscoelastic gel. This behavior is not observed in other acidic gels, as they contain more water and have bigger pores, resulting in higher ductility.

Ductility is defined as the strain at maximum strength. As illustrated in Figure 5.4e, all ductile gels—including all basic gels made with phosphoric acid and boric acid, and acidic gels with a waterglass-to-water weight ratio of 1:3 and 1:5—show an increase in strength up to a strain of 0.5. In contrast, brittle gels, the acidic gel with a waterglass-to-water weight ratio of 1:1, exhibit a decrease in ductility over time, with the average strain at maximum strength dropping from 0.5 to 0.27. It is important to note that even though some gels may show damage or cracks (as detailed in the following sections), they remain sub-critical.

Densification is the final region in all stress-strain curves of hydrogels under compression. Plastic strains in compression cause the cell walls to crush together and the pores to collapse and close, leading to densification of the material. As a result, the stress-strain curves rise steeply to a limiting strain. This process can be accompanied by water being expelled from the gels, with the extent depending on the silicate particle size, their protonation (number of SiOH groups), pore size, and amount of water. Generally, the gels that had higher water content exuded more water. In case of concentrated 1:1 gels with same water content, basic gels were observed to exude more water due to their larger pores and higher strain at the end of test.

5.5.1.3. Deformation and Failure Mechanism

Having identified the possible different regions in the compressive stress-strain curves of silica hydrogels, the next critical question is how to precisely determine their onset and conclusion points. The strain ranges corresponding to these regions provide significant insights into the mechanical behavior of the hydrogels. Another challenge is how to appropriately report the strength and mechanical properties of hydrogels. The two common ways are to report the maximum compressive stress recorded during the test, as we did in Figure 5.4, or to report the strength at a specific strain (usually 50%) for ductile gels without fractures. However, depending on the application, entering the densification stage might not be acceptable. Therefore, it is crucial to consider these stages when evaluating mechanical properties. Employing the 1st-derivative of the compressive stress-strain curve could provide a more detailed understanding of the different deformation regions, which has been used by other researchers[435,436]. Here, we are going to investigate the derivative(s) of compressive stress-strain curves of silica hydrogels for the first time to get more details about the transition points of different deformation regions, and their relevance to our real-time observations of their deformation (such as crack initiation and propagation).

The first derivatives of the engineering stress-strain curves of silica hydrogels are shown in Figure 5.6. Initially, at t = 15 minutes, all the hydrogels exhibit a smooth increase in slope. Shortly after gelation, the hydrogel structure is not fully developed, with new hydrogen bonds still forming between particles. The early stages of gel formation result in a less rigid and more ductile network that deforms continuously under increasing stress. As more time passes ($t \geq 15$ minutes), distinct behaviors emerge, corresponding to the different patterns observed in stress-strain curves: type i (acidic 1:1), type ii (acidic 1:3, acidic 1:5, basic 1:5), and type iii (basic 1:1 and basic 1:3).

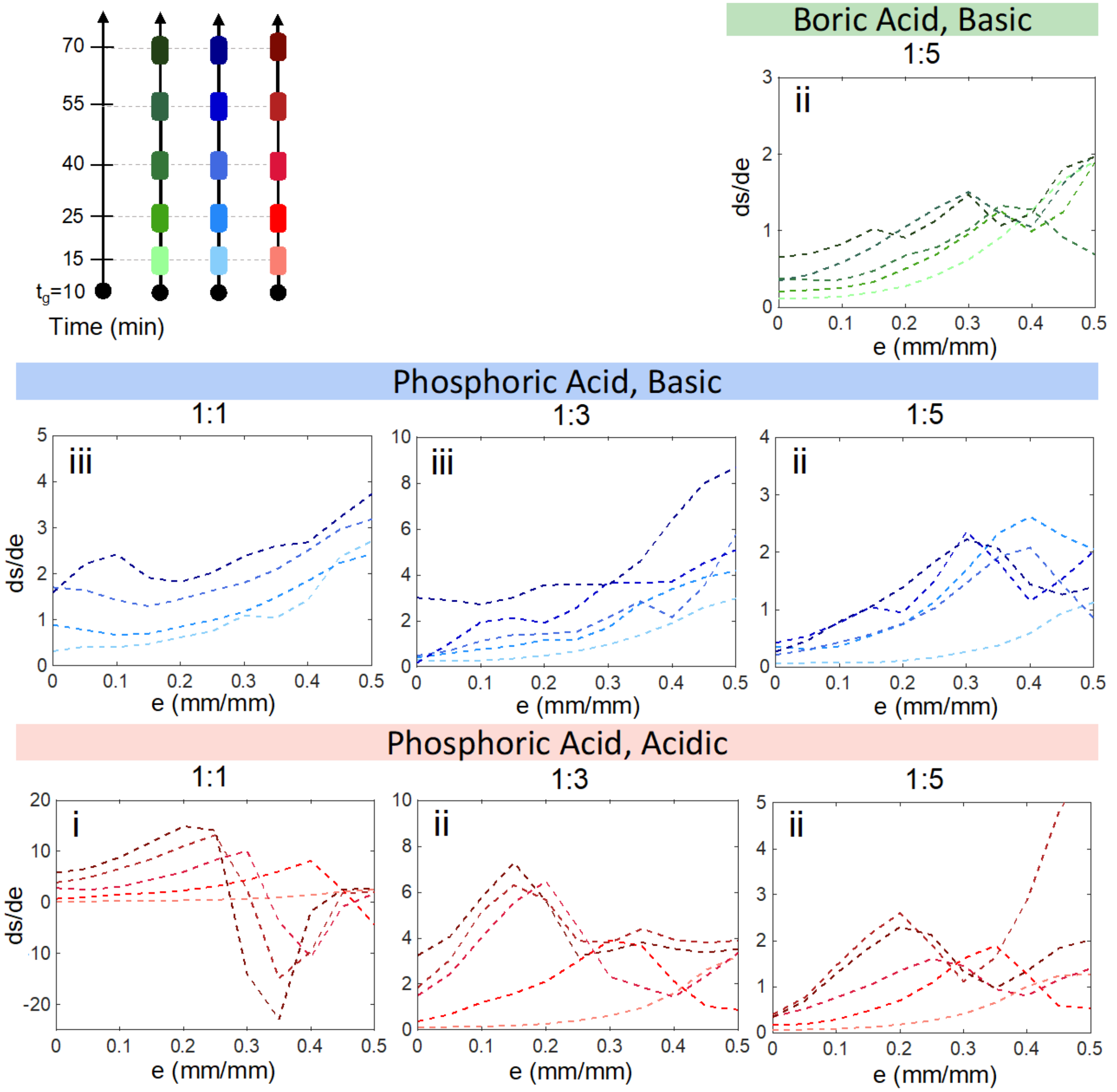

Figure 5.6 Gradient (first-derivative) of compressive engineering stress-strain curves of basic silica hydrogels made with boric acid at a waterglass:water weight ratio of 1:5, and for basic and acidic silica hydrogels made with phosphoric acid at ratios of 1:1, 1:3, and 1:5. The stress-strain curves are shown at 5, 15, 30, 45, and 60 minutes post-gelation, represented by progressively darker shades in different color palettes.

In type i hydrogels, the stress-strain slope increases to a maximum before decreasing. When the slope reaches zero, indicating the maximum in the stress-strain curves, it marks the point of brittle fracture, resulting in a sudden drop in force. The strain at which the slope reaches zero decreases over time, indicating increased brittleness as the hydrogel ages. Type ii hydrogels also show an initial increase in the stress-strain slope, followed by a decrease. However, unlike type i hydrogels, type ii hydrogels are ductile and continue to deform, with the force continuing to increase. The slope then starts to rise again due to densification, which becomes more pronounced over time. Type iii gels demonstrate a gradual increase in the stress-strain slope with some fluctuations, corresponding to their continuous increase in stress-strain curves without a plateau.

Notably, at t = 15 minutes, hydrogels of all types exhibit a constant slope up to 0.1-0.2 strain, indicating a linear elastic region. However, most fully developed gels show a gradual increase in slope with increased deformation, even at very small strains. This finding contrasts conventional methods, where the Young's modulus of elasticity for hydrogels is calculated by a linear fit along the engineering stress-strain curve between 5% and 10% strain[399,421,437]. Figure 5.6 illustrates the non-linear nature of compressive stress-strain curves, suggesting that calculating the slope of the linear portion is ambiguous since there is no true linear portion. Some researchers have indicated the elastic region based on the initial 'instant fit' (tangent) to the engineering stress-strain derived from the crosshead displacement curve . However, the accuracy of these initial data points can be problematic due to load cell inaccuracies, noise, and non-ideal surface flatness. Krupa et al.[433] proposed averaging values in a nearly-linear region or approximating the Young's modulus to strain dependence after extrapolating to zero deformation. Since the Young's modulus calculated from the stress-strain curve is not an "intrinsic" property for silica hydrogels—due to the strong dependence on microstructure, pore volume fraction, and interactions among silicate units, particles, aggregates/agglomerates, and water—calculating Young's modulus is mainly useful for comparison and contrast, provided all external and environmental conditions remain constant.

To relate the rate of stress-strain to different deformation stages, we hypothesized that points where a sharp change occurs in the slope of the gradient stress-strain curve indicate changes in the material's deformation mechanism. We then correlated these points with the critical points observed during real-time imaging of the cross-sectional area. Before proceeding, we need to define these critical points:

- **Crack Initiation Point**: The strain where a visible crack forms.
- **Crack Propagation Point**: The strain where there is a visible change in the length of the initial crack or where new cracks form.

- **Yield Point**: The strain where the gradient stress-strain curve shows a maximum, followed by a sharp decrease toward breaking. This point should not be confused with elastic-to-plastic yielding.
- **Brittle Failure**: The strain where the sample breaks, accompanied by a drop in the initial force-displacement curve.
- **End of Test**: The point where the strain reaches 0.5.

Due to uncertainties about the elastic-to-plastic transition and the lack of corresponding visual changes in the cross-sectional area during this type of transition, this point was not considered. The results for one acidic and one basic gel are shown in Figure 5.7 and Figure 5.8. Five minutes after gelation (t = 15 minutes), no sharp changes are observed in the stress-strain slope of basic gels, and no visible cracks appear (Figure 5.7). However, after this period, basic gels exhibit a sharp increase in slope, coinciding with visible crack initiation. Subsequent changes in the slope were accompanied by crack propagation and formation of new cracks. In cases where the slope temporary remained constant or decreased after cracks initiate, videos showed that the open cracks were being closed by compression or filled with water. By the end of the test, all gels exhibited plastic behavior despite crack formation, indicated by the fact that there was no drop in force during the test and the cracks did not completely break the specimens. Moreover, examining the strains at which crack initiation occurs revealed a clear trend over time. Five minutes after gelation, no cracks were observed up to a strain of 0.5. Over time, cracks began to initiate at strains of 0.25 and eventually at 0.1, indicating that the gels become more brittle as they gain strength.

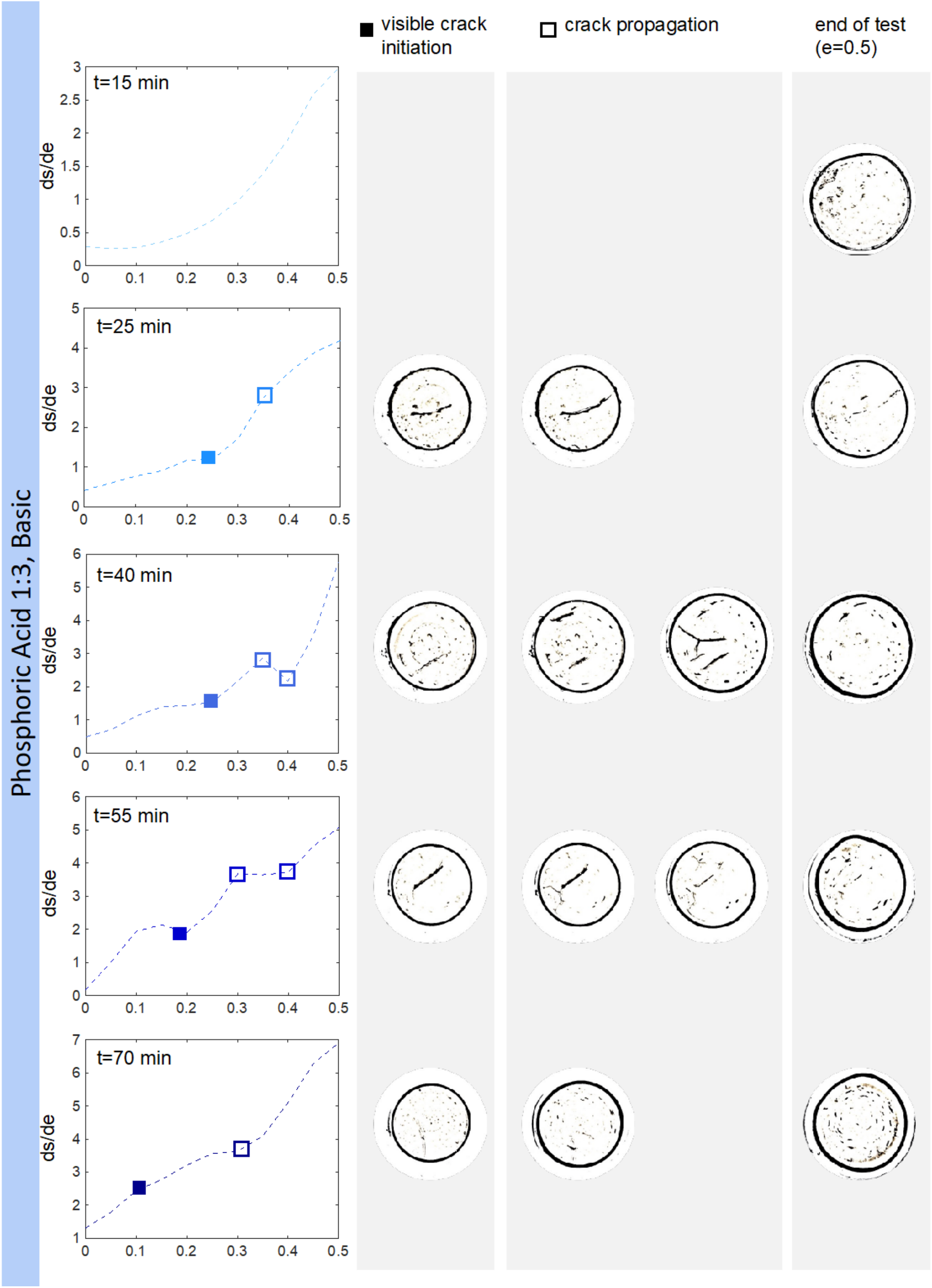

Figure 5.7 First-derivative graphs of basic 1:3 silica hydrogels at various times after gelation (left). Critical points, identified by sharp changes in slope, are correlated with key observations from real-time monitoring of the compressed cross-sectional area (right)—namely, crack formation and growth.

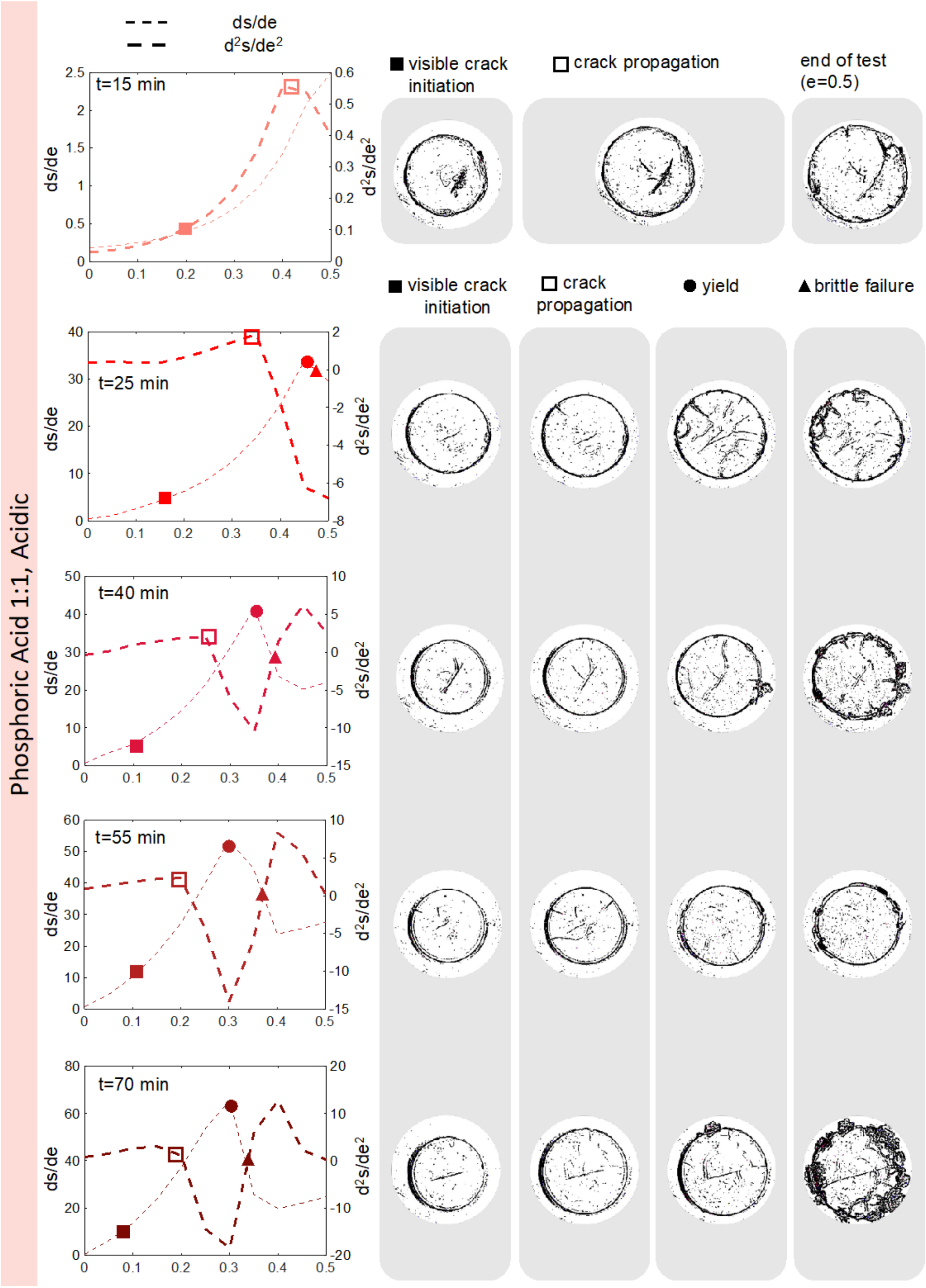

Figure 5.8 First- and Second-derivative graphs of acidic 1:1 silica hydrogels at various times after gelation, shown on left and right y-axis, respectively (at left). Critical points, identified by sharp changes in slope, are correlated with key observations of gel damage from real-time monitoring of the compressed cross-sectional area (right).

The gradient curves of brittle acidic 1:1 hydrogels differ from that of basic gels. Due to the complexity, we included the second derivative of the stress-strain curve to enhance resolution and highlight subtle features in acidic gels (Figure 5.8). Five minutes after gelation (t = 15 minutes), the behavior of acidic hydrogels is very similar to that of the basic gels in Figure 5.7, exhibiting ductility. The only difference is that the cracks are more visible, likely due to their larger size or the higher transparency of these gels compared to the basic ones. After this point, the hydrogels show a change in slope at the crack initiation point, followed by another increase at the crack propagation point (evident in the second-derivative graph), leading to the yield point. All samples exhibited brittle fracture shortly after this point. The strains at which crack initiation occurs decrease from 0.20 to 0.08, crack propagation from 0.33 to 0.18, yield from 0.45 to 0.31, and brittle fracture from 0.47 to 0.35 as time progresses up to an hour after gelation. This behavior is similar to that of basic gels, indicating that the gels become more brittle as they gain strength.

5.5.1.4. Fractography

Macrographs of dyed hydrogels' surfaces (facing the upper platen) can be evaluated in Figure 5.9. These images show the end of the test (0.5 strain) for plastic hydrogels (type iii and type ii) and fracture point for brittle hydrogels (type i). As can be seen, dying the samples revealed many microcracks that were not visible during real-time imaging. Cracks do not grow under compression; growing cracks imply that there are local tensile/shear forces due to *internal stresses*, which are larger than the remote compressive stresses that tend to close the crack[439].

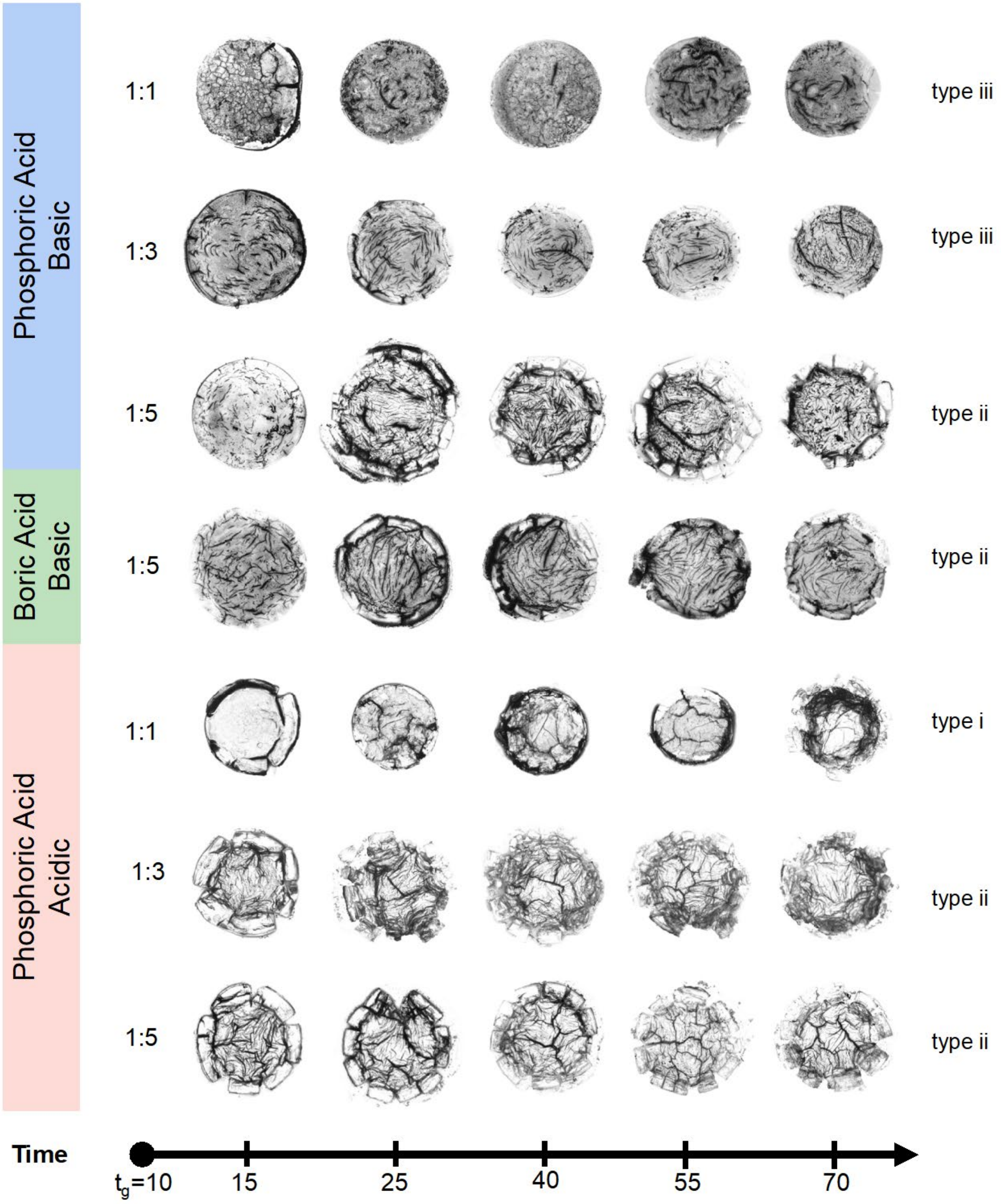

Figure 5.9 Fractography of dyed compressed hydrogels at maximum strength (0.5 strain for ductile gels and the break point for brittle gels) at 5, 15-, 30-, 45-, and 60-minutes post-gelation.

Before assessing the hydrogels, we need to identify different modes of fracture and categorize the cracks formed. Fracture mechanics is generally broken into three modes of fractures (mode I, II, and III) based on the forces acting on the body[440]. Mode I is the opening mode caused by tensile stress perpendicular to the fracture plane. Mode II is the sliding mode (i.e., the in-plane shear mode), which results from shear stress acting parallel to the fracture surface. Mode III is the tearing mode (i.e., the anti-plane shear mode), which is induced by shear stress acting parallel to both the fracture surface and the fracture front. Based on mode of fracture, the location and shape of cracks, and observations during real-time imaging, cracks and features observed in fractography in silica hydrogels can be divided into these categories (Figure 5.10):

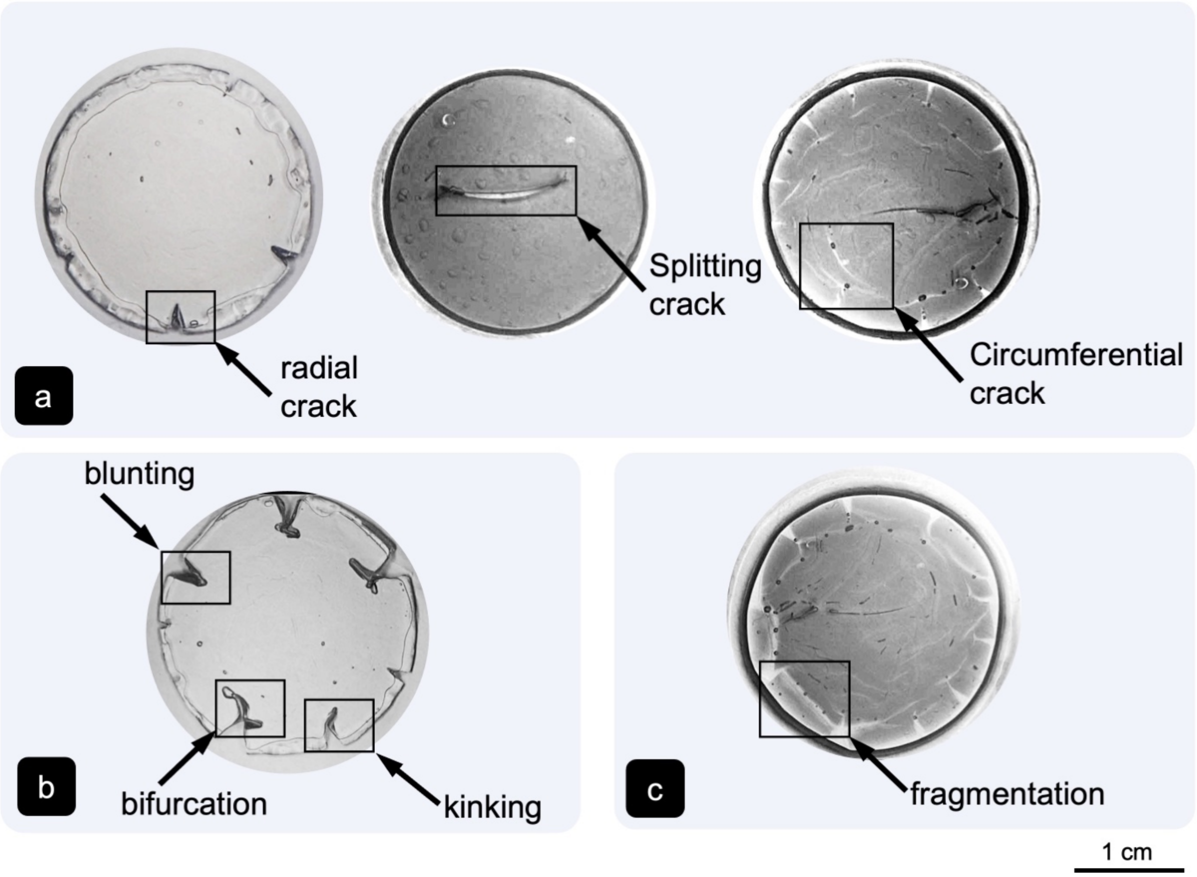

Figure 5.10 Macrographs taken from real-time videos displaying (a) various crack types in compressed silica hydrogels: radial cracks, splitting cracks, and circumferential cracks (b) potential developments after a radial crack forms: blunting, kinking, and bifurcation. (c) fragmentation resulting from kinked radial cracks and circumferential cracks joining, or kink cracks joining.

1) Radial cracks:

Cracks that initiate on the edge (circumferential surface) and grow toward the center (see Figure 5.10a). As the disk expands radially, the hydrogel surface is stretched, generating a tensile hoop stress, which acts circumferentially around the disk. If the tensile hoop stress exceeds the material's tensile strength, it can initiate radial cracks (mode I). After forming, these radial cracks may stop growing (via blunting). The stress at the crack tip leads to plastic deformation, increasing the overall energy consumption at the crack tip, resulting in blunted cracks. Thus, the energy available for crack propagation is significantly reduced, improving fracture toughness[441]. The tip of the radial crack may initiate a kink crack if the in-plane shear stress is greater than the local hoop stress (the tensile stress at the crack tip to open the radial crack). Therefore, kinking is a result of incipient crack growth under mixed-mode I and mode II (in-plane shear) loading[442]. After kinking, the crack continues to grow along a smooth curve. Bifurcation may also occur instead of kinking in one direction. It should be noted that radial cracks initiated from circumferential stress can increase the stress and cause more cracks to form. Formation of radial cracks and the subsequent possibilities of blunting, kinking and bifurcations are illustrated in Figure 5.10b.

2) Splitting cracks:

Longitudinal splitting cracks initiate due to tensile stress parallel to the top and bottom surfaces (mode I). These splitting cracks can either form on the surface or extend throughout the bulk of the material (axial splitting), depending on the stress distribution and material properties. Brittle gels are more prone to axial splitting because they lack the ability to deform plastically and absorb energy, leading to rapid crack initiation and propagation and brittle failure (axial splitting happens after their yield point). An example of splitting crack is shown in Figure 5.10a.

3) Circumferential cracks:

Under compression, and unavoidable friction between the specimen surfaces and the platens, there is not only a significant shear stress induced on the surface, but also a gradient in shear stress at different heights within the sample (highest at mid-height), which can lead to circumferential cracks. Brittle gels may exhibit circumferential cracks due to lack of plastic deformation, while very soft gels form curved cracks to adapt to the gel's high surface area changes. An example is shown in Figure 5.10a.

4) Branching:

As the main crack grows, the stress at the crack tip intensifies, leading to localized areas of deformation. These localizations cause smaller cracks to merge (coalescence), forming micro-branches[443]. As the stress continues to build, these micro-branches extend and develop into larger macro-branches, creating a complex network of cracks, which can be seen in most of the hydrogels in Figure 5.9.

5) Fragmentation:

The kinking cracks can join together or join with circumferential cracks, leading to fragmentation. The higher stress concentration in the outer part of the hydrogels makes the outer regions more susceptible to crack initiation and propagation, creating isolated fragments and resulting in a fragmented zone near the edge of the disk. Fragmentation could be a result of mixed-mode consisting of mode I and mode III (antiplane shear), causing segmented fracture fronts. The gradient in shear stress on the surface controls the direction of fragmentation, which is mostly circumferential. An example of fragmentation is shown in Figure 5.10c.

Now that different crack types and phenomena are defined, the following observations can be drawn from Figure 5.9:

- **Final Cross-Sectional Area:** there is an inverse relationship between the final cross-sectional area and the gel's strength and plasticity. Acidic 1:1 hydrogels, which experienced brittle failure, had the lowest final cross-sectional area;
- **Crack Density and length:** the density of microcracks generally decreases over time, while the density of larger cracks increases. Microcracks indicate plasticity and weaker strength, whereas larger cracks suggest brittleness and higher strength;
- **Radial Cracks:** all hydrogels exhibited some degree of radial cracking as the surface area increased;
- **Crack Blunting:** primarily observed in hydrogels five minutes after gelation (t = 15 minutes) and in type iii gels, which are softer and undergo more plastic deformation;
- **Radial Crack Kinking:** all hydrogels exhibited radial crack kinking, except those that exhibited radial crack tip blunting;

- **Fragmentation:** results from the joining of kinked radial and circumferential cracks, mainly seen in type i and type ii gels. The fragmentation zone is concentrated in the outer 1/4 of the radius due to higher tensile hoop stresses and boundary effects. Type iii weak, plastic hydrogels tended to deform and absorb energy rather than fragment;
- **Axial Splitting Cracks:** occur only in brittle hydrogels (type i gels or some gels an hour post gelation). Surface splitting cracks were observed in all types of gels except shortly after gelation (t = 15 minutes);
- **Gel Composition:** all gels made with an initial water-to-waterglass concentration of 1:5 (using boric or phosphoric acid) closely resemble each other. However, there is a distinct difference between the fractography of concentrated acidic and basic gels.

5.5.1.5. True versus engineering stress-strain

The compressive true stress-strain curves of the basic and acidic silica hydrogels can be compared with the corresponding compressive engineering stress-strain curves in Figure 5.11 and Figure 5.12, respectively. As can be seen, generally the true stress is lower than the corresponding engineering stress due to the constant increase in cross-sectional area of the hydrogels during compression and the final true strain is 0.40 instead of 0.5. The difference between the engineering and true stress at the maximum stress point (at e = 0.5 for ductile hydrogels and at the fracture point with e = 0.3-0.5 strain for brittle hydrogels) relative to the value of engineering stress is shown in Figure 5.13. The results show that engineering stress is 28-55% and 25-62% higher than its true value in basic gels and acidic gels, respectively. This suggests that engineering stress significantly overestimates the strength at higher strains due to the reduction in cross-sectional area during plastic deformation and densification, regardless of processing conditions. In the basic group, the basic 1:3 gel, and the acidic 1:1 gel in the acidic group had the lowest change between true and engineering stress. Both of these samples also exhibited the highest strength in their respective groups. This result implies that gels with higher strength tend to have a less pronounced difference between engineering and true stress, potentially due to a more stable cross-sectional area during compression. Converting the engineering compressive stress-strain to true stress-strian did not change the overall tend observed in hydrogels.

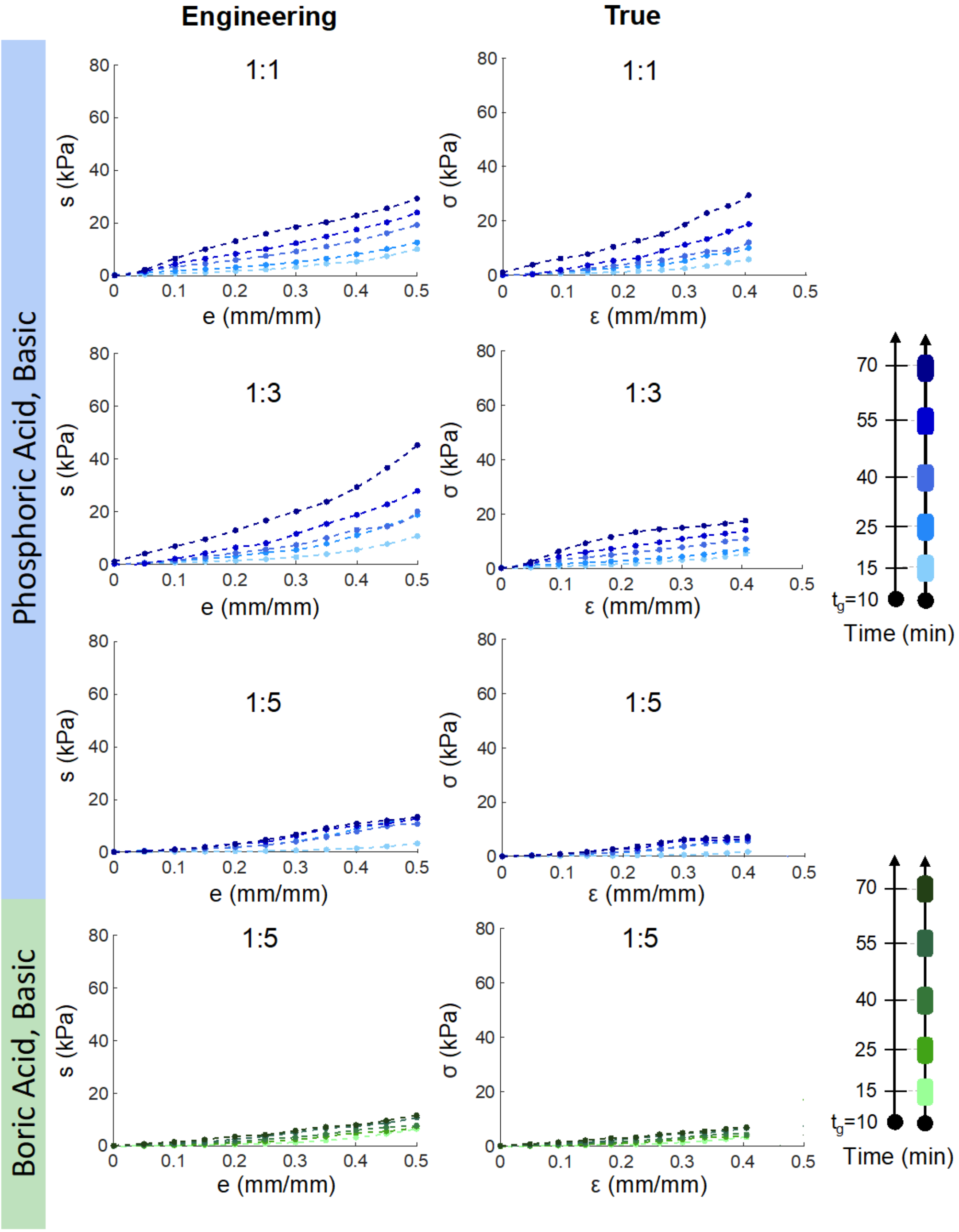

Figure 5.11 Engineering compressive stress-strain curve (left) versus true compressive stress-strain curve (right) for basic silica hydrogels made with boric acid at a waterglass-to-water weight ratio of 1:5, and phosphoric acid at ratios of 1:1, 1:3, and 1:5 (n = 1). The stress-strain curves, shown at 5, 15, 30, 45, and 60 minutes post-gelation. The curves are plotted based on 11 points with cubic spline extrapolation, using real-time monitoring of cross-sectional area to obtain true stress data.

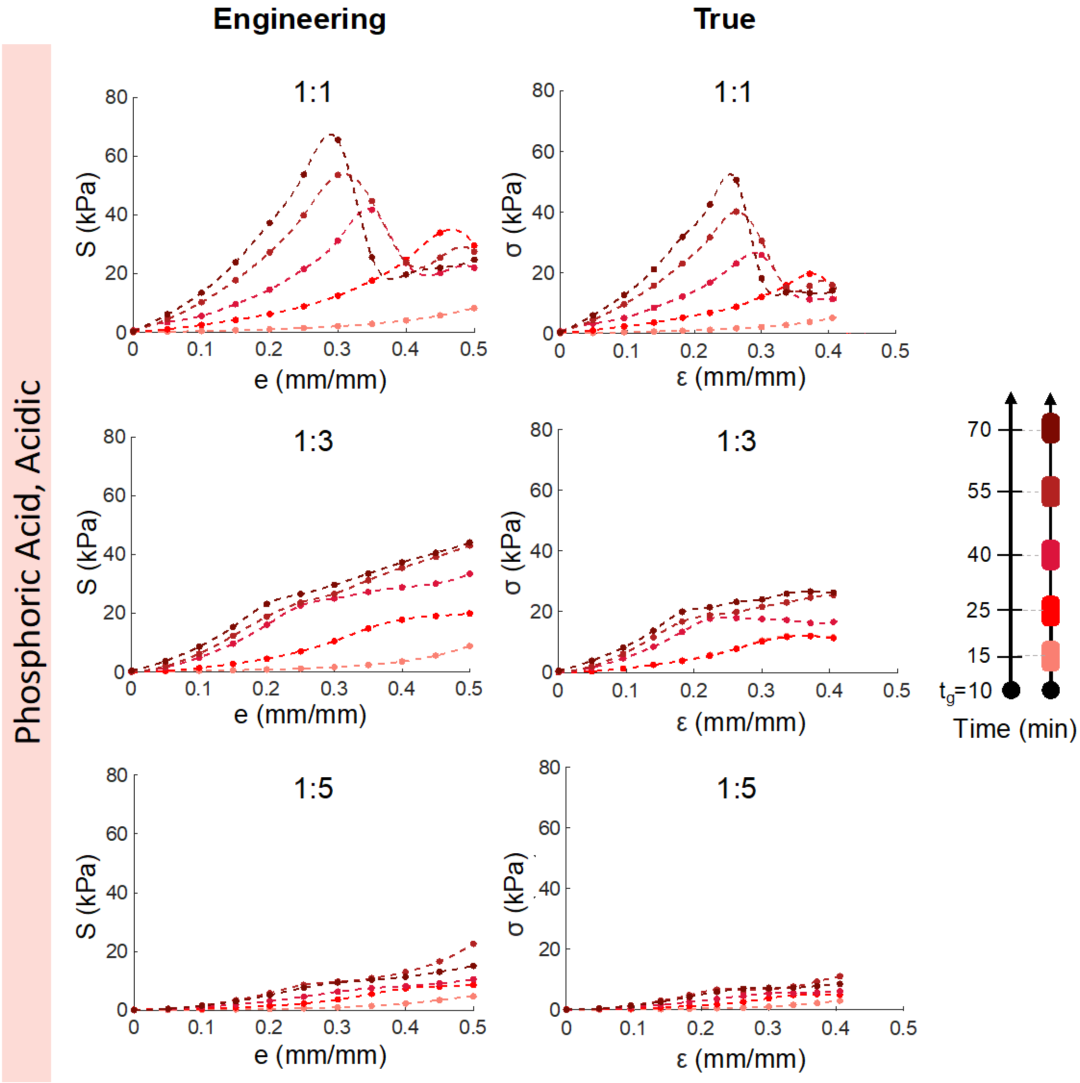

Figure 5.12 Engineering compressive stress-strain curve (left) versus true compressive stress-strain curve (right) for acidic silica hydrogels made with phosphoric acid at ratios of 1:1, 1:3, and 1:5. The stress-strain curves, shown at 5, 15, 30, 45, and 60 minutes post-gelation (N=1). The curves are plotted based on 11 points with cubic spline extrapolation, using real-time monitoring of cross-sectional area to obtain true stress data.

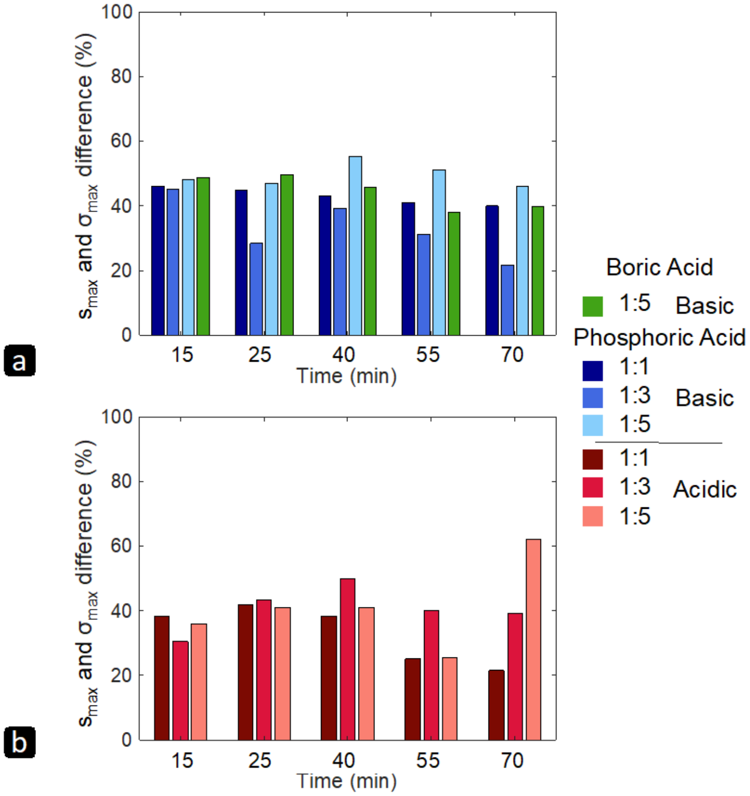

Figure 5.13 Percentage of the overestimation of maximum engineering stress relative to the maximum compressive stress obtained from true stress-strain curves of (a) basic silica hydrogels made with boric acid at a waterglass-to-water weight ratio of 1:5, and phosphoric acid at ratios of 1:1, 1:3, and 1:5 (N=1), at 5, 15, 30, 45, and 60 minutes post-gelation; and(b) acidic silica hydrogels made with phosphoric acid at ratios of 1:1, 1:3, and 1:5 (N=1), at 5, 15, 30, 45, and 60 minutes post-gelation.

5.5.2. Microstructure, and its connection to molecular structure and mechanical properties

The micrographs of different acid-initiated hydrogels five and sixty minutes after gelation are shown in Figure 5.14. Agglomeration of silicate particles in a basic medium results in the formation of a uniform porous mesh-like network structure, with pore sizes ranging from 3 µm to 20 µm (Figure 5.13(a–d)). The pore size tends to increase with increasing water content and appears very similar between basic 1:5 gels made with boric acid and phosphoric acid, as they contain the same amount of water. These 3D networks appear as a continuous network of walls less than a micrometer thick. The porous mesh-like network structure is more uniform at higher waterglass concentrations, though it becomes non-uniform and significantly distorted when water content exceeds 75 wt.% (basic 1:5 gels).

The higher maximum strength in basic 1:3 gels compared to basic 1:1 gels can also be explained by the observed microstructure. In basic 1:3 gels, the network remains intact (except for larger pores and pore volume) and is not distorted as in the 1:5 gels. Although there is less silica compared to the 1:1 gels (25% versus 50% waterglass), the large number of connections between the silicate particles and strong hydrogen bonding with water contribute to the enhanced strength. Additionally, the wall thickness in the 1:3 gels appears even thicker than in the concentrated 1:1 gels. The pore size distribution is quite wide for all basic hydrogels.

Concentrated acidic and basic gels differ significantly in microstructure shortly after gelation (Figure 5.14a and Figure 5.14e). Concentrated acidic gels show a fused-sphere-like microstructure, with spheres connected throughout the whole sample volume. The size of these spheres ranges from approximately 1 to 3 μm. This fused-sphere morphology creates voids between the agglomerated spheres, forming a continuous pore space. The structure of the 1:1 acidic gel is denser than that of the basic gel. This structure, with numerous small pores, may result in lower syneresis and greater water-holding capacity, thus promoting the stability of the gel and giving it a more rigid and brittle behavior. As more water is introduced into acidic gels (Figure 5.14(e-g)), the microstructure becomes more similar to that of basic gels, with a distorted 3D network of walls and large pores. The structure of acidic 1:5 gels is very similar to that of basic 1:5 gels, aligning with their similar mechanical properties.

The gel point does not indicate the completion of gel structure formation. An hour after gelation, the walls in all basic gels become thicker, and the pore size reduces, ranging from roughly 1 μm to 15 μm (Figure 5.14(h-k)). At this point, the gel network is more developed and has aged. Two events are believed to occur simultaneously during the aging process, leading to increased wall thickness: deposition of smaller dissolved particles on larger particles and neck growth between deposited silica particles[444]. It should be noted that the pores are not filled with pure water; many silicate oligomers or small particles can still deposit on the silicate particles and agglomerates. In acidic gels, a homogeneous, non-macroporous structure forms after aging. The structure in concentrated acidic gels is so packed that it gives a glass-like appearance. Similar to the state five minutes after gelation, acidic 1:5 gels behave similarly to their basic counterparts.

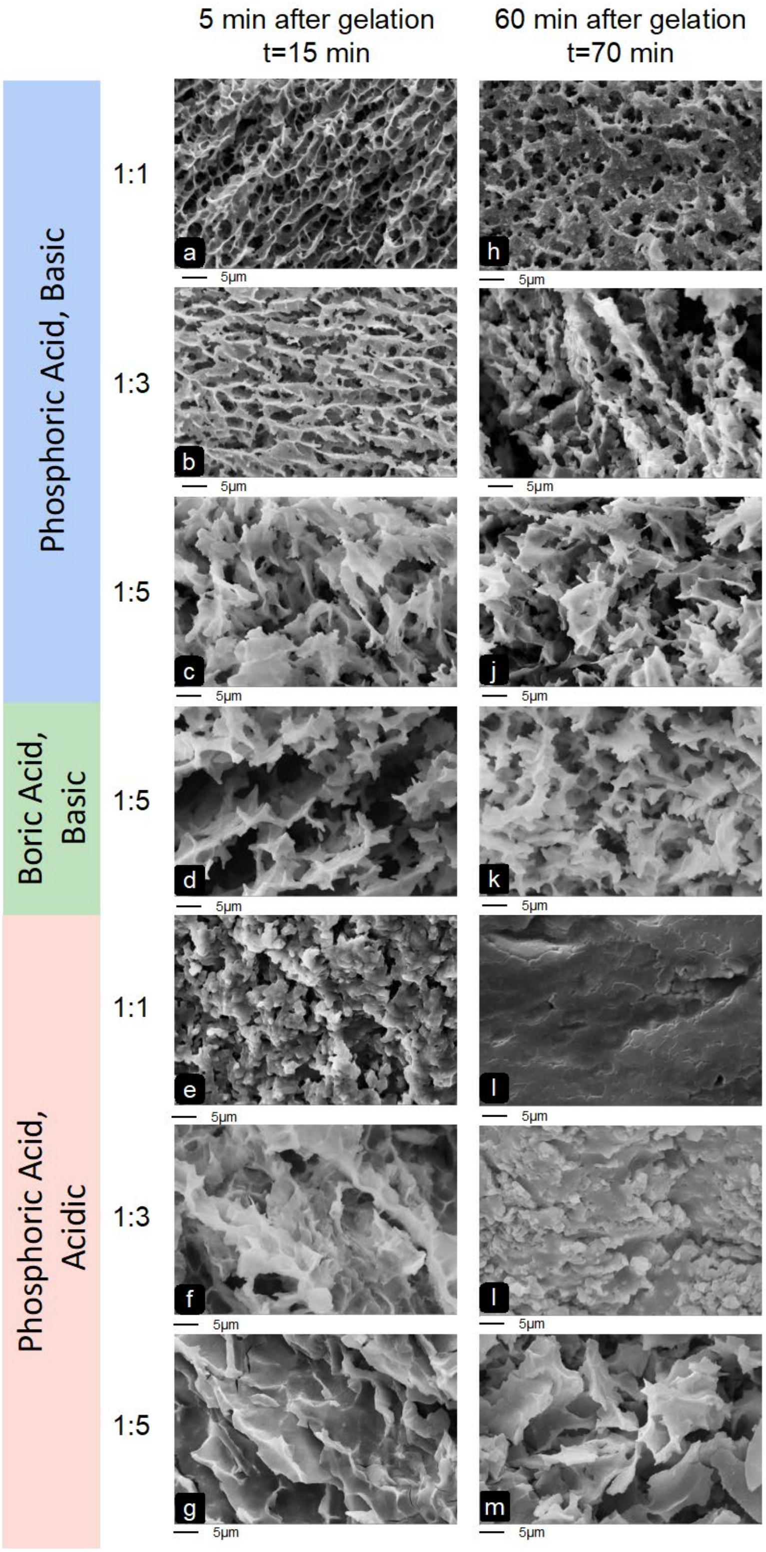

Figure 5.14 SEM micrographs of silica hydrogels made with phosphoric acid and boric acid at basic and acidic pH and different water:waterglass ratios, 5 minutes after gelation point (a-g) and 60 minutes after gelation point (h-m).

The differences between these gel systems may be attributed to the size of their structural units, the size of primary and secondary silicate particles, and the density of physical bond formation within the network, which consequently affect the microstructure, pore size, and mechanical properties. From previous chapters, we observed that gelation in silica hydrogels occurs through the agglomeration of silicate particles via physical interactions such as hydrogen bonding and electrostatic interactions.

The larger and bulkier structural units in basic gels form larger and looser particles due to their fewer active sites, steric hindrance, and some degree of negative charge repulsion. These factors prevent them from forming packed structures when agglomerated, so they tend to spread as walls throughout the space, creating mesh-like structures with large spaces between them filled with liquid. The low density and the freedom of large silicate particles to move and slide over one another give the material a ductile mechanical behavior. Over time, the walls thicken and the pores become smaller.

In contrast, the smaller structural units in acidic gels form smaller and more tightly packed particles. Upon agglomeration, these particles form packed spherical structures due to their high surface area and numerous active sites. These particles form strong connections both with each other and with the trapped water inside the pores, leading to a fused-sphere-like microstructure with rough surfaces and many tiny pores. The high density and rigid connections between the small silicate particles and water molecules give acidic gels a brittle behavior. Over time, the structure becomes more packed with smoother surfaces.

5.6. Conclusion

In this study, we investigated the effects of processing conditions (pH, waterglass concentration, and type of acid initiator) on the mechanical properties, deformation, and failure mechanisms of acid-initiated silica hydrogels. Using an innovative experimental setup to monitor changes in cross-sectional area in real-time under compression, we gained insights into compressive stress-strain behavior and failure mechanisms. Key findings include:

- Silica hydrogels showed varied responses under compression depending on their preparation conditions. Basic gels transitioned from continuous strain hardening to showing a plastic plateau with increased water content. Acidic gels exhibited brittle fracture but shifted towards a plastic plateau with more water;

- Mechanical strength depended on both composition and aging time, increasing over time in all hydrogels, though this effect was reduced with dilution. Basic 1:3 gels and acidic 1:1 gels exhibited the highest stress in their groups, with 38.03 ± 11.23 MPa and 53.65 ± 11.43 MPa, respectively. Although their maximum strengths were not statistically different, their behaviors differed: basic gels were ductile up to 0.5 strain, while acidic gels experienced brittle fracture at 0.3 strain. Basic gels made with boric acid and phosphoric acid at the same waterglass concentration showed similar mechanical strength and deformation behavior, highlighting the influence of pH and waterglass concentration over the type of acid on mechanical response;
- Engineering stress underestimated maximum strength at higher strains—due to significant cross-sectional area increases during deformation—with differences of 21-55% for basic gels and 21-66% for acidic gels;
- The first and second derivatives of stress-strain curves provided insights into transition points of different deformation regions, correlating with real-time deformation observations such as crack initiation and propagation;
- Fractography at maximum strength revealed various crack types and phenomena, including radial cracks, circumferential cracks, splitting, fragmentation, and microcrack networks;
- Microstructural analysis showed that the arrangement of large silicate particles and flexible connections, along with large pores (3-5 μm), resulted in ductile behavior in concentrated basic gels. In contrast, small silicate particles and rigid connections in acidic gels resulted in brittle behavior. Both gel types exhibited increased ductility and larger pore sizes (15-20 μm) upon dilution.

These insights into the mechanical properties of silica hydrogels can inform the design of chemically controlled routes for modifying the macroscopic properties of final gels for specific applications, including the development of formable, *in situ* setting bioactive glass-waterglass composite bone scaffolds.

Chapter 6: Conclusions and Future Work

6.1 Experimental conclusions

The key findings of this research include:

- **Gelation kinetics of sodium silicate solutions can be controlled by adjusting the processing conditions.**
    a. Gelation time versus pH data were fit to exponential and fourth-order polynomial equations in the basic (7-11) and acidic (2-7) regions, respectively. A relation was found between the fitted equation parameters and waterglass concentration, allowing prediction of gelation time for any given concentration and pH.

    b. Gelation time showed a maximum at pH~2 for all waterglass concentrations and showed an instant gelation time zone at different pH ranges, depending on the waterglass concentration. The ranges were: narrowing down from 10.5 to 3.8, from 10.2 to 5.5, and from 9.5 to 5.8 as the waterglass:water weight ratio increased from 1:5, 1:3, to 1:1 respectively.

    c. Any gelation time, including the target 10 minutes gelation time, could be achieved in both acidic and basic regions. The specific pH for the target gelation time could be adjusted toward neutral by decreasing the initial waterglass concentration. However, the final microstructure and optical properties of these gels would be significantly different for concentrated gels, with the difference diminishing as waterglass is diluted.

    d. With boric acid, being weaker than phosphoric acid, pH was only lowered in the basic region. Because a vast volume of boric acid is required to lower the pH of waterglass, the waterglass:water ratio was changed from 1:1 to 1:5 after introducing the acid. Overall, the effect of acid type was found to be less significant in contrast with pH and waterglass concentration. However, the large fluctuation in the water volume concomitant with acid introduction makes controlling and predicting their gelation kinetics more difficult in contrast to using phosphoric acid.

- **Studying the optical properties of gels provided insights into both gelation kinetics and microstructure.**
    a. UV-VIS spectroscopy proved useful for indicating the gel point, marked by a rapid decrease in the light transmittance rate over time. Differentiating light transmittance spectra using various orders of derivatives enhanced resolution for a more accurate determination of the gelation point.

    b. Generally, the gelation point obtained by light transmittance data was shorter than the ones obtained from the tube inversion method (~8 minutes versus ~10 minutes), indicating that the former points to the onset of gelation while the latter points to the formation of a rigid network.

    c. The light transmittance data, in combination with SEM micrographs, revealed that acidic gels are composed of smaller particles and smaller pores with less light scattering, whilst basic gels have larger particles and larger pores, leading to more light scattering and opacity.

    d. The optical properties and microstructure of basic 1:5 gels made with boric acid were similar to what was observed for 1:3 and 1:5 basic gels made with phosphoric acid, respectively. This finding highlights a similar outcome found for gelation kinetics: controlling and predicting gels' properties becomes more challenging when using boric acid.

- **A revised interpretation of Raman spectroscopy data and a theory of gelation mechanism were provided for silicate solutions.**
    a. Re-examination of the commonly cited Raman peaks for silicate solutions and gels revealed that the assignment of Si-O-Si bending modes to plain n-membered ring structures is inconsistent with silicate structures identified by 29Si NMR in these solutions.

    b. A fresh approach for interpreting the 400-700 cm^{-1} region of Raman shift spectra was provided based on silicate species identified by 29Si NMR. Silicate structural units were divided into 3-membered, 3,4-membered, 4-membered, and 5-membered rings, encompassing various structures such as cage-like, quasi-cage, simple, and double-ring units, with the complexity and size of polymerized species increasing moving toward lower wavenumbers.

   c. Most silicate structural units present in sodium silicate solutions are within the colloidal particle size range (>1 nm) and act as primary particles during gelation. This fact suggests that the formation of new Si-O-Si bonds is not essential for gel formation, which contradicts the widely accepted theory that new Si-O-Si bonds are a prerequisite for gelation.

- **Real-time Raman spectroscopy proved to be an effective technique for quantitatively studying the sol-gel transition at molecular level in acid-initiated sodium silicate solutions under different processing conditions.**

   a. In acidic conditions, hydrolysis proceeds more rapidly than condensation, leading to depolymerization and the formation of smaller, lower-order silicate units. Conversely, in basic conditions, polymerization dominates, resulting in larger, higher-order units.

   b. Basic gels are made of large, loose secondary particles that agglomerate into a gel network with large pores, while acidic gels are made of small, compact secondary particles that agglomerate into a dense gel network with small pores.

   c. Observing no change in the Raman spectra during the sol-gel transition suggests that particle aggregation is primarily driven by fast-acting physical interactions, such as hydrogen bonding and electrostatic interactions.

   d. The presence of more water in the system promotes hydrolysis/depolymerization in acidic conditions and polymerization in basic conditions, though it does not affect the dominance of higher-order or lower-order silicate species. Silicate structural units in basic gels made with boric acid were similar to basic gels made with phosphoric acid, indicating that the pH is the main factor in dictating molecular structure. For the microstructure, however, the waterglass concentration is inversely proportional to the pore size.

- **Mechanical properties of silica hydrogels was greatly dependent on processing conditions and time.**
    a. Basic gels transitioned from continuous strain hardening to showing a plastic plateau with increased water content. Acidic gels exhibited brittle fracture but shifted towards a plastic plateau with increasing water content.
    b. Mechanical strength increased over time in all hydrogels, though this effect was reduced with dilution. Basic 1:3 gels and acidic 1:1 gels exhibited the highest strength in their groups, with engineering strengths of 38.0 ± 11.2 MPa and 53.7 ± 11.4 MPa, respectively. Although their maximum strengths were not statistically different, their behaviors significantly differed: basic gels were ductile up to 0.5 strain, while acidic gels experienced brittle fracture at 0.3 strain.
    c. Basic gels made with boric acid and phosphoric acid, at the same waterglass concentration, showed similar mechanical strength and deformation behavior, highlighting the greater influence of pH and waterglass concentration over the type of acid on mechanical response.
- **Real-time monitoring of cross-sectional area under compression gave valuable insights into mechanical behaviour of hydrogels.**
    a. Engineering stress overerestimated strength at higher strains due to cross-sectional area reduction during deformation, with differences of +21-55% for basic gels and +21-66% for acidic gels.
    b. The first and second derivatives of stress-strain curves provided insights into transition points of different deformation regions, correlating with real-time deformation observations such as crack initiation and propagation.
    c. Fractography at maximum strength revealed various crack types and phenomena, including radial cracks, circumferential cracks, splitting, fragmentation, and microcrack networks.
- **A direct relationship was found between processing conditions, the resulting molecular-and micro-structure, and mechanical behavior of the silica hydrogels.**
    a. Structural analysis at molecular, micro, and macro levels showed that the arrangement of large silicate particles and flexible connections, along with large

pores (3-5 μm), resulted in ductile behavior in concentrated basic gels. In contrast, small silicate particles and rigid connections in acidic gels resulted in brittle behavior. Both gel types exhibited increased ductility and larger pore sizes (15-20 μm) upon dilution.

6.2. Speculations on optimum sol-gel processing conditions for gel binders in bone tissue scaffolds

Based on current findings, silica gels prepared with higher waterglass-to-water weight ratios appear promising for practical applications. These gels exhibit gelation at more moderate pH levels, which is advantageous for compatibility with biological environments. Additionally, their gelation time demonstrates a shallower slope relative to pH, simplifying the control of gelation kinetics because of decreased sensitivity to pH changes.

Furthermore, regardless of acidity or alkalinity, diluted waterglass gels (with a waterglass-to-water ratio of 1:5) exhibit remarkably similar microstructure and ductile behavior. Despite their lower compressive strength compared to more concentrated gels, their soft and ductile nature enables the composite scaffold to deform plastically under stress, rather than fracturing. This characteristic is crucial as it helps the scaffold absorb energy and maintain structural integrity. Moreover, the reversible nature of these gels, facilitated by the formation of new hydrogen bonds post-deformation, suggests potential self-healing properties and aids in degradation processes. This dual functionality not only enhances the scaffold's mechanical stability but also contributes to its longevity and biocompatibility in biological applications.

In summary, exploring the behavior of silica gels at varying waterglass-to-water ratios provided valuable insights into optimizing composite bone scaffold binders. Future research should focus on refining these processing conditions by characterising the composite scaffolds.

6.3. Limitations

This section discusses the limitations and potential sources of error in this research, which stemmed from experimental constraints and methodological choices. Addressing these limitations is crucial for refining methodologies and enhancing the applicability of the results in future work.

1. **Limitations of Real-Time Raman Spectroscopy:** Real-time Raman spectroscopy was performed 2-3 minutes after mixing the waterglass with the acid solution. The instrument's

setup did not permit mixing solutions while performing analysis, leading to missing a critical time window for observing the transition from the initial waterglass Raman spectrum to the final gel Raman spectrum. Additionally, the procedure for background removal from the container and for removing acid peaks was non-standard and introduced some uncertainty.

2. **Lack of Standardized Methods for Mechanical Testing:** The absence of a universally accepted method for testing hydrogels poses a challenge. Some studies rely on ASTM D69526[420], which is tailored for rigid plastics and does not accurately reflect the mechanical behavior of hydrogels. Variations in specimen aspect ratios can lead to differences in stress distribution, with non-standard ratios potentially causing buckling or bending under load and resulting in inaccurate measurements. Moreover, the friction between the specimen and testing machine could also be a source of error. Despite using silicone oil as a lubricant, barrel deformation was observed during compression. Furthermore, hydrogel behavior, including fracture onset, crack propagation, and mechanical damage, is strain-rate dependent. While relative assessments within this study were possible due to similar testing conditions, comparisons with other studies, particularly at large deformations, remain problematic.

   It should be noted that while the stress-strain behavior of materials is ideally size-independent, practical factors can introduce size-dependence, particularly in soft materials like silica hydrogels. Geometric effects, boundary conditions, and the presence of defects or inhomogeneities can alter how a material deforms under load, leading to variations in mechanical performance. Additionally, the surface area-to-volume ratio can influence behavior, as surface defects may significantly affect larger specimens. Therefore, while strength values may vary among different gels, the deformation mechanisms likely remain consistent. Deformation mechanisms are primarily governed by the strength of the connections between particles, which is influenced by pH and waterglass concentration and is expected to be independent of gel size.

3. **Microstructural Analysis Challenges:** Microstructural analysis was conducted using scanning electron microscopy (SEM), where hydrogels were frozen and then freeze-dried. Despite using liquid nitrogen to achieve the fastest cooling rate, the process of ice

crystallization and its impact on the pores and gel network could not be fully controlled. This limitation may have affected the accuracy of the observed pore structure and network integrity.

6.4. Future work

Building upon the key findings of this study, several areas for future research are essential to optimize the processing and fabrication of waterglass-bioactive glass composite scaffolds for bone tissue engineering:

1. **Composite Scaffold Mechanical Properties:** Future research should investigate how various silica gel processing conditions affect the mechanical properties of the composite scaffolds, including: evaluating mechanical strength, deformation, and failure mechanisms. Other key variables to consider are the waterglass-to-bioactive glass ratio, aging time, the size and size distribution of bioactive glass particles, and the force applied during molding. Understanding these factors will be crucial for enhancing the scaffold's mechanical behavior, as well as finding the optimum silica gel composition.
2. **Composite Scaffold Microstructure and Porosity:** A detailed analysis of the scaffold's microstructure, including pore size and distribution, open versus closed porosity, and pore volume is necessary to ensure that the scaffolds support optimal bone cell infiltration and tissue regeneration. The effects of waterglass gelation conditions, the ratio of waterglass to bioactive glass, and the molding force on the microstructural characteristics should be thoroughly examined.
3. **In-Vitro and In-Vivo Degradation Studies:** As silica hydrogels are physical gels, they are expected to degrade at a notable rate in simulated body fluid (SBF)/inside body. Future studies should focus on the *in-vitro* and *in-vivo* degradation rates of both silica gels and the composite scaffolds. This research should also include studying how degradation kinetics affect mechanical properties and overall stability of bone tissue scaffold, while inside a bone defect, or simulated bone defect. Moreover, cell culture studies should be performed to investigate the viability of cells growing on, and in the environment produced by, the gel and scaffold materials.

4. **Investigation of pH Effects on Surrounding Media:** The impact of the pH of silica gels on the pH of SBF or other relevant media should be carefully studied. This study should include examining how exposure to acidic, neutral, or basic gels affects the surrounding medium's pH. Similar tests should be conducted for composite scaffolds to understand their influence on pH fluctuations.

6.5. Concluding remarks

This study has made four major contributions to the field:

1. By studying and modeling the gelation kinetics of silica gels over a broad pH range (2-11), this research provided crucial data for controlling silica gel formation in various applications. Previous studies have been limited to much narrower pH ranges, making this comprehensive data a big step for a better understanding of the processing of silica gels.
2. In-situ Raman spectroscopy for real-time analysis of the sol-gel transition of waterglass was performed for the first time. This approach uncovered significant inconsistencies between widely cited Raman peaks and the actual silicate species present in solutions. The findings also challenged existing theories on silica gelation mechanisms and provided evidence for the physical and chemical nature of the gels.
3. An innovative setup was developed to monitor real-time changes in cross-sectional area under compression. This new approach offered valuable insights into compressive mechanical behavior, including deformation and failure mechanisms, overcoming the limitations of previous side-view observations and providing a direct view of cross-sectional area changes along with damage mechanisms and accumulation.
4. The research established meaningful links between processing conditions, molecular and microstructural features, and the optical and mechanical properties of silica gels. This integration of data helps to fill gaps in the processing-structure-property relationships, providing a more complete understanding of silica gel behavior.

Bibliography

(1) Einhorn, T. A.; Gerstenfeld, L. C. Fracture Healing: Mechanisms and Interventions. *Nature Reviews Rheumatology* **2015**, *11* (1), 45–54. https://doi.org/10.1038/nrrheum.2014.164.Fracture.

(2) Stewart, S.; Bryant, S. J.; Ahn, J.; Hankenson, K. D. Bone Regeneration. In *Translational Regenerative Medicine*; Elsevier Inc., 2015; pp 313–333. https://doi.org/10.1016/B978-0-12-410396-2.00041-4.

(3) Braithwaite, R. S.; Col, N. F.; Wong, J. B. Estimating Hip Fracture Morbidity, Mortality and Costs. *Journal of the American Geriatrics Society* **2003**, *51* (3), 364–370. https://doi.org/10.1046/j.1532-5415.2003.51110.x.

(4) Arrington, E. D.; Smith, W. J.; Chambers, H. G.; Bucknell, A. L.; Davino, N. A. Complications of Iliac Crest Bone Graft Harvesting. *Clinical Orthopaedics and Related Research* **1996**, *329*, 300–309. https://doi.org/10.1097/00003086-199608000-00037.

(5) Goulet, J. A.; Senunas, L. E.; DeSilva, G. L.; Greenfield, M. L. V. H. Autogenous Iliac Crest Bone Graft. Complications and Functional Assessment. *Clinical Orthopaedics and Related Research* **1997**, *339*, 76–81.

(6) Shrivats, A. R.; Alvarez, P.; Schutte, L.; Hollinger, J. O. Bone Regeneration. In *Principles of Tissue Engineering: Fourth Edition*; Elsevier, 2013; pp 1201–1221. https://doi.org/10.1016/B978-0-12-398358-9.00055-0.

(7) Schlickewei, W.; Schlickewei, C. The Use of Bone Substitutes in the Treatment of Bone Defects - The Clinical View and History. *Macromolecular Symposia* **2007**, *253*, 10–23. https://doi.org/10.1002/masy.200750702.

(8) Smith, J. O.; Aarvold, A.; Tayton, E. R.; Dunlop, D. G.; Oreffo, R. O. C. Skeletal Tissue Regeneration: Current Approaches, Challenges, and Novel Reconstructive Strategies for an Aging Population. *Tissue Engineering - Part B: Reviews* **2011**, *17* (5), 307–320. https://doi.org/10.1089/ten.teb.2011.0143.

(9) Grand View Research. *Bone Grafts And Substitutes Market Size, Share & Trends Analysis Report By Material Type (Allograft, Synthetic), By Application Type (Spinal Fusion, Craniomaxillofacial, Long Bone), By Region, And Segment Forecasts, 2019 - 2026*; 2019.

(10) Langer, R.; Vacanti, J. P. Tissue Engineering. *Science* **1993**, *260* (5110), 920–926. https://doi.org/10.1080/00131725009342110.

(11) Gentleman, E.; Polak, J. M. Historic and Current Strategies in Bone Tissue Engineering: Do We Have a Hope in Hench? *Journal of Materials Science: Materials in Medicine* **2006**, *17* (11), 1029–1035. https://doi.org/10.1007/s10856-006-0440-z.

(12) Hench, L. L. The Story of Bioglass®. *Journal of Materials Science: Materials in Medicine* **2006**, *17* (11), 967–978. https://doi.org/10.1007/s10856-006-0432-z.

(13) Hench, L. L.; Splinter, R. J.; Allen, W. C.; Greenlee, T. K. Bonding Mechanisms at the Interface of Ceramic Prosthetic Materials. *Journal of Biomedical Materials Research* **1971**, *5* (6), 117–141. https://doi.org/10.1002/jbm.820050611.

(14) Yuan, H.; De Bruijn, J. D.; Zhang, X.; Van Blitterswijk, C. A.; De Groot, K. Bone Induction by Porous Glass Ceramic Made from Bioglass® (45S5). *Journal of Biomedical Materials Research* **2001**, *58* (3), 270–276. https://doi.org/10.1002/1097-4636(2001)58:3<270::AID-JBM1016>3.0.CO;2-2.

(15) Fujishiro, Y.; Hench, L. L.; Oonishi, H. Quantitative Rates of in Vivo Bone Generation for Bioglass® and Hydroxyapatite Particles as Bone Graft Substitute. *Journal of Materials Science: Materials in Medicine* **1997**, *8* (11), 649–652. https://doi.org/10.1023/A:1018527621356.

(16) Jones, J. R. Review of Bioactive Glass: From Hench to Hybrids. *Acta Biomaterialia* **2013**, *9* (1), 4457–4486. https://doi.org/10.1016/j.actbio.2012.08.023.

(17) Filho, O. P.; Latorre, G. P.; Hench, L. L. Effect of Crystallization on Apatite-Layer Formation of Bioactive Glass 45S5. *Journal of Biomedical Materials Research* **1996**, *30* (4), 509–514. https://doi.org/10.1002/(SICI)1097-4636(199604)30:4<509::AID-JBM9>3.0.CO;2-T.

(18) Rahaman, M. N.; Day, D. E.; Sonny Bal, B.; Fu, Q.; Jung, S. B.; Bonewald, L. F.; Tomsia, A. P. Bioactive Glass in Tissue Engineering. *Acta Biomaterialia* **2011**, *7* (6), 2355–2373. https://doi.org/10.1016/j.actbio.2011.03.016.

(19) Webber, M. J.; Khan, O. F.; Sydlik, S. A.; Tang, B. C.; Langer, R. A Perspective on the Clinical Translation of Scaffolds for Tissue Engineering. *Annals of Biomedical Engineering* **2015**, *43* (3), 641–656. https://doi.org/10.1007/s10439-014-1104-7.

(20) Baino, F.; Novajra, G.; Vitale-Brovarone, C. Bioceramics and Scaffolds: A Winning Combination for Tissue Engineering. *Frontiers in Bioengineering and Biotechnology* **2015**, *3* (December), 1–17. https://doi.org/10.3389/fbioe.2015.00202.

(21) Hollister, S. J. Scaffold Engineering: A Bridge to Where? *Biofabrication* **2009**, *1* (1). https://doi.org/10.1088/1758-5082/1/1/012001.

(22) Henkel, J.; Woodruff, M. A.; Epari, D. R.; Steck, R.; Glatt, V.; DIckinson, I. C.; Choong, P. F. M.; Schuetz, M. A.; Hutmacher, Di. W. Bone Regeneration Based on Tissue Engineering Conceptions-A 21st Century Perspective. *Bone Research* **2013**, *1*, 216–248. https://doi.org/10.4248/BR201303002.

(23) Guzzo, C. M.; Nychka, J. Fabrication of a Porous and Formable Ceramic Composite Bone Tissue Scaffold at Ambient Temperature. *Metallurgical and Materials Transactions A* **2020**, *12*, 1–17. https://doi.org/10.1007/s11661-020-05924-9.

(24) Guzzo, C. M.; Nychka, J. A. Bone 'Spackling' Paste: Mechanical Properties and in Vitro Response of a Porous Ceramic Composite Bone Tissue Scaffold. *Journal of the Mechanical Behavior of Biomedical Materials* **2020**, *112* (May), 103958. https://doi.org/10.1016/j.jmbbm.2020.103958.

(25) Atterton, D. V. The Carbon-Dioxide Process. *AFS Transactions* **1956**, *64*, 14–18.

(26) Ikeda, K. Preparation of Fly Ash Monoliths Consolidated with a Sodium Silicate Binder at Ambient Tempreture. *Cement and Concrete Research* **1997**, *27* (5), 657–663.

(27) Tognonvi, M. T.; Kouassi, S. S.; Maeda, T.; Soro, J.; Rossignol, S.; Bonnet, J. P. Use of Sodium Silicate Gel as Precursor of Binder for Cold Consolidated Materials. *Advances in Science and Technology* **2010**, *69*, 57–62. https://doi.org/10.4028/www.scientific.net/ast.69.57.

(28) Nychka, J. New Processing Route to Porous Bioactive Glass Composites for Bone Tissue Scaffolds.

(29) Konttinen, Y. T.; Milošev, I.; Trebše, R.; van der Linden, R.; Pieper, J.; Sillat, T.; Virtanen, S.; Tiainen, V. M. Metals for Joint Replacement. In *Joint Replacement Technology (Second Edition)*; 2014; pp 81–151. https://doi.org/10.1533/9780857098474.2.81.

(30) Turnbull, G.; Clarke, J.; Picard, F.; Riches, P.; Jia, L.; Han, F.; Li, B.; Shu, W. 3D Bioactive Composite Scaffolds for Bone Tissue Engineering. *Bioactive Materials* **2018**, *3* (3), 278–314. https://doi.org/10.1016/j.bioactmat.2017.10.001.

(31) Yusop, A. H.; Bakir, A. A.; Shaharom, N. A.; Abdul Kadir, M. R.; Hermawan, H. Porous Biodegradable Metals for Hard Tissue Scaffolds: A Review. *International Journal of Biomaterials* **2012**, *2012*. https://doi.org/10.1155/2012/641430.

(32) Stevens, B.; Yang, Y.; Mohandas, A.; Stucker, B.; Nguyen, K. T. A Review of Materials, Fabrication Methods, and Strategies Used to Enhance Bone Regeneration in Engineered Bone Tissues. *Journal of Biomedical Materials Research - Part B Applied Biomaterials* **2008**, *85* (2), 573–582. https://doi.org/10.1002/jbm.b.30962.

(33) Puppi, D.; Chiellini, F.; Piras, A. M.; Chiellini, E. Polymeric Materials for Bone and Cartilage Repair. *Progress in Polymer Science* **2010**, *35* (4), 403–440. https://doi.org/10.1016/j.progpolymsci.2010.01.006.

(34) Iannazzo, D.; Pistone, A.; Salamò, M.; Galvagno, S. Hybrid Ceramic/Polymer Composites for Bone Tissue Regeneration. In *Hybrid Polymer Composite Materials: Processing*; 2017; pp 125–155. https://doi.org/10.1016/B978-0-08-100789-1.00006-X.

(35) Liu, X.; Ma, P. X. Polymeric Scaffolds for Bone Tissue Engineering. *Annals of Biomedical Engineering* **2004**, *32* (3), 477–486. https://doi.org/10.1023/B:ABME.0000017544.36001.8e.

(36) Dorozhkin, S. V. Bioceramics of Calcium Orthophosphates. *Biomaterials* **2010**, *31* (7), 1465–1485. https://doi.org/10.1016/j.biomaterials.2009.11.050.

(37) Bohner, M.; Galea, L.; Doebelin, N. Calcium Phosphate Bone Graft Substitutes: Failures and Hopes. *Journal of the European Ceramic Society* **2012**, *32* (11), 2663–2671. https://doi.org/10.1016/j.jeurceramsoc.2012.02.028.

(38) Hench, L. L. Ceramics, Glasses, and Glass-Ceramics,. In *Biomaterilas Science: An Introduction to Materials in Medicine*; 1996; pp 73–84. https://doi.org/10.1017/CBO9781107415324.004.

(39) Gross, U.; Kinne, R.; Schmitz, H. J.; Strunz, V. The Response of Bone to Surface-Active Glasses/Glass-Ceramics. *Critical Reviews in Biocompatibility* **1988**, *4* (2), 155–179.

(40) Hench, L. L. Bioceramics. *Journal of American Ceramic Society* **1998**, *27* (2), 1705–1728. https://doi.org/10.1007/BF00543915.

(41) Hench, L. L. *An Introduction to Bioceramics, Second Edition*; 2013. https://doi.org/10.1142/9781908977168_0004.

(42) Hench, L. L.; Paschall, H. A. Direct Chemical Bond of Bioactive Glass-ceramic Materials to Bone and Muscle. *Journal of Biomedical Materials Research* **1973**, *7* (3), 25–42. https://doi.org/10.1002/jbm.820070304.

(43) Ducheyne, P.; Qiu, Q. Bioactive Ceramics: The Effect of Surface Reactivity on Bone Formation and Bone Cell Function. *Biomaterials* **1999**, *20* (23–24), 2287–2303. https://doi.org/10.1016/S0142-9612(99)00181-7.

(44) Hench, L. L. Bioactive Ceramics: Theory and Clinical Applications. In *Bioceramics, Volume 7*; 1994; pp 61–66.

(45) Cao, W.; Hench, L. L. Bioactive Materials. *Ceramics International* **1996**, *22* (6), 493–507. https://doi.org/10.1016/0272-8842(95)00126-3.

(46) Hench, L. L. Bioceramics: From Concept to Clinic. *Journal of the American Ceramic Society* **1991**, *74* (7), 1487–1510. https://doi.org/10.1111/j.1151-2916.1991.tb07132.x.

(47) Renno, A. C. M.; Bossini, P. S.; Crovace, M. C.; Rodrigues, A. C. M.; Zanotto, E. D.; Parizotto, N. A. Characterization and In Vivo Biological Performance of Biosilicate. *BioMed Research International* **2013**, *2013*, 1–7. https://doi.org/10.1155/2013/141427.
(48) El-Ghannam, A.; Ducheyne, P.; Shapiro, I. M. Effect of Serum Proteins on Osteoblast Adhesion to Surface-modified Bioactive Glass and Hydroxyapatite. *Journal Orthopaedic Research* **1999**, *17* (3), 340–345. https://doi.org/10.1002/jor.1100170307.
(49) Xynos, I. D.; Edgar, A. J.; Buttery, L. D. K.; Hench, L. L.; Polak, J. M. Gene-Expression Profiling of Human Osteoblasts Following Treatment with the Ionic Products of Bioglass® 45S5 Dissolution. *Journal of Biomedical Materials Research* **2001**, *55* (2), 151–157. https://doi.org/10.1002/1097-4636(200105)55:2<151::AID-JBM1001>3.0.CO;2-D.
(50) Baino, F. Bioactive Glasses – When Glass Science and Technology Meet Regenerative Medicine. *Ceramics International* **2018**, *44* (13), 14953–14966. https://doi.org/10.1016/j.ceramint.2018.05.180.
(51) Li, R.; Clark, A. E.; Hench, L. L. An Investigation of Bioactive Glass Powders by Sol-Gel Processing. *Journal of applied biomaterials : an official journal of the Society for Biomaterials* **1991**, *2* (4), 231–239. https://doi.org/10.1002/jab.770020403.
(52) Hench, L. L.; West, J. K. The Sol-Gel Process. *Chemical Reviews* **1990**, *90* (1), 33–72. https://doi.org/10.1021/cr00099a003.
(53) Sepulveda, P.; Jones, J. R.; Hench, L. L. In Vitro Dissolution of Melt-Derived 45S5 and Sol-Gel Derived 58S Bioactive Glasses. *Journal of Biomedical Materials Research* **2002**, *61* (2), 301–311. https://doi.org/10.1002/jbm.10207.
(54) Chen, Q. Z.; Thompson, I. D.; Boccaccini, A. R. 45S5 Bioglass®-Derived Glass-Ceramic Scaffolds for Bone Tissue Engineering. *Biomaterials* **2006**, *27* (11), 2414–2425. https://doi.org/10.1016/j.biomaterials.2005.11.025.
(55) Fu, Q.; Rahaman, M. N.; Sonny Bal, B.; Brown, R. F.; Day, D. E. Mechanical and in Vitro Performance of 13-93 Bioactive Glass Scaffolds Prepared by a Polymer Foam Replication Technique. *Acta Biomaterialia* **2008**, *4* (6), 1854–1864. https://doi.org/10.1016/j.actbio.2008.04.019.
(56) Brown, R. F.; Day, D. E.; Day, T. E.; Jung, S.; Rahaman, M. N.; Fu, Q. Growth and Differentiation of Osteoblastic Cells on 13-93 Bioactive Glass Fibers and Scaffolds. *Acta Biomaterialia* **2008**, *4* (2), 387–396. https://doi.org/10.1016/j.actbio.2007.07.006.
(57) Fiume, E.; Barberi, J.; Verné, E.; Baino, F. Bioactive Glasses: From Parent 45S5 Composition to Scaffold-Assisted Tissue-Healing Therapies. *Journal of Functional Biomaterials* **2018**, *9* (1). https://doi.org/10.3390/jfb9010024.
(58) Liang, W.; Rahaman, M. N.; Day, D. E.; Marion, N. W.; Riley, G. C.; Mao, J. J. Bioactive Borate Glass Scaffold for Bone Tissue Engineering. *Journal of Non-Crystalline Solids* **2008**, *354* (15–16), 1690–1696. https://doi.org/10.1016/j.jnoncrysol.2007.10.003.
(59) Han, X.; Day, D. E. Reaction of Sodium Calcium Borate Glasses to Form Hydroxyapatite. *Journal of Materials Science: Materials in Medicine* **2007**, *18* (9), 1837–1847. https://doi.org/10.1007/s10856-007-3053-2.
(60) Conzone, S. D.; Brown, R. F.; Day, D. E.; Ehrhardt, G. J. In Vitro and in Vivo Dissolution Behavior of a Dysprosium Lithium Borate Glass Designed for the Radiation Synovectomy Treatment of Rheumatoid Arthritis. *Journal of Biomedical Materials Research* **2002**, *60* (2), 260–268. https://doi.org/10.1002/jbm.10047.

(61) Ahmed, I.; Lewis, M.; Olsen, I.; Knowles, J. C. Phosphate Glasses for Tissue Engineering: Part 1. Processing and Characterisation of a Ternary-Based P2O5-CaO-Na 2O Glass System. *Biomaterials* **2004**, *25* (3), 491–499. https://doi.org/10.1016/S0142-9612(03)00546-5.

(62) Ahmed, I.; Lewis, M.; Olsen, I.; Knowles, J. C. Phosphate Glasses for Tissue Engineering: Part 2. Processing and Characterisation of a Ternary-Based P2O5-CaO-Na 2O Glass Fibre System. *Biomaterials* **2004**, *25* (3), 501–507. https://doi.org/10.1016/S0142-9612(03)00547-7.

(63) Abou Neel, E. A.; Pickup, D. M.; Valappil, S. P.; Newport, R. J.; Knowles, J. C. Bioactive Functional Materials: A Perspective on Phosphate-Based Glasses. *Journal of Materials Chemistry* **2009**, *19* (6), 690–701. https://doi.org/10.1039/b810675d.

(64) Salih, V.; Franks, K.; James, M.; Hastings, G. W.; Knowles, J. C.; Olsen, I. Development of Soluble Glasses for Biomedical Use Part II: The Biological Response of Human Osteoblast Cell Lines to Phosphate-Based Soluble Glasses. *Journal of Materials Science: Materials in Medicine* **2000**, *11* (10), 615–620. https://doi.org/10.1023/A:1008901612674.

(65) Kaur, G.; Pandey, O. P.; Singh, K.; Homa, D.; Scott, B.; Pickrell, G. A Review of Bioactive Glasses: Their Structure, Properties, Fabrication and Apatite Formation. *Journal of Biomedical Materials Research - Part A* **2014**, *102* (1), 254–274. https://doi.org/10.1002/jbm.a.34690.

(66) Fu, Q.; Rahaman, M. N.; Fu, H.; Liu, X. Silicate, Borosilicate, and Borate Bioactive Glass Scaffolds with Controllable Degradation Rate for Bone Tissue Engineering Applications. I. Preparation and in Vitro Degradation. *Journal of Biomedical Materials Research - Part A* **2010**, *95* (1), 164–171. https://doi.org/10.1002/jbm.a.32824.

(67) Hu, S.; Chang, J.; Liu, M.; Ning, C. Study on Antibacterial Effect of 45S5 Bioglass®. *Journal of Materials Science: Materials in Medicine* **2009**, *20* (1), 281–286. https://doi.org/10.1007/s10856-008-3564-5.

(68) Bachoura, A.; Guitton, T. G.; Malcolm Smith, R.; Vrahas, M. S.; Zurakowski, D.; Ring, D. Infirmity and Injury Complexity Are Risk Factors for Surgical-Site Infection after Operative Fracture Care. *Clinical Orthopaedics and Related Research* **2011**, *469* (9), 2621–2630. https://doi.org/10.1007/s11999-010-1737-2.

(69) Al-Mulhim, F. A.; Baragbah, M. A.; Sadat-Ali, M.; Alomran, A. S.; Azam, M. Q. Prevalence of Surgical Site Infection in Orthopedic Surgery: A 5-Year Analysis. *International Surgery* **2014**, *99* (3), 264–268. https://doi.org/10.9738/INTSURG-D-13-00251.1.

(70) Baino, F.; Fiume, E.; Barberi, J.; Kargozar, S.; Marchi, J.; Massera, J.; Verné, E. Processing Methods for Making Porous Bioactive Glass-Based Scaffolds—A State-of-the-Art Review. *International Journal of Applied Ceramic Technology* **2019**, *16* (5), 1762–1796. https://doi.org/10.1111/ijac.13195.

(71) Fu, Q.; Saiz, E.; Rahaman, M. N.; Tomsia, A. P. Bioactive Glass Scaffolds for Bone Tissue Engineering: State of the Art and Future Perspectives. *Materials Science and Engineering: C* **2011**, *31* (7), 1245–1256. https://doi.org/10.1016/j.msec.2011.04.022.

(72) Jones, J. R.; Ehrenfried, L. M.; Hench, L. L. Optimising Bioactive Glass Scaffolds for Bone Tissue Engineering. *Biomaterials* **2006**, *27* (7), 964–973.

(73) Gough, J. E.; Jones, J. R.; Hench, L. L. Nodule Formation and Mineralisation of Human Primary Osteoblasts Cultured on a Porous Bioactive Glass Scaffold. *Biomaterials* **2004**, *25* (11), 2039–2046.

(74) Jones, J. R.; Ahir, S.; Hench, L. L. Large-Scale Production of 3D Bioactive Glass Macroporous Scaffolds for Tissue Engineering. *Journal of sol-gel science and technology* **2004**, *29*, 179–188.

(75) Baino, F.; Verné, E.; Vitale-Brovarone, C. 3-D High-Strength Glass–Ceramic Scaffolds Containing Fluoroapatite for Load-Bearing Bone Portions Replacement. *Materials Science and Engineering: C* **2009**, *29* (6), 2055–2062.

(76) Bellucci, D.; Cannillo, V.; Ciardelli, G.; Gentile, P.; Sola, A. Potassium Based Bioactive Glass for Bone Tissue Engineering. *Ceramics international* **2010**, *36* (8), 2449–2453.

(77) Zhang, H.; Ye, X.-J.; Li, J.-S. Preparation and Biocompatibility Evaluation of Apatite/Wollastonite-Derived Porous Bioactive Glass Ceramic Scaffolds. *Biomedical materials* **2009**, *4* (4), 045007.

(78) Vitale-Brovarone, C.; Verné, E.; Robiglio, L.; Martinasso, G.; Canuto, R. A.; Muzio, G. Biocompatible Glass–Ceramic Materials for Bone Substitution. *Journal of Materials Science: Materials in Medicine* **2008**, *19*, 471–478.

(79) Vitale-Brovarone, C.; Baino, F.; Verné, E. High Strength Bioactive Glass-Ceramic Scaffolds for Bone Regeneration. *Journal of materials science: materials in medicine* **2009**, *20*, 643–653.

(80) Xia, W.; Chang, J. Bioactive Glass Scaffold with Similar Structure and Mechanical Properties of Cancellous Bone. *Journal of Biomedical Materials Research Part B: Applied Biomaterials* **2010**, *95* (2), 449–455.

(81) Renghini, C.; Komlev, V.; Fiori, F.; Verné, E.; Baino, F.; Vitale-Brovarone, C. Micro-CT Studies on 3-D Bioactive Glass–Ceramic Scaffolds for Bone Regeneration. *Acta Biomaterialia* **2009**, *5* (4), 1328–1337.

(82) Fu, Q.; Rahaman, M. N.; Bal, B. S.; Kuroki, K.; Brown, R. F. In Vivo Evaluation of 13-93 Bioactive Glass Scaffolds with Trabecular and Oriented Microstructures in a Subcutaneous Rat Implantation Model. *Journal of biomedical materials research Part A* **2010**, *95* (1), 235–244.

(83) Deville, S.; Saiz, E.; Nalla, R. K.; Tomsia, A. P. Freezing as a Path to Build Complex Composites. *Science* **2006**, *311* (5760), 515–518.

(84) Hunger, P. M.; Donius, A. E.; Wegst, U. G. Structure–Property-Processing Correlations in Freeze-Cast Composite Scaffolds. *Acta biomaterialia* **2013**, *9* (5), 6338–6348.

(85) Franco, J.; Hunger, P.; Launey, M. E.; Tomsia, A. P.; Saiz, E. Direct Write Assembly of Calcium Phosphate Scaffolds Using a Water-Based Hydrogel. *Acta biomaterialia* **2010**, *6* (1), 218–228.

(86) Xiao, W.; Zaeem, M. A.; Bal, B. S.; Rahaman, M. N. Creation of Bioactive Glass (13–93) Scaffolds for Structural Bone Repair Using a Combined Finite Element Modeling and Rapid Prototyping Approach. *Materials Science and Engineering: C* **2016**, *68*, 651–662.

(87) Del Val, J.; López-Cancelos, R.; Riveiro, A.; Badaoui, A.; Lusquiños, F.; Quintero, F.; Comesaña, R.; Boutinguiza, M.; Pou, J. On the Fabrication of Bioactive Glass Implants for Bone Regeneration by Laser Assisted Rapid Prototyping Based on Laser Cladding. *Ceramics International* **2016**, *42* (1), 2021–2035.

(88) Hollister, S. J. Porous Scaffold Design for Tissue Engineering. *Nature materials* **2005**, *4* (7), 518–524.
(89) Healy, J. F. Technology: Glass. In *Pliny the Elder on science and technology*; Clarendon Press, 1999.
(90) Eichholz, D. E. *Pliny: Natural History, Volume X: Books 36-37*; Loeb Classical Library 419, Cambridge, MA, Harvard University Press, 1962; p 151.
(91) van Helmont, J. B. De Lithiasi. In *Opuscula medica inaudita*; Sumptibus HC Paulli, 1644.
(92) de Morveau, L.-B. G.; Maret, H.; Durande, J.-F. *Élémens de Chymie, Théorique et Pratique*; Chez LN Frantin, Imprimeur du Roi, rue St. Etienne, 1777.
(93) von Goethe, J. W. *The Auto-Biography of Goethe: Truth and Poetry: From My Life*; Godwin, P., Ed.; Wiley and Putnam, 1846; Vol. 1.
(94) Fuchs, J. N. Ueber Ein Neues Product Aus Kieselerde Und Kali; Und Dessen n ü Zzliche Anwendung Als Schuzmittel Gegen Schnelle Verbreitung Des Feuers in Theatern, Als Bindemittel, Zu Firni ß Artigen Anstrichen Usw Dinglers Polytech. *Polytechnisches Journal* **1825**, *17*, 465–481.
(95) Vail, J. G.; Wills, J. *Soluble Silicates - Their Properties and Uses*; 1952; Vol. 1, p 669.
(96) Bitard, A. *Les Arts et Métiers Illustrés*; Paris, 1883; Vol. 1.
(97) Research, G. V. *Sodium Silicate Market Analysis Report By Application (Catalysts, Pulp & Paper, Food & Healthcare, Detergents, Elastomers), By Region (North America, Europe, APAC, CSA, MEA), And Segment Forecasts, 2019 - 2025*; https://www.grandviewresearch.com/industry-analysis/sodium-silicate-market; 2019. https://www.grandviewresearch.com/industry-analysis/sodium-silicate-market.
(98) Harris, R. K.; Knight, C. T. G.; Hull, W. E. NMR Studies of the Chemical Structure of Silicates in Solution. In *Soluble Silicates*; 1982; pp 79–93.
(99) Glasser, L. S. D.; Lachowaki, E. E. Silicate Species in Solution. Part 1. Experimental Observations. *Journal of the Chemical Society, Dalton Transactions* **1980**, *3*, 393–398.
(100) Lentz, C. W. Silicate Minerals as Sources of Trimethylsilyl Silicates and Silicate Structure Analysis of Sodium Silicate Solutions. *Inorganic Chemistry* **1964**, *3* (4), 574–579. https://doi.org/10.1021/ic50014a029.
(101) Fortnum, D.; Edwards, J. O. The Raman Spectrum and the Structure of the Aqueous Silicate Ion. *Journal of Inorganic and Nuclear Chemistry* **1956**, *2* (4), 264–265.
(102) Iler, R. K. *The Chemistry of Silica: Solubility, Polymerization, Colloid and Surface Properties, and Biocehmistry*; A Wiley-Interscience publication; A Wiley-Interscience Publication, 1979.
(103) Iler, R. K. *The Colloid Chemistry of Silica and Silicates*; LWW, 1955; Vol. 80.
(104) Marsmann, H. C. 29Si NMR Studies on Silicate Solutions in Water. *ZEITSCHRIFT FUR NATURFORSCHUNG SECTION B-A JOURNAL OF CHEMICAL SCIENCES* **1974**, *B 29* (7–8), 495–499.
(105) Engelhardt, G.; Radeglia, R.; Lippmaa, E.; Magi, M. Structure Determination for Siloxanes by Silicon-29 NMR Spectroscopy. *Organic Magnetic Resonance* **1973**, 561–566.
(106) Harris, R. K.; Knight, C. T. G. Silicon-29 Nuclear Magnetic Resonance Studies of Aqueous Silicate Solutions. Part 5 .-First-Order Patterns in Potassium Silicate Solutions Enriched with Silicon-29. *Journal of the Chemical Society, Faraday Transactions 2:*

Molecular and Chemical Physics **1983**, *79* (10), 1525–1560. https://doi.org/10.1002/mrc.1260241005.
(107) Knight, C. T. G.; Balec, R. J.; Kinrade, S. D. The Structure of Silicate Anions in Aqueous Alkaline Solutions. *Angewandte Chemie* **2007**, *119* (43), 8296–8300. https://doi.org/10.1002/ange.200702986.
(108) Harris, R. K.; Knight, C. T. G. Silicon-29 Nuclear Magnetic Resonance Studies of Aqueous Silicate Solutions. Part 6.—Second-Order Patterns in Potassium Silicate Solutions Enriched with Silicon-29. *Journal of the Chemical Society, Faraday Transactions 2: Molecular and Chemical Physics* **1983**, *79* (10), 1539–1561. https://doi.org/10.1002/mrc.1260241005.
(109) Visser, J. H. M. Fundamentals of Alkali-Silica Gel Formation and Swelling: Condensation under Influence of Dissolved Salts. *Cement and Concrete Research* **2018**, *105* (November 2017), 18–30. https://doi.org/10.1016/j.cemconres.2017.11.006.
(110) Tognonvi, M. T.; Rossignol, S.; Bonnet, J. P. Physical-Chemistry of Sodium Silicate Gelation in an Alkaline Medium. *Journal of Sol-Gel Science and Technology* **2011**, *58* (3), 625–635. https://doi.org/10.1007/s10971-011-2437-4.
(111) Stavland, A.; Jonsbråten, H. C.; Vikane, O.; Skrettingland, K.; Fischer, H. In-Depth Water Diversion Using Sodium Silicate on Snorre - Factors Controlling in-Depth Placement. *Society of Petroleum Engineers - 9th European Formation Damage Conference 2011* **2011**, *1* (1985), 516–527. https://doi.org/10.2118/143836-ms.
(112) Sjöberg, S. Silica in Aqueous Environments. *Journal of Non-Crystalline Solids* **1996**, *196*, 51–57. https://doi.org/10.1016/0022-3093(95)00562-5.
(113) Shi, C.; Krivenko, P. V.; Roy, D. Alkaline Activators. In *Alkali-activated cements and concretes*; CRC Press, 2003; pp 6–29.
(114) Halasz, I.; Agarwal, M.; Li, R.; Miller, N. What Can Vibrational Spectroscopy Tell about the Structure of Dissolved Sodium Silicates ? *Microporous and Mesoporous Materials* **2010**, *135* (1–3), 74–81. https://doi.org/10.1016/j.micromeso.2010.06.013.
(115) Katoueizadeh, E.; Rasouli, M.; Zebarjad, S. M. A Comprehensive Study on the Gelation Process of Silica Gels from Sodium Silicate. *Journal of Materials Research and Technology* **2020**, *9* (5), 10157–10165. https://doi.org/10.1016/j.jmrt.2020.07.020.
(116) Wijnen, P. W. J. G.; Beelen, T. P. M.; van Santen, R. A. Silica Gels from Aqueous Silicate Solutions: Combined 29Si NMR and Small-Ange X-Ray Scattering Spectroscopic Study. In *Colloidal Silica: fundamentals and applications*; CRC Press, 2005; pp 597–604.
(117) Vidal, L.; Gharzouni, A.; Rossignol, S. Alkaline Silicate Solutions: An Overview of Their Structure, Reactivity, and Applications. In *Handbook of Sol-Gel Science and Technology: Processing, Characterization and Applications*; 2018; pp 181–204. https://doi.org/10.1007/978-3-319-32101-1_88.
(118) Bergna, H. E.; Roberts, W. O. *Colloidal Silica: Fundamentals and Applications*; CRC Press; 2005; p 897.
(119) Falcone, J. S. *Soluble Silicates*; Journal of the Franklin Institute; 1982; Vol. 255, p 254. https://doi.org/10.1016/0016-0032(53)90023-4.
(120) Knight, C. T. G.; Kinrade, S. D. A Primer on the Aqueous Chemistry of Silicon. In *Silicon in Agriculture*; 2001; pp 57–84.
(121) Novotny, R.; Hoff, A.; Schuertz, J. Process for Hydrothermal Production of Sodium Silicate Solutions. **1991**, 10–10.

(122) Pfeiffer, T.; Enke, D.; Roth, R.; Roggendorf, H. Hydrothermal Dissolution of Opal in Sodium Hydroxide Lyes for the Synthesis of Water Glass. *Advances in Chemical Engineering and Science* **2017**, *07* (01), 76–90. https://doi.org/10.4236/aces.2017.71007.

(123) Tong, K. T.; Vinai, R.; Soutsos, M. N. Use of Vietnamese Rice Husk Ash for the Production of Sodium Silicate as the Activator for Alkali-Activated Binders. *Journal of Cleaner Production* **2018**, *201*, 272–286. https://doi.org/10.1016/j.jclepro.2018.08.025.

(124) Andreola, F.; Barbieri, L.; Lancellotti, I. The Environmental Friendly Route to Obtain Sodium Silicate Solution from Rice Husk Ash: A Comparative Study with Commercial Silicates Deflocculating Agents. *Waste and Biomass Valorization* **2020**, *11* (11), 6295–6305.

(125) Živica, V. Effectiveness of New Silica Fume Alkali Activator. *Cement and Concrete Composites* **2006**, *28* (1), 21–25.

(126) Bernal, S. A.; Rodríguez, E. D.; Mejía de Gutiérrez, R.; Provis, J. L. Performance at High Temperature of Alkali-Activated Slag Pastes Produced with Silica Fume and Rice Husk Ash Based Activators. *Materiales de construcción* **2015**, *65* (318).

(127) Vinai, R.; Soutsos, M. Production of Sodium Silicate Powder from Waste Glass Cullet for Alkali Activation of Alternative Binders. *Cement and Concrete Research* **2019**, *116* (November 2018), 45–56. https://doi.org/10.1016/j.cemconres.2018.11.008.

(128) Torres-Carrasco, M.; Palomo, J. G.; Puertas, F. Sodium Silicate Solutions from Dissolution of Glasswastes. Statistical Analysis. *Materiales de Construccion* **2014**, *64* (314). https://doi.org/10.3989/mc.2014.05213.

(129) Engelhardt, V. G.; Zeigan, D.; Jancke, H.; Wieker, W. 29Si NMR Spectroscopy of Silicate Solutions. II. On the Dependence of Structure of Silicate Anions in Water Solutions from the Na:Si Ratio. *Zeitschrift für anorganische und allgemeine Chemie* **1975**, *418* (17), 17–28.

(130) Engelhardt, G.; Jancke, H.; Hoebbel, D.; Wieker, W. Structural Studies in Aqueous Solutions of Silicate Anions by 29 Si NMR Spectroscopy. *Zeitschrift fuer Chemie* **1974**, *14* (3), 109–110.

(131) Marsmann, H. C. NMR Measurements of the Silicon Isotope, Silicon-29. *Chem.-Ztg.* **1973**, *97*, 128–133.

(132) Harris, R. K.; Jones, J.; Knight, C. T. G.; Pawson, D. Silicon-29 NMR Studies of Aqueous Silicate Solutions. Part II. Isotopic Enrichment. *Journal of Molecular Structure* **1980**, *69* (C), 95–103. https://doi.org/10.1016/0022-2860(80)85268-9.

(133) Harris, R. K.; Knight, C. T. G.; Hull, W. E. Nature of Species Present in an Aqueous Solution of Potassium Silicate. *Journal of the American Chemical Society* **1981**, *103* (6), 1577–1578. https://doi.org/10.1021/ja00396a056.

(134) McCormick, A. V.; Bell, A. T.; Radke, C. J. *Application of 29Si and 27Al NMR to Determine the Distribution of Anions in Sodium Silicate and Sodium Alumino-Silicate Solutions*; Studies in Surface Science and Catalysis; Kodansha Ltd., 1986; Vol. 28, p 254. https://doi.org/10.1016/S0167-2991(09)60880-6.

(135) Svensson, I. L.; Sjöberg, S.; Öhman, L. O. Polysilicate Equilibria in Concentrated Sodium Silicate Solutions. *Journal of the Chemical Society, Faraday Transactions 1: Physical Chemistry in Condensed Phases* **1986**, *82* (12), 3635–3646. https://doi.org/10.1039/F19868203635.

(136) Kinrade, S. D.; Swaddle, T. W. Silicon-29 NMR Studies of Aqueous Silicate Solutions. 2. Transverse Silicon-29 Relaxation and the Kinetics and Mechanism of Silicate Polymerization. *Inorganic Chemistry* **1988**, *27* (23), 4259–4264.

(137) Kinrade, S. D.; Pole, D. L. Effect of Alkali-Metal Cations on the Chemistry of Aqueous Silicate Solutions. *Inorganic Chemistry* **1992**, *31* (22), 4558–4563. https://doi.org/10.1021/ic00048a023.

(138) Harris, R. K.; Bahlmann, E. K. F.; Metcalfe, K.; Smith, E. G. Quantitative Silicon-29 NMR Investigations of Highly Concentrated High-ratio Sodium Silicate Solutions. *Magnetic Resonance in Chemistry* **1993**, *31* (8), 743–747. https://doi.org/10.1002/mrc.1260310810.

(139) Roggendorf, H.; Grand, W.; Hurbanic, M. Structural Characterization of Concentrated Alkaline Silicate Solutions by 29Si-NMR Spectroscopy, FT-IR Spectroscopy, Light Scattering, and Electron Microscopy - Molecules, Colloids, and Dissolution Artefacts. *Glass Science and Technology: Glastechnische Berichte* **1996**, *69* (7), 216–231.

(140) Bass, J. L.; Turner, G. L. Anion Distributions in Sodium Silicate Solutions. Characterization by 29SI NMR and Infrared Spectroscopies, and Vapor Phase Osmometry. *Journal of Physical Chemistry B* **1997**, *101* (50), 10638–10644. https://doi.org/10.1021/jp9715282.

(141) Gaboriaud, F.; Nonat, A.; Chaumont, D.; Craievich, A.; Hanquet, B. 29Si NMR and Small-Angle x-Ray Scattering Studies of the Effect of Alkaline Ions (Li+, Na+, and K+) in Silico-Alkaline Sols. *Journal of Physical Chemistry B* **1999**, *103* (12), 2091–2099. https://doi.org/10.1021/jp984074x.

(142) Harris, R. K.; O′Connor, M. J.; Curzon, E. H.; Howarth, O. W. Two-Dimensional Silicon-29 NMR Studies of Aqueous Silicate Solutions. *Journal of Magnetic Resonance* **1984**, *57* (1), 115–122. https://doi.org/10.1016/0022-2364(84)90239-7.

(143) Knight, C. T. G. A Two-Dimensional Silicon-29 Nuclear Magnetic Resonance Spectroscopic Study of the Structure of the Silicate Anions Present in an Aqueous Potassium Silicate Solution. *Journal of the Chemical Society, Dalton Transactions* **1988**, No. 6, 1457–1460. https://doi.org/10.1039/DT9880001457.

(144) Cho, H.; Felmy, A. R.; Craciun, R.; Keenum, J. P.; Shah, N.; Dixon, D. A. Solution State Structure Determination of Silicate Oligomers by 29 Si NMR Spectroscopy and Molecular Modeling. *Journal of the American Chemical Society* **2006**, *128* (7), 2324–2335. https://doi.org/10.1021/ja0559202.

(145) Haouas, M.; Taulelle, F. Revisiting the Identification of Structural Units in Aqueous Silicate Solutions by Two-Dimensional Silicon-29 INADEQUATE. *Journal of Physical Chemistry B* **2006**, *110* (45), 3007–3014. https://doi.org/10.1021/jp0661600.

(146) Tognonvi, M. T.; Massiot, D.; Lecomte, A.; Rossignol, S.; Bonnet, J. P. Identification of Solvated Species Present in Concentrated and Dilute Sodium Silicate Solutions by Combined 29Si NMR and SAXS Studies. *Journal of Colloid and Interface Science* **2010**, *352* (2), 309–315. https://doi.org/10.1016/j.jcis.2010.09.018.

(147) Alvarez, R.; Sparks, D. L. Polymerization of Silicate Anions in Solutions at Low Concentrations. *Nature* **1985**, *318* (6047), 649–651. https://doi.org/10.1038/318649a0.

(148) Dutta, P. K.; Shieh, D. C. Raman Spectral Study of the Composition of Basic Silicate Solutions. *Applied Spectroscopy* **1985**, *39* (2), 343–346. https://doi.org/10.1366/0003702854248971.

(149) Halasz, I.; Agarwal, M.; Li, R.; Miller, N. Monitoring the Structure of Water Soluble Silicates. *Catalysis Today* **2007**, *126* (1–2), 196–202. https://doi.org/10.1016/j.cattod.2006.09.032.

(150) Hunt, J. D.; Kavner, A.; Schauble, E. A.; Snyder, D.; Manning, C. E. Polymerization of Aqueous Silica in H2O-K2O Solutions at 25-200°C and 1bar to 20kbar. *Chemical Geology* **2011**, *283* (3–4), 161–170. https://doi.org/10.1016/j.chemgeo.2010.12.022.

(151) Steele-MacInnis, M.; Schmidt, C. Silicate Speciation in H2O-Na2O-SiO2 Fluids from 3 to 40mol% SiO2, to 600°C and 2GPa. *Geochimica et Cosmochimica Acta* **2014**, *136*, 126–141. https://doi.org/10.1016/j.gca.2014.04.009.

(152) Vidal, L.; Gharzouni, A.; Joussein, E.; Colas, M.; Cornette, J.; Absi, J.; Rossignol, S. Determination of the Polymerization Degree of Various Alkaline Solutions: Raman Investigation. *Journal of Sol-Gel Science and Technology* **2017**, *83* (1), 1–11. https://doi.org/10.1007/s10971-017-4394-z.

(153) Beard, Wi. C. Infrared Studies of Aqueous Silicate Solutions. In *Molecular Sieves*; ACS Publications, 1973; pp 162–168.

(154) Bass, J. L.; Turner, G. L.; Morris, M. D. Vibrational and 29Si NMR Spectroscopies of Soluble Silicate Oligomers. *Macromolecular Symposia* **1999**, *140*, 263–270. https://doi.org/10.1002/masy.19991400126.

(155) Osswald, J.; Fehr, K. T. FTIR Spectroscopic Study on Liquid Silica Solutions and Nanoscale Particle Size Determination. *Journal of Materials Science* **2006**, *41* (5), 1335–1339. https://doi.org/10.1007/s10853-006-7327-8.

(156) Halasz, I.; Agarwal, M.; Li, R.; Miller, N. Molecular Spectroscopy of Alkaline Silicate Solutions. *Studies in Surface Science and Catalysis* **2008**, *174* (B), 787–792. https://doi.org/10.1016/S0167-2991(08)80008-0.

(157) Falcone, J. S.; Bass, J. L.; Angelella, M.; Schenk, E. R.; Brensinger, K. A. The Determination of Sodium Silicate Composition Using ATR FT-IR. *Industrial and Engineering Chemistry Research* **2010**, *49* (14), 6287–6290. https://doi.org/10.1021/ie1002747.

(158) Vidal, L.; Joussein, E.; Colas, M.; Cornette, J.; Sanz, J.; Sobrados, I.; Gelet, J. L.; Absi, J.; Rossignol, S. Controlling the Reactivity of Silicate Solutions: A FTIR, Raman and NMR Study. *Colloids and Surfaces A: Physicochemical and Engineering Aspects* **2016**, *503*, 101–109. https://doi.org/10.1016/j.colsurfa.2016.05.039.

(159) Knight, C. T. G.; Balec, R. J.; Kinrade, S. D. Aqueous Alkali-Metal Silicate Anions Containing Fully Condensed Four-Coordinate Sites. *Angewandte Chemie* **2012**, *124* (39), 10038–10041. https://doi.org/10.1002/ange.201205606.

(160) Freund, E. Laser Raman Spectroscopic Study of Aqueous-Solutions of Sodium Silicates. 1. Experimental Results. *BULL. SOC. CHIM. FR* **1973**, No. 7–8, 2238–2243.

(161) Marinangeli, A.; MA, M. A Raman and Infrared Study of Aqueous Solutions of Sodium Silicates as a Function of pH. **1978**.

(162) Halasz, I.; Agarwal, M.; Li, R.; Miller, N. Vibrational Spectra and Dissociation of Aqueous Na2SiO3 Solutions. *Catalysis Letters* **2007**, *117* (1–2), 34–42. https://doi.org/10.1007/s10562-007-9141-6.

(163) Mikhailova, O.; Del Campo, A.; Rovnanik, P.; Fernández, J. F.; Torres-Carrasco, M. In Situ Characterization of Main Reaction Products in Alkali-Activated Slag Materials by Confocal Raman Microscopy. *Cement and Concrete Composites* **2019**, *99*, 32–39.

(164) Caggiani, M. C.; Coccato, A.; Barone, G.; Finocchiaro, C.; Fugazzotto, M.; Lanzafame, G.; Occhipinti, R.; Stroscio, A.; Mazzoleni, P. Raman Spectroscopy Potentiality in the Study of Geopolymers Reaction Degree. *Journal of Raman Spectroscopy* **2022**, *53* (3), 617–629.

(165) Halasz, I.; Kierys, A.; Goworek, J.; Liu, H.; Patterson, R. E. 29Si NMR and Raman Glimpses into the Molecular Structures of Acid and Base Set Silica Gels Obtained from TEOS and Na-Silicate. *Journal of Physical Chemistry C* **2011**, *115* (50), 24788–24799. https://doi.org/10.1021/jp207534e.

(166) Yang, X.; Roonasi, P.; Holmgren, A. A Study of Sodium Silicate in Aqueous Solution and Sorbed by Synthetic Magnetite Using in Situ ATR-FTIR Spectroscopy. *Journal of Colloid and Interface Science* **2008**, *328* (1), 41–47. https://doi.org/10.1016/j.jcis.2008.08.061.

(167) Andersson, K. R.; Dent Glasser, L. S.; Smith, D. N. Polymerization and Colloid Formation in Silicate Solutions. In *Soluble Silicates*; 1982; pp 115–131. https://doi.org/10.1021/bk-1982-0194.ch008.

(168) Provis, J. L.; Duxson, P.; Lukey, G. C.; Separovic, F.; Kriven, W. M.; Van Deventer, J. S. J. Modeling Speciation in Highly Concentrated Alkaline Silicate Solutions. *Industrial and Engineering Chemistry Research* **2005**, *44* (23), 8899–8908. https://doi.org/10.1021/ie050700i.

(169) Nordström, J.; Nilsson, E.; Jarvol, P.; Nayeri, M.; Palmqvist, A.; Bergenholtz, J.; Matic, A. Concentration- and pH-Dependence of Highly Alkaline Sodium Silicate Solutions. *Journal of Colloid and Interface Science* **2011**, *356* (1), 37–45. https://doi.org/10.1016/j.jcis.2010.12.085.

(170) Brinker, C. J.; Scherer, G. W. Hydrolysis and Condensation II Silicates. In *Sol-Gel Science: The Physics and Chemistry of Sol-Gel Processing*; ACADEMIC PRESS, INC, 1990; pp 97–228. https://doi.org/10.1016/C2009-0-22386-5.

(171) Nowak, M.; Behrens, H. The Speciation of Water in Haplogranitic Glasses and Melts Determined by in Situ Near-Infrared Spectroscopy. *Geochimica et Cosmochimica Acta* **1995**, *59* (16), 3445–3450.

(172) Harman, R. W. Aqueous Solutions of Sodium Silicates. VIII. General Summary and Theory of Constitution. Sodium Silicates as Colloidal Electrolytes. *The journal of physical chemistry* **2002**, *32* (1), 44–60.

(173) Nordström, J.; Sundblom, A.; Jensen, G. V.; Pedersen, J. S.; Palmqvist, A.; Matic, A. Silica/Alkali Ratio Dependence of the Microscopic Structure of Sodium Silicate Solutions. *Journal of Colloid and Interface Science* **2013**, *397*, 9–17. https://doi.org/10.1016/j.jcis.2013.01.048.

(174) Iler, R. K. Colloidal Components in Solutions of Sodium Silicate. In *Soluble Silicates*; 1982; pp 95–114. https://doi.org/10.1021/bk-1982-0194.ch007.

(175) Dietzel, M.; Usdowski, E. Depolymerization of Soluble Silicate in Dilute Aqueous Solutions. *Colloid & Polymer Science* **1995**, *273* (6), 590–597. https://doi.org/10.1007/BF00658690.

(176) Nauman, R. V.; Debye, P. Light-Scattering Investigations of Carefully Filtered Sodium Silicate Solutions. *Journal of Physical and Colloid Chemistry* **1951**, *55* (1), 1–9. https://doi.org/10.1021/j150484a001.

(177) Böschel, D.; Janich, M.; Roggendorf, H. Size Distribution of Colloidal Silica in Sodium Silicate Solutions Investigated by Dynamic Light Scattering and Viscosity Measurements.

Journal of Colloid and Interface Science **2003**, *267* (2), 360–368. https://doi.org/10.1016/j.jcis.2003.07.016.

(178) Pavlova, A.; Trinh, T. T.; Van Santen, R. A.; Meijer, E. J. Clarifying the Role of Sodium in the Silica Oligomerization Reaction. *Physical Chemistry Chemical Physics* **2013**, *15* (4), 1123–1129. https://doi.org/10.1039/c2cp42436c.

(179) Dupuis, R.; Rodrigues, D. G.; Champenois, J. B.; Pellenq, R. J. M.; Poulesquen, A. Time Resolved Alkali Silicate Decondensation by Sodium Hydroxide Solution. *JPhys Materials* **2020**, *3* (1). https://doi.org/10.1088/2515-7639/ab5ce9.

(180) Carman, P. C. Constitution of Colloidal Silica. *Transactions of the Faraday Society* **1940**, *36* (964), 964–973. https://doi.org/10.1039/tf9403600964.

(181) Marinkov, N.; Markova-Velichkova, M.; Gyurov, S.; Kostova, Y.; Spassova, I.; Rabadjieva, D.; Kovacheva, D.; Penkov, I.; Tzvetkova, C.; Gentscheva, G. Preparation and Characterization of Silicagel from Silicate Solution Obtained by Autoclave Treatment of Copper Slag. *Journal of Sol-Gel Science and Technology* **2018**, *87* (2), 331–339. https://doi.org/10.1007/s10971-018-4741-8.

(182) Lazaro, A.; Van De Griend, M. C.; Brouwers, H. J. H.; Geus, J. W. The Influence of Process Conditions and Ostwald Ripening on the Specific Surface Area of Olivine Nano-Silica. *Microporous and Mesoporous Materials* **2013**, *181*, 254–261. https://doi.org/10.1016/j.micromeso.2013.08.006.

(183) Gerber, T.; Himmel, B.; Hübert, C. WAXS and SAXS Investigation of Structure Formation of Gels from Sodium Water Glass. *Journal of Non-Crystalline Solids* **1994**, *175* (2–3), 160–168. https://doi.org/10.1016/0022-3093(94)90008-6.

(184) Knoblich, B.; Gerber, T. Aggregation in SiO2 Sols from Sodium Silicate Solutions. *Journal of Non-Crystalline Solids* **2001**, *283* (1–3), 109–113. https://doi.org/10.1016/S0022-3093(01)00356-8.

(185) Gaboriaud, F.; Nonat, A.; Chaumont, D.; Craievich, A. Structural Model of Gelation Processes of a Sodium Silicate Sol Destabilized by Calcium Ions: Combination of SAXS and Rheological Measurements. *Journal of Non-Crystalline Solids* **2005**, *351* (4), 351–354. https://doi.org/10.1016/j.jnoncrysol.2004.11.019.

(186) van Santen, R. A.; Beelen, T. P. M.; van Garderen, H. F.; Dokter, W. H.; Pantos, E. Aggregation and Aging in Silica Gel. *Nuclear Inst. and Methods in Physics Research, B* **1995**, *97* (1–4), 231–237. https://doi.org/10.1016/0168-583X(95)00194-8.

(187) Bałdyga, J.; Jasińska, M.; Jodko, K.; Petelski, P. Precipitation of Amorphous Colloidal Silica from Aqueous Solutions-Aggregation Problem. *Chemical Engineering Science* **2012**, *77*, 207–216. https://doi.org/10.1016/j.ces.2012.03.046.

(188) Obut, A.; Girgin, I. Preparation of Sodium Borosilicates Using Sodium Silicate and Boric Acid. *Journal of Sol-Gel Science and Technology* **2006**, *39* (2), 79–83. https://doi.org/10.1007/s10971-006-8974-6.

(189) Boschel, D.; Roggendorf, H. Water-Based Sodium Borosilicate Sols and Their Gelation-Characterisation by Viscosimetry, UV/VIS- and Infrared Spectroscopy.

(190) Berrier, E.; Courtheoux, L.; Bouazaoui, M.; Capoen, B.; Turrell, S. Correlation between Gelation Time, Structure and Texture of Low-Doped Silica Gels. *Physical Chemistry Chemical Physics* **2010**, *12* (43), 14477–14484. https://doi.org/10.1039/c0cp01090a.

(191) Hamouda, A. A.; Amiri, H. A. A. Factors Affecting Alkaline Sodium Silicate Gelation for In-Depth Reservoir Profile Modification. *Energies* **2014**, *7* (2), 568–590. https://doi.org/10.3390/en7020568.

(192) Al-Anazi, M. S.; Al-Mutairi, S. H.; Al-Khaldi, M. H.; Al-Zahrani, A. A.; Al-Yami, I. S.; Gurmen, M. N. Laboratory Evaluation of Organic Water Shut-off Gelling System for Carbonate Formations. *Society of Petroleum Engineers - 9th European Formation Damage Conference 2011* **2011**, *2* (2001), 824–844. https://doi.org/10.2118/144082-ms.

(193) Pham, L. T.; Hatzignatiou, D. G. Rheological Evaluation of a Sodium Silicate Gel System for Water Management in Mature, Naturally-Fractured Oilfields. *Journal of Petroleum Science and Engineering* **2016**, *138*, 218–233. https://doi.org/10.1016/j.petrol.2015.11.039.

(194) Hatzignatiou, D. G.; Askarinezhad, R.; Giske, N. H.; Stavland, A. Laboratory Testing of Environmentally Friendly Sodium Silicate Systems for Water Management through Conformance Control. *SPE Production and Operations* **2016**, *31* (4), 337–350. https://doi.org/10.2118/173853-PA.

(195) Quarch, K.; Kind, M. Inorganic Precipitated Silica Gel. Part 1: Gelation Kinetics and Gel Properties. *Chemical Engineering and Technology* **2010**, *33* (6), 1034–1039. https://doi.org/10.1002/ceat.201000080.

(196) Okkerse, C. Physical and Chemical Aspects of Adsorbents and Catalysts. *Linsen, BG, Fortuin, JMH, Okkerse, C., Steggerda, JJ, Eds* **1970**.

(197) Wilhelm, S.; Kind, M. Gelation, Fragmentation and Reorganization of Precipitated Silica. In *Colloid Process Engineering*; 2015; pp 175–204. https://doi.org/10.1007/978-3-319-15129-8.

(198) Zerda, T. W.; Artaki, I.; Jonas, J. Study of Polymerization Processes in Acid and Base Catalyzed Silica Sol-Gels. *Journal of Non-Crystalline Solids* **1986**, *81* (3), 365–379. https://doi.org/10.1016/0022-3093(86)90503-X.

(199) Heald, I. A.; Coates, K. B.; Edwards, J. E. Factors Influencing the Time of Gelation of Acid ‘Modified’ Sodium Silicate. *Journal of Applied Chemistry* **1955**, *5* (8), 425–436. https://doi.org/10.1002/jctb.5010050811.

(200) Merrill, R. C.; Spencer, R. W. Gelation of Sodium Silicate Effect of Sulfuric Acid, Hydrochloric Acid, Ammonium Sulfate, and Sodium Aluminate. *Journal of Physical and Colloid Chemistry* **1950**, *54* (6), 806–812. https://doi.org/10.1021/j150480a009.

(201) Kristensen, R.; Lund, T.; Titov, V. I.; Akimov, N. I. Laboratory Evaluation and Field Tests of a Silicate Gel System Intended for Use under North Sea Conditions. *Geological Society Special Publication* **1995**, *84* (84), 251–259. https://doi.org/10.1144/GSL.SP.1995.084.01.25.

(202) Milonjić, S. K. A Relation between the Amounts of Sorbed Alkali Cations and the Stability of Colloidal Silica. *Colloids and Surfaces* **1992**, *63* (1–2), 113–119. https://doi.org/10.1016/0166-6622(92)80077-F.

(203) Matijević, E. Colloid Stability and Complex Chemistry. *Journal of Colloid and Interface Science* **1973**, *43* (2), 217–245. https://doi.org/10.1016/0021-9797(73)90371-8.

(204) Van Der Linden, M.; Conchúir, B. O.; Spigone, E.; Niranjan, A.; Zaccone, A.; Cicuta, P. Microscopic Origin of the Hofmeister Effect in Gelation Kinetics of Colloidal Silica. *Journal of Physical Chemistry Letters* **2015**, *6* (15), 2881–2887. https://doi.org/10.1021/acs.jpclett.5b01300.

(205) Bishop Jr, A. D.; Bear, J. L. The Thermodynamics and Kinetics of the Polymerization of Silicic Acid in Dilute Aqueous Solution. *Thermochimica Acta* **1972**, *3* (5), 399–409.

(206) Israelachvili, J. N. *Intermolecular and Surface Forces*; Academic press, 2011.

(207) Hatami, S.; Hughes, T. J.; Sun, H.; Roshan, H.; Walsh, S. D. C. On the Application of Silica Gel for Mitigating CO2 Leakage in CCS Projects: Rheological Properties and Chemical Stability. *Journal of Petroleum Science and Engineering* **2021**, *207* (February), 109155–109155. https://doi.org/10.1016/j.petrol.2021.109155.

(208) Wilhelm, S.; Kind, M. On the Relation between Natural and Enforced Syneresis of Acidic Precipitated Silica. *Polymers* **2014**, *6* (12), 2896–2911. https://doi.org/10.3390/polym6122896.

(209) Wilhelm, S.; Kind, M. Influence of pH, Temperature and Sample Size on Natural and Enforced Syneresis of Precipitated Silica. *Polymers* **2015**, *7* (12), 2504–2521. https://doi.org/10.3390/polym7121528.

(210) Tognonvi, M. T.; Lecomte, A.; Rossignol, S.; Bonnet, J.-P. Ripening of Na-Silicate Gels in Basic Media: Identification of Involved Chemical Species. *Journal of Non-Crystalline Solids* **2019**, *522*, 119482. https://doi.org/10.1016/j.jnoncrysol.2019.119482.

(211) Scherer, G. W. Aging and Drying of Gels. *Journal of Non-Crystalline Solids* **1988**, *100* (Aging ans Drying of Gels), 77–92.

(212) Vysotskii, Z. Z.; Strazhesko, D. N. Isoelectric State of Disperse Silicas and Ion Exchange in Acid Solutions, Adsorption and Adsorbents. **1973**.

(213) Trinh, T. T.; Jansen, A. P. J.; Van Santen, R. A. Mechanism of Oligomerization Reactions of Silica. *Journal of Physical Chemistry B* **2006**, *110* (46), 23099–23106. https://doi.org/10.1021/jp063670l.

(214) Trinh, T. T.; Jansen, A. P. J.; Santen, R. A. V.; Meijer, E. J. Role of Water in Silica Oligomerization. *Journal of Physical Chemistry C* **2009**, *113* (7), 2647–2652. https://doi.org/10.1021/jp076372c.

(215) White, C. E.; Provis, J. L.; Kearley, G. J.; Riley, D. P.; Van Deventer, J. S. J. Density Functional Modelling of Silicate and Aluminosilicate Dimerisation Solution Chemistry. *Dalton Transactions* **2011**, *40* (6), 1348–1355. https://doi.org/10.1039/c0dt01042a.

(216) Rao, N. Z.; Gelb, L. D. Molecular Dynamics Simulations of the Polymerization of Aqueous Silicic Acid and Analysis of the Effects of Concentration on Silica Polymorph Distributions, Growth Mechanisms, and Reaction Kinetics. *Journal of Physical Chemistry B* **2004**, *108* (33), 12418–12428. https://doi.org/10.1021/jp049169f.

(217) Malani, A.; Auerbach, S. M.; Monson, P. A. Probing the Mechanism of Silica Polymerization at Ambient Temperatures Using Monte Carlo Simulations. *Journal of Physical Chemistry Letters* **2010**, *1* (21), 3219–3224. https://doi.org/10.1021/jz101046y.

(218) Jing, Z.; Xin, L.; Sun, H. Replica Exchange Reactive Molecular Dynamics Simulations of Initial Reactions in Zeolite Synthesis. *Physical Chemistry Chemical Physics* **2015**, *17* (38), 25421–25428. https://doi.org/10.1039/c5cp03063c.

(219) Zhang, X. Q.; Trinh, T. T.; Van Santen, R. A.; Jansen, A. P. J. Mechanism of the Initial Stage of Silicate Oligomerization. *Journal of the American Chemical Society* **2011**, *133* (17), 6613–6625. https://doi.org/10.1021/ja110357k.

(220) Dupuis, R.; Béland, L. K.; Pellenq, R. J. M. Molecular Simulation of Silica Gels: Formation, Dilution, and Drying. *Physical Review Materials* **2019**, *3* (7), 1–7. https://doi.org/10.1103/PhysRevMaterials.3.075603.

(221) Abdusalamov, R.; Scherdel, C.; Itskov, M.; Milow, B.; Reichenauer, G.; Rege, A. Modeling and Simulation of the Aggregation and the Structural and Mechanical Properties of Silica Aerogels. *The Journal of Physical Chemistry B* **2021**, *125* (7), 1944–1950.

(222) Gruy, F.; Kamińska, M.; Valente, J. Dynamics of Oligomerization of Silicate Solution Studied by Molecular Dynamics. *Colloids and Surfaces A: Physicochemical and Engineering Aspects* **2021**, *628* (July). https://doi.org/10.1016/j.colsurfa.2021.127238.

(223) Moqadam, M.; Riccardi, E.; Trinh, T. T.; Lervik, A.; Van Erp, T. S. Rare Event Simulations Reveal Subtle Key Steps in Aqueous Silicate Condensation. *Physical Chemistry Chemical Physics* **2017**, *19* (20), 13361–13371. https://doi.org/10.1039/c7cp01268c.

(224) Depla, A.; Lesthaeghe, D.; Van Erp, T. S.; Aerts, A.; Houthoofd, K.; Fan, F.; Li, C.; Van Speybroeck, V.; Waroquier, M.; Kirschhock, C. E. A.; Martens, J. A. 29Si NMR and UV-Raman Investigation of Initial Oligomerization Reaction Pathways in Acid-Catalyzed Silica Sol-Gel Chemistry. *Journal of Physical Chemistry C* **2011**, *115* (9), 3562–3571. https://doi.org/10.1021/jp109901v.

(225) Pereira, J. C. G.; Catlow, C. R. A.; Price, G. D. Silica Condensation Reaction: An Ab Initio Study. *Chemical Communications* **1998**, No. 13, 1387–1388. https://doi.org/10.1039/a801816b.

(226) Henschel, H.; Schneider, A. M.; Prosenc, M. H. Initial Steps of the Sol-Gel Process: Modeling Silicate Condensation in Basic Medium. *Chemistry of Materials* **2010**, *22* (17), 5105–5111. https://doi.org/10.1021/cm100401f.

(227) Pereira, J. C. G.; Catlow, C. R. A.; Price, G. D. Ab Initio Studies of Silica-Based Clusters. Part I. Energies and Conformations of Simple Clusters. *The Journal of Physical Chemistry A* **1999**, *103* (17), 3252–3267.

(228) Tossell, J. A. Theoretical Study on the Dimerization of Si (OH) 4 in Aqueous Solution and Its Dependence on Temperature and Dielectric Constant. *Geochimica et Cosmochimica Acta* **2005**, *69* (2), 283–291.

(229) Du, T.; Li, H.; Sant, G.; Bauchy, M. New Insights into the Sol-Gel Condensation of Silica by Reactive Molecular Dynamics Simulations. *Journal of Chemical Physics* **2018**, *148* (23). https://doi.org/10.1063/1.5027583.

(230) Kamińska, M.; Gruy, F.; Valente, J. Dynamics of Non-Dense Sodium Silicate - Water System Studied By Molecular Dynamics. *Colloids and Surfaces A: Physicochemical and Engineering Aspects* **2020**, *603*. https://doi.org/10.1016/j.colsurfa.2020.125226.

(231) Shere, I.; Adapa, S.; Malani, A. Development of Coarse-Grained Potential of Silica Species. *Molecular Simulation* **2022**, *48* (15), 1343–1355. https://doi.org/10.1080/08927022.2022.2088745.

(232) Emami, F. S.; Puddu, V.; Berry, R. J.; Varshney, V.; Patwardhan, S. V.; Perry, C. C.; Heinz, H. Force Field and a Surface Model Database for Silica to Simulate Interfacial Properties in Atomic Resolution. *Chemistry of Materials* **2016**, *28* (1), 406–407. https://doi.org/10.1021/acs.chemmater.5b04760.

(233) Verma, C.; Lgaz, H.; Verma, D.; Ebenso, E. E.; Bahadur, I.; Quraishi, M. Molecular Dynamics and Monte Carlo Simulations as Powerful Tools for Study of Interfacial Adsorption Behavior of Corrosion Inhibitors in Aqueous Phase: A Review. *Journal of Molecular Liquids* **2018**, *260*, 99–120.

(234) Zhang, X. Q.; Van Santen, R. A.; Jansen, A. P. J. Kinetic Monte Carlo Modeling of Silicate Oligomerization and Early Gelation†. *Physical Chemistry Chemical Physics* **2012**, *14* (34), 11969–11973. https://doi.org/10.1039/c2cp41194f.

(235) Jin, L.; Auerbach, S. M.; Monson, P. A. Modeling Three-Dimensional Network Formation with an Atomic Lattice Model: Application to Silicic Acid Polymerization. *Journal of Chemical Physics* **2011**, *134* (13). https://doi.org/10.1063/1.3575188.

(236) White, C. E.; Provis, J. L.; Proffen, T.; Van Deventer, J. S. J. Quantitative Mechanistic Modeling of Silica Solubility and Precipitation during the Initial Period of Zeolite Synthesis. *Journal of Physical Chemistry C* **2011**, *115* (20), 9879–9888. https://doi.org/10.1021/jp2006217.

(237) Alkhraisat, M. H.; Rueda, C.; Jerez, L. B.; Tamimi Mariño, F.; Torres, J.; Gbureck, U.; Lopez Cabarcos, E. Effect of Silica Gel on the Cohesion, Properties and Biological Performance of Brushite Cement. *Acta Biomaterialia* **2010**, *6* (1), 257–265. https://doi.org/10.1016/j.actbio.2009.06.010.

(238) Lakrat, M.; Mejdoubi, E. M.; Ozdemir, F.; Santos, C. Effect of Sodium Silicate Concentration on the Physico-Chemical Properties of Dual-Setting Bone-like Apatite Cements. *Materials Today Communications* **2022**, *31* (February), 103421–103421. https://doi.org/10.1016/j.mtcomm.2022.103421.

(239) Komlev, V. S.; Rau, J. V.; Fosca, M.; Fomin, A. S.; Gurin, A. N.; Barinov, S. M.; Caminiti, R. Single-Phase Bone Cement Based on Dicalcium Phosphate Dihydrate Powder and Sodium Silicate Solution. *Materials Letters* **2012**, *73*, 115–118. https://doi.org/10.1016/j.matlet.2012.01.010.

(240) Farrag, H. A.; Abdallah, N.; Shehata, M. M.; Awad, E. M. Natural Outer Membrane Permeabilizers Boost Antibiotic Action against Irradiated Resistant Bacteria. *Journal of Biomedical Science* **2019**, *26*, 1–14.

(241) Nakanishi, K. Properties and Applications of Sol–Gel Materials: Functionalized Porous Amorphous Solids (Monoliths). *The Sol-Gel Handbook* **2015**, 745–766.

(242) Cardea, S.; Pisanti, P.; Reverchon, E. Generation of Chitosan Nanoporous Structures for Tissue Engineering Applications Using a Supercritical Fluid Assisted Process. *The Journal of Supercritical Fluids* **2010**, *54* (3), 290–295.

(243) Lynch, K. J.; Skalli, O.; Sabri, F. Investigation of Surface Topography and Stiffness on Adhesion and Neurites Extension of PC12 Cells on Crosslinked Silica Aerogel Substrates. *PLoS One* **2017**, *12* (10), e0185978.

(244) Sala, M. R.; Chandrasekaran, S.; Skalli, O.; Worsley, M.; Sabri, F. Enhanced Neurite Outgrowth on Electrically Conductive Carbon Aerogel Substrates in the Presence of an External Electric Field. *Soft Matter* **2021**, *17* (17), 4489–4495.

(245) Mohammadian, M.; Kashi, T. S. J.; Erfan, M.; Soorbaghi, F. P. Synthesis and Characterization of Silica Aerogel as a Promising Drug Carrier System. *Journal of Drug Delivery Science and Technology* **2018**, *44*, 205–212.

(246) Jahed, F. S.; Hamidi, S.; Zamani-Kalajahi, M.; Siahi-Shadbad, M. Biomedical Applications of Silica-Based Aerogels: A Comprehensive Review. *Macromol. Res.* **2023**, *31* (6), 519–538. https://doi.org/10.1007/s13233-023-00142-9.

(247) Ponader, S.; Brandt, H.; Vairaktaris, E.; Von Wilmowsky, C.; Nkenke, E.; Schlegel, K. A.; Neukam, F. W.; Holst, S.; Müller, F. A.; Greil, P. In Vitro Response of hFOB Cells to

Pamidronate Modified Sodium Silicate Coated Cellulose Scaffolds. *Colloids and Surfaces B: Biointerfaces* **2008**, *64* (2), 275–283. https://doi.org/10.1016/j.colsurfb.2008.02.002.

(248) Oliveira, A. Sodium Silicate Gel as a Precursor for the in Vitro Nucleation and Growth of a Bone-like Apatite Coating in Compact and Porous Polymeric Structures. *Biomaterials* **2003**, *24* (15), 2575–2584. https://doi.org/10.1016/S0142-9612(03)00060-7.

(249) Oliveira, A. L.; Alves, C. M.; Reis, R. L. Cell Adhesion and Proliferation on Biomimetic Calcium-Phosphate Coatings Produced by a Sodium Silicate Gel Methodology; 2002; Vol. 13, pp 1181–1188. https://doi.org/10.1023/A:1021106525097.

(250) Martins, M.; Barros, A. A.; Quraishi, S.; Gurikov, P.; Raman, S.; Smirnova, I.; Duarte, A. R. C.; Reis, R. L. Preparation of Macroporous Alginate-Based Aerogels for Biomedical Applications. *The Journal of Supercritical Fluids* **2015**, *106*, 152–159.

(251) Sani, N. S.; Malek, N. A. N. N.; Jemon, K.; Kadir, M. R. A.; Hamdan, H. Effect of Mass Concentration on Bioactivity and Cell Viability of Calcined Silica Aerogel Synthesized from Rice Husk Ash as Silica Source. *Journal of Sol-Gel Science and Technology* **2017**, *82*, 120–132.

(252) Kakkar, P.; Madhan, B. Fabrication of Keratin-Silica Hydrogel for Biomedical Applications. *Materials Science and Engineering: C* **2016**, *66*, 178–184. https://doi.org/10.1016/j.msec.2016.04.067.

(253) Nieto, A.; Areva, S.; Wilson, T.; Viitala, R.; Vallet-Regi, M. Cell Viability in a Wet Silica Gel. *Acta Biomaterialia* **2009**, *5* (9), 3478–3487. https://doi.org/10.1016/j.actbio.2009.05.033.

(254) Hench, L. L. The Story of Bioglass®. *Journal of Materials Science: Materials in Medicine* **2006**, *17* (11), 967–978. https://doi.org/10.1007/s10856-006-0432-z.

(255) Sepulveda, P.; Jones, J. R.; Hench, L. L. Bioactive Sol-gel Foams for Tissue Repair. *Journal of Biomedical Materials Research: An Official Journal of The Society for Biomaterials, The Japanese Society for Biomaterials, and The Australian Society for Biomaterials and the Korean Society for Biomaterials* **2002**, *59* (2), 340–348.

(256) Chen, Q. Z.; Thompson, I. D.; Boccaccini, A. R. 45S5 Bioglass®-Derived Glass-Ceramic Scaffolds for Bone Tissue Engineering. *Biomaterials* **2006**, *27* (11), 2414–2425. https://doi.org/10.1016/j.biomaterials.2005.11.025.

(257) Baino, F.; Fiume, E.; Barberi, J.; Kargozar, S.; Marchi, J.; Massera, J.; Verné, E. Processing Methods for Making Porous Bioactive Glass-Based Scaffolds—A State-of-the-Art Review. *International Journal of Applied Ceramic Technology* **2019**, *16* (5), 1762–1796. https://doi.org/10.1111/ijac.13195.

(258) Hench, L. L.; Jones, J. R. Bioactive Glasses: Frontiers and Challenges. *Front. Bioeng. Biotechnol.* **2015**, *3*. https://doi.org/10.3389/fbioe.2015.00194.

(259) Ribas, R. G.; Schatkoski, V. M.; Montanheiro, T. L. do A.; de Menezes, B. R. C.; Stegemann, C.; Leite, D. M. G.; Thim, G. P. Current Advances in Bone Tissue Engineering Concerning Ceramic and Bioglass Scaffolds: A Review. *Ceramics International* **2019**, *45* (17), 21051–21061. https://doi.org/10.1016/j.ceramint.2019.07.096.

(260) Sandberg, J.; Alvesson, M. Ways of Constructing Research Questions: Gap-Spotting or Problematization? *Organization* **2011**, *18* (1), 23–44. https://doi.org/10.1177/1350508410372151.

(261) Guzzo, C. M.; Nychka, J. Fabrication of a Porous and Formable Ceramic Composite Bone Tissue Scaffold at Ambient Temperature. *Metallurgical and Materials Transactions A* **2020**, *12*, 1–17. https://doi.org/10.1007/s11661-020-05924-9.

(262) Guzzo, C. M.; Nychka, J. A. Bone 'Spackling' Paste: Mechanical Properties and in Vitro Response of a Porous Ceramic Composite Bone Tissue Scaffold. *Journal of the Mechanical Behavior of Biomedical Materials* **2020**, *112* (May), 103958–103958. https://doi.org/10.1016/j.jmbbm.2020.103958.

(263) Morsy, R. Development and Evaluation of Degradable Hydroxyapatite/Sodium Silicate Composite for Low-Dose Drug Delivery Systems. *Bull Mater Sci* **2016**, *39* (5), 1273–1278. https://doi.org/10.1007/s12034-016-1269-9.

(264) Matinfar, M.; Nychka, J. A. A Review of Sodium Silicate Solutions: Structure, Gelation, and Syneresis. *Advances in Colloid and Interface Science* **2023**, 103036.

(265) Tognonvi, M. T.; Rossignol, S.; Bonnet, J.-P. Physical-Chemistry of Sodium Silicate Gelation in an Alkaline Medium. *J Sol-Gel Sci Technol* **2011**, *58* (3), 625–635. https://doi.org/10.1007/s10971-011-2437-4.

(266) Owoeye, S. S.; Abegunde, S. M.; Oji, B. Effects of Process Variable on Synthesis and Characterization of Amorphous Silica Nanoparticles Using Sodium Silicate Solutions as Precursor by Sol–Gel Method. *Nano-Structures & Nano-Objects* **2021**, *25*, 100625. https://doi.org/10.1016/j.nanoso.2020.100625.

(267) Pangesti, G. G.; Pandiangan, K. D.; Simanjuntak, W.; Sascori, S.; Rilyanti, M. Synthesis of Zeolite-Y from Rice Husk Silica and Food Grade Aluminum Foil Using Modified Hydrothermal Method; IOP Publishing, 2021; Vol. 1751, p 012089.

(268) Wang, X.; Wang, C.; Li, P.; Tian, D.; Wang, J.; Liu, B. Experimental Study on New Grouting Material of Acidic Sodium Silicate and Its Properties of Grouted-Sand. *Construction and Building Materials* **2023**, *392*, 131955. https://doi.org/10.1016/j.conbuildmat.2023.131955.

(269) Zhang, J.; Ji, Y.; Ma, Z.; Xu, Z.; Zhang, Z.; Xu, S. The Stabilization Mechanism of Nano-SiO2 Precursor Solution. *Materials* **2022**, *15* (20), 7207. https://doi.org/10.3390/ma15207207.

(270) Fleury, M.; Sissmann, O.; Brosse, E.; Chardin, M. A Silicate Based Process for Plugging the Near Well Bore Formation. *Energy Procedia* **2017**, *114*, 4172–4187. https://doi.org/10.1016/j.egypro.2017.03.1558.

(271) Mujkanović, A.; Jovanović, M. Synthesis of Precipitated Silica from Sodium Silicate Solution by Carbonation Method. *Periodicals of Engineering and Natural Sciences* **2021**, *9* (2), 808–819. https://doi.org/10.21533/pen.v9i2.1878.

(272) Huck-Iriart, C.; Morales, N. J.; Herrera, M. L.; Candal, R. J. Micro to Mesoporous SiO2xerogels: The Effect of Acid Catalyst Type in Sol–Gel Process. *J Sol-Gel Sci Technol* **2022**, *102* (1), 197–207. https://doi.org/10.1007/s10971-021-05601-2.

(273) Ulu, A.; Balcioglu, S.; Birhanli, E.; Sarimeseli, A.; Keskin, R.; Koytepe, S.; Ates, B. Poly (2-hydroxyethyl Methacrylate)/Boric Acid Composite Hydrogel as Soft Contact Lens Material: Thermal, Optical, Rheological, and Enhanced Antibacterial Properties. *Journal of Applied Polymer Science* **2018**, *135* (35), 46575.

(274) Tan, Y.; Liu, Y.; Grover, L. Effect of Phosphoric Acid on the Properties of Magnesium Oxychloride Cement as a Biomaterial. *Cement and concrete research* **2014**, *56*, 69–74.

(275) Prentice, L. H.; Tyas, M. J.; Burrow, M. F. The Effects of Boric Acid and Phosphoric Acid on the Compressive Strength of Glass-Ionomer Cements. *Dental Materials* **2006**, *22* (1), 94–97.

(276) Kabay, N.; Bryjak, M.; Hilal, N. The Chemistry of Boron in Water. In *Boron separation processes*; Elsevier, 2015; pp 35–64.

(277) Lackey, H. E.; Nelson, G. L.; Lines, A. M.; Bryan, S. A. Reimagining pH Measurement: Utilizing Raman Spectroscopy for Enhanced Accuracy in Phosphoric Acid Systems. *Anal. Chem.* **2020**, *92* (8), 5882–5889. https://doi.org/10.1021/acs.analchem.9b05708.

(278) Böschel, D.; Roggendorf, H. Water-Based Sodium Borosilicate Sols and Their Gelation-Characterisation by Viscosimetry, UV/VIS- and Infrared Spectroscopy. *Journal of Sol-Gel Science and Technology* **2002**, *25* (3), 191–200. https://doi.org/10.1023/A:1020283206199.

(279) Stavland, A.; Jonsbråten, H.; Vikane, O.; Skrettingland, K.; Fischer, H. In-Depth Water Diversion Using Sodium Silicate-Preparation for Single Well Field Pilot on Snorre. *16th European Symposium on Improved Oil Recovery 2011* **2011**, No. April, 638–652. https://doi.org/10.3997/2214-4609.201404788.

(280) Knoblich, B.; Gerber, T. The Arrangement of Fractal Clusters Dependent on the pH Value in Silica Gels from Sodium Silicate Solutions. *Journal of Non-Crystalline Solids* **2001**, *296* (1–2), 81–87. https://doi.org/10.1016/S0022-3093(01)00871-7.

(281) Owoeye, S. S.; Jegede, F. I.; Borisade, S. G. Preparation and Characterization of Nano-Sized Silica Xerogel Particles Using Sodium Silicate Solution Extracted from Waste Container Glasses. *Materials Chemistry and Physics* **2020**, *248*, 122915–122915.

(282) Mäntele, W.; Deniz, E. UV–VIS Absorption Spectroscopy: Lambert-Beer Reloaded. *Spectrochimica Acta Part A: Molecular and Biomolecular Spectroscopy* **2017**, *173*, 965–968. https://doi.org/10.1016/j.saa.2016.09.037.

(283) Israelachvili, J. N. Electrostatic Forces between Surfaces in Liquids. In *Intermolecular and surface forces*; Academic press, 2011; pp 291–338.

(284) Kaide, A.; Saeki, T. Development of Preparation Method to Control Silica Sol–Gel Synthesis with Rheological and Morphological Measurements. *Advanced Powder Technology* **2014**, *25* (2), 773–779. https://doi.org/10.1016/j.apt.2013.11.010.

(285) Krishnamurti, K. Investigations on the Scattering of Light in Colloidal Solutions and Gels. Part I—Agar Sol and Gel. *Proceedings of the Royal Society of London. Series A, Containing Papers of a Mathematical and Physical Character* **1929**, *122* (789), 76–103.

(286) Hříbalová, S.; Pabst, W. Modeling Light Scattering by Spherical Pores for Calculating the Transmittance of Transparent Ceramics–All You Need to Know. *Journal of the European Ceramic Society* **2021**, *41* (4), 2169–2192.

(287) Raychoudhury, T.; Tufenkji, N.; Ghoshal, S. Aggregation and Deposition Kinetics of Carboxymethyl Cellulose-Modified Zero-Valent Iron Nanoparticles in Porous Media. *Water research* **2012**, *46* (6), 1735–1744.

(288) Keshavarz, B.; Rodrigues, D. G.; Champenois, J.-B.; Frith, M. G.; Ilavsky, J.; Geri, M.; Divoux, T.; McKinley, G. H.; Poulesquen, A. Time–Connectivity Superposition and the Gel/Glass Duality of Weak Colloidal Gels. *Proc. Natl. Acad. Sci. U.S.A.* **2021**, *118* (15), e2022339118. https://doi.org/10.1073/pnas.2022339118.

(289) Yablonskii, G.; Lazman, M. Non-Linear Steady-State Kinetics of Complex Catalytic Reactions: Theory and Applications. *Studies in Surface Science and Catalysis* **1997**, *109*, 371–378.

(290) Lazman, M.; Yablonskii, G. Kinetic Polynomial: A New Concept of Chemical Kinetics, in '"Patterns and Dynamics in Reactive Media, The IMA Volumes in Mathematics and Its Applications."' **1991**.

(291) Marin, G. B.; Yablonsky, G. S.; Constales, D. Kinetic Polynomials. In *Kinetics of chemical reactions: decoding complexity*; John Wiley & Sons, 2019.

(292) Qin, Y.; Liao, R.; Luo, S.; Li, J. The Thermal Gelation Behavior and Performance Evaluation of High Molecular Weight Nonionic Polyacrylamide and Polyethyleneimine Mixtures for In-Depth Water Control in Mature Oilfields. *Materials* **2020**, *13* (18), 4142.

(293) Singh, R.; Mahto, V. Study of the Polymer Concentration and Polymer/Crosslinker Ratio Effect on Gelation Time of a Novel Grafted Polymer Gel for Water Shutoff Using a Central Composite Design Method. *Polymers for advanced technologies* **2016**, *27* (2), 204–212.

(294) Gommes, C.; Blacher, S.; Goderis, B.; Pirard, R.; Heinrichs, B.; Alié, C.; Pirard, J.-P. In Situ SAXS Analysis of Silica Gel Formation with an Additive. *The Journal of Physical Chemistry B* **2004**, *108* (26), 8983–8991.

(295) Kobayashi, M.; Juillerat, F.; Galletto, P.; Bowen, P.; Borkovec, M. Aggregation and Charging of Colloidal Silica Particles: Effect of Particle Size. *Langmuir* **2005**, *21* (13), 5761–5769. https://doi.org/10.1021/la046829z.

(296) Cametti, C.; Codastefano, P.; Tartaglia, P. Aggregation Kinetics in Model Colloidal Systems: A Light Scattering Study. *Journal of Colloid and Interface Science* **1989**, *131* (2), 409–422. https://doi.org/10.1016/0021-9797(89)90183-5.

(297) Calcabrini, M.; Onna, D. Exploring the Gel State: Optical Determination of Gelation Times and Transport Properties of Gels with an Inexpensive 3D-Printed Spectrophotometer. *Journal of Chemical Education* **2019**, *96* (1), 116–123. https://doi.org/10.1021/acs.jchemed.8b00529.

(298) Alanazi, S. J. F. A Multi-Analytical Investigation of the Hydrogel Phase. Doctoral dissertation, The University of Leeds, 2022.

(299) Bosch Ojeda, C.; Sanchez Rojas, F. Recent Developments in Derivative Ultraviolet/Visible Absorption Spectrophotometry. *Analytica Chimica Acta* **2004**, *518* (1–2), 1–24. https://doi.org/10.1016/j.aca.2004.05.036.

(300) Hříbalová, S.; Pabst, W. Modeling Light Scattering by Spherical Pores for Calculating the Transmittance of Transparent Ceramics – All You Need to Know. *Journal of the European Ceramic Society* **2021**, *41* (4), 2169–2192. https://doi.org/10.1016/j.jeurceramsoc.2020.11.046.

(301) Hulst, H. C.; van de Hulst, H. C. *Light Scattering by Small Particles*; Courier Corporation, 1981.

(302) Homburg, S. V.; Patel, A. V. Silica Hydrogels as Entrapment Material for Microalgae. *Polymers* **2022**, *14* (7), 1391. https://doi.org/10.3390/polym14071391.

(303) Pisal, A. A.; Rao, A. V. Comparative Studies on the Physical Properties of TEOS, TMOS and Na2SiO3 Based Silica Aerogels by Ambient Pressure Drying Method. *J Porous Mater* **2016**, *23* (6), 1547–1556. https://doi.org/10.1007/s10934-016-0215-y.

(304) Owens, G. J.; Singh, R. K.; Foroutan, F.; Alqaysi, M.; Han, C. M.; Mahapatra, C.; Kim, H. W.; Knowles, J. C. Sol-Gel Based Materials for Biomedical Applications. *Progress in Materials Science* **2016**, *77*, 1–79. https://doi.org/10.1016/j.pmatsci.2015.12.001.

(305) Videira-Quintela, D.; Martin, O.; Montalvo, G. Emerging Opportunities of Silica-Based Materials within the Food Industry. *Microchemical Journal* **2021**, *167*, 106318.

(306) Harris, R. K.; Knight, C. T. G. Silicon-29 Nuclear Magnetic Resonance Studies of Aqueous Silicate Solutions. Part 5.—First-Order Patterns in Potassium Silicate Solutions Enriched with Silicon-29. *Journal of the Chemical Society, Faraday Transactions 2: Molecular and Chemical Physics* **1983**, *79* (10), 1525–1538.

(307) Ullah, F.; Othman, M. B. H.; Javed, F.; Ahmad, Z.; Akil, H. Md. Classification, Processing and Application of Hydrogels: A Review. *Materials Science and Engineering: C* **2015**, *57*, 414–433. https://doi.org/10.1016/j.msec.2015.07.053.

(308) Tognonvi, M. T.; Rossignol, S.; Bonnet, J.-P. Effect of Alkali Cation on Irreversible Gel Formation in Basic Medium. *Journal of Non-Crystalline Solids* **2011**, *357* (1), 43–49. https://doi.org/10.1016/j.jnoncrysol.2010.10.003.

(309) Driouich, A.; El Hassani, S. E. A.; Chajri, F.; Britel, O.; Digua, K.; Chaair, H. Synthesis and Characterization of Silicate Gel by Using Sol-Gel Process: Experiments and DFT Calculations. *Mediterr.J.Chem.,* **2020**, *9* (6), 411–421. https://doi.org/10.13171/mjc9602001011134hc.

(310) Kierys, A.; Goworek, J.; Rawski, M.; Halasz, I. On The Molecular Basis Of Silica Gel Morphology. *Adv. Mater. Lett.* **2015**, *6* (1), 40–46. https://doi.org/10.5185/amlett.2015.amwc1194.

(311) Balachandran, C.; Muñoz, J. F.; Arnold, T. Characterization of Alkali Silica Reaction Gels Using Raman Spectroscopy. *Cement and Concrete Research* **2017**, *92*, 66–74. https://doi.org/10.1016/j.cemconres.2016.11.018.

(312) Parkinson, B. G.; Holland, D.; Smith, M. E.; Larson, C.; Doerr, J.; Affatigato, M.; Feller, S. A.; Howes, A. P.; Scales, C. R. Quantitative Measurement of Q3 Species in Silicate and Borosilicate Glasses Using Raman Spectroscopy. *Journal of Non-Crystalline Solids* **2008**, *354* (17), 1936–1942. https://doi.org/10.1016/j.jnoncrysol.2007.06.105.

(313) Drewitt, J. W. E.; Hennet, L.; Neuville, D. R. From Short to Medium Range Order in Glasses and Melts by Diffraction and Raman Spectroscop. In *Geological melts*; Reviews in mineralogy and geochemistry; Mineralogical society of America Geochemical society: Chantilly [Washington, DC], 2022.

(314) O′Shaughnessy, C.; Henderson, G. S.; Nesbitt, H. W.; Bancroft, G. M.; Neuville, D. R. The Influence of Modifier Cations on the Raman Stretching Modes of Qn Species in Alkali Silicate Glasses. **2020**, No. 103, 3991–4001.

(315) Liu, H.; Hahn, S. H.; Ren, M.; Thiruvillamalai, M.; Gross, T. M.; Du, J.; Van Duin, A. C. T.; Kim, S. H. Searching for Correlations between Vibrational Spectral Features and Structural Parameters of Silicate Glass Network. *J Am Ceram Soc* **2020**, *103* (6), 3575–3589. https://doi.org/10.1111/jace.17036.

(316) Liu, H.; Kaya, H.; Lin, Y.; Ogrinc, A.; Kim, S. H. Vibrational Spectroscopy Analysis of Silica and Silicate Glass Networks. *J Am Ceram Soc.* **2022**, *105* (4), 2355–2384. https://doi.org/10.1111/jace.18206.

(317) Rimsza, J. M.; Du, J. Nanoporous Silica Gel Structures and Evolution from Reactive Force Field-Based Molecular Dynamics Simulations. *npj Materials Degradation* **2018**, *2* (1), 1–10. https://doi.org/10.1038/s41529-018-0039-0.

(318) Kamińska, M.; Gruy, F.; Valente, J. Dynamics of Non-Dense Sodium Silicate - Water System Studied by Molecular Dynamics. *Colloids and Surfaces A: Physicochemical and Engineering Aspects* **2020**, *603*. https://doi.org/10.1016/j.colsurfa.2020.125226.

(319) Geisler, T.; Dohmen, L.; Lenting, C.; Fritzsche, M. B. K. Real-Time in Situ Observations of Reaction and Transport Phenomena during Silicate Glass Corrosion by Fluid-Cell Raman Spectroscopy. *Nat. Mater.* **2019**, *18* (4), 342–348. https://doi.org/10.1038/s41563-019-0293-8.

(320) De Ferri, L.; Lorenzi, A.; Lottici, P. P. OctTES/TEOS System for Hybrid Coatings: Real-Time Monitoring of the Hydrolysis and Condensation by Raman Spectroscopy: OctTES/TEOS System for Hybrid Coatings. *J. Raman Spectrosc.* **2016**, *47* (6), 699–705. https://doi.org/10.1002/jrs.4881.

(321) Marino, I.-G.; Lottici, P. P.; Bersani, D.; Raschellà, R.; Lorenzi, A.; Montenero, A. Micro-Raman Monitoring of Solvent-Free TEOS Hydrolysis. *Journal of Non-Crystalline Solids* **2005**, *351* (6–7), 495–498. https://doi.org/10.1016/j.jnoncrysol.2004.11.023.

(322) Takahashi, N.; Tsujimori, T.; Kamada, S.; Nakamura, M. In-Situ Raman Spectroscopic Analysis of Dissolved Silica Structures in Na2CO3 and NaOH Solutions at High Pressure and Temperature. *Contributions to Mineralogy and Petrology* **2022**, *177* (3), 1–15. https://doi.org/10.1007/s00410-022-01892-y.

(323) Koroleva, O. N.; Anfilogov, V. N.; Shatskiy, A.; Litasov, K. D. Structure of Na2O–SiO2 Melt as a Function of Composition: In Situ Raman Spectroscopic Study. *Journal of Non-Crystalline Solids* **2013**, *375*, 62–68. https://doi.org/10.1016/j.jnoncrysol.2013.04.060.

(324) Zotov, N.; Keppler, H. In-Situ Raman Spectra of Dissolved Silica Species in Aqueous Fluids to 900 °C and 14 Kbar. *American Mineralogist* **2000**, *85* (3–4), 600–604. https://doi.org/10.2138/am-2000-0423.

(325) Balköse, D. Effect of Preparation pH on Properties of Silica Gel. *J of Chemical Tech & Biotech* **1990**, *49* (2), 165–171. https://doi.org/10.1002/jctb.280490207.

(326) Brinker, C. J.; Scherer, G. W. *Sol-Gel Science: The Physics and Chemistry of Sol-Gel Processing*; Academic press, 1990.

(327) Van Speybroeck, V.; Hemelsoet, K.; Joos, L.; Waroquier, M.; Bell, R. G.; Catlow, C. R. A. Advances in Theory and Their Application within the Field of Zeolite Chemistry. *Chemical Society Reviews* **2015**, *44* (20), 7044–7111. https://doi.org/10.1039/c5cs00029g.

(328) Innocenzi, P. *The Sol-to-Gel Transition*; SpringerBriefs in Materials; Springer International Publishing: Cham, 2019. https://doi.org/10.1007/978-3-030-20030-5.

(329) Depla, A.; Lesthaeghe, D.; Van Erp, T. S.; Aerts, A.; Houthoofd, K.; Fan, F.; Li, C.; Van Speybroeck, V.; Waroquier, M.; Kirschhock, C. E. A.; Martens, J. A. 29Si NMR and UV-Raman Investigation of Initial Oligomerization Reaction Pathways in Acid-Catalyzed Silica Sol-Gel Chemistry. *Journal of Physical Chemistry C* **2011**, *115* (9), 3562–3571. https://doi.org/10.1021/jp109901v.

(330) Mysen, B. O.; Finger, L. W.; Virgo, D.; Seifert, F. A. Curve-Fitting of Raman Spectra of Silicate Glasses. *American Mineralogist* **1982**, *67* (7–8), 686–695.

(331) Richet, P.; Mysen, BjornO.; Andrault, D. Melting and Premelting of Silicates: Raman Spectroscopy and X-Ray Diffraction of Li2SiO3 and Na2SiO3. *Phys Chem Minerals* **1996**, *23* (3). https://doi.org/10.1007/BF00220727.

(332) Manara, D.; Grandjean, A.; Neuville, D. R. Advances in Understanding the Structure of Borosilicate Glasses: A Raman Spectroscopy Study. *American Mineralogist* **2009**, *94* (5–6), 777–784. https://doi.org/10.2138/am.2009.3027.

(333) O′Shaughnessy, C.; Henderson, G. S.; Nesbitt, H. W.; Bancroft, G. M.; Neuville, D. R. The Influence of Modifier Cations on the Raman Stretching Modes of Qn Species in Alkali Silicate Glasses. *Journal of the American Ceramic Society* **2020**, *103* (7), 3991–4001. https://doi.org/10.1111/jace.17081.

(334) Bancroft, G. M.; Nesbitt, H. W.; Henderson, G. S.; O′Shaughnessy, C.; Withers, A. C.; Neuville, D. R. Lorentzian Dominated Lineshapes and Linewidths for Raman Symmetric Stretch Peaks (800–1200 cm−1) in Qn (N = 1–3) Species of Alkali Silicate Glasses/Melts. *Journal of Non-Crystalline Solids* **2018**, *484* (October 2017), 72–83. https://doi.org/10.1016/j.jnoncrysol.2018.01.018.

(335) O′Shaughnessy, C.; Henderson, G. S.; Nesbitt, H. W.; Bancroft, G. M.; Neuville, D. R. Structure-Property Relations of Caesium Silicate Glasses from Room Temperature to 1400 K: Implications from Density and Raman Spectroscopy. *Chemical Geology* **2017**, *461*, 82–95. https://doi.org/10.1016/j.chemgeo.2016.11.028.

(336) Krüger, M. E.; Thome, V.; Hilbig, H.; Kaliwoda, M.; Heinz, D. Investigations on Alkali-Silica Reaction Products Using Raman Spectroscopy. *materconstrucc* **2022**, *72* (346), e281. https://doi.org/10.3989/mc.2022.15621.

(337) Halasz, I.; Kierys, A.; Goworek, J.; Liu, H.; Patterson, R. E. 29Si NMR and Raman Glimpses into the Molecular Structures of Acid and Base Set Silica Gels Obtained from TEOS and Na-Silicate. *Journal of Physical Chemistry C* **2011**, *115* (50), 24788–24799. https://doi.org/10.1021/jp207534e.

(338) Halasz, I.; Agarwal, M.; Li, R.; Miller, N. What Can Vibrational Spectroscopy Tell about the Structure of Dissolved Sodium Silicates ? *Microporous and Mesoporous Materials* **2010**, *135* (1–3), 74–81. https://doi.org/10.1016/j.micromeso.2010.06.013.

(339) Vidal, L.; Gharzouni, A.; Joussein, E.; Colas, M.; Cornette, J.; Absi, J.; Rossignol, S. Determination of the Polymerization Degree of Various Alkaline Solutions: Raman Investigation. *Journal of Sol-Gel Science and Technology* **2017**, *83* (1), 1–11. https://doi.org/10.1007/s10971-017-4394-z.

(340) Halasz, I.; Li, R.; Agarwal, M.; Miller, N. Dissociation, Molweight, and Vibrational Spectra of Aqueous Sodium Silicate Solutions. In *Studies in Surface Science and Catalysis*; Elsevier B.V., 2007; Vol. 170, pp 800–805. https://doi.org/10.1016/S0167-2991(07)80924-4.

(341) Pasquarello, A.; Car, R. Identification of Raman Defect Lines as Signatures of Ring Structures in Vitreous Silica. *Phys. Rev. Lett.* **1998**, *80* (23), 5145–5147. https://doi.org/10.1103/PhysRevLett.80.5145.

(342) Sharma, S. K.; Mammone, J. F.; Nicol, M. F. Raman Investigation of Ring Configurations in Vitreous Silica. *Nature* **1981**, *292* (5819), 140–141. https://doi.org/10.1038/292140a0.

(343) Bancroft, G. M.; Nesbitt, H. W.; Henderson, G. S.; O′Shaughnessy, C.; Withers, A. C.; Neuville, D. R. Lorentzian Dominated Lineshapes and Linewidths for Raman Symmetric

Stretch Peaks (800−1200 Cm−1) in Qn (n = 1−3) Species of Alkali Silicate Glasses/Melts. *Journal of Non-Crystalline Solids* **2018**, *484*, 72−83. https://doi.org/10.1016/j.jnoncrysol.2018.01.018.

(344) Malfait, W. J.; Zakaznova-Herzog, V. P.; Halter, W. E. Quantitative Raman Spectroscopy: Speciation of Na-Silicate Glasses and Melts. In *American Mineralogist*; 2008; Vol. 93, pp 1505−1518. https://doi.org/10.2138/am.2008.2783.

(345) Hehlen, B.; Neuville, D. Raman Response of Network Modifier Cations in Alumino-Silicate Glasses. *The Journal of Physical Chemistry B* **2015**, *119* (10), 4093−4098.

(346) Peyne, J.; Gautron, J.; Doudeau, J.; Joussein, E.; Rossignol, S. Influence of Silicate Solution Preparation on Geomaterials Based on Brick Clay Materials. *Journal of Non-Crystalline Solids* **2017**, *471* (May), 110−119. https://doi.org/10.1016/j.jnoncrysol.2017.05.017.

(347) Halasz, I.; Agarwal, M.; Li, R.; Miller, N. Molecular Spectroscopy of Alkaline Silicate Solutions. *Studies in Surface Science and Catalysis* **2008**, *174* (B), 787−792. https://doi.org/10.1016/S0167-2991(08)80008-0.

(348) Kupka, N.; Kaden, P.; Jantschke, A.; Schach, E.; Rudolph, M. Acidified Water Glass in the Selective Flotation of Scheelite from Calcite, Part II: Species in Solution and Related Mechanism of the Depressant. *Physicochemical Problems of Mineral Processing* **2020**, *56* (5), 797−817. https://doi.org/10.37190/PPMP/125639.

(349) Halasz, I.; Agarwal, M.; Patterson, R. E. *Molecular Aspects of Solid Silica Formation*; Elsevier Masson SAS, 2010; Vol. 175. https://doi.org/10.1016/S0167-2991(10)75026-6.

(350) Bärtsch, M.; Bornhauser, P.; Calzaferri, G.; Imhof, R. Correlation of the Vibrational Structure of H8Si8O12 and H10Si10O15. *Vibrational Spectroscopy* **1995**, *8* (2), 305−308. https://doi.org/10.1016/0924-2031(94)00027-E.

(351) Bornhauser, P.; Calzaferri, G. Ring-Opening Vibrations of Spherosiloxanes. *J. Phys. Chem.* **1996**, *100* (6), 2035−2044. https://doi.org/10.1021/jp952198t.

(352) Peng, M.; Jiang, J.; Liu, X.; Ma, Y.; Jiao, M.; Xu, H.; Wu, H.; He, M.; Wu, P. Breaking Structural Energy Constraints: Hydrothermal Crystallization of High-Silica Germanosilicates by a Building-Unit Self-Growth Approach. *Chemistry - A European Journal* **2018**, *24* (50), 13297−13305. https://doi.org/10.1002/chem.201802255.

(353) Inagaki, S.; Nakatsuyama, K.; Saka, Y.; Kikuchi, E.; Kohara, S.; Matsukata, M. Elucidation of Medium-Range Structure in a Dry Gel-Forming *BEA-Type Zeolite. *Journal of Physical Chemistry C* **2007**, *111* (28), 10285−10293. https://doi.org/10.1021/jp0668044.

(354) Yu, Y.; Xiong, G.; Li, C.; Xiao, F.-S. Characterization of Aluminosilicate Zeolites by UV Raman Spectroscopy. *Microporous and Mesoporous Materials* **2001**, *46* (1), 23−34. https://doi.org/10.1016/S1387-1811(01)00271-2.

(355) Kubicki, J. D.; Sykes, D. Molecular Orbital Calculations of Vibrations in Three-Membered Aluminosilicate Rings. *Phys Chem Minerals* **1993**, *19* (6). https://doi.org/10.1007/BF00202975.

(356) McMillan, P. Structural Studies of Silicate Glasses and Melts-Applications and Limitations of Raman Spectroscopy. *American Mineralogist* **1984**, *69* (7−8), 622−644.

(357) Neuville, D. R.; De Ligny, D.; Henderson, G. S. Advances in Raman Spectroscopy Applied to Earth and Material Sciences. *Reviews in Mineralogy and Geochemistry* **2014**, *78* (1), 509−541. https://doi.org/10.2138/rmg.2013.78.13.

(358) Yadav, A. K.; Singh, P. A Review of the Structures of Oxide Glasses by Raman Spectroscopy. *RSC Adv.* **2015**, *5* (83), 67583–67609. https://doi.org/10.1039/C5RA13043C.
(359) Sharma, S. K.; Mammone, J. F.; Nicol, M. F. Raman Investigation of Ring Configurations in Vitreous Silica. *Nature* **1981**, *292* (5819), 140–141. https://doi.org/10.1038/292140a0.
(360) Brawer, S. A.; White, W. B. Raman Spectroscopic Investigation of the Structure of Silicate Glasses. I. The Binary Alkali Silicates. *The Journal of Chemical Physics* **1975**, *63* (6), 2421–2432. https://doi.org/10.1063/1.431671.
(361) Matson, D. W.; Sharma, S. K.; Philpotts, J. A. The Structure of High-Silica Alkali-Silicate Glasses. A Raman Spectroscopic Investigation. *Journal of Non-Crystalline Solids* **1983**, *58* (2–3), 323–352. https://doi.org/10.1016/0022-3093(83)90032-7.
(362) Spiekermann, G.; Steele-Macinnis, M.; Schmidt, C.; Jahn, S. Vibrational Mode Frequencies of Silica Species in SiO2-H2O Liquids and Glasses from Ab Initio Molecular Dynamics. *Journal of Chemical Physics* **2012**, *136* (15). https://doi.org/10.1063/1.3703667.
(363) Depla, A.; Verheyen, E.; Veyfeyken, A.; Van Houteghem, M.; Houthoofd, K.; Van Speybroeck, V.; Waroquier, M.; Kirschhock, C. E. A.; Martens, J. A. UV-Raman and 29Si NMR Spectroscopy Investigation of the Nature of Silicate Oligomers Formed by Acid Catalyzed Hydrolysis and Polycondensation of Tetramethylorthosilicate. *Journal of Physical Chemistry C* **2011**, *115* (22), 11077–11088. https://doi.org/10.1021/jp200568j.
(364) Artaki, I.; Bradley, M.; Zerda, T. W.; Jonas, J. NMR and Raman Study of the Hydrolysis Reaction in Sol-Gel Processes. *J. Phys. Chem.* **1985**, *89* (20), 4399–4404. https://doi.org/10.1021/j100266a050.
(365) Mysen, B. O. Solution Mechanisms of Silicate in Aqueous Fluid and H2O in Coexisting Silicate Melts Determined In-Situ at High Pressure and High Temperature. *Geochimica et Cosmochimica Acta* **2009**, *73* (19), 5748–5763. https://doi.org/10.1016/j.gca.2009.06.023.
(366) Arnoult, M.; Perronnet, M.; Autef, A.; Rossignol, S. How to Control the Geopolymer Setting Time with the Alkaline Silicate Solution. *Journal of Non-Crystalline Solids* **2018**, *495* (February), 59–66. https://doi.org/10.1016/j.jnoncrysol.2018.02.036.
(367) Kittel, C.; McEuen, P. *Introduction to Solid State Physics*; John Wiley & Sons, 2018.
(368) Humlíček, J. Transverse and Longitudinal Vibration Modes in α-Quartz. *Philosophical Magazine B* **1994**, *70* (3), 699–710.
(369) Sarnthein, J.; Pasquarello, A.; Car, R. Origin of the High-Frequency Doublet in the Vibrational Spectrum of Vitreous SiO $_2$. *Science* **1997**, *275* (5308), 1925–1927. https://doi.org/10.1126/science.275.5308.1925.
(370) Galeener, F. L.; Lucovsky, G. Longitudinal Optical Vibrations in Glasses: GeO2 and SiO2. *Phys. Rev. Lett.* **1976**, *37* (22), 1474–1478. https://doi.org/10.1103/PhysRevLett.37.1474.
(371) Nesbitt, H. W.; Henderson, G. S.; Bancroft, G. M.; O′Shaughnessy, C. Electron Densities over Si and O Atoms of Tetrahedra and Their Impact on Raman Stretching Frequencies and Si-NBO Force Constants. *Chemical Geology* **2017**, *461*, 65–74. https://doi.org/10.1016/j.chemgeo.2016.11.022.
(372) Nesbitt, H. W.; Bancroft, G. M.; Henderson, G. S.; Ho, R.; Dalby, K. N.; Huang, Y.; Yan, Z. Bridging, Non-Bridging and Free (O2−) Oxygen in Na2O-SiO2 Glasses: An X-Ray Photoelectron Spectroscopic (XPS) and Nuclear Magnetic Resonance (NMR) Study.

Journal of Non-Crystalline Solids **2011**, *357* (1), 170−180. https://doi.org/10.1016/j.jnoncrysol.2010.09.031.
(373) Ching, W.; Murray, R.; Lam, D.; Veal, B. Comparative Studies of Electronic Structures of Sodium Metasilicate and α and β Phases of Sodium Disilicate. *Physical Review B* **1983**, *28* (8), 4724.
(374) Nesbitt, H. W.; O′Shaughnessy, C.; Henderson, G. S.; Michael Bancroft, G.; Neuville, D. R. Factors Affecting Line Shapes and Intensities of Q3 and Q4 Raman Bands of Cs Silicate Glasses. *Chemical Geology* **2019**, *505*, 1−11. https://doi.org/10.1016/j.chemgeo.2018.12.009.
(375) Drewitt, J. W. E.; Hennet, L.; Neuville, D. R. From Short to Medium Range Order in Glasses and Melts by Diffraction and Raman Spectroscopy. In *Reviews in Mineralogy and Geochemistry*; 2022; Vol. 87, pp 55−103. https://doi.org/10.2138/rmg.2022.87.02.
(376) Bordiga, S.; Lamberti, C.; Bonino, F.; Travert, A.; Thibault-Starzyk, F. Probing Zeolites by Vibrational Spectroscopies. *Chemical Society Reviews* **2015**, *44* (20), 7262−7341.
(377) Knops-Gerrits, P.-P.; De Vos, D. E.; Feijen, E. J. P.; Jacobs, P. A. Raman Spectroscopy on Zeolites. *Microporous Materials* **1997**, *8* (1−2), 3−17. https://doi.org/10.1016/S0927-6513(96)00088-0.
(378) Dutta, P. K.; Shieh, D. C.; Puri, M. Correlation of Framework Raman Bands of Zeolites with Structure. *Zeolites* **1988**, *8* (4), 306–309. https://doi.org/10.1016/S0144-2449(88)80127-1.
(379) Suzuki, Y.; Wakihara, T.; Kohara, S.; Itabashi, K.; Ogura, M.; Okubo, T. Mechanistic Study on the Synthesis of a Porous Zincosilicate VPI-7 Containing Three-Membered Rings. *J. Phys. Chem. C* **2011**, *115* (2), 443–446. https://doi.org/10.1021/jp109373z.
(380) Uzunova, E. L.; St. Nikolov, G. Vibrational Modes of Double Four-Member Rings of Oxygen-Bridged Silicon and Aluminum Atoms: A DFT Study. *J. Phys. Chem. B* **2000**, *104* (31), 7299−7305. https://doi.org/10.1021/jp0006680.
(381) Jiang, J.; Jorda, J. L.; Diaz-Cabanas, M. J.; Yu, J.; Corma, A. The Synthesis of an Extra-Large-Pore Zeolite with Double Three-Ring Building Units and a Low Framework Density. *Angew. Chem., Int. Ed* **2010**, *49* (29), 4986–4988.
(382) Mozgawa, W. The Relation between Structure and Vibrational Spectra of Natural Zeolites. *Journal of Molecular Structure* **2001**, *596* (1−3), 129−137. https://doi.org/10.1016/S0022-2860(01)00741-4.
(383) Mozgawa, W.; Jastrzębski, W.; Handke, M. Vibrational Spectra of D4R and D6R Structural Units. *Journal of Molecular Structure* **2005**, *744*, 663−670.
(384) Lynn, A.; Bonfield, W. A Novel Method for the Simultaneous, Titrant-Free Control of pH and Calcium Phosphate Mass Yield. *Accounts of chemical research* **2005**, *38* (3), 202–207.
(385) Kabay, N.; Bryjak, M. Boron Removal from Seawater Using Reverse Osmosis Integrated Processes. In *Boron separation processes.*; Elsevier: Amsterdam, Netherland:, 2015; pp 219−235.
(386) Applegarth, L. M. S. G. A.; Pye, C. C.; Cox, J. S.; Tremaine, P. R. Raman Spectroscopic and Ab Initio Investigation of Aqueous Boric Acid, Borate, and Polyborate Speciation from 25 to 80 °C. *Ind. Eng. Chem. Res.* **2017**, *56* (47), 13983−13996. https://doi.org/10.1021/acs.iecr.7b03316.

(387) Rigsby, M. A.; Spurlin, T. A.; Reid, J. D. The Multi-Functional Role of Boric Acid in Cobalt Electrodeposition and Superfill. *J. Electrochem. Soc.* **2020**, *167* (11), 112507. https://doi.org/10.1149/1945-7111/aba640.

(388) Falcone, J. S. Silicon Compounds: Anthropogenic Silicas and Silicates. *Kirk-Othmer Encyclopedia of Chemical Technology* **2015**, No. 2, 1–32. https://doi.org/10.1002/0471238961.1925142006011203.a01.pub3.

(389) Chakoumakos, B. C.; Hill, R.; Gibbs, C. A Molecular Orbital Study of Rings in Silicates and Siloxanes. *American Mineralogist* **1981**, *66* (11–12), 1237–1249.

(390) Cypryk, M.; Apeloig, Y. Mechanism of the Acid-Catalyzed Si–O Bond Cleavage in Siloxanes and Siloxanols. A Theoretical Study. *Organometallics* **2002**, *21* (11), 2165–2175. https://doi.org/10.1021/om011055s.

(391) Bangi, U. K. H.; Parvathy Rao, A.; Hirashima, H.; Venkateswara Rao, A. Physico-Chemical Properties of Ambiently Dried Sodium Silicate Based Aerogels Catalyzed with Various Acids. *J Sol-Gel Sci Technol* **2009**, *50* (1), 87–97. https://doi.org/10.1007/s10971-008-1887-9.

(392) Yue, D.-C.; Ma, T.-B.; Hu, Y.-Z.; Yeon, J.; Van Duin, A. C. T.; Wang, H.; Luo, J. Tribochemical Mechanism of Amorphous Silica Asperities in Aqueous Environment: A Reactive Molecular Dynamics Study. *Langmuir* **2015**, *31* (4), 1429–1436. https://doi.org/10.1021/la5042663.

(393) Wang, M.; Winter, H. H.; Auernhammer, G. K. Time and Frequency Dependent Rheology of Reactive Silica Gels. *Journal of Colloid and Interface Science* **2014**, *413*, 159–166. https://doi.org/10.1016/j.jcis.2013.09.035.

(394) Wijnen, P. W. J. G.; Beelen, T. P. M.; Rummens, K. P. J.; Saeijs, H. C. P. L.; Van Santen, R. A. Silica Gel from Water Glass: A SAXS Study of the Formation and Ageing of Fractal Aggregates. *Journal of Applied Crystallography* **1991**, *24* (pt 5), 759–764. https://doi.org/10.1107/S0021889891000924.

(395) Acker, E. G. The Characterization of Acid-Set Silica Hydrosols, Hydrogels, and Dried Gel. *Journal of Colloid and Interface Science* **1970**, *32* (1), 41–54. https://doi.org/10.1016/0021-9797(70)90099-8.

(396) Falcone, J. S.; Bass, J. L.; Krumrine, P. H.; Brensinger, K.; Schenk, E. R. Characterizing the Infrared Bands of Aqueous Soluble Silicates. *Journal of Physical Chemistry A* **2010**, *114* (7), 2438–2446. https://doi.org/10.1021/jp908113s.

(397) Kaide, A.; Saeki, T. Rheology of Silica Gel Obtained from Alkaline Sol Transition. *J. Soc. Rheol., Jpn* **2012**, *40* (4), 165–170. https://doi.org/10.1678/rheology.40.165.

(398) Oh, J. K.; Kohli, N.; Zhang, Y.; Min, Y.; Jayaraman, A.; Cisneros-Zevallos, L.; Akbulut, M. Nanoporous Aerogel as a Bacteria Repelling Hygienic Material for Healthcare Environment. *Nanotechnology* **2016**, *27* (8), 085705.

(399) Oh, J.-S.; Park, J.-S.; Han, C.-M.; Lee, E.-J. Facile in Situ Formation of Hybrid Gels for Direct-Forming Tissue Engineering. *Materials Science and Engineering: C* **2017**, *78*, 796–805. https://doi.org/10.1016/j.msec.2017.04.111.

(400) Lin, H.-R.; Ling, M.-H.; Lin, Y.-J. High Strength and Low Friction of a PAA-Alginate-Silica Hydrogel as Potential Material for Artificial Soft Tissues. *Journal of Biomaterials Science, Polymer Edition* **2009**, *20* (5–6), 637–652. https://doi.org/10.1163/156856209X426448.

(401) Tian, J.; Fu, C.; Li, W.; Li, N.; Yao, L.; Xiao, J. Biomimetic Tri-Layered Artificial Skin Comprising Silica Gel-Collagen Membrane-Collagen Porous Scaffold for Enhanced Full-Thickness Wound Healing. *International Journal of Biological Macromolecules* **2024**, *266*, 131233. https://doi.org/10.1016/j.ijbiomac.2024.131233.
(402) Diab, R.; Canilho, N.; Pavel, I. A.; Ha, F. B.; Girardon, M.; Pasc, A. Silica-Based Systems for Oral Delivery of Drugs, Macromolecules and Cells. *Advances in Colloid and Interface Science* **2017**, *249* (February), 346–362. https://doi.org/10.1016/j.cis.2017.04.005.
(403) Parfenyuk, E. V.; Dolinina, E. S. Silica Hydrogel Composites as a Platform for Soft Drug Formulations and Cosmetic Compositions. *Materials Chemistry and Physics* **2022**, *287*, 126160. https://doi.org/10.1016/j.matchemphys.2022.126160.
(404) Dolinina, E. S.; Parfenyuk, E. V. Silica Hydrogels as a Basis of Novel Soft Dosage Forms and Cosmetic Compositions. *Russ. J. Inorg. Chem.* **2022**, *67* (3), 401–407. https://doi.org/10.1134/S0036023622030068.
(405) Oliveira, A. L.; Malafaya, P. B.; Reis, R. L. Sodium Silicate Gel as a Precursor for the in Vitro Nucleation and Growth of a Bone-like Apatite Coating in Compact and Porous Polymeric Structures. *Biomaterials* **2003**, *24* (15), 2575–2584. https://doi.org/10.1016/S0142-9612(03)00060-7.
(406) Miyaji, F.; Kim, H. M.; Handa, S.; Kokubo, T.; Nakamura, T. Bonelike Apatite Coating on Organic Polymers: Novel Nucleation Process Using Sodium Silicate Solution. *Biomaterials* **1999**, *20* (10), 913–919. https://doi.org/10.1016/S0142-9612(98)00235-X.
(407) Schloßmacher, U.; Schröder, H. C.; Wang, X.; Feng, Q.; Diehl-Seifert, B.; Neumann, S.; Trautwein, A.; Müller, W. E. G. Alginate/Silica Composite Hydrogel as a Potential Morphogenetically Active Scaffold for Three-Dimensional Tissue Engineering. *RSC Adv.* **2013**, *3* (28), 11185. https://doi.org/10.1039/c3ra23341c.
(408) Prasadh, S.; Wong, R. C. W. Unraveling the Mechanical Strength of Biomaterials Used as a Bone Scaffold in Oral and Maxillofacial Defects. *Oral Science International* **2018**, *15* (2), 48–55. https://doi.org/10.1016/S1348-8643(18)30005-3.
(409) Jones, J. R.; Brauer, D. S.; Hupa, L.; Greenspan, D. C. Bioglass and Bioactive Glasses and Their Impact on Healthcare. *International Journal of Applied Glass Science* **2016**, *7* (4), 423–434. https://doi.org/10.1111/ijag.12252.
(410) Baino, F.; Fiume, E. Mechanical Characterization of 45S5 Bioactive Glass-Derived Scaffolds. *Materials Letters* **2019**, *245*, 14–17. https://doi.org/10.1016/j.matlet.2019.02.086.
(411) Baino, F.; Fiume, E. Elastic Mechanical Properties of 45S5-Based Bioactive Glass–Ceramic Scaffolds. *Materials* **2019**, *12* (19), 3244. https://doi.org/10.3390/ma12193244.
(412) Kaur, G.; Kumar, V.; Baino, F.; Mauro, J. C.; Pickrell, G.; Evans, I.; Bretcanu, O. Mechanical Properties of Bioactive Glasses, Ceramics, Glass-Ceramics and Composites: State-of-the-Art Review and Future Challenges. *Materials Science and Engineering: C* **2019**, *104*, 109895. https://doi.org/10.1016/j.msec.2019.109895.
(413) Woignier, T.; Primera, J.; Alaoui, A.; Etienne, P.; Despestis, F.; Calas-Etienne, S. Mechanical Properties and Brittle Behavior of Silica Aerogels. *Gels* **2015**, *1* (2), 256–275. https://doi.org/10.3390/gels1020256.
(414) Maleki, H.; Durães, L.; Portugal, A. An Overview on Silica Aerogels Synthesis and Different Mechanical Reinforcing Strategies. *Journal of Non-Crystalline Solids* **2014**, *385*, 55–74. https://doi.org/10.1016/j.jnoncrysol.2013.10.017.

(415) Sodium Silicate-Based Aerogels by Ambient Pressure Drying. In *Springer Handbook of Aerogels*; Rao, A. V., Shanyu, Z., Gerard, M. P., Bangi, U. k. H., Rao, A. P., Koebel, M. M., Eds.; Springer Handbooks; Springer International Publishing: Cham, 2023. https://doi.org/10.1007/978-3-030-27322-4.

(416) Parmenter, K. E.; Milstein, F. Mechanical Properties of Silica Aerogels. *Journal of Non-Crystalline Solids* **1998**, *223* (3), 179–189. https://doi.org/10.1016/S0022-3093(97)00430-4.

(417) Oyen, M. L. Mechanical Characterisation of Hydrogel Materials. *International Materials Reviews* **2014**, *59* (1), 44–59. https://doi.org/10.1179/1743280413Y.0000000022.

(418) Anseth, K. S.; Bowman, C. N.; Brannon-Peppas, L. Mechanical Properties of Hydrogels and Their Experimental Determination. *Biomaterials* **1996**, *17* (17), 1647–1657. https://doi.org/10.1016/0142-9612(96)87644-7.

(419) Kloxin, A. M.; Kloxin, C. J.; Bowman, C. N.; Anseth, K. S. Mechanical Properties of Cellularly Responsive Hydrogels and Their Experimental Determination. *Advanced Materials* **2010**, *22* (31), 3484–3494. https://doi.org/10.1002/adma.200904179.

(420) Dourbash, A.; Buratti, C.; Belloni, E.; Motahari, S. Preparation and Characterization of Polyurethane/Silica Aerogel Nanocomposite Materials. *J of Applied Polymer Sci* **2017**, *134* (8), app.44521. https://doi.org/10.1002/app.44521.

(421) Ahmed, N. B.; Ronsin, O.; Mouton, L.; Sicard, C.; Yéprémian, C.; Baumberger, T.; Brayner, R.; Coradin, T. The Physics and Chemistry of Silica-in-Silicates Nanocomposite Hydrogels and Their Phycocompatibility. *J. Mater. Chem. B* **2017**, *5* (16), 2931–2940. https://doi.org/10.1039/C7TB00341B.

(422) Parfenyuk, E.; Dolinina, E. Silica Hydrogels as Platform for Delivery of Hyaluronic Acid. *Pharmaceutics* **2022**, *15* (1), 77. https://doi.org/10.3390/pharmaceutics15010077.

(423) Zhang, Y. R.; Xu, K. J.; Bai, Y. L.; Tang, L. Q.; Jiang, Z. Y.; Liu, Y. P.; Liu, Z. J.; Zhou, L. C.; Zhou, X. F. Features of the Volume Change and a New Constitutive Equation of Hydrogels under Uniaxial Compression. *Journal of the Mechanical Behavior of Biomedical Materials* **2018**, *85*, 181–187. https://doi.org/10.1016/j.jmbbm.2018.06.004.

(424) Nafar Dastgerdi, J.; Koivisto, J. T.; Orell, O.; Rava, P.; Jokinen, J.; Kanerva, M.; Kellomäki, M. Comprehensive Characterisation of the Compressive Behaviour of Hydrogels Using a New Modelling Procedure and Redefining Compression Testing. *Materials Today Communications* **2021**, *28*, 102518. https://doi.org/10.1016/j.mtcomm.2021.102518.

(425) Kontou, E.; Farasoglou, P. Determination of the True Stress–Strain Behaviour of Polypropylene.

(426) Alemán, J. V.; Chadwick, A. V.; He, J.; Hess, M.; Horie, K.; Jones, R. G.; Kratochvíl, P.; Meisel, I.; Mita, I.; Moad, G.; Penczek, S.; Stepto, R. F. T. Definitions of Terms Relating to the Structure and Processing of Sols, Gels, Networks, and Inorganic-Organic Hybrid Materials (IUPAC Recommendations 2007). *Pure and Applied Chemistry* **2007**, *79* (10), 1801–1829. https://doi.org/10.1351/pac200779101801.

(427) Scherer, G. W. Mechanics of Syneresis I. Theory. *Journal of Non-Crystalline Solids* **1989**, *108* (1), 18–27. https://doi.org/10.1016/0022-3093(89)90328-1.

(428) Kim, O. V.; Litvinov, R. I.; Weisel, J. W.; Alber, M. S. Structural Basis for the Nonlinear Mechanics of Fibrin Networks under Compression. *Biomaterials* **2014**, *35* (25), 6739–6749. https://doi.org/10.1016/j.biomaterials.2014.04.056.

(429) Maleki, H.; Shahbazi, M.-A.; Montes, S.; Hosseini, S. H.; Eskandari, M. R.; Zaunschirm, S.; Verwanger, T.; Mathur, S.; Milow, B.; Krammer, B.; Hüsing, N. Mechanically Strong Silica-Silk Fibroin Bioaerogel: A Hybrid Scaffold with Ordered Honeycomb Micromorphology and Multiscale Porosity for Bone Regeneration. *ACS Appl. Mater. Interfaces* **2019**, *11* (19), 17256–17269. https://doi.org/10.1021/acsami.9b04283.

(430) Zhu, Y.; Lu, W.; Guo, Y.; Chen, Y.; Wu, Y.; Lu, H. Biocompatible, Stretchable and Mineral PVA−Gelatin−nHAP Hydrogel for Highly Sensitive Pressure Sensors. *RSC Adv.* **2018**, *8* (65), 36999–37007. https://doi.org/10.1039/C8RA06193A.

(431) Xu, Q.; Engquist, B.; Solaimanian, M.; Yan, K. A New Nonlinear Viscoelastic Model and Mathematical Solution of Solids for Improving Prediction Accuracy. *Sci Rep* **2020**, *10* (1), 2202. https://doi.org/10.1038/s41598-020-58240-y.

(432) Gravelle, A. J.; Marangoni, A. G. The Influence of Network Architecture on the Large Deformation and Fracture Behavior of Emulsion-Filled Gelatin Gels. *Food Structure* **2021**, *29*, 100193. https://doi.org/10.1016/j.foostr.2021.100193.

(433) Krupa, I.; Nedelčev, T.; Račko, D.; Lacík, I. Mechanical Properties of Silica Hydrogels Prepared and Aged at Physiological Conditions: Testing in the Compression Mode. *Journal of Sol-Gel Science and Technology* **2010**, *53* (1), 107−114. https://doi.org/10.1007/s10971-009-2064-5.

(434) Gibson, L. J.; Ashby, M. F. *Cellular Solids: Structure and Properties*, 2nd ed.; Cambridge University Press, 1997. https://doi.org/10.1017/CBO9781139878326.

(435) Zhu, Y.; Zhang, X.; Xue, B.; Liu, H.; Wen, Y.; Xu, C. High-Strain-Rate Compressive Behavior of UHMWPE Fiber Laminate. *Applied Sciences* **2020**, *10* (4), 1505. https://doi.org/10.3390/app10041505.

(436) Chen, P.; Su, J.; Wang, H.; Yang, L.; Cai, H.; Li, M.; Li, Z.; Liu, J.; Wen, S.; Zhou, Y.; Yan, C.; Shi, Y. Mechanical Properties and Microstructure Characteristics of Lattice-Surfaced PEEK Cage Fabricated by High-Temperature Laser Powder Bed Fusion. *Journal of Materials Science & Technology* **2022**, *125*, 105−117. https://doi.org/10.1016/j.jmst.2022.03.009.

(437) Cai, Z.; Wu, J.; Wu, M.; Li, R.; Wang, P.; Zhang, H. Rheological Characterization of Novel Carboxymethylated Curdlan-Silica Hybrid Hydrogels with Tunable Mechanical Properties. *Carbohydrate Polymers* **2020**, *230*, 115578. https://doi.org/10.1016/j.carbpol.2019.115578.

(438) Kocen, R.; Gasik, M.; Gantar, A.; Novak, S. Viscoelastic Behaviour of Hydrogel-Based Composites for Tissue Engineering under Mechanical Load. *Biomed. Mater.* **2017**, *12* (2), 025004. https://doi.org/10.1088/1748-605X/aa5b00.

(439) Vasudevan, A. K.; Sadananda, K. Analysis of Fatigue Crack Growth under Compression–Compression Loading. *International Journal of Fatigue* **2001**, *23*, 365−374. https://doi.org/10.1016/S0142-1123(01)00172-4.

(440) Gibowicz, S. J.; Kijko, A. *An Introduction to Mining Seismology*; Elsevier, 2013.

(441) Klenam, D. E. P.; Oghenevweta, J. E.; Soboyejo, W. O. Fracture and Toughening of Intermetallics. In *Comprehensive Structural Integrity (Second Edition)*; Aliabadi, M. H. F., Soboyejo, W. O., Eds.; Elsevier: Oxford, 2023; pp 102−139. https://doi.org/10.1016/B978-0-12-822944-6.00070-0.

(442) Broberg, K. B. Elastostatic Cracks. In *Cracks and Fracture*; Elsevier, 1999; pp 99−246. https://doi.org/10.1016/B978-012134130-5/50005-2.

(443) Broberg, K. B. Differences Between Mode I and Mode II Crack Propagation. *Pure appl. geophys.* **2006**, *163* (9), 1867−1879. https://doi.org/10.1007/s00024-006-0101-7.

(444) Piletska, E.; Yawer, H.; Canfarotta, F.; Moczko, E.; Smolinska-Kempisty, K.; Piletsky, S. S.; Guerreiro, A.; Whitcombe, M. J.; Piletsky, S. A. Biomimetic Silica Nanoparticles Prepared by a Combination of Solid-Phase Imprinting and Ostwald Ripening. *Scientific reports* **2017**, *7* (1), 11537.

(445) Atterton, D. V. The Carbon-Dioxide Process. *AFS Transactions* **1956**, *64*, 14−18.

(446) Rabbii, A. Sodium Silicate Glass as an Inorganic Binder in Foundry Industry. *Iranian Polymer Journal* **2001**, *10* (4), 229–235.

(447) Meier, W.; Keck, O. Laser Raman Scattering in Fuel-Rich Flames: Background Levels at Different Excitation Wavelengths. *Measurement Science and Technology* **2002**, *13* (5), 741.

Appendices

Appendix A – Why pure CO_2 gas did not work?

Carbon dioxide gas is widely used to harden the sodium silicate-bonded sand systems in the metal casting industry. The so called "CO_2 process" was first conceptualized in 1898 and has gained a lot of acceptance since the 1950s. The process is based on forming a bond by setting the waterglass through brief exposure to CO_2 gas to bind sand grains together. The following chemical equation has been suggested for representing the reaction between carbon dioxide and water glass:

$$Na_2O.xSiO_2.yH_2O + CO_2 \longrightarrow Na_2CO_3 + xSiO_2.yH_2O \quad (1)$$

This equation is believed to be over-simplified [445]. Nonetheless, it has been generally accepted that the bonding between the sand grains in the carbon dioxide process is due to the silica gel formation.

Based on the results of previous proof-of-concept work, it was hypothesised that the setting time of waterglass-bioglass composites could be accelerated by using concentrated CO_2 gas, instead of letting them to air-set with atmospheric CO_2. To put this hypothesis to test, a series of preliminary experiments were performed, as detailed below.

First, a bicycle tire CO_2 inflator was used to measure the effect of introducing CO_2 on lowering pH in aqueous environments. The tip of the inflator was inserted into glass vials containing water and waterglass solutions mixed with a pH indicator solution, and gas was introduced until no further change in the color of the solution was observed. The results are shown in Figure A.1, where the pH of the solutions can be compared before and after the introduction of CO_2 gas. As seen, the pH was lowered in both the water and waterglass solutions due to the formation of carbonic acid. However, the lowest pH achieved in waterglass was approximately pH = 10.

Figure A.1 Water and waterglass solutions before and after CO_2 gassing using a bicycle CO_2 inflator. Each solution contains pH indicator, with the color change representing the decrease in pH due to the introduction of CO_2.

Next, a Soda Stream machine (SodaStream, London, U.K.) was used to apply concentrated CO_2 gas to a mixture of waterglass and 45S5 bioactive glass paste. With its higher pressure, the soda stream machine reduced the pH of the water to approximately 4 (see Figure A.2a), which is lower compared to the tire inflator. However, with waterglass, the pH remained around 10. This lack of significant change compared to the CO_2 tire inflator could be due to carbonic acid being a weak acid and the buffering ability of waterglass. Although the formation of silica gel after about 15 minutes was confirmed using the tube inversion method (Figure A.2b), the gel was only formed on the surface and not throughout the entire bulk, stopping the flow of the entire solution. This skin-effect was evident when stirring the solution with a glass rod; it reverted to a solution state.

After mixing bioactive glass and waterglass (according to the optimal ratios in Guzzo's work [23]), the paste was inserted into an open-ended cylindrical mold. The CO_2 gas was guided to the surface of the paste using a plastic tube and a nozzle with a pressure gauge (see Figure A.2c). The pressure was fluctuating between 2-20 psi and in some cases the concentrated pressure was so high that it destroyed the entire specimen (see Figure A.2d). To solve this problem, a long plastic cylindrical tube with the same width as the mold was used on top of the mold to increase the distance from the tip of the nozzle. However, the problem of having no control over the pressure and flow persisted, and in some cases, the specimens were pierced due to the high pressure (see Figure A.2e).

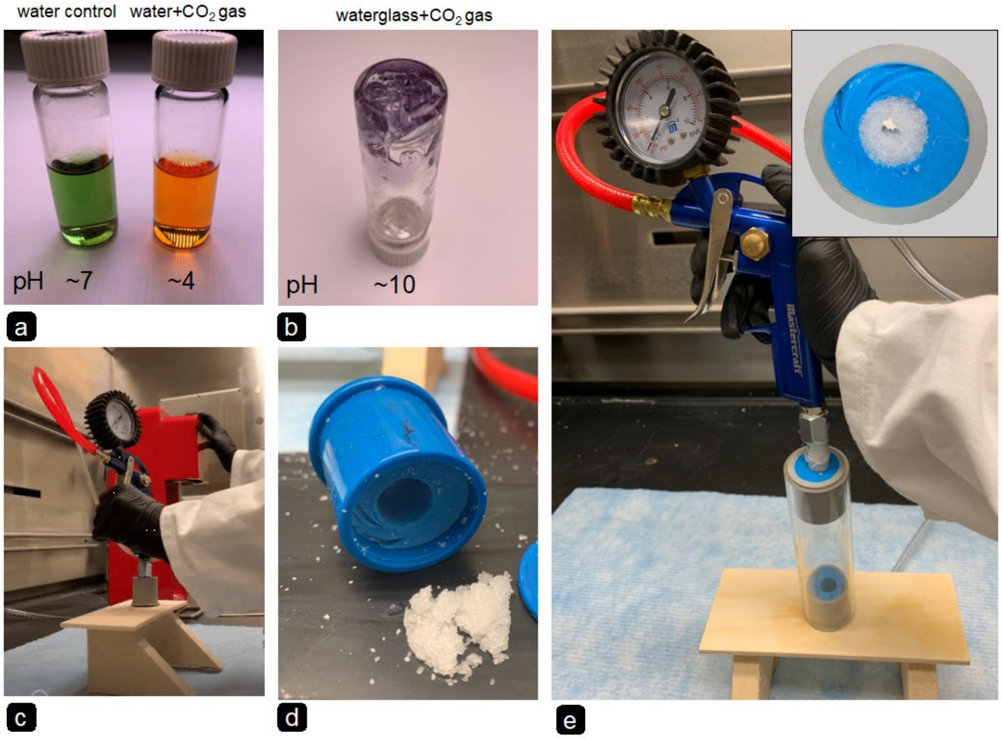

Figure A.2 (a) Water solutions containing pH indicator before and after CO_2 gassing using a Soda Stream machine. (b) Waterglass containing pH indicator after CO_2 gassing using a Soda Stream machine, with a layer of gel formed after gassing. (c) The procedure of CO_2 gassing of waterglass-bioactive glass paste inside an open cylindrical mold using a Soda Stream machine. (d) Damage to the waterglass-bioactive glass paste due to high concentrated pressure. (e) Using a long plastic cylinder to increase the distance of the nozzle. However, some specimens were still damaged by the concentrated pressure, as shown in the top right.

For better control over the gas pressure and flow, a CO_2 gas setup was used, consisting of a medical-grade CO_2 gas cylinder (Praxair, Danbury, CT, U.S.A), a pressure regulator (Harris Products Group, Mason, OH, U.S.A), LLDPE tubing (0.25" by 0.17", max 140 psi at 70°F), a flowmeter (Cole-Parmer, Vernon Hills, IL, U.S.A), and a nozzle (50a). Waterglass was poured into silicone rubber moulds measuring 0.4x0.4x1.0 cm. To initiate gelation, a gas stream was introduced by positioning the nozzle as close as possible to the surface of the solution and moving it side to side to ensure even coverage. The gas flow rate was maintained below 5 L/min to prevent splashing. A thin gel film was observed forming on the surface, which could be easily removed with tweezers (see (50b). Despite five minutes of gassing, only this thin film of gel was observed, with no gelation occurring in the bulk of the solution. This behavior can be attributed to mass transport limitations, where the rate of gelation at the surface outpaces the diffusion of reactants (CO_2 gas) into the bulk solution, thereby inhibiting the formation of a gel network throughout the entire volume.

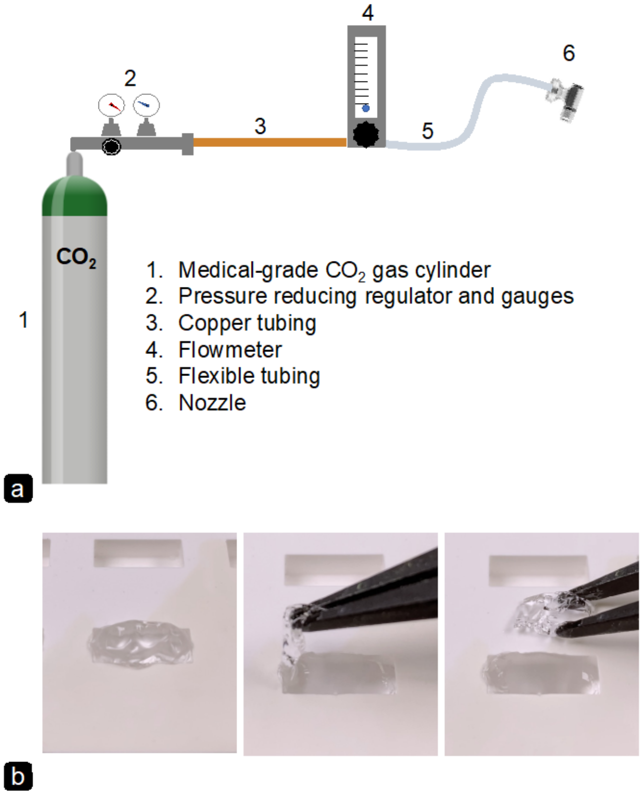

Figure A.3 Illustration detailing the components used to assemble a medical-grade concentrated CO_2 gas system (b) Image showing a negative silicone mold filled with waterglass, highlighting the formation of a thin silica gel film after exposure to medical-grade CO_2.

At this point, it was hypothesized that since the bioactive glass particles would be coated with thin layers of waterglass binder after mixing, forming a thin layer of gel might be sufficient to set the entire composite. Therefore, the mixture of bioactive glass and waterglass was poured into cylindrical molds and gassed using the CO_2 setup. The gassed composites were then tested in compression immediately after gassing from both sides using a PASCO materials testing tabletop machine equipped with a 7100 N load cell (PASCO Scientific Inc., Roseville, CA, U.S.A).

The strength of the composite compact is influenced by factors such as the SiO_2 ratio of the sodium silicate, gassing time, flow rate, and the water content of the silica gel [446]. We explored various gassing times (30-360 seconds) and flow rates (5, 7, and 10 L/min) at a constant pressure of 5 psi. Although the final composites retained their shape and integrity after gassing (see Figure A.4a), the mechanical testing results were generally inconsistent, and no meaningful correlation was found between compressive strength and the gassing variables. An example of the compressive stress-strain curves for air-set and CO_2-set composites is shown in Figure A.4b. Generally, the lower strength of CO_2-set composites contrasted to the air-set ones was expected, as the air-set composites had completely dried over a 10-day period, whereas the CO_2-set composites remained in a wet state.

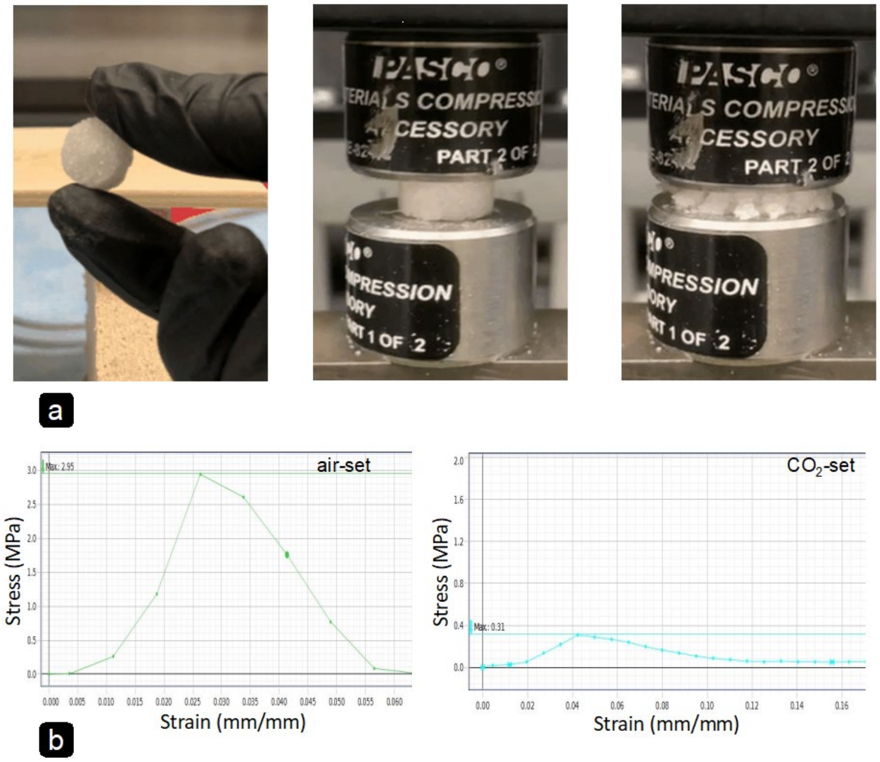

Figure A.4 The image on the left shows the composite holding its shape after waterglass gelation. The two images on the right demonstrate how the composite deforms under compressive load (b) These curves compare the mechanical properties of air-set and CO2-set waterglass-bioactive glass composites.

Despite successfully setting the composite within minutes, several major drawbacks were encountered with this method, which are detailed below:

1. **Mass transport limitations**: The setting reaction is mass-transport limited, meaning that it is limited by diffusion of CO_2 gas into waterglass. As gasification progresses, the surface viscosity increases to a point where it hinders further reaction, often leaving the reaction incomplete.

2. **Ambiguities in Reaction Kinetics and Setting Point**: Monitoring or controlling the setting point or the degree of gelation within the bulk is challenging. Chemical analysis techniques like SEM/EDX, XRD, Raman, and FTIR spectroscopy are not very useful due to the common elements and chemical bonds between sodium-silicate gel and bioactive glass, as well as their amorphous nature. Physical analysis methods such as Micro-CT or light microscopy are also limited due to the similar densities and the transparent nature of the components.
3. **Risk of under-gassing/over-gassing**: Finding the optimal gassing conditions for ideal gelation kinetics is crucial. Insufficient gassing can result in incomplete reaction, while excessive gassing—known as "over-gassing"—can significantly reduce binder strength. Over-gassing occurs due to gel dehydration, accelerated evaporation, hydration of sodium carbonate crystals, or formation of sodium bicarbonate [445]. Since the reaction kinetics cannot be easily monitored, both of these cases are likely to happen.
4. **Limited pH Range**: The pH of waterglass is a key factor in controlling gelation kinetics and final gel properties. Ideally, a wide pH range should be explored to find the best processing conditions for our application and target gelation time. However, the carbonic acid introduced from CO_2 gas is a weak acid and, combined with the buffering ability of the waterglass solution, cannot lower the pH below ~10. This limitation is problematic because the minimum gelation time in silica-water systems typically occurs around neutral pH, which is also ideal for biological applications to reduce tissue damage.
5. **Lack of Repeatability**: No meaningful correlation was found between gassing variables (such as time and flow rate) and the final compressive strength. Other factors, including the sample's height, the binder-to-bioactive glass ratio, the type of nozzle, and binder viscosity, also influence the results. With so many variables and no control or clear understanding of the gelation progression, achieving consistent results became nearly impossible.

Therefore, due to these limitations, it was decided to use acid solutions instead of CO_2 gas to induce gelation in waterglass.

Appendix B - Raman parameters–decisions made and why

Preliminary experiments were conducted to optimize parameters such as laser wavelength, laser power, exposure time, and the number of accumulations. Adjusting these parameters is crucial, as they influence the intensity of Raman scattering and, consequently, the overall spectral quality.

The first thing to find out was the laser wavelength. The Renishaw inVia Qontor confocal Raman microscope is equipped with 3 lasers of 532 nm (50 mW), 633 nm (17 mW) and 785 nm (300 mW). Figure 52 shows the Raman spectra of waterglass obtained by each laser. As can be seen, the spectrum obtained by 532 nm is the most intense with the least noise, and therefore, 532 nm laser was chosen for this study.

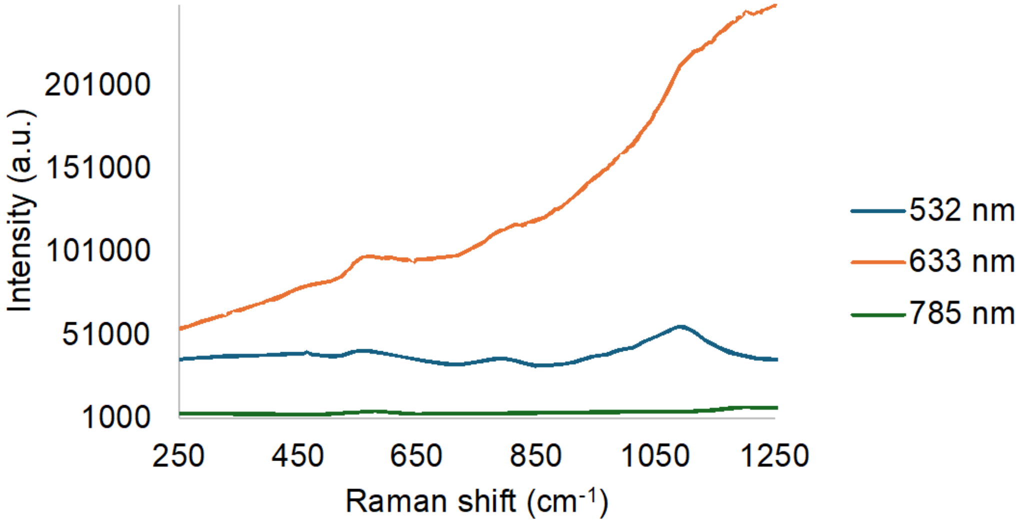

Figure B.1 Raman spectrum of waterglass at different laser wavelength (nm).

The choice of a 532 nm laser over 632 nm and 785 nm lasers for analyzing silicate solutions can be influenced by several factors:

1. **Fluorescence**: Fluorescence can interfere with Raman measurements by introducing background noise. Generally, longer wavelength lasers (such as 785 nm) tend to produce less fluorescence compared to shorter wavelengths (such as 532 nm).
2. **Intensity and Signal Strength**: The 532 nm laser generally produces a stronger Raman signal compared to longer wavelengths like 632 nm and 785 nm. This feature is due to the

λ−4 dependence of Raman scattering intensity, where λ is the wavelength. Shorter wavelengths yield more intense Raman scattering[447], which can be advantageous for detecting weaker signals from silicates.

3. **Resolution and Sensitivity**: The 532 nm laser can provide better spatial resolution and sensitivity in Raman spectroscopy, which is important for capturing detailed information about the silicate structures.

Therefore, while the 785 nm laser might produce less fluorescence, the 532 nm laser was chosen as it offered a stronger Raman signal and better sensitivity, making it more suitable for analyzing silicate solutions in this context.

Next was optimizing the laser power. It should be noted that laser power refers to the power at the sample surface, not just the laser beam. The laser power with Renishaw Raman could be adjusted to 5%, 10%, 50% and 100%. The strength of the Raman signal is directly proportional to the power of the Raman laser exciting the sample, so the best practice is to use full laser power whenever possible. However, full laser power can cause some samples to burn or, in our case, make waterglass to lose some water, and/or affect gelation kinetics due to the rise in temperature. A laser power of 50% was found to be the minimum required to obtain clear spectra with sufficient intensity and resolution (Figure 53).

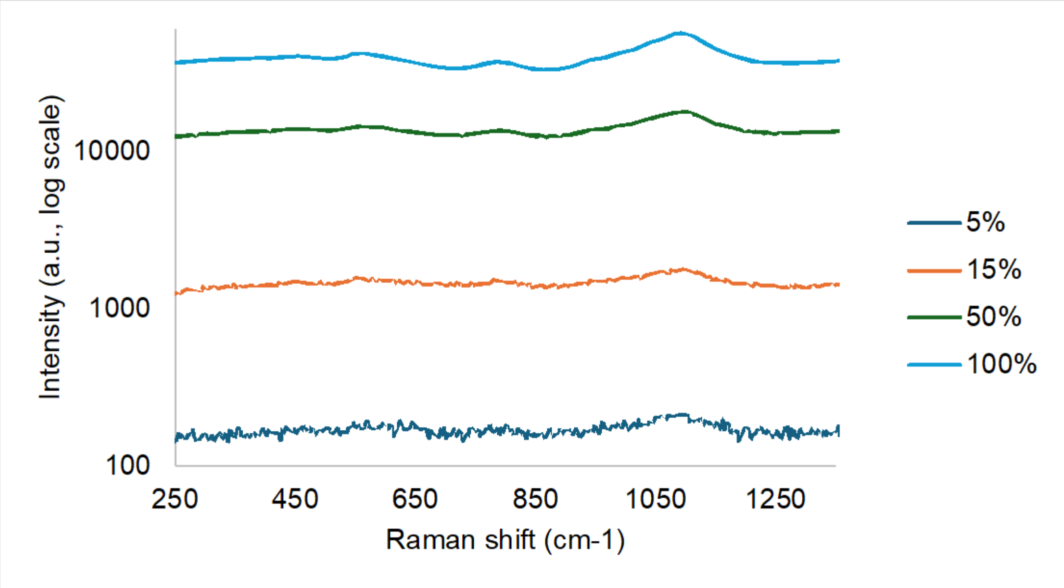

Figure B.2 Raman spectrum of waterglass at different laser powers (%).

Next, the variables considered were the exposure time (t_e) and the number of accumulations (N). Exposure time refers to the duration of each scan, while scan accumulation represents the number of scans performed repeatedly on the same spot. This set of variables is analogous to a photographic camera: a longer exposure time captures more detail in low light, yielding a clearer picture. Similarly, in Raman spectroscopy, a longer exposure time or more scan accumulations enhances the signal-to-noise ratio through averaging out the signal. Raman signals are measured in counts per second (cps). While increasing the exposure time or averaging more spectra does not increase the signal, it significantly reduces the noise, leading to a clearer spectrum. As shown in B.3, an exposure time of 1 second provided an acceptable signal-to-noise ratio. When combined with 60 accumulations, the signal-to-noise ratio was further improved, making the combination of these settings suitable for this study (Figure B.4).

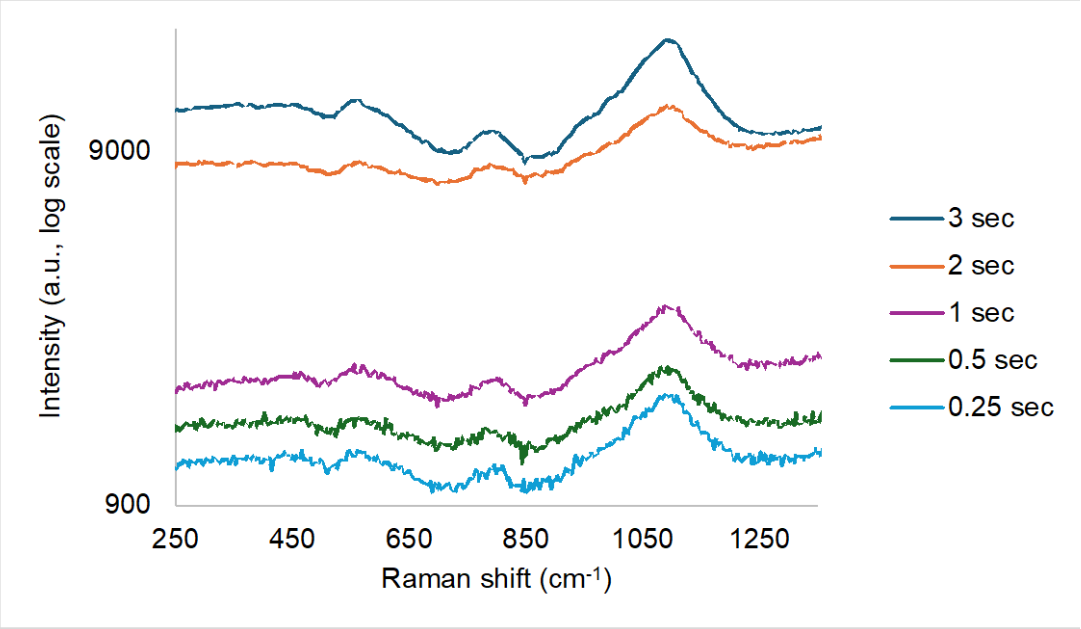

Figure B.3 Raman spectrum of waterglass with different exposure times. The number of accumulations was 60 for all spectra.

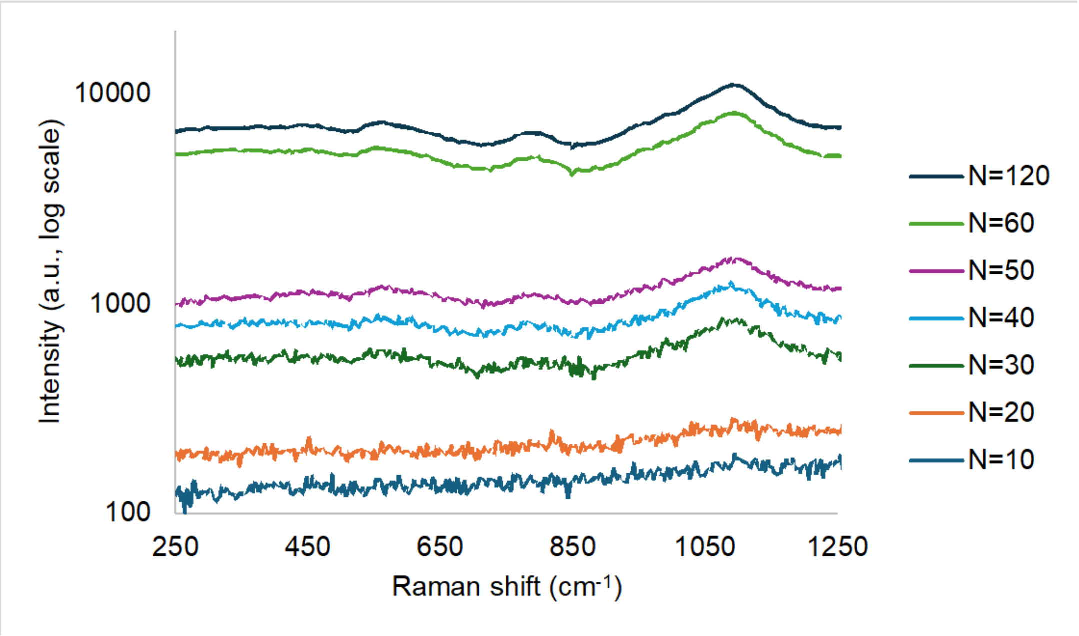

Figure B.4 Raman spectrum of waterglass with different number of accumulations (N). the exposure time was 1 second for all spectra.

A polystyrene multi-well plate was used as a container for performing Raman spectroscopy on silicate solutions. However, because polystyrene is Raman-active and produces peaks in the region of interest (see Figure B.5a), it was essential to eliminate any interference from the polymer. To address this issue, a Raman-inactive metallic screw (see Figure B.5b) was placed upright into each well, and the objective lens was precisely focused on the screw tip's surface. The well was then filled with the solution up to the tip of the screw, creating a very thin layer of solution covering the tip. This procedure ensured that the objective was kept focused on the solution surface. The spectrum was then acquired and compared with the polystyrene spectrum to ensure no peaks had originated from the container. Figure B.5c shows the difference in waterglass spectrum before and after putting the screw in the polystyrene plate containing the waterglass. The sharp peak at ~1000 cm^{-1} is form polystyrene, which was absent after putting the Raman-inactive screw in the well.

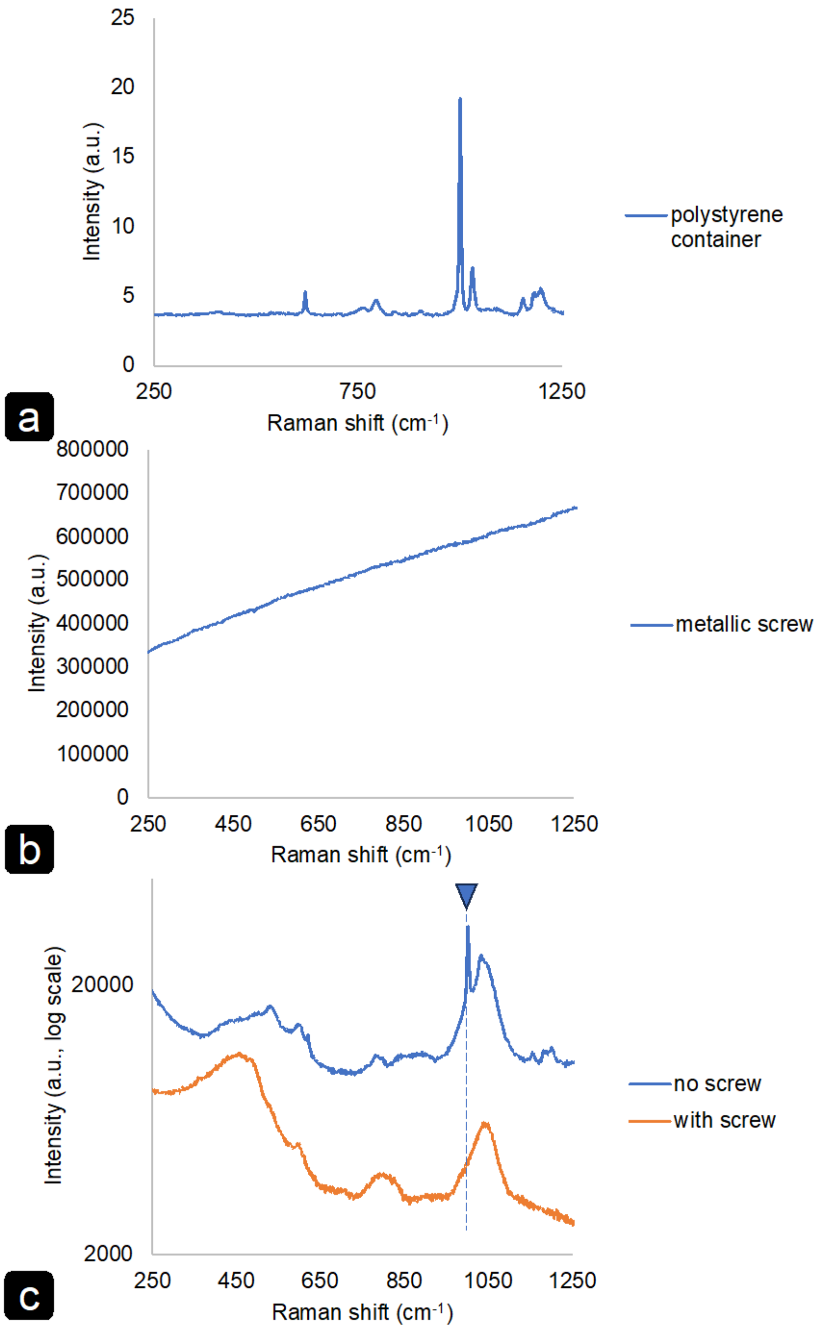

Figure B.5 (a) Raman spectrum of polystyrene (PS) container, showing strong peaks in the region of study (b) Raman spectrum of metallic screw, showing no peaks in the region of study (c) Raman spectra of waterglass, before and after putting a Raman-inactive screw inside the polystyrene container. The triangular marker and dashed line indicate the location of the PS Raman peak, which was absent when the metallic screw base was used to contain the liquid specimen being analysed.